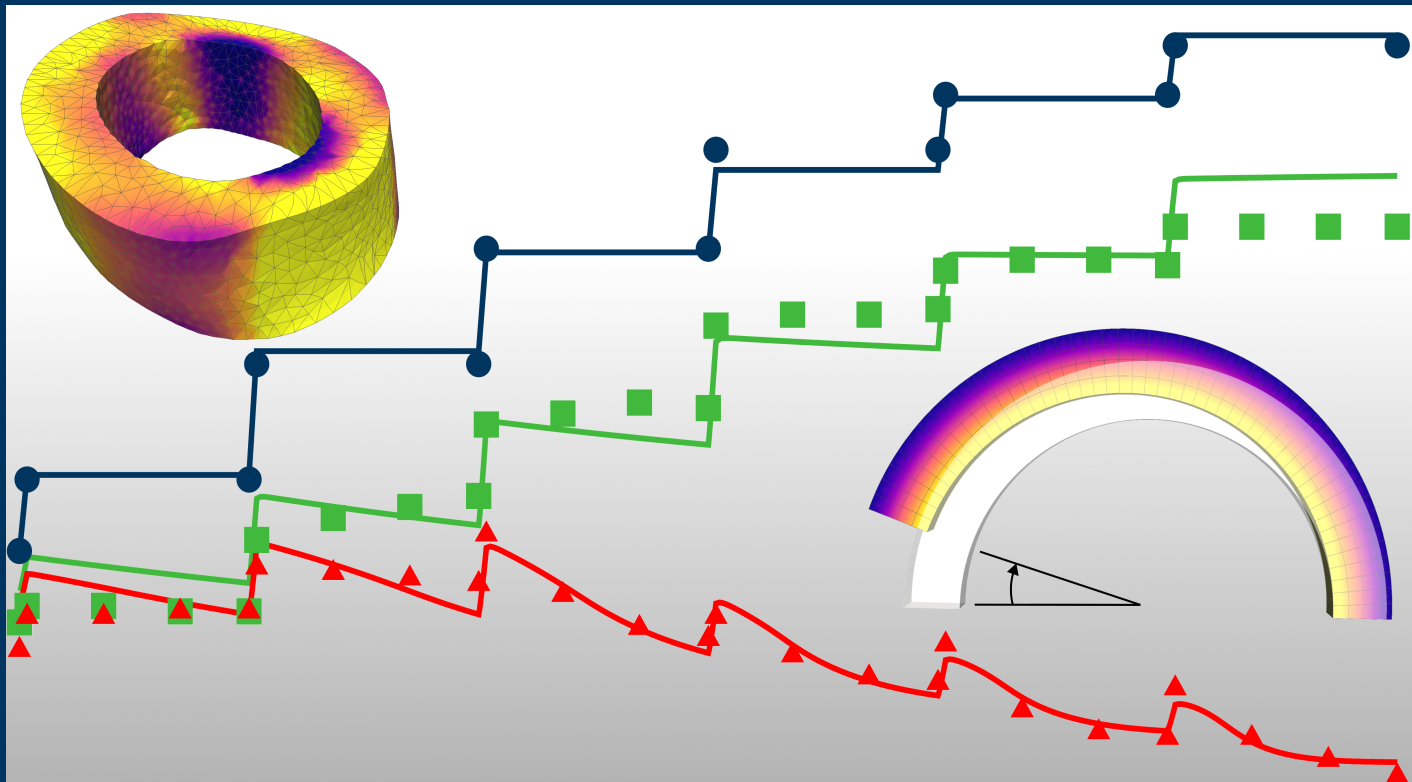


Modeling, Simulation and Analysis of Adaptive and Active Processes in Muscular Arteries

Klemens Uhlmann



Modeling, Simulation and Analysis of Adaptive and Active Processes in Muscular Arteries

Zur Erlangung des Grades
Doktor-Ingenieur (Dr.-Ing.)
an der Fakultät Bau- und Umweltingenieurwissenschaften
der Ruhr-Universität Bochum
genehmigte Dissertation

von

Klemens Uhlmann

Bochum 2024

**Mitteilungen aus dem Institut für Mechanik
Nr. 197**

Publisher:

Institute of Mechanics
Ruhr University Bochum
D-44780 Bochum

Prof. Dr.-Ing. habil. Daniel Balzani
Chair of Continuum Mechanics

Herausgeber:

Institut für Mechanik
Ruhr-Universität Bochum
D-44780 Bochum

Prof. Dr.-Ing. habil. Daniel Balzani
Lehrstuhl für Kontinuumsmechanik

ISBN: 978-3-935892-75-9

This material is presented to ensure timely dissemination of scholarly and technical work. Copyright and all rights therein are retained by the copyright holders. All persons copying this information are expected to adhere to the terms and constraints invoked by the author's copyright. These works or parts of it may not be used to repost reprint/republish or for creating new collective works for resale or redistribution to servers or lists without the explicit permission of the copyright holder.

Dieses Werk ist urheberrechtlich geschützt. Die dadurch begründeten Rechte, insbesondere die der Übersetzung, des Nachdrucks, des Vortrags, der Entnahme von Abbildungen und Tabellen, der Funksendung, der Mikroverfilmung oder der Vervielfältigung auf anderen Wegen und der Speicherung in Datenverarbeitungsanlagen, bleiben, auch bei nur auszugsweiser Verwertung, vorbehalten. Eine Vervielfältigung dieses Werkes oder von Teilen dieses Werkes ist zulässig. Sie ist grundsätzlich vergütungspflichtig. Zuwiderhandlungen unterliegen den Strafbestimmungen des Urheberrechtsgesetzes.

©2024 Klemens Uhlmann

Tag der Einreichung (thesis submission): 27.08.2024
Tag der mündlichen Prüfung (thesis defense): 14.11.2024

Erstgutachter (first referee): Prof. Dr.-Ing. habil. Daniel Balzani
Zweitgutachter (second referee): Prof. Dr.-Ing. Johanna Waimann
Prüfungsvorsitz (committee chair): Prof. Dr.-Ing. Justin Geistefeldt

Preface

I come from a family oriented towards science and teaching, so it's something that's always been a part of my life. Being raised in a loving, supportive and ambitious environment has led me to develop an interest in academia and allowed me the opportunity to tutor my peers in maths as early as in high school.

My biggest thanks and gratitude go to Professor DANIEL BALZANI, who continuously steered me further into the direction of academic studies and took me already on as a part of his team in the year 2015, while I was studying Civil Engineering at Technische Universität Dresden. Furthermore, he supported me to broaden my horizon by going to an English-speaking-country, USA, as a part of my study program. Being included in the laboratory for MRI research at University of California Los Angeles ignited the spark of my fascination and love for biomechanics.

After finishing my diploma in the end of 2017, I followed Professor DANIEL BALZANI to his new position as Chair of Continuum Mechanics at the Ruhr University Bochum (RUB). In the nearly 7 years spent in Bochum I got the opportunity to develop my own ideas and formulated multiple papers with colleagues and research partners.

My coworkers here, at RUB, proved to be great companions and greatly helped me in achieving my goals and created a fun work atmosphere. Especially one in particular - my colleague and friend - NIKLAS MISKA, who has been answering my requests for technical support with kindness and patience throughout my whole time here.

I also want to give special thanks to my childhood friend TZWÄNN KURRER for always lending me a listening ear and trying to keep me sane in the writing process. As well as my wife AGNIESZKA UHLMANN, who provided me with love and support these past few years.

Thank you.

Abstract

With the objective to put mechanical simulations of diseased muscular arteries on the clinical map, adaptive and active processes of the arterial tissue have to be captured in a mechanical model. In this thesis, the contraction of smooth muscle cells (SMCs) as well as anisotropic growth are characterized based on the current state of biological knowledge and associated obtainable experimental data. The proposed active material model couples stretch-dependent stimulation of receptors of the cell membrane directly with activation of contractile units of the SMCs which leads to vasoconstriction. Residual stresses are automatically computed by a novel kinematic growth model which, in contrast to other growth models, does not depend on an exact run-time for an optimal homogenization of stresses over the arterial wall. Based on this property, the combination of active material response and growth model is straightforward in numerical simulations. Time-dependency of the active material is considered as predominant while growth velocity is adjusted to enable robust and stable simulations. Disadvantages and uncertain parameters of the model are overcome by formulating an optimization procedure for simulations with idealized geometry of the arterial wall. In consequence, a reliable mechanical description of a healthy middle cerebral artery of a rat is obtained. The potential of the active and growth model is further demonstrated in a simulation with a realistic geometry of an artery segment. The presented models provide opportunities for expansions such as modeling the influence of antihypertensive drugs. One possible model adjustment for separated growth of different components of the arterial tissue is demonstrated in a numerical simulation which might be a necessary expansion to predict growth in diseased arteries sufficiently.

Zusammenfassung

Mit dem Ziel, mechanische Simulationen von erkrankten muskulären Arterien in den klinischen Alltag einzubinden, müssen die adaptiven und aktiven Prozesse des arteriellen Gewebes in einem mechanischen Modell abgebildet werden. In dieser Doktorarbeit werden die Kontraktion von glatter Muskulatur sowie das anisotrope Wachstum auf der Grundlage des aktuellen Stands des biologischen Wissens und der damit verbundenen verfügbaren experimentellen Daten charakterisiert. Das vorgeschlagene aktive Materialmodell koppelt die dehnungsabhängige Stimulation von Rezeptoren der Zellmembran direkt mit der Aktivierung von kontraktilen Proteinen in den glatten Muskelzellen, was zu einer Vasokonstriktion führt. Eigenspannungen werden automatisch durch ein neu formuliertes kinematisches Wachstumsmodell berechnet, welches im Gegensatz zu anderen Wachstumsmodellen nicht von einer exakten Laufzeit für eine optimale Homogenisierung der Spannungen über der Arterienwand abhängig ist. Diese Eigenschaft ermöglicht eine einfache Kombination von aktiver Materialantwort und Wachstumsmodell in numerischen Simulationen. Die Zeitabhängigkeit des aktiven Materials ist bestimmend für die Zeitschrittweite, während die Wachstumsgeschwindigkeit des Gewebes angepasst wird, um robuste und stabile Simulationen zu realisieren. Nachteile und unklare Parameter der Modelle werden durch die Ausführung eines Optimierungsverfahrens in Simulationen mit idealisierter Geometrie der Arterienwand bewältigt. Dies führt zu einer zuverlässigen mechanischen Beschreibung einer gesunden

mittleren Hirnarterie einer Ratte. Des Weiteren wird das Potenzial des aktiven Materialmodells und des Wachstumsmodells in einer Simulation mit realistischer Geometrie eines Arteriensegments demonstriert. Die vorgestellten Modelle bieten Möglichkeiten für Erweiterungen wie etwa die Modellierung des Einflusses von blutdrucksenkenden Medikamenten. Eine mögliche Modellanpassung für das getrennte Wachstum verschiedener Komponenten des Arteriengewebes wird in einer numerischen Simulation demonstriert, welche notwendig sein könnte, um das Wachstum in erkrankten Arterien zuverlässig vorherzusagen.

Contents

1	Introduction	1
1.1	Motivation	1
1.2	Structure of the Thesis	4
2	Biological Basics for Characterization of the Mechanical Behavior of Arterial Walls	7
2.1	Structure of Arteries	8
2.1.1	Tunica Intima	8
2.1.2	Tunica Media	10
2.1.3	Tunica Adventitia	12
2.2	Contractile vascular SMCs	13
2.2.1	Contractile Unit of SMC	14
2.2.2	Phosphorylation and Dephosphorylation of Myosin Heads	15
2.2.3	Stretch-Dependent Stimulation of GPCRs	18
2.2.4	Mechanical In Vitro Experiments for SMC Contraction	20
2.3	Adaptation Processes of the Arterial Wall	23
2.3.1	Protein Synthesis	24
2.3.2	Arterial Adaptation by Different Phenotypes of SMCs	27
2.3.3	Arterial Adaptation by Fibroblasts and Myofibroblasts	30
2.3.4	Age-dependent Adaptation of the Arterial Wall and Conclusion for Mechanical Modeling	32
3	Continuum Mechanical Basics	35
3.1	Kinematics	35
3.2	Stress Measures	39
3.3	Balance Equations	40
3.3.1	Balance of Mass	40
3.3.2	Balance of Linear Momentum	41
3.3.3	Balance of Angular Momentum	42
3.3.4	Balance of Energy (First Law of Thermodynamics)	43
3.3.5	Balance of Entropy (Second Law of Thermodynamics)	44
4	Finite Element Method	47
4.1	Variational Problem	47
4.2	Linearization	49
4.3	Discretization	50
5	Numerical Modeling of the Contraction of Vascular SMCs	59
5.1	State of the Art: Vascular SMCs	60
5.2	Mechanical Model of the Arterial Wall	63
5.2.1	Mechanical-Chemical Coupling	63
5.2.2	Chemical-Mechanical Coupling	68
5.2.3	Inclusion of the Passive Response and Formulation of the Total Strain-Energy Density Function	70
5.3	Numerical Implementation	71

6	Numerical Simulation with Active Material Response	81
6.1	Model Parameters: Adjustment and Validation	81
6.1.1	Optimization of the Model Parameters	83
6.1.2	Comparison of Simulation Results and Experimental Data	84
6.1.3	Investigation of the Contraction at a Material Point	86
6.2	Application of Pressure Waves in an Artery	88
7	Numerical Modeling for the Automatic Calculation of Residual Stresses	93
7.1	State of the Art: Residual Stresses	94
7.2	Multiplicative Decomposition of the Deformation Gradient for Inclusion of Growth Processes	98
7.2.1	Adjustment of Balance Equations for Growing Systems	100
7.3	Anisotropic, Kinematic Growth Model based on Cauchy Stresses as Driving Force	102
7.3.1	Calculation of Stresses and Tangent Modulus	104
7.4	Numerical Implementation	105
8	Numerical Investigation of Growth Model and Optimization: Passive Response	109
8.1	Principal Deformations of Arterial Rings based on Predefined Fields for the Growth Factors	110
8.2	Formulation of Optimization Procedure to Obtain Accurate Geometry and Material Behavior	114
8.3	Results for First Application of Optimization	119
8.4	Homogenization of Stresses is Independent from exact Run-Time for Proposed Growth Model	122
8.5	Efficiency of Optimization: Variation of Fiber Direction or Axial Growth Conditions	125
9	Combination of Growth and Active Response for Optimal Structural Problem	129
9.1	Adjustment of the Growth Model	129
9.2	Adjustment of the Optimization Procedure	130
9.3	Optimization of the Structural Problem with Inclusion of the Active Material Response	131
10	Combination of Growth and Active Contraction in Realistic Geometry	137
10.1	Creation of Finite Element Mesh and Determination of Realistic Fiber Orientation	137
10.2	Consideration of Growth Directions and Adjustments of Growth Model	140
10.3	Execution of the Simulation	141
11	Outlook: Separated Growth for Different Parts of Material	145
11.1	Additive Split of Material Model and Separated Growth	145
11.2	Optimization with Inclusion of Active Material Response	147
12	Conclusion and Outlook	153

A	Optimized Parameters for Adjusted, Active Case	157
B	Previous Growth Model with Elastic Part of Mandel Stress as Driving Force	158
C	Numerical Investigation of Optimization: Axial Stretch and Growth Factor	160
D	Growth with Active Response and Trace of Cauchy Stress as Driving Force	162
	List of Figures	164
	List of Tables	165
	List of Acronyms	167
	References	184
	Curriculum Vitae	185

1 Introduction

1.1 Motivation

Treatment for cardiovascular diseases (CVDs) improved recognizably over the last decades. The implantation of a stent or a bypass extends the life span of patients with ischaemic strokes or heart diseases considerably. Compared to 1990, the world wide mortality rate from CVDs decreased by 30% [190]. Nevertheless, CVDs still accounted for 42% of all deaths in Europe in 2021 [174] (see Fig. 1.1). Therefore, as a preventative measure hypertension is treated widely with antihypertensive drugs to decrease risks of atherosclerosis and plaque rupture in patients' arteries. Antihypertensive drugs can be divided into five main classes, angiotensin-converting enzyme inhibitors (ACEIs), calcium channel blockers (CCBs), diuretics, beta blockers (BBs), and angiotensin II receptor blockers (ARBs). The majority of patients is prescribed ACEIs, CCBs and ARBs [93], all of which reduce the contractility of smooth muscle cells (SMCs) in the arterial wall (see Fig. 1.2). The selection of drug type and dosage typically follows medical studies and depends on the experience of the attending physician. While the choice of drug type might be less significant for preventative measures, the mechanical impact of antihypertensive drugs on arteries of patients with acute symptoms is hardly predictable. The material properties of atherosclerotic plaque differ substantially from the tissue of the arterial wall [127]. Fibrous plaque builds a cap which protects from rupture. Underneath, the plaque can consist of fibrofatty, calcifications, and a necrotic core [93]. Especially in atherosclerotic plaque of patients with infections, the inflammation of the tissue leads to swelling as a consequence of which the fibrous part of the plaque is thinning and makes rupturing more likely [135]. From a mechanical point of view, a reduction of the contractility of the arterial wall resulting from a prescription of an antihypertensive drug could lead to a further increase of the stresses in the fibrous plaque. Therefore, computational simulations of arterial walls in a state of health or disease can be a promising tool to investigate the mechanical behavior of the tissue and plaque to optimize medical treatment as well as to develop new diagnostic approaches.

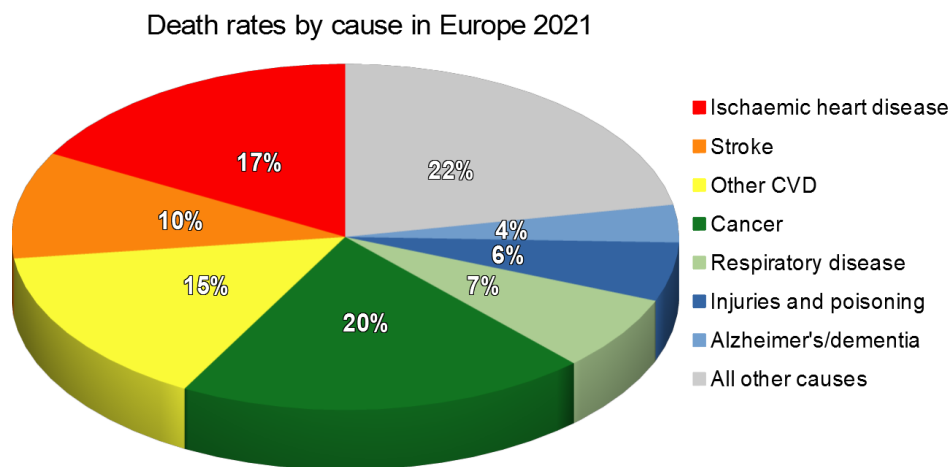


Figure 1.1: Illustration of death rates by cause in Europe in 2021 [174]. 17 of out 20 strokes are ischaemic in nature [121], hence, more than 25% of deaths are connected to blocked blood vessels.

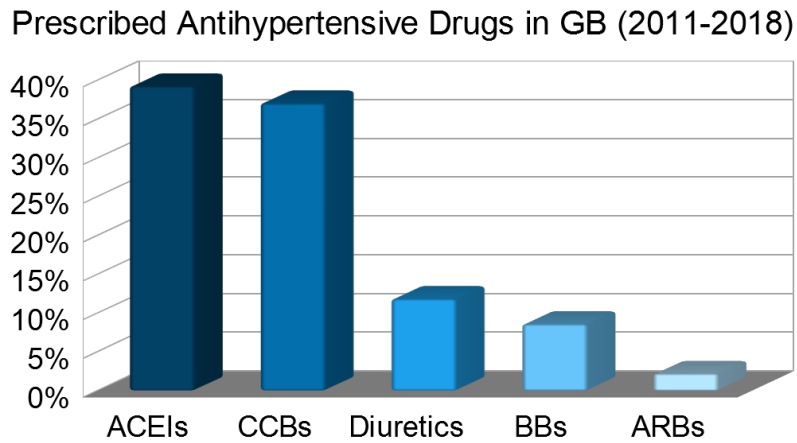


Figure 1.2: Distribution of first-line therapy prescribed antihypertensive drugs in Great Britain from 2011 to 2018 [93]. To prevent deaths connected to blocked blood vessels, 77.9% of prescribed antihypertensive drugs decrease the contractility of arteries. Note that more than one drug can be prescribed to a single patient and, consequently, the sum of the percentage exceeds 100%.

To accomplish these objectives, numerical simulations have to include all specifics of the arterial wall to enable an accurate calculation of the stress and stretch distributions. Next to the strongly nonlinear and anisotropic passive behavior of the extracellular matrix (ECM) of the arterial tissue with elastin and collagen fibers, the active material response has to be considered. Especially in muscular arteries, contraction of the SMCs is mechanically predominant to protect the tissue from damage by overstretching. Furthermore, the adaptability of resistance arteries enables a regulation of the blood flow in times of higher levels of physical activity to reduce the supply of inner organs and provide the active muscles with oxygen-rich blood. Mechanical experiments demonstrate that the contractile behavior of a muscular artery can even decrease its diameter after a considerable increase of the blood pressure [94]. Currently, mechanical models for the active response are mainly incapable of establishing such a contractility in numerical simulations. To model contractions properly, the mechanical model should include the stretch-dependency of the biological tissue. This stretch-dependency is connected to G-protein coupled receptors at the membrane of the SMC which are, e.g., activated by angiotensin II but can also initiate the intracellular reaction chain for the contraction mechanism when the cell membrane is stretched due to an increased blood pressure. The resulting contraction of the cell can remain for a long time after blood pressure recovers to a normal level which has to be covered by the mechanical model.

Additionally, experiments illustrate that arteries shorten when excised from the body and open up when cut longitudinally [92]. Accordingly, the mechanical behavior of arteries is substantially controlled by residual stresses which enable a uniform absorption of the load on the artery over the entire wall thickness. In consequence, the mechanical stresses are equally distributed. Elastic arteries without residual stresses exhibit substantially larger stresses at the inner side of the arterial wall than at the outer side which is mechanically disadvantageous and would increase the chance of damage by overstretching. The adjustment of the residual stresses is based on the ability of the tissue to grow which occurs anisotropically. Accordingly, mechanical models aim to

construct a realistic stress distribution inside the arterial wall by replicating the growth process of the tissue. A realistic growth model could even be employed to predict the growth process of a patient-specific artery over the upcoming years. In consequence, treatments and check ups for patients can be planned ahead. Such an approach is aimed for by constraint mixture models [87]. However, the prediction of the growth process of the tissue is extraordinarily complicated. Various types of cells such as fibroblasts and phenotypes of SMCs regulate the growth processes for elastin, collagen and contractile SMCs quantitatively differently. Next to the size and location of the artery, growth processes are also modified by infections, inflammations and damage of the arterial wall which affect the phenotype modulation of the SMCs [195]. Excluding infections and inflammations of the arterial wall from the modeling process, a growth model could achieve long term predictions for distinct cases such as for patients with Marfan syndrome. There, the genetic disease causes aortic dilation based on abnormal growth processes of the tissue which is most likely connected to the absence of certain phenotypes of SMCs [137]. For a more general description of residual stresses in the arterial wall, the second approach for growth models is more applicable which is kinematic growth [148]. Especially when adaptive and active material processes have to be combined, a more straightforward model for growth is advantageous.

This thesis is based on the idea of coupling a realistic mechanical model for the contraction of SMCs in muscular arteries with a kinematic growth model which enables a reliable description of mechanical fields in the arterial wall. For this idea to be realized a couple of challenges have to be taken into account. A first challenge posed by the combination of the active processes mentioned is the time scale. After excitation, the contraction of SMCs occurs over a time range of several minutes and lasts up to a few hours. In contrast, growth processes proceed several days and the corresponding residual stresses are the result of growth over years. However, since the exact tracking of the temporal progress of the growth process is not a primary concern of the numerical simulations here, time-dependency can be considered as an abstract matter and the numerical growth process can be accelerated. A second challenge results from the dependency of both processes on the stresses and stretches of the material. The growth process leads to a volumetric change of the material which includes an adjustment of the stretches. A stretch of the SMCs results in a contraction of the tissue and, consequently, a change of the corresponding stresses. Simultaneously, the growth model is dependent on the stresses in the tissue and reacts correspondingly to the contraction of the active material response with a modification of the growth process. To solve this issue, one of both processes has to be heavily adjustable in the velocity while the final result of the process remains unchanged. Since the time-dependency of the growth process is only accounted for abstractly, the formulation of the growth model is the preferred candidate for adjustments to enable the coupling of growth and active response. Accordingly, simulations can be run in a realistic time frame for smooth muscle contraction coupled with a simultaneous growth process which is highly accelerated but still sufficiently slow to enable the active response to react on corresponding changes of the stretch.

However, when the coupling of growth and smooth muscle contraction results in simulations which present realistic stress distributions, these simulations are not describing the structural problem for the arterial wall appropriately. The resulting geometry at

the end of the simulations has to match the geometry of a real artery. But the referential state of the geometry can change significantly during the growth process based on the volumetric adjustments. A reliable prediction of the final state of the resulting geometry can only be achieved by knowing about the volumetric changes of the reference geometry during growth phases and, therewith, a correct choice of the corresponding reference configuration. This referential state can hardly be chosen manually, but rather automatic by performing an optimization. An additional challenge comes from the fitting of the material parameters. To optimize the material parameters to describe the mechanical behavior of the arterial wall appropriately, mechanical experiments are necessary to evaluate the deformation process of the arterial tissue under a certain loading scenario. In these experiments, the arterial tissue contains residual stresses that are often not considered in the simulations used to replicate the experimental results. Accordingly, the results of simulations which apply the values of these optimized material parameters are inadequate. The precision of the fitting of the material parameters can be increased when the growth process of the geometry is completed before the numerical replication of the experiments is performed.

Taking into account the discussed challenges, this thesis presents an optimization procedure that includes the simultaneous application of kinematic growth and smooth muscle contraction to improve the mechanical description of the structural problem of a muscular artery significantly. As a result of this optimization, the resulting state of the geometry matches measurements of a real artery. Furthermore, the material parameters are fitted to match experimental data after the growth process is accomplished. In consequence, computational simulations are able to describe the mechanical behavior of a healthy muscular artery adequately which constitutes a significant step towards improving treatment and diagnosis of cardiovascular diseases.

1.2 Structure of the Thesis

This thesis comprises twelve chapters which include theoretical background for modeling of muscular arteries from a biological and mechanical point of view and modeling, simulation, and analysis of the contraction of vascular SMCs as well as residual stresses by a growth model.

Subsequent to the introduction, Chapter 2 provides a general overview of the structure of arteries and the functions of the tissue components. In particular, the mechanism behind the contraction of vascular SMCs and associated intravascular reactions chains are described. Furthermore, the growth process of different components of the arterial tissue is characterized to outline the adaptation of the arterial wall. In Chapter 3, basics of continuum mechanics are explained which cover kinematics, stress measures in the context of finite strain theory, and balance equations. Afterwards, Chapter 4 presents the finite element method which is applied for mechanical simulations in this thesis. A mechanical model for the contraction of vascular SMCs is described in Chapter 5 which also contains an overview of the state of the art of numerical modeling of vasoconstriction. The active material model includes the stretch-dependent stimulation of membrane receptors which leads to an activation of contractile units in the cell. Furthermore, the numerical implementation into *FEAP* is expressed in detail. Subse-

quently, Chapter 6 contains the description of numerical simulations with the active material model. The simulation results are presented which replicate experimental data of a middle cerebral artery of a rat. In additional simulations, the contraction of the arterial wall under intravascular pressure waves is investigated which mimics the pulse pressure in the physiological state of the artery. In Chapter 7, a novel kinematic growth model is formulated which bases on Cauchy stresses as driving forces for the growth process. The chapter includes an overview of the state of the art of numerical modeling of residual stresses in biological tissue as well as the influence on the balance equations when changes of mass are possible in simulations. Furthermore, the implementation into *FEAP* is expressed. The growth model is investigated in numerical simulations with regard to the passive material response, in Chapter 8. The simulations are coupled with an optimization procedure which allows a reliable description of the mechanical properties and fits the geometry of an arterial ring after growth to experimental data. It is shown that the proposed growth model does not depend on an exact run-time for an optimal homogenization of stresses over the arterial wall. In Chapter 9, the growth model is coupled with the active material model in numerical simulations. This includes an adjustment of the optimization procedure to further improve the simulations results. In consequence, a reliable mechanical description of a healthy middle cerebral artery of a rat is obtained. The potential of the active and growth model is further demonstrated in a simulation with a realistic geometry of an artery segment in Chapter 10. A possible adjustment of the growth model is described and tested in a simulation in Chapter 11 which enables separated growth of collagen fibers. Eventually, Chapter 12 finishes this thesis with concluding remarks and an outlook in which possible expansions for the description of diseased arteries are suggested.

2 Biological Basics for Characterization of the Mechanical Behavior of Arterial Walls

The structure of the arterial wall is complex, it contains various different cell types and protein networks which characterize its mechanical behavior. Moreover, depending on its location and size, the structure of an artery varies considerably. The network of arteries constitutes a system for pulmonary and systemic circulation where oxygen-poor blood is transported to the lungs and oxygen-rich blood is delivered to body tissues, respectively. To enable both circulations, the heart consists of four chambers: the right and left atrium which receive the blood as well as the right and left ventricle which pump the blood into lung and body. Chamber walls of the left ventricle are substantially thicker than walls of the right ventricle and generate higher pressure. The associated variation between systolic and diastolic pressure must be endured by the aorta, the largest artery in the human body with a diameter of up to 3 cm and a wall thickness of 4 mm [50]. Due to the load on the arterial wall, the aorta and other large arteries are mostly elastic, with elastin and collagen fibers predominant in their mechanical behavior. The farther an artery is from the heart, the higher the proportion of SMCs in the tissue of the arterial wall. Accordingly, these medium and small sized arteries are regarded as muscular arteries capable of considerable contraction. The strongest contractions occur in resistance arteries, which include small arteries with diameters up to 400 μm [33], and arterioles. Arterioles with diameters less than 100 μm [88], provide blood to the organs and are primarily composed of SMCs. The smallest blood vessels are capillaries which transport oxygen and nutrients to cells of the body. Capillaries contain no SMCs and are defined as vessels with diameters less than 10 μm consisting of one single layer of endothelial cells. Although the lack of SMCs suggests that capillaries cannot contract, more recent studies demonstrate that pericytes, spatially isolated cells at the capillary, can regulate blood flow physiologically through neuronal activity [70]. However, for modeling the contraction of the arterial wall, capillaries and their potential regulation by pericytes are not considered in this thesis.

To enable a viable description of the mechanical behavior of the arterial wall, the fundamental constituents of the tissue must be identified and their functions investigated. In this chapter, the different layers of the arterial wall are briefly introduced, and their functions are discussed with reference to the latest biological and medical findings. The focus is on the intracellular biochemical reaction chains in SMCs to describe the various initiators of cell contraction. This is particularly important for comprehending the contraction of resistance arteries which can narrow in response to increased blood pressure. The contraction of SMCs in larger arteries can be addressed by more general approaches that describe the nonlinear material behavior from a macroscopic perspective, which will be discussed in the state-of-the-art modeling of the active material response in Chapter 5. However, even with a detailed description of the biochemical reaction chains, experimentally quantifying the reagents and products at every step is currently unachievable. Therefore, the most significant mechanisms of the active contraction have to be identified to enable an applicable formulation of the model that describes the mechanical reaction of the arterial wall reliably.

Additionally, the growth behavior of the tissue, which is responsible for the residual stresses in the artery, is characterized. While collagen growth based on the activity of cells such as fibroblasts has been well-known for decades [26], the significance of different phenotypes SMC in the growth process has only been highlighted in more recent publications. This chapter explains functions of these SMC phenotypes during tissue growth.

2.1 Structure of Arteries

Elastic and muscular arteries, as well as arterioles, consist of three distinct layers: the tunica intima, tunica media and tunica adventitia. While these layers are fundamentally similar across different types of arteries, the structure and mechanical behavior of the tissue vary significantly. These variations are related to the size and location of the artery, its function, and the corresponding blood pressure. In a healthy human, systemic arterial blood pressure typically measures 110–120 mmHg systolic and 70–80 mmHg diastolic. The difference between systolic and diastolic blood pressure is known as pulse pressure. The hyperelastic material behavior of the large arteries, such as the aorta, significantly reduces the variation in pressure between contraction and relaxation in the left ventricle of the heart resulting in a pulse pressure of approximately 40 mmHg. Generally, both, blood pressure and pulse pressure, decrease as its distance from the heart increases [66]. Resistance arteries are the most efficient regulators of blood pressure due to their ability to actively contract. Consequently, blood flow through resistance arteries decreases the pressure from roughly 80 mmHg to 25 mmHg, protecting the capillary tissue from damage due to overstretching. To enable the characterization of the mechanical behavior of the arterial tissue, the constituents of the three layers and the differences between elastic and muscular arteries, as well as arterioles and capillaries, are discussed in the following sections. The structure of a typical elastic or muscular artery is illustrated in Fig. 2.1.

2.1.1 Tunica Intima

The tunica intima is the innermost layer of the arterial wall. In the majority of arteries, the tunica intima consists of a single layer of endothelial cells attached to a thin basal lamina. Uniquely, capillaries contain an additional cell type called pericyte which are spatially isolated cells to control the contraction. Endothelial cells play several crucial roles in maintaining the healthy and homeostatic state of the arterial wall which has a combined surface area of 3000–6000 m² in the human body and comprises over 10¹³ cells [103]. Endothelial cells are the first to build a new blood vessel during embryonic development. They also rapidly generate new vessels in response to tissue injury or hypoxic conditions in mature arteries, through a highly orchestrated process called angiogenesis [103]. The permeability of blood cells and macromolecules, such as fats and proteins, through the tissue of an arterial wall is regulated by the structure of endothelial cells. In elastic and muscular arteries, the permeability is very low, ensuring a regulated blood transport. It increases slightly in arterioles and significantly in capillaries to allow the supply of tissues with oxygen-rich blood and nutrients. In cases of acute or chronic inflammation, cancer, or wound healing, vascular permeability

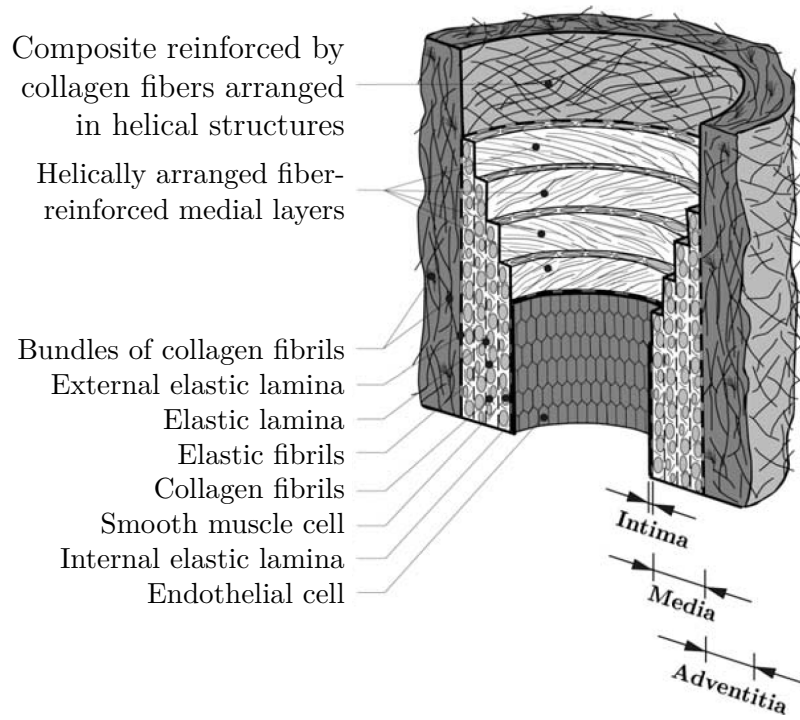


Figure 2.1: Illustration of the structure of a common elastic or muscular artery. The arterial wall consists of three basic layers: the tunica intima, tunica media and tunica adventitia. Depending on size and location of the artery, the constituents differ in proportion, orientation and structure. Especially the density of smooth muscle cells is substantially higher in the media of muscular arteries than in elastic arteries. Illustration is adopted from HOLZAPFEL ET AL. [80].

dramatically increases [125].

The shape of endothelial cells varies depending on the type of artery, but they are generally elongated in the axial direction of the artery: measuring roughly 30-50 μm in length, 10-30 μm in width, and 0.1-10 μm in thickness. The elongation of endothelial cells enables them to sense shear stresses at the arterial wall exerted by flowing blood. In consequence, the endothelial cells enhance the production of nitric oxide (NO) when shear stresses are increased which is a well-known vasodilator. NO activity levels can be determined in experiments investigating the impact of inhibitors of endothelial NO synthase such as N(G)-Nitro-L-arginine methyl ester [111].

The exact reaction chain leading to the relaxation of SMCs based on higher levels of NO is not completely understood yet. However, Krüppel-like factor 2 (KLF2) is a mechanosensitive transcription factor in endothelial cells [42]. Its activation induces endothelial NO synthase. NO is transmitted to vascular SMCs via myoendothelial gap junctions which are channels that connect the cytoplasm of both cells types directly [37]. Consequently, NO activates soluble guanylyl cyclase, an enzyme that converts guanosine triphosphate (GTP) into cyclic guanosine monophosphate (cGMP) and pyrophosphate within SMCs. Pyrophosphate leads to the phosphorylation of several substrate proteins, though their identities are not completely established [110]. It is likely that the IP_3 R-associated cGMP kinase substrate decreases the release of calcium ions (Ca^{2+}) from the sarcoplasmic reticulum [102], a membrane-bound struc-

ture in muscle cells that stores ions. An additional function of KLF2 in endothelial cells is the regulation of genes which participate in anti-thrombotic, antioxidant, and anti-inflammatory activities [42]. Low blood flow and oscillatory flow inside of the artery lead to lower shear stresses including a decreased activity of KLF2 which induces a pro-inflammatory, pro-thrombotic state with high cell turnover and increases the development and progression of atherosclerosis. This decreased activity of KLF2 is highly relevant for the disease of muscular arteries. However, in elastic arteries, the basal activity of KLF2 and production of NO in endothelial cells are considerably higher [111]. This suggests that higher activity helps prevent the stiffening of elastic arteries, maintaining their blood pulse-smoothing properties, and protecting the tissue of the arterial wall from dysfunctions. Consequently, the risk for atherosclerosis is substantially higher in muscular arteries than in elastic arteries which makes the mechanical modeling of the characteristics of muscular arteries for improved diagnostics and therapy even more important.

Nonetheless, based on the minor thickness of the tunica intima and the corresponding negligible mechanical impact, simulations of the arterial wall mostly exclude the representation of this tissue layer in the geometry, an approach also taken in this thesis. Therefore, the mechanical properties are not further described. The role of endothelial cells as producer of vasodilators and vasoconstrictors is more important. This process is controlled by the magnitude of the axial shear stress at the inner surface of the arterial wall. Next to NO, prostaglandin I₂ and endothelium-derived hyperpolarizing factor act as less dominant vasodilators and endothelin-1 (ET-1) as vasoconstrictor which collectively comprise four products from endothelial cells [59]. Especially ET-1 has a significant impact on the contraction of SMCs [182]. However, distinguishing the influence of one product from the stimulation of another is highly difficult. Consequently, the inclusion of the intima with the impact of endothelial cells on the contraction of SMCs into the mechanical model is recognizably complicated and demands various experiments which are not available at the current state of art. Furthermore, a reliable consideration of the shear-stress-regulated production of vasodilators and vasoconstrictors requires the coupling of fluid and solid within of the mechanical simulation, an approach that could be applied in the future but is not covered by the simulations in this thesis.

2.1.2 Tunica Media

From a mechanical point of view, the tunica media is the most important layer of the arterial wall. The tunica media is separated from the tunica intima by the internal elastic lamina, a thin sheet of elastic fibers which is fenestrated for myoendothelial gap junctions [151]. Furthermore, the tunica media consists of several layers, also called lamellar units, with elastic fibers, collagen fibers, and SMCs which, themselves, are separated by additional elastic lamina [133]. These additional layers are also called medial lamellar units, they are 12 to 17 μm thick, and their number depends on the size of the artery ranging between 40 and 60 medial lamellar units in a human aorta [16]. The elastic fibers in the tissue of the tunica media are composed of bundles of elastin. They build a connective structure for cells while not being organized parallelly, but in the form of branching strands. Consequently, this constituent of the tissue builds an elastic matrix that is modeled as the isotropic part of the passive material response of

the media and is usually labeled as elastin.

The second part of the elastic material behavior is constituted by the collagen fibers of the media tunica, the central load bearing components in the axial and circumferential direction of the wall. Comparable to a string, collagen fibers are wavyly embedded into the tissue and, therefore, do not actively contribute to the mechanical behavior of the arterial wall in an unstretched state. Depending on the growth process, stretch levels at which the collagen becomes mechanically active differs from fiber to fiber. In consequence, mechanical experiments show a high non-linearity for the stress-strain relationship. Interestingly, mechanical experiments with arteries are usually conducted *ex vivo*/*in vitro*, which leads to a relaxation of the tissue and alters its initial mechanical response. As a result, a series of loading-unloading cycles has to be performed to precondition the sample until the stress-strain response becomes repeatable [116]. Mechanical experiments of the tunica media in human coronary arteries [81], the human abdominal aorta [8], and the human carotid artery [163] indicate a lower stretch in circumferential direction than in axial direction at the same stress level (see, e.g., Fig. 2.2a). This mechanical behavior aligns with the orientation of collagen fibers, which are primarily aligned in the circumferential direction. However, studies of fiber orientation in arteries of varying sizes and locations in the body show that fiber orientation is strongly dependent on the specific artery. Generally, in larger arteries such as the aorta [152], collagen fibers of the media tend to align in axial direction as well, which could be connected to the elastic behavior of the tissue that leads to larger variations of the stretch in axial direction when blood pressure levels change. As opposed to the aorta, the fiber direction of collagen in the common iliac artery [152] are more closely aligned with the circumferential direction of the arterial wall. Studies of arteries from the human brain, showed that the collagen fibers were nearly circumferential [54] indicating that fibers in the media of muscular arteries have almost no axial alignment. It needs to be emphasized that the orientation of collagen fibers in the media is dispersed, even though a clear tendency of the fiber direction can be determined.

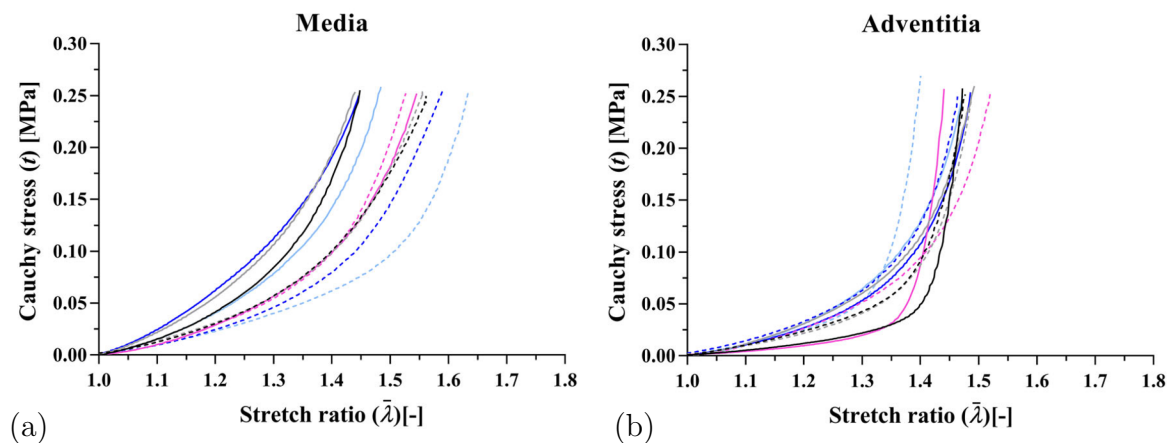


Figure 2.2: Illustration of stretch-stress curves from uniaxial tension tests of (a) the media and (b) adventitia of pig upper thoracic aortas. Solid lines represent data from tension tests in circumferential direction. Dashed lines indicate data from tests in axial direction. Data originates from GIUDICI ET AL. [64]. SMCs cannot contract during the experiment. Data from tests of the media indicate that collagen fibers are primarily oriented into circumferential direction. Axial and circumferential material behavior of the adventitia is comparable.

While modeling the collagen fibers as anisotropic part of the elastic material model with two fiber directions is sufficient to replicate the data of mechanical experiments with numerical simulations (see, e.g., in [8]), the inclusion of fiber dispersion into the model could lead to more reliable results [96].

Another crucial mechanical constituents of the tunica media considered in the mechanical models are SMCs. The contraction of SMCs is governed by a network of intracellular proteins and is affected by dozens of reaction chains initiated intra- and extracellularly. Studies of distinct influences on the contraction allow some insights into the functions of the cell which are discussed in Section 2.2.

2.1.3 Tunica Adventitia

Similar to the boundary between tunica intima and tunica media, the tunica adventitia is separated from the tunica media by an external elastic lamina. The tissue of the tunica adventitia consists of fibroblasts, elastin, collagen fibers, macrophages, and contains terminal nerve fibers. The adventitia plays a key role in vascular health of the artery and its most obvious function is the integration of the artery into the surrounding tissue. In larger arteries, the supply of the outer layers of the arterial wall with oxygen and nutrients is ensured by vasa vasorum which are smallest blood vessels within the adventitia. Furthermore, the nervi vasorum (vascular nerves) inside of the adventitia innervate the SMCs of the media and partially regulate vasodilation and vasoconstriction. From a mechanical point of view, the adventitia is significantly less relevant than the media. A comparison between the passive mechanical behavior of the media and the adventitia of pig upper thoracic aortas is illustrated in Fig. 2.2. The adventitia is mainly composed of fibroblasts which, unlike SMCs, do not express α -actin or myosin and, therefore, show a lower mechanical stability and no contractile mechanism. Consequently, the adventitia could rather be considered as connective tissue than as an additional layer of the arterial wall. However, a recent study of different elastic and muscular arteries from pigs, dogs, and cats demonstrated that, depending on the type of artery, the structure of the adventitia should be more accurately described as two-layered [189]. Especially in larger muscular arteries, a first more compact layer with many collagen fibers oriented into longitudinal direction is located next to the media. This compact layer is relatively thin in elastic arteries and basically not existent in small muscular arteries. The existence and relative thickness of this compact layer in different types of arteries could be explained by the mechanical properties of the media. Collagen fibers in the media of elastic arteries are the predominant mechanical component and partially oriented longitudinally [152]. Consequently, the artery does not require a considerable mechanical influence from the adventitia. However, collagen fibers and SMCs in larger muscular arteries are primarily aligned in circumferential direction to enable a sufficient contraction of the arterial wall. Since the pulse pressure in these arteries is still considerably high and displacements due to body motion affect the tissue frequently, a further stabilization of the arterial wall in axial direction by longitudinal collagen fibers in the adventitia is effective. In small muscular arteries, the load in axial direction is less significant than in larger muscular arteries and, hence, the adventitia in such arteries contains comparably less collagen, leaving a compact layer unidentifiable.

While fibroblasts may seem negligible in the mechanical description of the arterial wall, their role in maintaining arterial wall health is comparable to that of endothelial cells in the intima [183]. Firstly, under injury of the tissue, fibroblasts can differentiate into myofibroblasts which have a similar contractile mechanism as SMCs and play a crucial role in wound healing [35]. Furthermore, the production of NO in the adventitia is considerably higher than in the media of the arterial wall [99], even though the main source of NO are endothelial cells of the intima. Experiments with fibroblasts of the adventitia also demonstrated the release of ET-1 after a stimulation with angiotensin II [6] which naturally occurs in the human body through the activity of the angiotensin-converting enzyme. Consequently, the production of vasodilators and vasoconstrictors in the adventitia may influence smooth muscle contraction. However, as with many biochemical processes, the amount of NO and ET-1 which is directly synthesized in the adventitia is challenging to quantify and the corresponding impact of a changing concentration of NO or ET-1 on the contraction of SMCs requires further investigation.

2.2 Contractile vascular SMCs

SMCs exist in all hollow organs of the human body and enable the contraction of organs such as the urinary bladder, the uterus, or arterial walls. SMC tissues differentiate into multiunit SMCs and single-unit SMCs, where arteries contain the single-unit type which contracts simultaneously [149]. SMCs can adapt to their environment and adjust their functionality when inflammations or injuries of the tissue occur. Accordingly, different phenotypes of SMCs exist and exhibit variations in structure and biochemical mechanisms. This section focuses on the vascular SMCs in their contractile state and describes the contractile mechanisms which lead to an autoregulation of the blood flow through muscular arteries. Note that the state of knowledge about intracellular reaction chains which lead to a variation of the mechanical response of SMCs increases every year. However, discovery of new details of certain biochemical mechanisms often amplifies the complexity of cell functioning thereby raising many unanswered questions. Consequently, results of experiments can lead to contradictory conclusions about the predominant mechanisms which control the relaxation or contraction of vascular SMCs. To avoid such contradictions, the recently published book by GAO [59] is used as fundamental source that contains detailed illustrations and explanation for the current state of knowledge of vascular SMCs.

In a healthy artery, vascular SMCs mostly exist in the contractile state being 50 to 200 μm long and 2 to 8 μm wide. The SMC contraction is governed by several constituents of the cell which include the cytoskeleton, the cell membrane with membrane receptors and ion channels, the sarcoplasmic reticulum, and mitochondria. Mitochondria are the power house of the cell and generate the majority of adenosine triphosphate (ATP) which serves as an energy provider to drive and support processes in living cells. Furthermore, mitochondria might play a crucial role in the migration of vascular SMCs to the inner side of the arterial wall when tissue injuries occur, thereby enabling SMCs to repair the ECM [126]. The cytoskeleton builds a protein network of microfilaments, intermediate filaments, and microtubules inside the cell which shape the cell and enhance its mechanical resistance against deformations. The scaffold inside the cell is also

involved in endocytosis, cell migration, and cellular division, and, most importantly, contains the contractile units which are responsible for SMC contraction. Similar to striated muscles, the contraction of SMCs is affected by the concentration of Ca^{2+} in cytosol. This concentration can be regulated by the influx of calcium to the SMC through open ion channels of the cell membrane and the sarcoplasmic reticulum. The sarcoplasmic reticulum (SR) serves as Ca^{2+} storage of the cell with a concentration up to 2,000 times higher than in the cytosol. It is mostly located in the cell membrane to directly influence the ion flow of potassium, sodium, chlorine, and calcium through membrane channels. Especially the stimulation of membrane receptors can influence the intensity of calcium influx, but also regulate the activity of enzymes inside the cell. Stimulation can result from the extracellular binding of an agonist to the receptor, but also includes a stretch-dependent activation of G protein-coupled receptors. While studies of the arterial tissue include mostly *ex vivo* experiments, knowledge about *in vivo* processes such as the interaction of blood vessels with the autonomic nervous system remains scarce. However, it is known that the activity of the sympathetic and parasympathetic nervous system leads to a release of norepinephrine, ATP, and Neuropeptide Y which act as vasoconstrictors as well as acetylcholine and calcitonin gene-related peptide (CGRP) which are vasodilators [161]. While the neurotransmitters delivered from the varicosities interact with SMCs at the corresponding receptors (such as α , β receptors, P1, P2 receptors, muscarinic acetylcholine receptors, CGRP1 receptors), they also stimulate receptors at endothelial cells which regulates functions such as the production of further agonists of SMCs (e.g., ET-1). The autonomic nervous system is able to increase the contraction of SMCs in the arterial wall under acute stress, but also plays an essential role in maintaining physiological homeostasis. Homeostasis generally refers to coordinated physiological reactions that maintain most of the steady states in the body. Nonetheless, for the mechanical modeling of the arterial wall, the autonomic nervous system can only be considered as regulator of the basal contractile state as the execution of *in vivo* experiments are crucial to determine the variation of the mechanical response of the arterial issue as response to neural activity.

To explain the well-understood parts of the SMC contraction mechanisms, in the following segments of this chapter, structure and functionality of the contractile units of vascular SMCs are represented. Furthermore, the influence of stimulated G protein-coupled receptors in the cell membrane of SMCs and the resulting intracellular reaction chains which lead to a change of the contractile state of the cell are described.

2.2.1 Contractile Unit of SMC

Contractile units of SMCs, also referred to as myofilaments, consist of thin and thick filaments. Thin filaments are composed of double helices of actin monomers with a width of 7 nm which build the microfilaments of the cytoskeleton and are connected to dense bodies. Actin occurs in SMCs in three different forms: α smooth muscle actin accounts for 60%, β actin for 20% and γ actin for another 20% [192]. Only α smooth muscle actin is part of the contractile units. While γ actin is mainly located in the cell cortex and β actin is associated with dense bodies, α smooth muscle actin filaments span along the length of the SMC. Accordingly, SMC contraction affects primarily its length which makes the orientation of the cell significant to conceive the mechanical behavior of the arterial tissue. Furthermore, experiments demonstrated that the length

of thin filaments could increase due to actin polymerization during the contracted state of the SMC [14] which could lead to a higher contraction of the cell.

The thick filament of the contractile unit is formed by type II myosin molecules. Two intertwined myosin heavy chains (MHCs) form a long double helical structure. At the amino termini (end of the proteins), the chains build separate globular structures which form two myosin heads. The lever arm of a myosin head contains binding domain for a regulatory myosin light chain (MLC) and an essential MLC. The phosphorylation of the myosin head, which is actually a phosphorylation of serine 19 at the regulatory MLC, enables the myosin heads to build cross-bridges to the thin filament and perform power strokes which bend the attached myosin head and result in a contraction of the cell [168]. While the role of the essential MLC is not entirely understood, the interaction of the regulatory MLC with the helix-A of the essential MLC is supposed to be significant for the phosphorylation process [173]. Thick filaments seem to be relatively short in general, though their length and the associated number of myosin heads vary [113]. However, just as for the thin filament, polymerization of monomeric free myosin probably leads to an elongation of thick filaments which improves the contractility of vascular SMCs [32]. Another important feature of the myosin heads is the latch-bridge configuration. After a stimulation of the SMC which leads to a contraction, the rate of phosphorylation falls to a lower level. To avoid the relaxation of the cell, myosin heads are able to stay attached to actin after dephosphorylation (latch state) [145] which enables maintaining the stress state. As a result, SMCs can prolong contractions without paying energetic costs of rapidly cycling cross-bridges. Generally, the SMC physiology with the unique characteristics of cross-bridge cycling, allows the cell to consume remarkably less energy and to sustain the contraction as opposed to striated muscles. A scheme of the SMC contraction and mechanisms in the contractile units is illustrated in Fig. 2.3.

2.2.2 Phosphorylation and Dephosphorylation of Myosin Heads

The phosphorylation of myosin heads and the corresponding ability to perform power strokes is governed by activated myosin light-chain kinase (MLCK), an intracellular enzyme whose activity is coupled to the concentration of Ca^{2+} in the cytosol. Calcium ions interact with calmodulin (CaM) which is a multifunctional intermediate calcium-binding messenger protein and also influences the calcium flow from membrane channels and the SR [100]. CaM has four EF-hand Ca^{2+} binding sites and activates MLCK as $\text{Ca}^{2+}/\text{CaM}$ complex. In consequence, the activated MLCK enzyme leads to a binding of phosphate to serine 19 at the regulatory MLC. The concentration of MLCK in the SMC is relatively low compared to the amount of myosin heads of thick filaments inside the cell. Therefore, the rapid phosphorylation of myosin heads after a stimulation to contract the cell is remarkable. Surprisingly, studies using total internal reflection fluorescence microscopy revealed that MLCK moves on actin bundles and stress fibers of the SMC cytoskeleton by a random 1D diffusion mechanism [84] which increases the ability to phosphorylate the regulatory MLC significantly. Another factor for the rapid phosphorylation is the phosphorylation of MLCK itself. A substantial increase of the cytosolic Ca^{2+} concentration leads to an activation of $\text{Ca}^{2+}/\text{CaM}$ -dependent protein kinase II which can interact with MLCK and cause a phosphorylation [17]. Phosphorylated MLCK exhibits a higher activity than non-phosphorylated MLCK and,

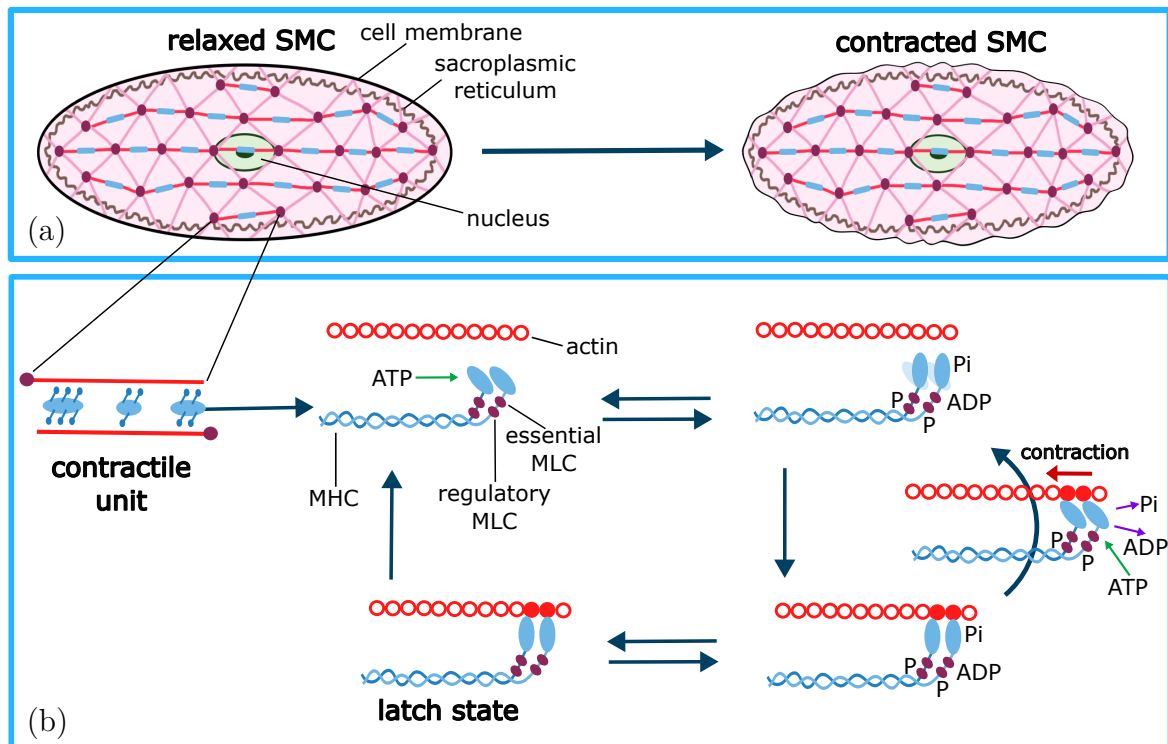


Figure 2.3: Schematic illustration of vascular SMC and the contractile mechanism. (a) SMC in relaxed and contracted state. Contractile units are mainly oriented in longitudinal direction of SMC which results in a corresponding contraction of the cell. (b) Contractile unit and interaction of myosin heads with actin filaments. Contractile units contain several myosin filaments of different lengths. Myosin heads can attach to actin filament after phosphorylation and perform power strokes which leads to the contraction. Adenosine triphosphate (ATP) serves as energy provider. Dephosphorylated myosin heads are able to stay attached to actin which is considered the latch state. Myosin heads in the latch state enable SMCs to maintain the contracted state.

consequently, interacts faster with the regulatory MLC of myosin heads and resulting in a stronger contraction of the cell.

Inflow and outflow of Ca^{2+} is regulated by various channels in the SMC membrane and the SR, a process detailed in TYKOCKI ET AL. [175] and thereby only briefly described here. The basal intracellular Ca^{2+} concentration of a SMC is $0.1 \mu\text{M}$ at rest, it can rise to $1.5 \mu\text{M}$ when maximally stimulated [97]. In contrast, the Ca^{2+} concentration is approximately $200 \mu\text{M}$ in the SR and 2 mM extracellular [18] which is up to 20,000 times higher than in the SMC. For the contraction of the SMC, voltage-gated L-type calcium channels (LTCCs) are the long lasting main Ca^{2+} influx pathway. Voltage-dependent T-type channels and transient receptor potential channels (TRPCs) play an additional, but less significant role for the influx of extracellular Ca^{2+} [138]. The opening probability of voltage-dependent calcium channels is directly associated with the membrane potential, that is the difference in electric potential between the interior and the exterior of a biological cell. The electric potential of the SMC is primarily controlled by the concentration of calcium, potassium, sodium and chloride ions in the cytosol. A certain amount of LTCCs, but also store-opened calcium channels (SOCCs) [143] are permanently open leading to a continuous Ca^{2+} inflow. Consequently, a basic out-

flow of cytosolic Ca^{2+} by SR Ca^{2+} -ATPase, plasma membrane calcium ATPases and sodium-calcium exchangers (NCXs) is necessary to remain a homeostatic state of the SMC. Furthermore, stimulation of inositol 1,4,5-trisphosphate (IP_3) gated channels and calcium-gated channels (ryanodine receptors; RyRs) of the SR play a crucial role in the signaling chain for the inflow of Ca^{2+} into the SMC which involves, e.g., calcium waves through the cell as well as calcium sparks and calcium puffs leading to a local increase of the Ca^{2+} concentration [4]. Overall, numerous participants are involved in the inflow and outflow of Ca^{2+} and the corresponding system is complex. An illustration of the described elements is shown in Fig. 2.4.

As a second crucial enzyme of the contraction mechanism of SMCs, active myosin light-chain phosphatase (MLCP) regulates the dephosphorylation of myosin heads. For this process, the phosphate at the regulatory MLC interacts with a water molecule, its

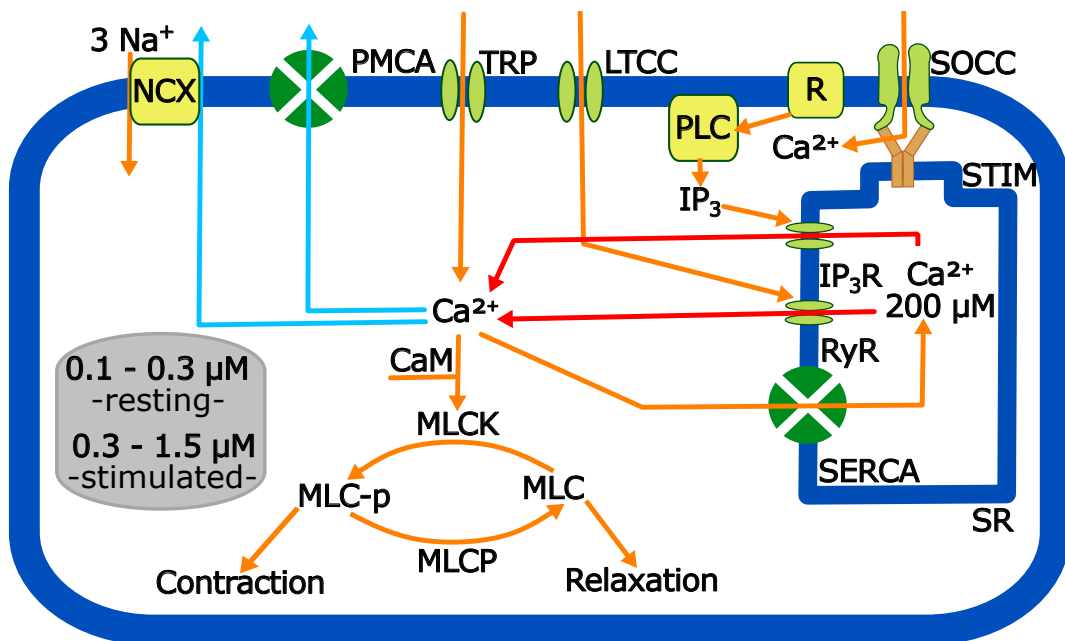


Figure 2.4: Regulation of intracellular calcium concentration Ca^{2+} in vascular SMCs. Concentration of Ca^{2+} in the extracellular space and the sarcoplasmic reticulum (SR) can be several thousand times higher than in the cell. A certain proportion of voltage-gated L-type calcium channels (LTCCs) and store-operated calcium channels (SOCCs) is opened even without cell stimulation. Homeostasis of the basal concentration is maintained by outflow of Ca^{2+} by plasma membrane calcium ATPases (PMCAs), sodium-calcium exchangers and by sequestration into the SR by SR Ca^{2+} ATPase (SERCA). A stimulation of receptors (Rs) can lead to a rapid increase of the Ca^{2+} concentration which causes an activation of myosin light-chain kinase (MLCK) by Ca^{2+} /calmodulin (CaM) complexes. In consequence, an increased phosphorylation of myosin light chains (MLCs) results in a contraction of the vascular SMC. A proportion of the Ca^{2+} inflow is achieved through the opening of voltage-gated calcium channels and TRPCs of the cell membrane. In addition, the stimulated Rs lead to an elevation of inositol inositol 1,4,5-trisphosphate (IP_3) which open channels with corresponding receptors of the SR. Simultaneously, RyRs are stimulated by the increased concentration of Ca^{2+} in the cytosol. The decrease of Ca^{2+} in the SR is sensed by the stromal interaction molecule which interacts with store-operated Ca^{2+} channels. Illustration is based on GAO [59].

reaction resulting in a split of the phosphate from the myosin head. The activity of MLCP can be changed by a phosphorylation of its myosin phosphatase target subunit 1 (MYPT1). However, depending on the phosphorylation site of MYPT1, the activity can be increased or decreased which is especially important in context of the regulation of the contractility of SMCs by vasodilators and vasoconstrictors [144]. Dozens of phosphorylation sites of MYPT1 were found and investigated, but only for the minority a relevant functional impact to MLCP could be demonstrated [115]. One clear inhibition of MLCP stems from phosphorylation at the phosphorylation sites Thr-696 and Thr-853 (human sequence) which is initiated, e.g., by an increased activity of Rho-associated coiled-coil kinase (ROCK) in context of a stimulated vasoconstriction. Contrarily, the phosphorylation sites Ser-695 and Ser-852 leads to increased MLCP activity and decreased contractility [201].

Consequently, the rate of phosphorylation and dephosphorylation of regulatory MLCs depends on various interactions of MLCK and MLCP with different elements of the SMC and its cytosol. Especially the influences of MLCP in the contractile mechanism was not recognized until the beginning of this century while the interaction of MLCK and the cytosolic Ca^{2+} -concentration was significantly better understood. Many of the interactions with MLCK and MLCP need further study, however, it is certain that the stimulation of G coupled-protein receptors plays an important role in the initiation of intracellular reactions chains which are associated with the activity of both enzymes.

2.2.3 Stretch-Dependent Stimulation of GPCRs

G protein-coupled receptors (GPCRs) consist of seven alpha-helices spanned through the cell membrane, the amino terminus and three transmembrane connecting loops positioned extracellularly as well as the carboxy terminus and three transmembrane connecting loops located intracellularly. GPCRs can be stimulated by the binding of an agonist extracellularly or by a stretch of the cell membrane which leads to comparable yet not equal reactions. The receptors exert their effect by G proteins inside the cell. G proteins can be divided into two types: monomeric small G proteins and heterotrimeric G proteins where the latter is bound to GPCRs. Heterotrimeric G protein consists of the α -subunit tightly associated with the $\beta\gamma$ -subunit dimer. Due to a stimulation of the GPCR, the α -subunit replaces guanosine diphosphate (GDP) with GTP followed by a dissociation of the α -subunit from the $\beta\gamma$ -subunit. Subsequently, the signaling proteins inside the SMC that directly depend on the α -subunit are activated.

Based on their effects after stimulation, G proteins are classified into four subclasses where only the G proteins which activate phospholipase C- β enzymes (G_q proteins; also referred to as $G_{q/11}$ or $G_{q/11/14/15}$) and the G proteins which activate guanine nucleotide exchange factors (GEFs) for RhoA small GTP-binding protein ($G_{12/13}$ proteins) are important for the contraction of SMCs [188]. A crucial feature of the GPCRs with G_q and $G_{12/13}$ proteins is the stretch-dependent activation which leads to several intracellular signaling pathways (see Fig. 2.5). The corresponding contractile mechanism of SMCs was already identified in 1902 by BAYLISS [12] and constitutes one of the most crucial instruments for resistance arteries to adjust their diameter to autoregulate the blood flow.

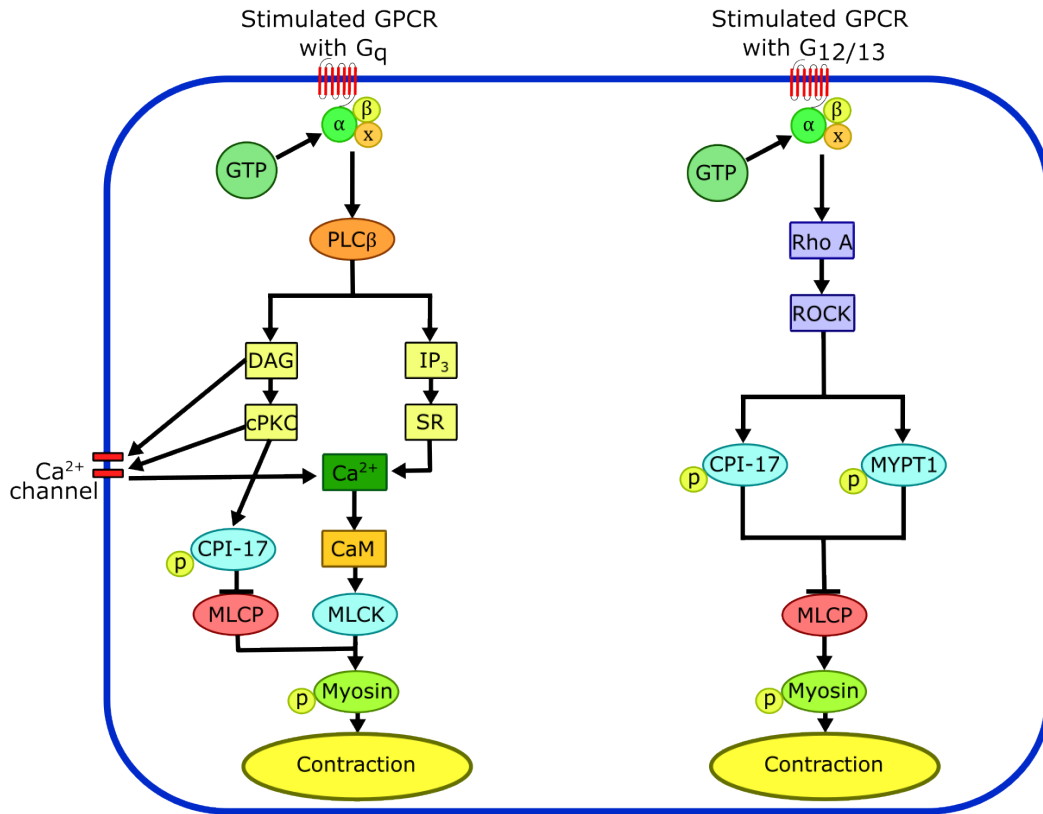


Figure 2.5: Schematic illustration of signal transduction pathways from stimulated receptors to phosphorylation of myosin leading to a contraction of SMCs. Signaling pathways on the left are initiated by stimulated G_q protein-coupled receptors leading to an activation of conventional PKC (cPKC) through PLC_β-DAG signaling pathway, followed by phosphorylation of CPI-17 and an inhibition of MLCP activity. Furthermore, Ca²⁺ inflow increases through the SMC membrane by activated cPKC and DAG as well as the SR by a binding of IP₃ on the IP₃-receptors which results in an activation of MLCK. The left signaling pathways control primarily the basal contraction of SMC and can protect from overstretch after a sudden increase of the intravascular pressure. A stimulation of G_{12/13} protein-coupled receptors triggers the right signaling pathways including the RhoA-ROCK signaling which increases phosphorylation of CPI-17 and MYPT1 at MLCP. As a result, a considerable inhibition of MLCP activity is obtained which leads to a long term contraction of the SMC. Illustration is based on DIMOPOULOS ET AL. [44].

The first detected mechanosensitive GPCR was the angiotensin II receptor of type 1 which is part of the GPCRs with G_q protein [165]. When G_q protein is bound to GTP, phospholipase C-β is stimulated to increase conversion of phosphatidylinositol 4,5-bisphosphate into IP₃ and diacylglycerol (DAG) [71]. A binding of IP₃ on the IP₃-receptor of the SR leads to a release of Ca²⁺ from the SR. Furthermore, DAG and an increased concentration of cytosolic Ca²⁺ activates the protein kinase C (PKC). Both, DAG and PKC are responsible for the opening of TRPCs which either release Ca²⁺ directly into the cell or influence different ion channels to increase the Ca²⁺ inflow [146]. Activated PKC is also involved in various other reaction chains, through interactions with the contraction of the SMC are not clear yet [49]. Additionally, the phosphorylation of the C-kinase potentiated protein phosphatase-1 inhibitor (CPI-17) might be involved which leads to an inhibition of MLCP and, therewith, a higher phosphorylation of regulatory MLCs [51]. In consequence, the activation of G_q proteins increases

the contraction of SMCs via various signaling chains which primarily initiates an inflow of Ca^{2+} , but is also involved in the downregulation of the dephosphorylation of myosin heads.

While stretch-sensitivity of GCPR in correspondence with G_q has already been established for decades based on the fundamental knowledge about the correlation of Ca^{2+} concentration with the cell contraction, studies have only been focusing on the involvement of activated $G_{12/13}$ proteins into the contraction process of SMCs over the last two decades [36]. The activation of $G_{12/13}$ proteins includes an activation of RhoA (Ras homolog gene family, member A) which is bound to the GTP at the α -subunit of the $G_{12/13}$ protein. RhoA increases ROCK which leads to a phosphorylation of Thr-696 and Thr-853 at the MYPT1 of the MLCP inhibiting the activity of this enzyme. Furthermore, the activity of ROCK might also involve a higher phosphorylation of CPI-17 [44]. However, the exact functionality of the intracellular reaction chains which led to an increased contraction of the SMC clearly depended on the location of the artery, the type of SMC, and the species which was investigated. This is probably connected to varying contributions of PKC in the excitation-contraction coupling which lead to controversy over its role in SMCs [51].

Important for the inclusion of GPCRs into mechanical models for the mechano-chemical coupling is to determine at which stretch value the receptors are activated. In vitro investigations of posterior cerebral arteries of rats have shown that the cytosolic concentration of Ca^{2+} primarily increases during changes at low pressure levels and less significantly when the pressure rises further to high values [131]. Accordingly, the stimulation of GPCRs with G_q proteins seems to be more dominant to regulate the basal contraction of the SMC by influencing the activity of MLCK due to a control of the concentration of Ca^{2+} . Furthermore, measurements in experiments with middle cerebral arteries of rats have demonstrated that the phosphorylation of MYPT1 increases mostly when the pressure rises from a normal state to higher values [94]. Therefore, it can be assumed that the activation of GPCRs with $G_{12/13}$ proteins and the corresponding inhibition of MLCP is predominant for the contraction of the SMCs at high body activity which is significant for the mechanical modeling of small muscular arteries in vivo [36].

2.2.4 Mechanical In Vitro Experiments for SMC Contraction

With the knowledge acquired about intracellular reaction processes with regard to the contraction of vascular SMCs and the corresponding stimulation or inhibition of extracellular sources such as binding of agonists to GPCRs or stretch of membrane receptors and ion channels, an extensive mechanical model could be created. However, representation of the actual contraction of the SMC can only be adequate when all considered intermediate reactions are quantified appropriately. This requires knowledge about intracellular reactions which can currently not be established in such detail. As a result, the available data has to be taken into account as good as possible to enable the formulation of a reliable mechanical model.

While in vivo real-time imaging such as Cine MRI advances from year to year, the resolution of this procedure is restricted and only appropriate for imaging of larger organs

such as the heart. Another possible imaging method of the movement of arteries could be ultrasound which is similarly limited in the quality of the image. However, non-invasive measurements of contracting arteries are possible as shown by BLUM ET AL. [20] with imaging of the arteries inside the eye. Nonetheless, additional information with regard to intracellular reaction chains cannot be obtained. The most detailed measurement of the contraction of arteries is obtained from arteries extracted from the body and, consequently, in vitro. These experiments are primarily performed when certain parts of intracellular reaction chains of SMCs or agents for the development of new antihypertensive drugs are investigated which mostly involves arteries of rats or mice.

In JOHNSON ET AL. [94], the impact of ROCK and PKC inhibitors on the contraction of middle cerebral arteries of rats were examined. The middle cerebral artery is located in the brain, it is the largest branch of an internal carotid artery. It constitutes a medium sized muscular artery with a diameter of 3 mm in humans [68]. As described in the previous sections, ROCK and PKC are crucial components in the intracellular reaction chain which decreases the activity of MLCP after GPCRs with $G_{12/13}$ of the cell membrane are stimulated. Accordingly, arteries with inhibited ROCK and PKC should show a suppressed contraction. One difficulty of in vitro experiments, which involve active material reactions, is maintaining the viability of the cells. SMCs can be tested for activity by applying potassium chloride into the solution around the arteries which influences the membrane potential of the cell and leads to an inflow of calcium ions. As a reaction, the increased intracellular calcium concentration results in a contraction of cells which is visible by a decrease of the diameter of the artery. To investigate the mechanical behavior of middle cerebral arteries in JOHNSON ET AL. [94], the arteries were fixated on cannulas of an arteriograph with nylon threads which is illustrated in Fig. 2.6a. Inside the arteriograph, the arteries were surrounded by normal Krebs solution which contains (in mmol^{-1}): NaCl 120, NaHCO_3 25, KCl 4.8, NaH_2PO_4 1.2, MgSO_4 1.2, glucose 11 and CaCl_2 1.8. Due to the cannulas, a distinct intravascular pressure value can be applied to the arterial wall. An increase of the intravascular pressure stimulates the stretch-dependent GPCRs and leads to a time-dependent contraction of the cells. The corresponding adjustment of the diameter of the artery is measured by the arteriograph. In the referred experiment, a sequence of intravascular pressure with increasing pressure values from 10 mmHg to 120 mmHg was applied where every pressure value was held over a time span of 300 s. In addition, this procedure was performed in three different scenarios for every artery in which the surrounding solution was varied to obtain different mechanical responses:

1. Solution with no variation - results in fully active material response,
2. Solution includes Y27632, H1152, GF109203X or Gö6976 - inhibition of ROCK or/and PKC which results in suppressed contraction,
3. Extraction of Ca^{2+} from the solution - no contraction which results in passive material response of the artery.

Results for three different arteries are illustrated in Fig. 2.6b-d. The graphs of the active material response show a significant contraction caused by the increasing intravascular pressure. Especially in the diagrams in Fig. 2.6b and 2.6d, the final diameter of the artery at 120 mmHg is considerably smaller than at a pressure value of 10 mmHg. The

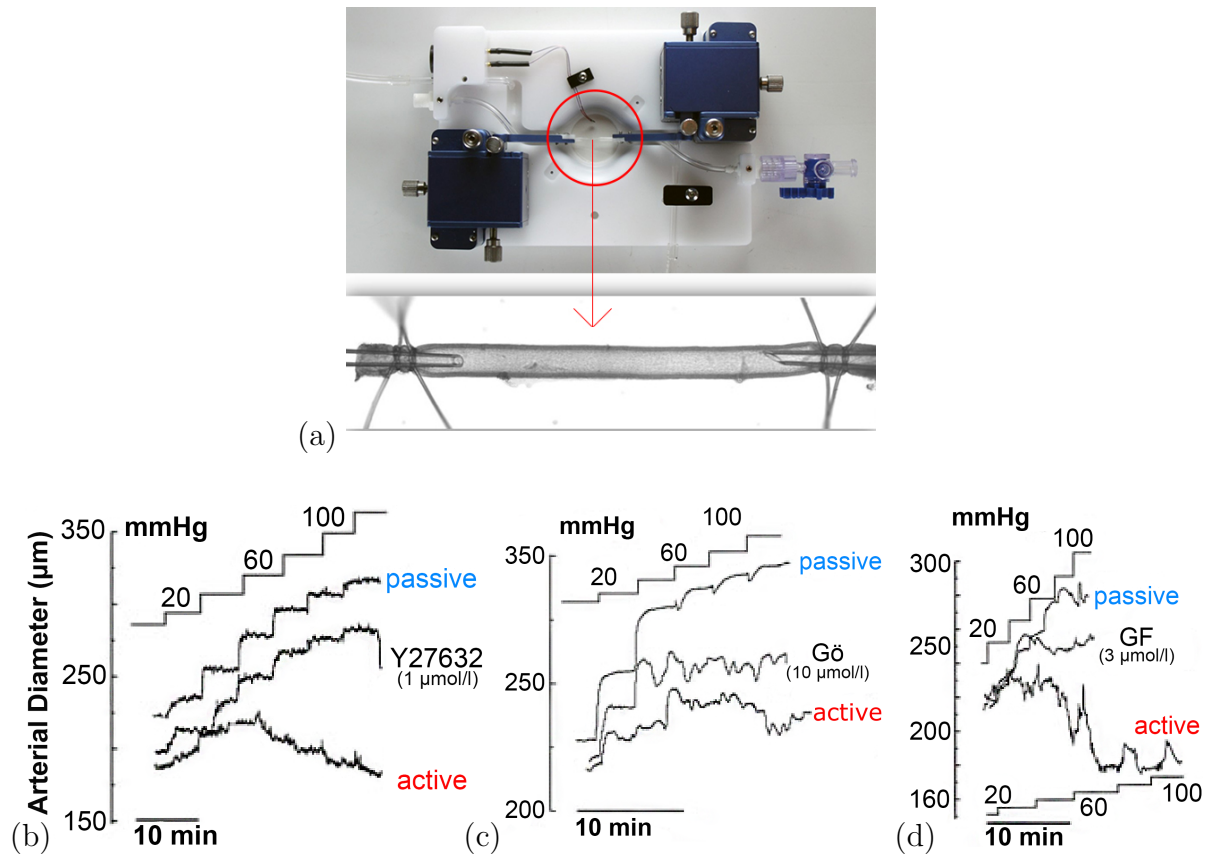


Figure 2.6: In vitro experiments for the active contraction of middle cerebral arteries of rats by JOHNSON ET AL. [94]. (a) Illustration of an arteriograph with artery fixated on cannulas [1]. Artery is surrounded by normal Krebs solution. Intravascular pressure can be applied and diameter of artery is measured. (b)-(d) Three different middle cerebral arteries are investigated in three different scenarios: active, passive and active with inhibited ROCK/PKC by inclusion of Y27632, Gö6976 (Gö) or GF109203X (GF) into surrounding solution. Intravascular pressure is increased from 10 mmHg to 120 mmHg over time. Each pressure value is held for 300s. Active contraction of arterial wall is demonstrated and therefore clearly mechanosensitive. Inhibition of ROCK/PKC reduces the contraction of the artery which proves the significance of MLCP in the mechanical behavior of SMCs.

difference of the diameters between fully active and passive material response is over 50%. The graphs, which illustrate the contraction of arteries with suppressed contraction caused by inhibition of ROCK and PKC, display notable higher diameter than for the fully active artery which confirms a substantial decrease of the cell contraction. This proves that the inhibition of the enzyme MLCP is crucial for the contraction of SMCs.

It has to be noted that the execution of in vitro experiments excludes the influence of the autonomic nervous system or vasoconstrictors and vasodilators such as NO and ET-1 in the investigation of the contraction of the arterial wall. However, the mechanosensitivity of the SMCs is clearly displayed by the experimental results which enables a quantification for the modeling of the contraction mechanism and thereby the coupling of chemistry and mechanics.

2.3 Adaptation Processes of the Arterial Wall

The arterial tissue is able to adjust through growth of proteins which passively stabilize the arterial wall and through migration and proliferation of cells such as vascular SMCs, endothelial cells and fibroblasts. As a consequence, residual stresses in the tissue are created which balance the mechanical load on the healthy artery over the entire wall thickness. To maintain the healthy state of the tissue, growth processes regulate the replacement of all constituents with minimal changes of the overall mass, the composition of the tissue, or its mechanical properties. Next to the binding of agonists on cell receptors, the growth processes are also controlled by mechanical stimulation. The preservation of a healthy mechanical state of the tissue is understood to be mechanical homeostasis [48] where homeostasis generally refers to coordinated physiological reactions that maintain most of the steady states in the body. The study by MATSUMOTO AND HAYASHI [118] indicates that tissue growth during hypertension leads to a significant thickening of the arterial wall but does not affect the number of lamellar units (tissue layers separated by elastic lamina). Correspondingly, longitudinal sections of the aortic wall for rats with different systolic blood pressure are illustrated in Fig. 2.7. Pace of growth processes varies depending on the constituent. While 0.02% of endothelial cells and 0.06% of SMCs are renewed per day, the half-life of collagen fibers ranges from a couple of weeks to months [86]. Elastin, on the other hand, is a long-living protein that degrades slowly in healthy tissues and carries a half-life of about 70 years [184]. Especially in elastic arteries, the growth behavior indicates that the mechanical behavior of the tissue is mostly sustained during aging by adding collagen and considerably less elastin. Nevertheless, some articles report that the ratio of elastin to collagen increased in aging muscular arteries which might be connected to the higher density of SMCs and their ability to synthesize elastin [73].

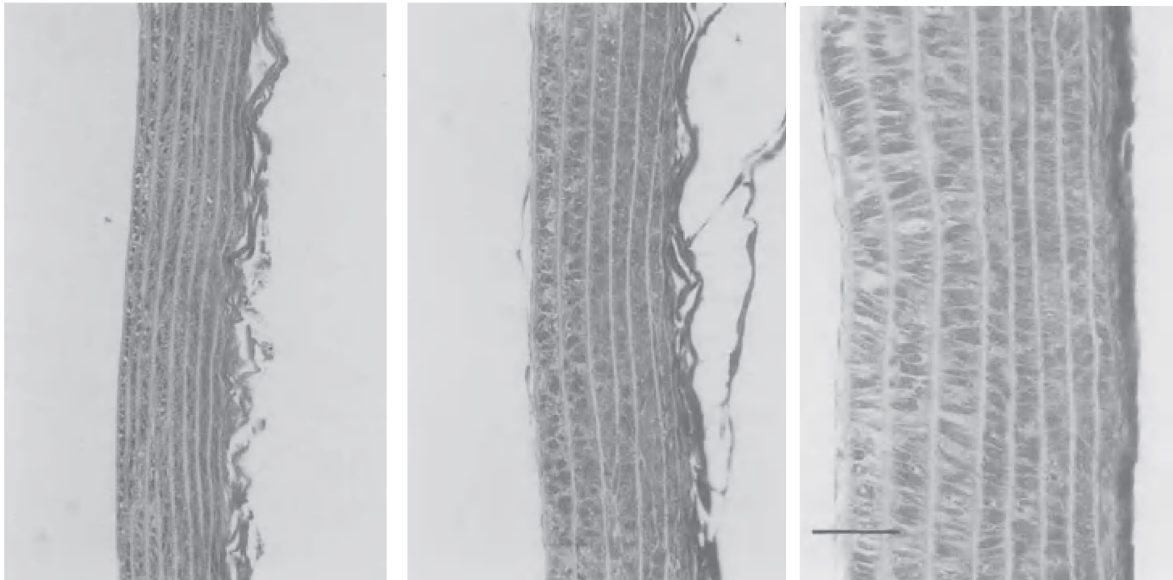


Figure 2.7: Illustration of longitudinal sections of the aortic wall in rats with a systolic blood pressure of (a) 145 mmHg, (b) 200 mmHg, and (c) 240 mmHg. The increased blood pressure results in a significant thickening of the artery. However, the growth process does not change the total number of lamellar units of the arterial wall. Illustration is adopted from MATSUMOTO AND HAYASHI [117].

Naturally, tissue regrowth is also required in healing processes when the tissue is injured or inflamed. In such cases, cells migrate to the injured tissue and are stimulated to increase the synthesis of mostly collagen which serves as scar tissue. Furthermore, cell proliferation and transitions to different phenotypes occur enabling the cells to fulfill their purpose more productively. However, especially when infectious pathogens inflict an inflammation of the tunica intima, the healing process can also cause atherosclerosis [108]. Due to the lower production of basal NO and the flow properties of blood in smaller arteries which simplify the interaction of the pathogens with the tissue of the wall, plaque develops mainly in small muscular arteries. The formation of fibrofatty tissue and calcifications involves, next to macrophages, also different phenotypes of the SMCs.

To understand the basic growth mechanisms of the arterial tissue and possible differences of growth processes in elastic and small muscular arteries, the synthesis of elastin and collagen is explained in the following sections. Furthermore, the transitions of fibroblasts and SMCs into different phenotypes in case of injury or inflammation of the tissue and changes for growth processes based on these phenotypes are described. Firstly, the current state of knowledge does not allow for a prediction of the growth process of a diseased artery precise enough to allow for a reliable estimation of the development of the health of the patient over the upcoming years. This is also connected to the possibility that some phenotypes are not detected yet. Secondly, age-dependent changes of large elastic arteries are decently investigated so that predictions of growth process are possible [92] and growth models can be involved in numerical simulations. Relevant data is presented at the end of this section.

2.3.1 Protein Synthesis

The synthesis of elastin and collagen is a multi-state process which starts intracellularly and finalizes extracellularly. An important component of involved eukaryotic cells is the rough endoplasmic reticulum (RER) which is responsible for the folding and modifying of proteins [24]. This is not restricted to elastin and collagen. The RER is also in charge of the maintenance of the cytoskeleton of the cell which includes, e.g., actin filaments in SMCs. The surface of the RER is covered with ribosomes giving it a rough structure and leading to the name of this part of the endoplasmic reticulum (ER). Ribosomes are crucial in the synthesis of collagen. In addition, cells contain a smooth endoplasmic reticulum (SER) which consists of proteins comparable to the RER, yet the SER has a smooth surface without ribosomes. In contrast to the RER, functions of the SER include synthesis of carbohydrates, lipids, and steroid hormones as well as detoxification of medications and poisons. Furthermore, the SER can be specialized to store calcium ions for the regulation of intracellular reactions as the contraction of SMCs in which case the SER is called sarcoplasmic reticulum. Due to its functions, the RER is primarily located at the inside of the cell next to the nucleus. Moreover the SER is a meshwork of fine distinct tubular membrane vesicles and part of a continuous membrane organelle within the cytoplasm of cells. In the following paragraphs, syntheses of elastin and collagen are described separately.

Elastin Synthesis The general structure of elastic fibers changes with the age of a human being. In fetal and postnatal stages of fiber organization, microfibrils predominate which serve as physical extracellular scaffold for alignment of tropoelastin monomers. In mature tissues, the fibers consist mostly of amorphous elastin (cross-linked tropoelastin monomers) [101]. While microfibrils are probably synthesised by fibroblast [47], the building of elastic fibers, which consist mostly of elastin, is governed by the synthesis of tropoelastin (see Fig. 2.8).

Synthesis of tropoelastin begins with the transcription of insoluble polymerized elastin gene in the nucleus of the cell [184]. Transcription describes the process of copying a segment of the DNA into ribonucleic acid (RNA). Subsequently, the mature messenger RNAs (mRNAs) move from the nucleus into the cytoplasm of the cell and are translated in the ribosomes of the RER into amino acid chains which build tropoelastin. Tropoelastin consists of two domains which can be categorized as either hydrophobic or hydrophilic (cross-linking; lysyl oxidase) based on their functionality and amino acid content [132]. Inside the RER, tropoelastin interacts with elastin-binding protein (EBP). Afterwards, tropoelastin is packaged into membrane-bound vesicles for transportation in the golgi and secreted to the cell surface for self-assembly. There are three possible assembly pathways reported for tropoelastin [101]. In the first pathway,

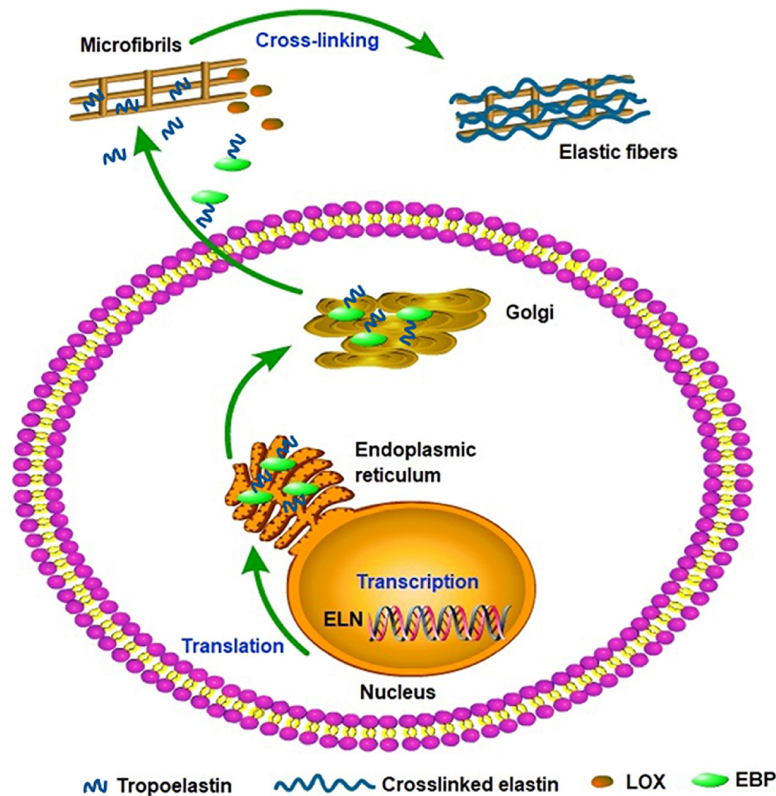


Figure 2.8: Schematic illustration of elastin synthesis. Synthesis begins with transcription of elastin gene in the nucleus. Tropoelastin interacts with elastin-binding protein (EBP) and is folded inside of the rough endoplasmic reticulum. After being packed into membrane-bound vesicles in the golgi, the complex of EBP and tropoelastin is transported to the cell surface. Tropoelastin deposits onto the microfibril scaffold after separation from EBP. Mature elastic fibers can form in presence of lysine oxidase (LOX) after cross-linking. Illustration is adopted from WANG ET AL. [184].

tropoelastin dissociates from EBP and deposits onto the microfibril scaffold. Based on the function of the hydrophilic domains, tropoelastin cross-links and eventually forms mature elastic fibers which is illustrated in Fig. 2.8. In the second pathway, tropoelastin is already partially cross-linked at the cell surface before it interacts with microfibrils. Thirdly, assembly and cross-linking can occur within a membrane-limited intracellular compartment and cross-linked elastin is then secreted inside of vesicles and interacts afterwards with microfibrils. Consequently, elastic fibers, generally termed elastin for the mechanical modeling of the arterial wall, are built out of microfibrils and cross-linked tropoelastin.

Collagen Synthesis While there are 28 different types of collagen in the human body, over 90% of it is collagen type I. Consequently type I synthesis is primarily investigated and presented here. The process of collagen I synthesis and extracellular maturation is illustrated in Fig. 2.9. Note that in arteries also type III collagen exists [79]. The synthesis of collagen I fibers contains more steps in concerning the RER, but the basic pathway is comparable to the synthesis of elastin. It begins with the transcription of the collagen I gene inside the nucleus which comprise the collagen I $\alpha 1$ chain and the collagen I $\alpha 2$ chain [130]. Subsequently, the mRNA is translated into polypeptide in the ribosomes of the RER where the polypeptide is folded and modified to propeptide based on enzyme activity. Two folded $\alpha 1$ chains assemble with one $\alpha 2$

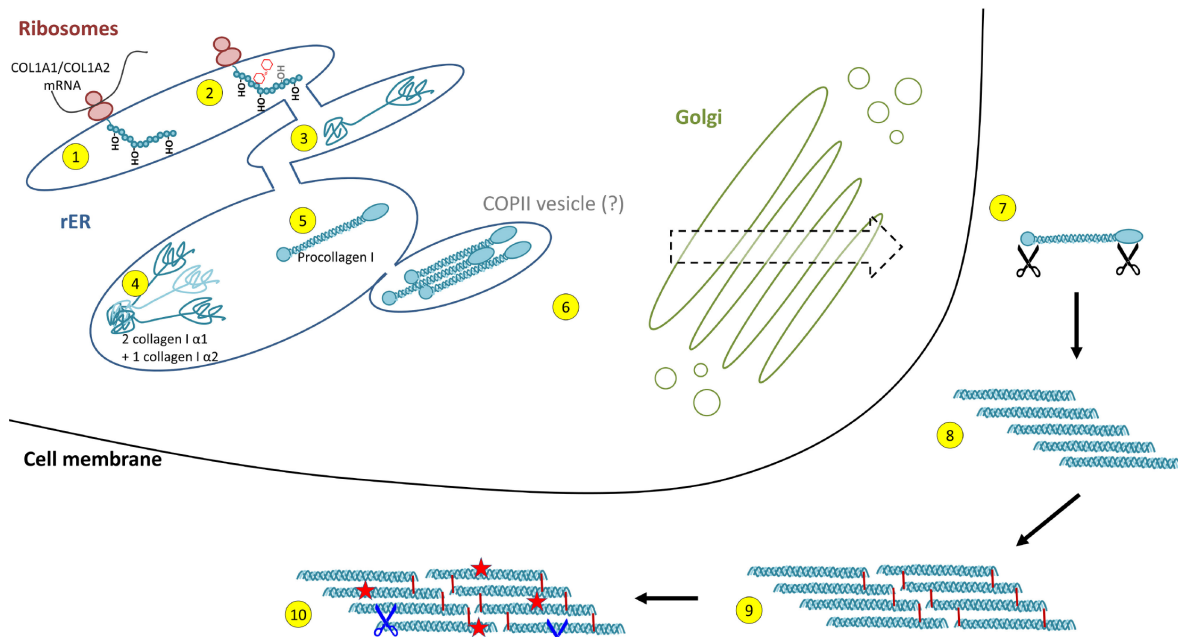


Figure 2.9: Synthesis and maturation scheme of collagen I. After transcription of the collagen gene in the nucleus, several processing steps are performed in the RER including (1) cotranslational prolyl-4- and lysyl-hydroxylation of the nascent collagen polypeptide chain, (2) glycosylation and prolyl-3-hydroxylation, (3) folding of the C- and N-terminal propeptides and (4-5) forming of the triple helix nucleus. Subsequently, the collagen triple helices are transported via golgi-network into the extracellular space. Maturation is performed by (7) cleavage of propeptide, (8) auto-assembly of collagen fibrils, and (9) cross-linking. (10) Mature collagen fibers can be damaged and degraded by extracellular proteases. Illustration is adopted from ONURSAL ET AL. [130].

chain and form the triple helix nucleus in a zipper-like fashion. In comparison, type III collagen is built out of three identical $\alpha 1$ chains. The triple helix is transported via golgi network and secreted into the extracellular space. After a subsequent cleavage of the N- and C-terminal propeptides, the collagen fibrils assemble to collagen fibers and stabilize by cross-linking which is catalysed by the enzyme of the lysyl oxidase.

2.3.2 Arterial Adaptation by Different Phenotypes of SMCs

SMCs of healthy arteries are primarily in the contractile state. However, the possibility to investigate biological tissue in more and more detail revealed an insight into cell transitions and enabled the discovery of biological markers which allow the identification of different phenotypes. Up until recently, vascular SMCs were only differentiated into the contractile or synthetic (dedifferentiated) type. In this section, the phenotypes of vascular SMCs from YAP ET AL. [195] are presented and their function in the growth process is described. In total, six different phenotypes are considered which are illustrated with the corresponding transitions in Fig. 2.10. Nonetheless, the discovery of additional phenotypes of the SMC can be expected in future studies.

Smooth muscle cell phenotypes

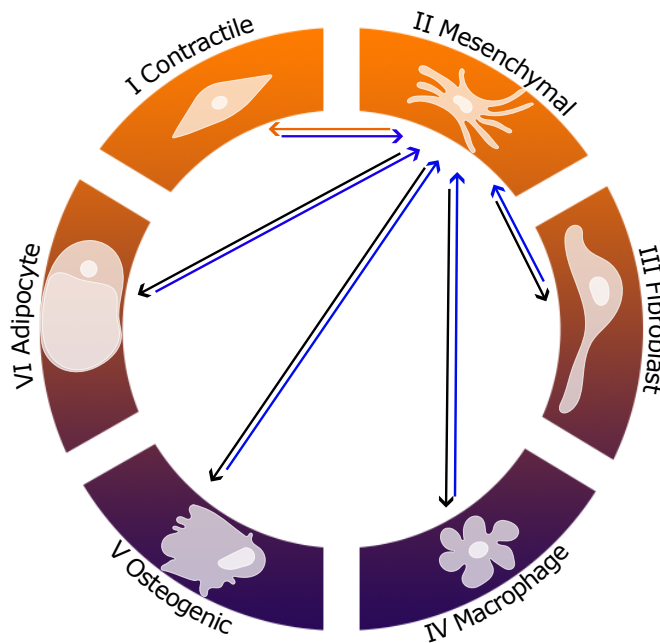


Figure 2.10: Schematic illustration of the transitions of different phenotypes of vascular SMCs. In healthy arteries, SMCs are primarily in the contractile state. Other phenotypes have a reduced contractility. After injury of arterial tissue, contractile vascular SMCs can switch to a mesenchymal-like state which constitutes the fundamental phenotype. Mesenchymal-like as well as fibroblast-like SMCs provide an increased tissue production and proliferation. SMCs in macrophage-like, osteoblast-like or adipocyte-like state can contribute to the development of atherosclerosis. Illustration is based on YAP ET AL. [195].

Contractile vascular SMC The main feature of the contractile SMC is the contraction via thin and thick filaments which was described in Section 2.2. However, contractile SMCs are the most reliable producer of elastin and collagen in the physiological state, especially in small muscular arteries where SMCs are abundant. The production of the proteins of the ECM can be increased considerably by the binding of transforming growth factor β (TGF- β) to specific, heteromeric complexes at the cell membrane that includes types I and II kinase receptors [67]. The production of TGF- β occurs primarily intracellularly which includes vascular SMCs themselves, but also fibroblast and endothelial cells. During the synthesis of TGF- β , latency associated peptide (LAP) binds the mature TGF- β dimer with high affinity during the processing in the RER building together the small latent TGF- β complex. As long as TGF- β is bound to LAP, it is not active and cannot connect to receptors of the SMC. Furthermore, the small latent TGF- β complex connects with a single latent TGF- β binding protein to form the large latent complex (LLC). This LLC is then secreted from the cell and fixated at the ECM by connecting to proteins such as fibronectin fibres or fibrillin microfibrils. There are several activators for TGF- β which liberate it from LAP. For the purpose of simplicity, the activators are not discussed in detail here, but can be reviewed in [147]. It has to be emphasized that stretch of the tissue plays a considerable role for the activation of TGF- β [76] which occurs naturally when the artery is injured or overstretched. Consequently, the synthesis of elastin and collagen in contractile SMCs is increased by the release of activated TGF- β from the ECM which might lead to a higher proportion of elastin in small aging muscular arteries [73] since other phenotypes of the vascular SMC produce substantially more collagen than the contractile type. Furthermore, the growth of aortic aneurysms in patients with Marfan syndrom is clearly connected to the TGF- β hyper-activity due to mutations in the gene FBN1 [28]. This gene encodes fibrillin-1, a glycoprotein which is the main constituent of the microfibrils of the ECM. In consequence, the reduced and abnormal fibrillin-1 leads to tissue weakness of the ECM and an increased activation of TGF- β . Further growth of weak tissue results in building of an aneurysm. Connected to this issue, the stimulation of GPCR (see Section 2.2.3) transactivates TGF- β receptors [29]. Therefore, treatment of patients with Marfan syndrom with antihypertensive drugs might not only have a positive effect through decreasing blood pressure, but also through an inhibition of the GPCR activity which leads directly to a reduced activation of TGF- β receptors.

Mesenchymal-like vascular SMC The mesenchymal-like vascular SMC is the fundamental phenotype enabling the transition into further states. Consequently, contractile SMCs can only switch into the mesenchymal-like state which overlaps biologically with mesenchymal stem cells with the capacity to differentiate into multiple lineages such as bone, cartilage, and fat cells [176]. The mesenchymal-like vascular SMC is characterized by the ability to proliferate and self-renew and comprises a reduced amount of contractile proteins in comparison to contractile SMCs. Switch of the phenotype from a contractile to a mesenchymal-like state is driven by the increase of the transcription of Krüppel-like factor 4 (KLF4), the key initiator for all transformations of vascular SMCs [53]. Increased transcription of KLF4 is directly connected to injury of the artery which enables the spread of platelet-derived growth factor BB (PDGF-BB). As described by the name, PDGF-BB is secreted by thrombocytes (blood platelets) which

flow through the body in the blood. Accordingly, the PDGF-BB can reach SMCs when the intima of the wall is injured which makes the structure of the endothelial cells permeable. The binding of PDGF-BB at corresponding membrane receptors expresses the transcription factor stimulating protein-1 which regulates the expression of KLF4 in SMCs [43]. This induced transformation of contractile SMCs into the mesenchymal-like state can only be suppressed by a high concentration of TGF- β and by miR-143/145. MiR-143/145 is a micro RNA which is most common in cardiovascular development and disease [181]. Both, TGF- β and miR-143/145, decrease the release of KLF4. In the physiological state, SMCs in the mesenchymal-like phenotype reside in the media and adventitia of the artery. An injury of the wall tissue leads to a migration of these cells into the media and even the intima to support tissue repairs which possibly results in neointimal thickening connected to the proliferation of the mesenchymal-like SMCs. However, for the crucial production of collagen fibers the vascular SMC has to switch into another phenotype which is called the fibroblast-like vascular SMC.

Fibroblast-like vascular SMC The fibroblast-like vascular SMC is also referred to as myofibroblast-like vascular SMC or fibromyocyte. Similar to the activity of fibroblasts and connected phenotypes, fibroblast-like SMCs are efficient producers of collagen fibers which serve in case of injury of the arterial wall as solid scar tissue. The increase of collagen synthesis is caused by a high activity of the RER. Furthermore, the active RER reveals an enhanced release of genes involved in adhesion, ECM organization and cellular proliferation. The fibroblast-like vascular SMC is the only synthetic phenotype which was observed in thoracic aortic aneurysms of mice with Marfan syndrome [137]. The deposition of collagen is considered the hall-mark for aneurysm formation in the aorta caused by aortic fibrosis and stiffness. The switch of mesenchymal-like vascular SMCs into the fibroblast-like state is connected to a further rise of KLF4 in the cell. However, the ER unfolding protein response (UPR) can lead to phenotype switching as well [30]. The cholesterol level is normally low in the ER. An accumulation of free cholesterol in the ER induces membrane dysfunction and ER stress (disruption of the protein folding process) which activates a signaling network called UPR [156]. In consequence, the UPR increases the biosynthetic capacity of the secretory pathway through upregulation of ER chaperone and foldase release. While UPR promotes the fibroblast-like vascular SMC, it is also connected to the switch to the macrophage-like state of SMCs which is associated with developing atherosclerotic plaques in the artery.

Macrophage-like vascular SMC Macrophages recruit other immune cells for the immune response to clear debris and combat pathogens [129]. Therefore, they are indispensable in all stages of inflammation and healing processes. The exposure of vascular SMCs to low-density lipoprotein (LDL) increases the release of KLF4 [27]. In combination, the transition into the macrophage-like vascular SMC phenotype is induced. Just as real macrophages, the transformed SMC clears the vascular wall of oxidized LDL which becomes part of the cytosol. In consequence, the macrophage-like vascular SMCs develop into foam cells which plays a role in the fibrofatty lesions of atherosclerosis [142]. The development of macrophage-like vascular SMCs can be inhibited by a high concentration of high-density lipoprotein (HDL) in the blood which is responsible for the efflux of cholesterol from the cells and its transport into the liver. In this context, high blood pressure patients with high LDL concentrations

receive prescriptions for statins which decrease the production of cholesterol in the liver, subsequently, lower the LDL concentration, and prevent the development of foam cells which would lead to atherosclerosis.

Osteoblast-like vascular SMC Osteoblasts and chondrocytes are responsible for the maintenance of bones and cartilage in the skeleton of the human body. Both cell types are of mesenchymal origin and share a common precursor. Mesenchymal-like vascular SMCs can transform into the osteoblast-like phenotype which also comprises SMCs with features of chondrocytes. A deposition of calcium phosphate, but also an exposure to bone morphogenetic protein, which is a member of the TGF- β family, can cause the phenotype switch. Osteoblast-like vascular SMCs are responsible for calcification in atherosclerosis plaque but can also cause calcification inside the media of the artery which leads to stiffening of the wall [45].

Adipocyte-like vascular SMC The adipocyte-like vascular SMC was only reported once in a scRNA-seq study as content of atherosclerosis plaque [31]. Based on their biological markers, these SMCs were classified as beige adipocytes which regulate thermogenesis by producing heat when burning fatty acids. Further investigation to determine the impact of this phenotype on plaque is needed.

2.3.3 Arterial Adaptation by Fibroblasts and Myofibroblasts

In general, all connective tissue cells, which are able to produce connective tissue substance such as collagen, are considered fibroblasts. They are distributed in the entire human body and maintain the homeostasis of the ECM by protein synthesis. Fibroblasts belong to a vastly heterogeneous group of mesenchymal cells which are able to self-renew and exhibit multilineage differentiation. Based on their basic structure, the identification of a cell as fibroblast is rather difficult. All molecular markers of fibroblasts are also expressed in SMCs and endothelial cells. Consequently, only exclusion criteria can be employed to distinguish fibroblastic cells from other common tissue cell types such as the absence of α smooth muscle actin which is a marker of SMCs [199]. With regard to the arterial wall, fibroblasts are primarily located in the adventitia. Mesenchymal stem cells (MSC), which reside in the adventitial connective tissue layer as well, are sometimes also considered as fibroblasts of the arterial wall. While both share certain similarities with regard to the tissue generation, MSCs are able to differentiate into multiple different cell types [120]. When the tissue of the arterial wall is damaged, fibroblasts can be activated which actually means that these cells transition into myofibroblasts and migrate into the inner layer of the wall to support the repair mechanism by releasing collagen. A schematic illustration of this transition is shown in Fig. 2.11. Myofibroblasts are comparable to fibroblast-like vascular SMCs. While fibroblasts are rather negligible for the mechanic behavior of the tissue, myofibroblasts are larger and develop α smooth muscle actin which builds a protein network inside the cell and enables active contractions [46]. Using contractions, myofibroblasts can stabilize the damaged tissue and lead to an initial closure of the wound.

Transition of fibroblasts into myofibroblasts is initiated and enhanced by several factors which are explained in detail in YOUNESI ET AL. [200]. The first trigger for the

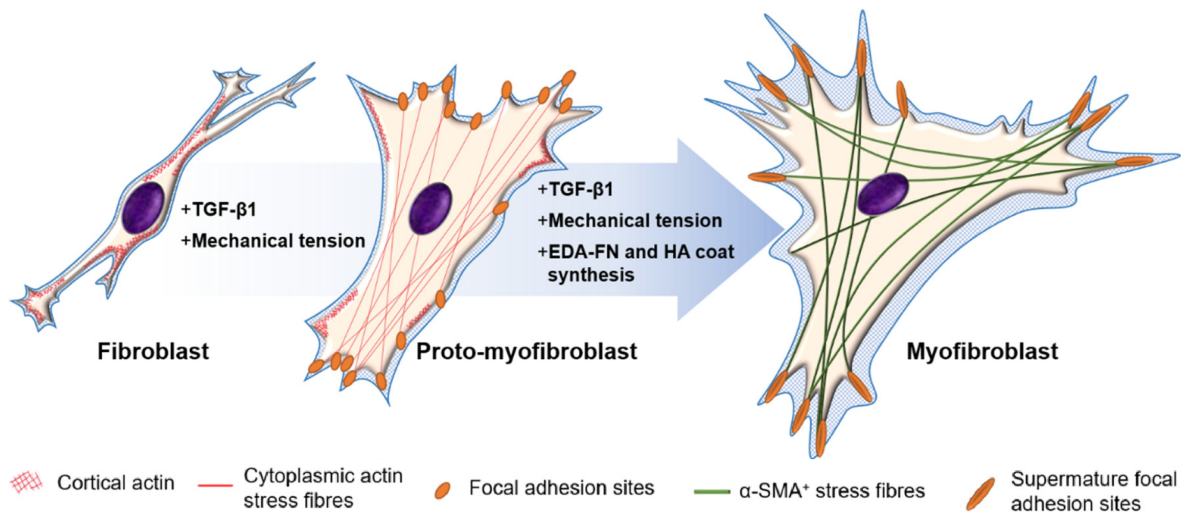


Figure 2.11: Illustration of the transition of fibroblasts into myofibroblasts. The differentiation is activated by increased concentration of TGF- β and conformational changes of integrins based on stiffening of the ECM. An intermediate stage is known as proto-myofibroblast with increased proliferation, migration, and protein synthesis. Only the mature myofibroblast contains α smooth muscle actin which enables the active contraction of the cell. Illustration is based on TAI ET AL. [171].

transition is an increased concentration of TGF- β in the extracellular space. Similar to the increased production of collagen from contractile vascular SMCs, TGF- β can bind to the corresponding receptors of the fibroblast and increase the protein synthesis of the cell. As described in the previous section, TGF- β has to be released from the LAP, which is bound to the ECM, before the growth factor is available for the receptors. The release of TGF- β is increased during a stretch of the ECM which naturally occurs when the tissue of the arterial wall is damaged and loses stiffness. In addition to the production of α smooth muscle actin [158], the collagen production of the fibroblastic cell is significantly increased in the RER which leads to scar tissue development to repair the damaged tissue. Another factor for the transition of fibroblasts into myofibroblasts is related to the stiffness of the ECM which can be recognized by integrin of the cell. Integrins are cell adhesion receptors which are anchored in the cell membrane and bound to proteins of the ECM or adjacent cells. Stiff tissue leads to a conformational change of the molecule which starts a recruitment cascade of structural and signaling proteins to the cytoplasmic portion of integrins and results in the formation of contractile units. In addition, GPCRs are stimulated by the cell stretch which leads not only to an increase of Ca^{2+} in the cytosol and a rise of the MLCK activity as well as an inhibition of MLCP, thereby enhancing the contraction of the cell. The stimulation of GPCR leads to an increased actin polymerization by regulating actin monomer-binding and polymer-binding proteins.

For a long time, myofibroblasts were considered to be the terminal state of fibroblasts resulting in apoptosis (programmed cell death) as soon as the damaged tissue is fully recovered [139]. However, it is clear now that myofibroblasts can remain in the tissue for a long time, mainly caused through maintaining of increased tissue stiffness and high concentration of TGF- β which leads eventually to tissue fibrosis [128].

2.3.4 Age-dependent Adaptation of the Arterial Wall and Conclusion for Mechanical Modeling

The previous sections layed out the fundamental mechanisms for growth processes on the cell level. With this biological knowledge, assumptions can be made for the microstructural changes of the tissue. While adjustments from growth processes are distinctly driven by mechanical triggers, e.g., the release of TGF- β from stretched LAP or the conformational change of the integrins of fibroblastic cells based on stretched (stiff) ECM, cause and effect relations of the tissue are not quantifiable. Therefore, it cannot be included into the mechanical modeling of growth processes without a considerable amount of uncertainty. A more reliable approach for a plausible growth model can be pursued with reasonable assumptions about the growth processes from a macroscopic point of view. One such assumption is that maintaining of the mechanical homeostasis of the tissue corresponds to maintaining of a homogeneous mechanical field (stresses or stretches) in the entire arterial wall. This hypothesis enables a variety of growth models, and is also the foundation of the proposed model in subsequent chapters of this thesis. To ensure that the results from simulations with new growth models are not only reliable in the homogeneity of mechanical fields, but also comparable to biological observations, data from several publications can be taken into account.

To describe the growth of an artery from a macroscopic point of view, changes of its geometry over the years must be considered. Corresponding data for small muscular arteries is scarce and studies with age-dependent information on this topic are unknown. Therefore, data for larger arteries is taken into account. JADIDI ET AL. [91] studied the superficial femoral artery (SFA) and the popliteal artery (PA) of 125 human subjects in the age of 13 to 92 years. SFA and PA constitute large muscular arteries where the SFA is positioned in the hip and upper leg (femoral) and the PA is the corresponding elongation of the SFA from the knee downwards. However, regarding their size, the mechanical properties are rather comparable to elastic arteries such as the aorta than to the considerably more contractive resistance arteries. Since the age range included in the study is comprehensive, corresponding assumptions for the age-dependent adjustments of the geometry are feasible. As an addition, the study identified the stage of diseases such as atherosclerosis inside of arteries. Naturally, the geometry of the artery is directly affected by the disease. However, the stage of the disease increases corresponding to the age of the subjects and can, therefore, rather be considered as normal age-related development of the artery. Based on the acquired data, the general tendency of quantities such as the wall thickness and the inner and outer radius (r_i , r_o) were calculated. Since residual stresses inside of the tissue of the arterial wall lead to observable deformations when the artery is cut open, measurements were not only performed for the load-free state of the artery, but also for the so-called stress-free state. Results from the study are shown in Fig. 2.12a-c. The labeling of the corresponding quantities is illustrated in Fig. 2.12d. As can be seen in the first diagram, the wall thicknesses h (load-free) and H (stress-free) of the SFA and PA significantly increase over the age span of a human being. This indicates that growth in radial direction occurs to maintain the homeostasis of the tissue. The graphs in Fig. 2.12b for the outer radius r_o of the load-free state of the artery match this tendency. However, also the inner radius r_i rises notably with the age of the subjects. This can hardly be explained by uniaxial growth in radial direction. If radial growth

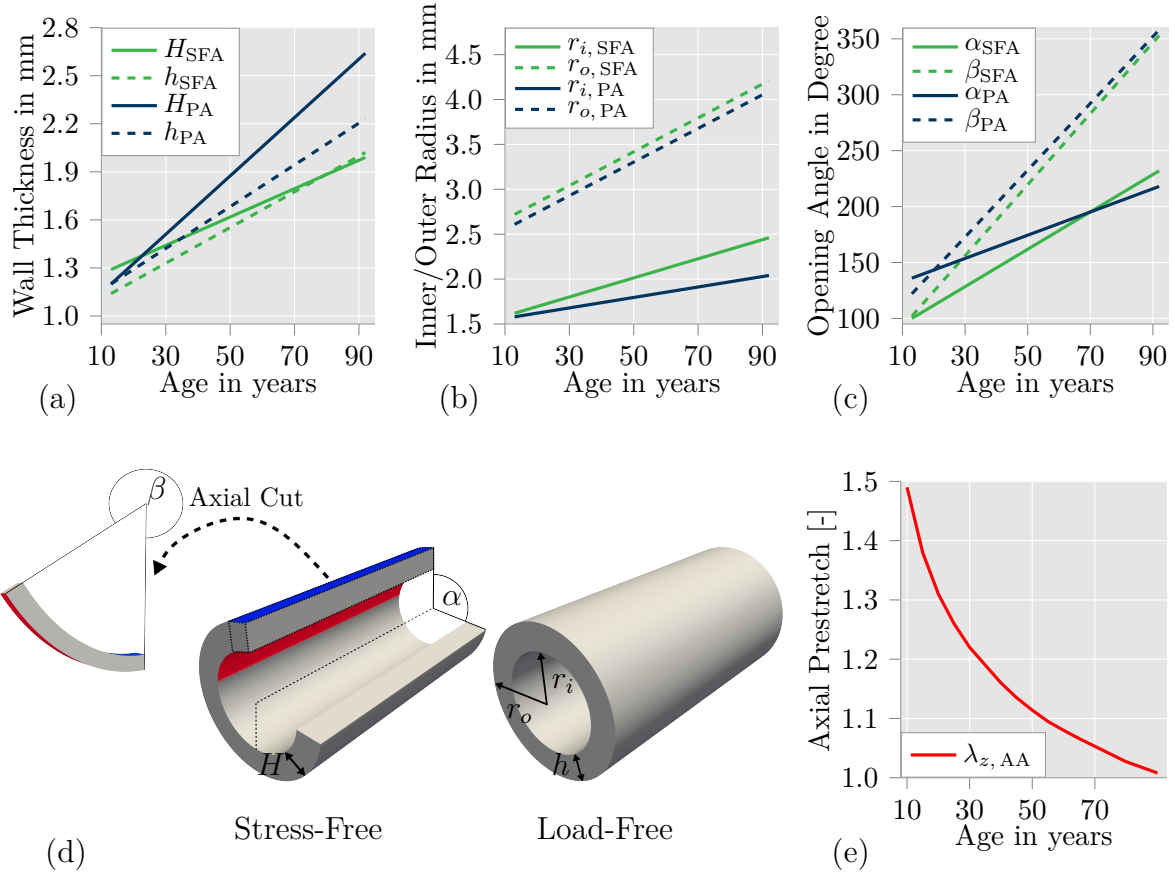


Figure 2.12: Evolution of geometric characteristics of (a) the wall thicknesses h (load-free) and H (stress-free), (b) the inner and outer radii r_i and r_o , and (c) the opening angles α and β after axial cuts through the arterial wall for the superficial femoral artery (SFA) and popliteal artery (PA). Data is adopted from [91]. Tendencies of the geometric quantities were determined based on measurements of arteries from 125 human donors in the age of 13 to 92 years. (d) illustrates the labeling of the quantities in the load-free and stress-free state. (e) shows additional data for the axial λ_θ of abdominal aortas (AA) from [85]. Increase of the wall thickness h and H by age of subject demonstrates growth in radial direction. Additional rise of inner radius r_i indicates growth in circumferential direction. Decrease of the axial prestretch λ_z shows growth in axial direction. The opening angles α and β suggest more dominant growth at the inner side of the wall which advances for older humans.

would be considered as only growth direction, the thickening would primarily appear at the inside of the wall, where the largest stresses occur, leading to a decrease of the inner radius. In consequence, it can be assumed that the growth process leads also to extensions of the tissue in circumferential direction which increases the inner and outer radius. In the third diagram, the opening angles of the artery are illustrated for axial cuts through the artery. The angle α describes the opening angle of the artery in circumferential direction. Bending of an axial strip of the artery is determined by the angle β , which is lower than 360° when the strip bends towards the outside of the arterial wall as pointed out in Fig. 2.12d by the red (inside) and blue (outside) colors. Both angles are commonly positive which is expected since stresses of a hollow cylinder under pressure without residual stresses lead generally to higher stress in axial and circumferential direction at the inner side of the wall. Consequently, the tissue at the center of the artery requires more growth for a homogenization of the stress over the entire wall thickness. Furthermore, the graphs show that both angles increase over

the age of the subjects. For the angle α , this could be connected to the thickening of the wall which might lead to more significant differences in the residual stresses at the inner and outer side of the wall to remain homeostasis. In contrast, an increase of the angle β describes a homogenization of the axial residual stresses over the wall which are exactly equal when $\beta = 360^\circ$.

An additional point of interest is the axial prestretch which is calculated based on the difference in length of the artery in situ and ex vivo. Especially larger arteries in the extremities or, e.g., carotid arteries in the neck have to sustain stretches primarily in axial direction caused by body movement. The stretches can lead to considerable changes of the stresses in axial, but more importantly, in circumferential direction. Several publications have shown that a basal axial prestretch leads to smaller variations in the stresses [163]. To describe the changes of the axial prestretch over the life span of humans, the publication by [85] is taken into account. Here, abdominal aortas of male tissue donors in the age of 10 to 91 years were investigated. The resulting evolution of the axial prestretch λ_z is illustrated in Fig. 2.12e by a regression curve. The axial prestretch λ_z is substantial with values over 1.4 for abdominal aortas of humans under the age of 20 years. Tissue growth leads to a notable decrease of the prestretch over the human life span. Abdominal aortas for donors over the age of 70 years showed exclusively axial prestretches under 1.1. This indicates that the growth process does not maintain the axial stretch and, therefore, the stress in axial direction might not be predominant for the mechanical homeostasis of the tissue. Other publications confirm these findings. For iliac arteries of donors aged between 52 and 87, an average axial prestretch λ_z of 1.07 was measured [157]. Investigations of carotid arteries of donors with average age of 77.6 years determined an axial prestretch λ_z of 0.98 for the intima and media of the artery [163].

Overall, the data validate a three-dimensional growth process in radial, axial and circumferential direction which was already suggested in HOLZAPFEL ET AL. [82]. Consequently, a reliable growth model has to consider all three directions in mechanical simulations. In addition, data for stretches in axial and circumferential direction identify considerable differences in the corresponding growth processes and associate a stronger impact of mechanical changes in circumferential direction on the tissue generation than caused by mechanical changes in axial direction.

3 Continuum Mechanical Basics

Conceptually, in continuum mechanics, the material of a physical body is described as a continuous medium. This concept allows for the analysis of the mechanical behavior of a body based on homogeneous field quantities. In consequence, deformations and stresses can be approximated without considering the exact microstructure of the material which is actually not continuous but specified by a certain arrangement of atoms. In this chapter, a brief overview of the underlying continuum mechanics is given to describe the mechanical fields of a deformable body and the material model for the anisotropic microstructure of the tissue of the arterial wall which is able to perform growth processes. Furthermore, balance equations are discussed which form the fundamental laws of continuum mechanics. Several textbooks deal extensively with this topic, they are the foundation for the information presented here, see e.g., HOLZAPFEL [78], BAŞAR AND WEICHERT [13], ALTENBACH [3] and WRIGGERS [191].

3.1 Kinematics

Kinematics is the basis of continuum mechanical considerations and describes the geometrical aspect of the position and motion of material points of a body over time. In the initial state, the undeformed body $\mathcal{B} \subset \mathbb{R}^3$ is a set of continuously distributed material points at the time $t = t_0$. The corresponding position of a material point of \mathcal{B} is defined by the position vector \mathbf{X} . This configuration is considered as the reference, material or Lagrangian configuration and is mainly applied to describe solid bodies. Load or surface displacements of the body lead to a deformation and possibly also rigid body motions. The transformation of a material point into the deformed state at the time t is described by the invertible mapping $\varphi(\mathbf{X}, t) : \mathcal{B} \rightarrow \mathcal{S}$. Each point $\mathbf{X} \in \mathcal{B}$ of the reference configuration is mapped onto its counterpart $\mathbf{x} \in \mathcal{S}$ which is considered the current, spatial, or Eulerian configuration. The Eulerian configuration is primarily used in fluid mechanics where the formulation of the mechanical fields as function of the current coordinates of \mathbf{x} is advantageous. The associated displacement vector \mathbf{u} of a point from the reference into the current configuration is defined as

$$\mathbf{u}(\mathbf{X}, t) = \mathbf{x} - \mathbf{X}, \quad (3.1)$$

which is illustrated in Fig. 3.1. For the description of all tensors in this chapter, an orthogonal Cartesian basis is assumed for both configurations. However, base vectors of the reference configuration are denoted as \mathbf{E}_I while base vectors of the current configuration are \mathbf{e}_i . Accordingly, letters and indices which are related to the reference configuration are expressed by capital letters. Small letters correspond to the current configuration.

The deformation of an infinitesimal environment in the current configuration is described by the deformation gradient \mathbf{F} as

$$\mathbf{F} = \text{Grad}[\varphi(\mathbf{X}, t)] = \frac{\partial \mathbf{x}}{\partial \mathbf{X}}. \quad (3.2)$$

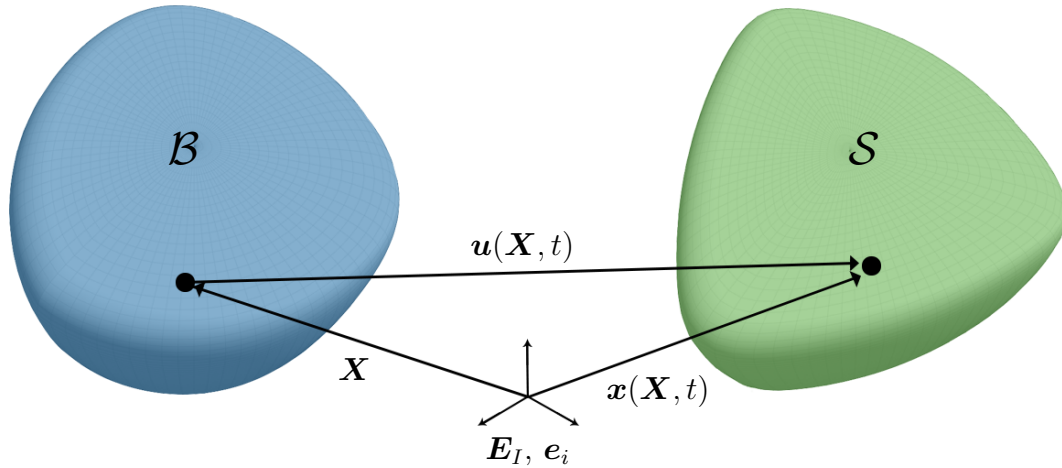


Figure 3.1: Motion of a body from the reference configuration \mathcal{B} into the current configuration \mathcal{S} at the time t . The position of a point of the body is changing from the vector \mathbf{X} at the referential state to the vector \mathbf{x} in current state which is described by the displacement \mathbf{u} . Base vectors \mathbf{E}_I and \mathbf{e}_i of the reference and current configuration, respectively, are assumed as orthogonal Cartesian.

Corresponding to the definition of the base vectors, this second-order tensor can be expressed in index notation as $\mathbf{F} = F_{iJ} \mathbf{e}_i \otimes \mathbf{E}_J$. The consideration of the correct base vectors of tensors is particularly important for the execution of mathematical operations which can only be performed between base vectors of the same configuration. In relation to the displacement vector \mathbf{u} , the deformation gradient \mathbf{F} can also be expressed as

$$\mathbf{F} = \mathbf{I} + \frac{\partial \mathbf{u}}{\partial \mathbf{X}} = \mathbf{I} + \mathbf{H}, \quad (3.3)$$

where \mathbf{I} is the second-order identity tensor and \mathbf{H} is the displacement gradient. To secure invertibility of the mapping between reference and current configuration, the inverse of the deformation gradient as

$$\mathbf{F}^{-1} = \text{grad}[\mathbf{X}] = \frac{\partial \mathbf{X}}{\partial \mathbf{x}} \quad (3.4)$$

has to be guaranteed. Consequently, the determinant of \mathbf{F} , which is referred to as Jacobian J , must be strictly positive

$$J := \det[\mathbf{F}] > 0. \quad (3.5)$$

This becomes even more clear, as the determinant of \mathbf{F} quantifies the volume change of an infinitesimal volume element dV into the current configuration dv by

$$dv = JdV. \quad (3.6)$$

A negative value of J would correspond to a negative volume after deformation of dV . Similarly, the deformation gradient \mathbf{F} describes the relation between an infinitesimal line element $d\mathbf{X}$ to its state in the current configuration $d\mathbf{x}$ as

$$d\mathbf{x} = \mathbf{F}d\mathbf{X}. \quad (3.7)$$

Furthermore, \mathbf{F} can be applied to describe the deformation of an area element by the formula of Nanson

$$d\mathbf{a} = \mathbf{n} da = J\mathbf{F}^{-T}\mathbf{N}dA = J\mathbf{F}^{-T}d\mathbf{A}. \quad (3.8)$$

The transformations of infinitesimal line, area and volume elements are illustrated in Fig. 3.2.

The deformation gradient \mathbf{F} comprises the local stretch and rotation of each material point of the continuum. By performing a unique right polar decomposition, the stretch and rotation can be separated into

$$\mathbf{F} = \mathbf{R}\mathbf{U}, \quad (3.9)$$

where \mathbf{R} is the orthogonal rotation tensor with $\mathbf{R}^{-1} = \mathbf{R}^T$ and \mathbf{U} is the symmetric right stretch tensor. Comparably, a unique left polar decomposition can be used to separate the deformation gradient into

$$\mathbf{F} = \mathbf{v}\mathbf{R}, \quad (3.10)$$

where the rotation tensor \mathbf{R} remains unchanged but is now on the right side of the product, and \mathbf{v} is the symmetric left stretch tensor.

With regard to material modeling, it is advantageous to formulate the strain measure in one configuration and thereby use a symmetric tensor. Therefore, one universally used strain tensor is the right Cauchy-Green tensor \mathbf{C} which is based on the deformation gradient as

$$\mathbf{C} = \mathbf{F}^T\mathbf{F} = (\mathbf{R}\mathbf{U})^T\mathbf{R}\mathbf{U} = \mathbf{U}^T\mathbf{R}^T\mathbf{R}\mathbf{U} = \mathbf{U}^2 = (U_{IJ})^2\mathbf{E}_I \otimes \mathbf{E}_J, \quad (3.11)$$

resulting in a symmetric tensor in the reference configuration excluding the rotation of the material point. Similarly build, the left Cauchy-Green tensor \mathbf{b} is symmetric in the current configuration with

$$\mathbf{b} = \mathbf{F}\mathbf{F}^T = \mathbf{v}\mathbf{R}(\mathbf{v}\mathbf{R})^T = \mathbf{v}\mathbf{R}\mathbf{R}^T\mathbf{v}^T = \mathbf{v}^2 = (v_{ij})^2\mathbf{e}_i \otimes \mathbf{e}_j. \quad (3.12)$$

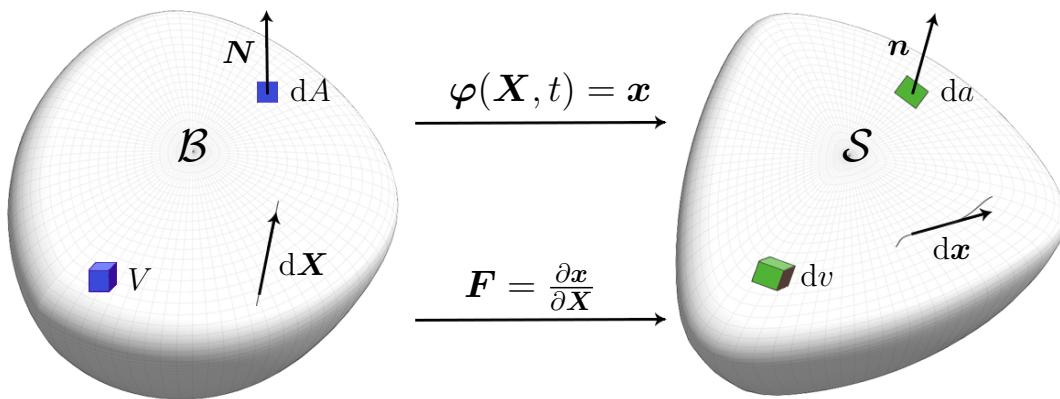


Figure 3.2: Deformation of infinitesimal line element $d\mathbf{X}$, area element dA and volume element dV from the reference configuration \mathcal{B} into the current configuration \mathcal{S} . Deformation of an infinitesimal environment can be described by the deformation gradient \mathbf{F} .

As mentioned above, for solid mechanics the Lagrangian configuration is preferred and, consequently, the right Cauchy-Green tensor \mathbf{C} is applied to formulate material models of the arterial wall. For this purpose, the strain energy density function $\Psi(\mathbf{C}) = \Psi(I_1, I_2, I_3)$ of an isotropic material depends on the principal invariants I_1 , I_2 and I_3 calculated from \mathbf{C} . Principal invariants can also be expressed directly using the eigenvalues of \mathbf{C} given by the square of eigenvalues λ_i of $\mathbf{F} = \sum_{i=1}^3 \lambda_i \mathbf{n}_i \otimes \mathbf{N}_I$ with eigenvectors \mathbf{n}_i in the current configuration and the eigenvectors \mathbf{N}_I in the reference configuration. This results in

$$\mathbf{C} = \sum_{i=1}^3 \lambda_i^2 \mathbf{N}_I \otimes \mathbf{N}_I \quad (3.13)$$

for the right Cauchy-Green tensor. With known \mathbf{C} or eigenvalues of \mathbf{F} (or \mathbf{C}), the principal invariants can be determined by

$$\begin{aligned} I_1 &= \text{tr}[\mathbf{C}] = \lambda_1^2 + \lambda_2^2 + \lambda_3^2, \\ I_2 &= \frac{1}{2}(\text{tr}^2[\mathbf{C}] - \text{tr}[\mathbf{C}^2]) = \lambda_1^2 \lambda_2^2 + \lambda_1^2 \lambda_3^2 + \lambda_2^2 \lambda_3^2, \quad \text{and} \\ I_3 &= \det[\mathbf{C}] = \lambda_1^2 \lambda_2^2 \lambda_3^2. \end{aligned} \quad (3.14)$$

Since the tissue of the arterial wall comprises collagen fibers and SMCs with an orientation, two mixed invariants are considered additionally,

$$I_4^{(f)} = \mathbf{C} \cdot \mathbf{M}^{(f)} \quad \text{and} \quad I_5^{(f)} = \mathbf{C}^2 \cdot \mathbf{M}^{(f)}, \quad (3.15)$$

where the concept of structural tensors $\mathbf{M}^{(f)} = \mathbf{a}^{(f)} \otimes \mathbf{a}^{(f)}$ [22] is applied to address the anisotropy of the material. Thereby, a fiber direction (f) of collagen or SMCs at a material point is regarded by the vector $\mathbf{a}^{(f)}$. It is worth mentioning that the invariant I_5 is not polyconvex on its own. However, polyconvexity is crucial to ensure the existence of minimizers and material stability [7]. Therefore, a combination of I_1 , I_4 and I_5 can be used to express the highly non-linear material behavior of collagen fibers with

$$K_3^{(f)} = I_1 I_4^{(f)} - I_5^{(f)}, \quad (3.16)$$

which fulfills the polyconvexity condition [155].

As an additional aspect, time derivatives of the kinematic quantities have to be considered. Widely used for fluid mechanics is the spatial velocity gradient \mathbf{l} with

$$\mathbf{l} = \frac{\partial \dot{\mathbf{x}}}{\partial \mathbf{x}}, \quad (3.17)$$

which describes the local changes of the velocity $\dot{\mathbf{x}} = \partial \mathbf{x} / \partial t$ at the material point in the current configuration. The spatial velocity gradient \mathbf{l} can also be directly expressed depending on the time derivative of the deformation gradient $\dot{\mathbf{F}}$ since

$$\dot{\mathbf{F}} = \frac{\partial}{\partial t} \left(\frac{\partial \mathbf{x}}{\partial \mathbf{X}} \right) = \frac{\partial \dot{\mathbf{x}}}{\partial \mathbf{X}} = \frac{\partial \dot{\mathbf{x}}}{\partial \mathbf{x}} \frac{\partial \mathbf{x}}{\partial \mathbf{X}} = \mathbf{l} \mathbf{F}, \quad (3.18)$$

which results in

$$\mathbf{l} = \dot{\mathbf{F}}\mathbf{F}^{-1}. \quad (3.19)$$

Furthermore, the time derivative of the Jacobian J is introduced for the following discussion of the balance equations as

$$\dot{J} = \frac{\partial J}{\partial t} = \frac{\partial J}{\partial \mathbf{F}} \cdot \frac{\partial \mathbf{F}}{\partial t} = J\mathbf{F}^{-\text{T}} \cdot \dot{\mathbf{F}} = J\text{tr}[\dot{\mathbf{F}}\mathbf{F}^{-1}] = J\text{tr}[\mathbf{l}] = J\text{div}[\dot{\mathbf{x}}]. \quad (3.20)$$

3.2 Stress Measures

An external force exerted on a physical body leads to an internal loading state. This state is grasped by the concept of stress which is defined as force per unit area. Stress associated with an arbitrary cutting plane can, e.g., be expressed by a stress vector $\mathbf{t} = d\mathbf{f}/da$ where \mathbf{f} is the force vector to the current cut surface area a . The stress vector \mathbf{t} contains a normal component in the direction of the unit normal vector \mathbf{n} and two perpendicular shear components. Consequently, the three dimensional stress state, which consists of three normal and six shear components, is not fully covered by the stress vector \mathbf{t} . Therefore, the Cauchy stress tensor $\boldsymbol{\sigma}$ is introduced. With regard to the stress vector \mathbf{t} , the Cauchy theorem can be applied:

$$\mathbf{t} = \boldsymbol{\sigma}\mathbf{n}. \quad (3.21)$$

Cauchy stress is used to express the final stress state of a body as $\boldsymbol{\sigma} = \sigma_{ij}\mathbf{e}_i \otimes \mathbf{e}_j$ describes the current force per unit area in the current configuration which is considered as true stress. Based on the balance of angular momentum, Cauchy stress is symmetric which will be briefly outlined in Section 3.3.3. However, in continuum mechanics it is often advantageous to formulate quantities in respect to the reference configuration. A stress vector with regard to the forces per unit area of the reference configuration is expressed as $\mathbf{T} = d\mathbf{f}/dA$. Furthermore, the first Piola-Kirchhoff stress tensor \mathbf{P} relates to \mathbf{T} by

$$\mathbf{T} = \mathbf{P}\mathbf{N}, \quad (3.22)$$

where \mathbf{N} is the unit normal vector on the cutting plane in the reference configuration. As the incremental force vector $d\mathbf{f}$ for the calculation of \mathbf{t} and \mathbf{T} is the same, the expression

$$\mathbf{T}dA = \mathbf{P}\mathbf{N}dA \stackrel{!}{=} \mathbf{t}dA = \boldsymbol{\sigma}\mathbf{n}da \quad (3.23)$$

is fulfilled. With the conversion of the normal vectors of the cutting plane in different configurations $\mathbf{n}da = J\boldsymbol{\sigma}\mathbf{F}^{-\text{T}}\mathbf{N}dA$, the following relation between first Piola-Kirchhoff stress and Cauchy stress $\boldsymbol{\sigma}$ holds:

$$\mathbf{P} = J\boldsymbol{\sigma}\mathbf{F}^{-\text{T}} = J\sigma_{ik}F_{kJ}^{-\text{T}}\mathbf{e}_i \otimes \mathbf{E}_J = P_{iJ}\mathbf{e}_i \otimes \mathbf{E}_J. \quad (3.24)$$

Consequently, the first Piola-Kirchhoff stress tensor describes the current force per unit area in the reference configuration. Associated with this, first Piola-Kirchhoff stress is not necessarily symmetric. Therefore, another mathematical advantage is obtained using the second Piola-Kirchhoff stress tensor \mathbf{S} which can be expressed as

$$\mathbf{S} = \mathbf{F}^{-1}\mathbf{P} = J\mathbf{F}^{-1}\boldsymbol{\sigma}\mathbf{F}^{-\text{T}} = JF_{Ik}^{-1}\sigma_{kl}F_{lJ}^{-\text{T}}\mathbf{E}_I \otimes \mathbf{E}_J = S_{IJ}\mathbf{E}_I \otimes \mathbf{E}_J, \quad (3.25)$$

resulting in a symmetric stress tensor. The second Piola-Kirchhoff stress \mathbf{S} does not have a physical interpretation. Nonetheless, \mathbf{S} can and will be used to describe the principles of the finite element method in Sec. 4 and the material model of the arterial wall.

3.3 Balance Equations

To satisfy characteristics of the real world, fundamental physical observations have to be fulfilled in our calculations. The relevant physical laws are expressed by the balance equations of mass, the linear momentum, the angular momentum, and the first and second law of thermodynamics. Subsequently, these balance equations will be discussed for a closed system which is sufficient for most basic mechanical simulations including simulations with active contraction of an arterial wall. However, later in this thesis, growth will be considered which requires an open system where mass can be generated or reduced. Necessary changes to balance equations are discussed in the corresponding chapter for growth in Sec. 7.2.1.

3.3.1 Balance of Mass

A physical body occupies a particular volume which can be observed as a closed system. The corresponding mass of the physical body can be obtained by considering its mass density. Mass density is not necessarily constant over all times since deformations of the body can lead to changes of the volume. Accordingly, the mass of the infinitesimal element is defined by

$$dM = \rho_0 dV \quad \text{and} \quad dm = \rho dv \quad (3.26)$$

in the reference and the current configuration respectively, with ρ_0 as mass density in the referential state and ρ as mass density in the current state. The balance of the mass states that the mass of a closed system does not change over time such that

$$m := \int_S \rho(\mathbf{x}, t) dv = \text{const.} \quad \text{and} \quad \dot{m} \stackrel{!}{=} 0. \quad (3.27)$$

Applying the Reynolds-Transport-Theorem (RTT), the derivative of the mass over time can be reformulated to

$$\dot{m} = \frac{dm}{dt} = \frac{d}{dt} \int_S \rho dv \stackrel{\text{(RTT)}}{=} \int_S \left(\frac{\partial \rho}{\partial t} + \text{div}[\rho \dot{\mathbf{x}}] \right) dv \stackrel{!}{=} 0. \quad (3.28)$$

Consequently, the balance of mass is fulfilled in a closed system if

$$\frac{\partial \rho}{\partial t} + \text{div}[\rho \dot{\mathbf{x}}] = 0 \quad (3.29)$$

is satisfied for any current mass element, which is considered the local form of the balance of mass. Furthermore, the first and second term of Eq. (3.29) can be transformed with $\partial \rho / \partial t = d\rho / dt - \text{grad}[\rho] \cdot \dot{\mathbf{x}}$ and $\text{div}[\rho \dot{\mathbf{x}}] = \text{grad}[\rho] \cdot \dot{\mathbf{x}} + \rho \text{div}[\dot{\mathbf{x}}]$ deriving to

$$\dot{\rho} + \rho \text{div}[\dot{\mathbf{x}}] = 0, \quad (3.30)$$

which is the continuity equation of mass.

3.3.2 Balance of Linear Momentum

The linear momentum \mathbf{p} of a physical body is defined as mass times velocity integrated over all material points. Due to the balance of linear momentum, the time derivative of the linear momentum $\dot{\mathbf{p}}$ must balance all forces \mathbf{f} which act on the body. The linear momentum and its time derivative are defined by

$$\mathbf{p} = \int_S \rho(\mathbf{x}, t) \dot{\mathbf{x}}(\mathbf{x}, t) dv \quad \text{and} \quad \dot{\mathbf{p}} = \frac{\partial}{\partial t} \mathbf{p} = \int_S \frac{\partial}{\partial t} (\rho(\mathbf{x}, t) \dot{\mathbf{x}}(\mathbf{x}, t) dv). \quad (3.31)$$

To solve the time derivative over all terms, the integral over the current configuration is exchanged with an integral over the reference configuration including $dv = JdV$. In this context, the time derivative of V is zero and the time derivative of J is known from Eq. (3.20) with $\dot{J} = J \operatorname{div}[\dot{\mathbf{x}}]$ resulting in

$$\dot{\mathbf{p}} = \int_{\mathcal{B}} (\dot{\rho} \dot{\mathbf{x}} J + \rho \ddot{\mathbf{x}} J + \rho \dot{\mathbf{x}} J \operatorname{div}[\dot{\mathbf{x}}]) dV = \int_{\mathcal{B}} \rho \ddot{\mathbf{x}} J dV + \int_{\mathcal{B}} (\dot{\rho} + \rho \operatorname{div}[\dot{\mathbf{x}}]) \dot{\mathbf{x}} J dV. \quad (3.32)$$

Since the continuity equation of mass from Eq. (3.30) shows that $\dot{\rho} + \rho \operatorname{div}[\dot{\mathbf{x}}] = 0$, the time derivative of the linear momentum can be reduced to

$$\dot{\mathbf{p}} = \int_{\mathcal{B}} \rho_0 \ddot{\mathbf{x}} dV \quad (3.33)$$

including the transformation of mass density into the reference configuration by $\rho = \rho_0/J$.

For the forces acting on the body, external forces on the surface of the body \mathbf{f}_t as well as volumetric forces \mathbf{f}_b have to be considered. Consequently, the forces \mathbf{f} are described by

$$\mathbf{f} = \underbrace{\int_S \rho \mathbf{b} dv}_{\mathbf{f}_b} + \underbrace{\int_{\partial S} \mathbf{t} da}_{\mathbf{f}_t}, \quad (3.34)$$

where \mathbf{b} is the volume acceleration and \mathbf{t} is the traction vector acting on the surface ∂S of the body. Transforming the forces to the reference configuration to enable the comparison with the time derivative of the linear momentum presented in Eq. (3.33) and applying the Gauss divergence theorem, the equation can be expressed as

$$\mathbf{f} = \int_{\mathcal{B}} \rho_0 \mathbf{b} dV + \int_{\mathcal{B}} \operatorname{Div}[\mathbf{P}] dV \quad \text{with} \quad \int_{\partial S} \mathbf{t} da = \int_S \operatorname{div}[\boldsymbol{\sigma}] dv = \int_{\mathcal{B}} \operatorname{Div}[\mathbf{P}] dV. \quad (3.35)$$

Eventually, the balance of linear momentum is described by

$$\int_{\mathcal{B}} \rho_0 \ddot{\mathbf{x}} dV = \int_{\mathcal{B}} \rho_0 \mathbf{b} dV + \int_{\mathcal{B}} \operatorname{Div}[\mathbf{P}] dV \quad (3.36)$$

which can be reduced to the local form

$$\rho_0 \ddot{\mathbf{x}} = \rho_0 \mathbf{b} + \text{Div}[\mathbf{P}]. \quad (3.37)$$

3.3.3 Balance of Angular Momentum

Similar to the balance of linear momentum, the balance of angular momentum states that the time derivative of the angular momentum $\dot{\mathbf{h}}$ of the physical body equals the resulting momentum from forces acting on the body. The angular momentum \mathbf{h} is in reference to the origin of the coordinate system and defined as

$$\mathbf{h} = \int_S \rho(\mathbf{x}, t) \mathbf{x} \times \dot{\mathbf{x}}(\mathbf{x}, t) dv, \quad (3.38)$$

in the current configuration. Using the product rule to form the time derivative of \mathbf{h} and inserting the local form of the balance of mass from Eq. (3.30), $\dot{\mathbf{h}}$ can be expressed as

$$\dot{\mathbf{h}} = \frac{d}{dt} \mathbf{h} = \frac{d}{dt} \int_S \rho \mathbf{x} \times \dot{\mathbf{x}} dv = \int_S \rho \mathbf{x} \times \ddot{\mathbf{x}} dv. \quad (3.39)$$

The resulting momentum of the forces acting on the body include the volumetric forces \mathbf{f}_b as well as the forces on the surface of the body \mathbf{f}_t . Accordingly, the resulting moment on the body is characterized by

$$\mathbf{M} = \int_S \rho \mathbf{x} \times \mathbf{b}(\mathbf{x}, t) dv + \int_{\partial S} \mathbf{x} \times \mathbf{t}(\mathbf{x}, t) da, \quad (3.40)$$

where \mathbf{b} and \mathbf{t} are acceleration of a point and the traction vector on the surface ∂S . Applying a modified version of the Gauss divergence theorem to formulate \mathbf{M} without reference to the body surface ∂S , \mathbf{M} can be reformulated to

$$\mathbf{M} = \int_S (\rho \mathbf{x} \times \mathbf{b}(\mathbf{x}, t) + \mathbf{x} \times \text{div} [\boldsymbol{\sigma}^T] + \mathbf{I} \cdot \times \boldsymbol{\sigma}^T) dv. \quad (3.41)$$

Consequently, the balance of angular momentum states that $\dot{\mathbf{h}} - \mathbf{M} = \mathbf{0}$ which results in

$$\dot{\mathbf{h}} - \mathbf{M} = \int_S \left[\mathbf{x} \times \underbrace{(\rho \ddot{\mathbf{x}} - \rho \mathbf{b} - \text{div} [\boldsymbol{\sigma}^T])}_{=0} - \mathbf{I} \cdot \times \boldsymbol{\sigma}^T \right] dv = \mathbf{0}, \quad (3.42)$$

where $\rho \ddot{\mathbf{x}} - \rho \mathbf{b} - \text{div} [\boldsymbol{\sigma}^T] = \mathbf{0}$ is the local form of the balance of linear momentum in the current configuration. The local form of the balance of angular momentum can be expressed as

$$\mathbf{I} \cdot \times \boldsymbol{\sigma}^T = \mathbf{0} \quad (3.43)$$

and be used to demonstrate that the Cauchy stress tensor $\boldsymbol{\sigma}$ as well as the second Piola-Kirchhoff stress tensor \mathbf{S} are symmetric and, consequently,

$$\boldsymbol{\sigma} = \boldsymbol{\sigma}^T \quad \text{and} \quad \mathbf{S} = \mathbf{S}^T \quad (3.44)$$

is satisfied at all times.

3.3.4 Balance of Energy (First Law of Thermodynamics)

Due to the balance of energy, also known as the first law of thermodynamics, the change of internal and kinetic energy of a physical body has to equal the work performed on it which is considered as the mechanical and thermal work here. Accordingly, the balance of energy can be expressed by the equation $\dot{\mathcal{E}} + \dot{\mathcal{K}} = \mathcal{P} + \mathcal{Q}$ where \mathcal{E} is the mechanical energy of the body, \mathcal{K} is the kinetic energy of the body, and \mathcal{P} and \mathcal{Q} are the mechanical and thermal work, respectively. The inner energy of the body is described by

$$\mathcal{E} = \int_S e \rho \, dv, \quad (3.45)$$

where e is a variable for the specific inner energy per unit reference mass. For the time derivative of \mathcal{E} , the product rule has to be applied in the reference configuration which results in

$$\dot{\mathcal{E}} = \int_B \left[\dot{e} \rho J + e \dot{\rho} J + e \rho \dot{J} \right] dV = \int_B \left[\dot{e} \rho + e \underbrace{(\dot{\rho} + \rho \operatorname{div} [\dot{\mathbf{x}}])}_{=0} \right] J dV = \int_B \dot{e} \rho_0 \, dV \quad (3.46)$$

considering the balance of mass from Eq. (3.30). Similar to $\dot{\mathcal{E}}$, the derivative of the kinetic energy can be built by including the balance of mass as well after the execution of the product rule where $\dot{\mathcal{K}}$ is reformulated to

$$\begin{aligned} \dot{\mathcal{K}} &= \frac{1}{2} \int_B \left[\dot{\rho} \dot{\mathbf{x}} \cdot \dot{\mathbf{x}} J + \rho \ddot{\mathbf{x}} \cdot \dot{\mathbf{x}} J + \rho \dot{\mathbf{x}} \cdot \ddot{\mathbf{x}} J + \rho \dot{\mathbf{x}} \cdot \dot{\mathbf{x}} \dot{J} \right] dV \\ &= \frac{1}{2} \int_B \left[\dot{\mathbf{x}} \cdot \dot{\mathbf{x}} \underbrace{(\dot{\rho} + \rho \operatorname{div} [\dot{\mathbf{x}}])}_{=0} + 2\rho \dot{\mathbf{x}} \cdot \ddot{\mathbf{x}} \right] J dV = \int_B \rho_0 \dot{\mathbf{x}} \cdot \ddot{\mathbf{x}} \, dV \end{aligned} \quad (3.47)$$

$$\text{with } \mathcal{K} = \frac{1}{2} \int_S \rho \dot{\mathbf{x}} \cdot \dot{\mathbf{x}} \, dv.$$

The mechanical work includes the volumetric forces as well as the forces acting at the surface $\partial\mathcal{S}$ of the body which are again included by the body acceleration \mathbf{b} and the traction vector \mathbf{t} . Applying the Gauss divergence theorem to include the mechanical work \mathcal{P} in the volumetric form of the current configuration, \mathcal{P} can be expressed as

$$\mathcal{P} = \int_S \rho \dot{\mathbf{x}} \cdot \mathbf{b} \, dv + \int_{\partial\mathcal{S}} \dot{\mathbf{x}} \cdot \mathbf{t} \, dv = \int_S (\rho \dot{\mathbf{x}} \cdot \mathbf{b} + \operatorname{div} [\boldsymbol{\sigma} \dot{\mathbf{x}}]) \, dv. \quad (3.48)$$

Furthermore, the equation can be transferred into the reference configuration and, subsequently, reformulated with $\operatorname{Div} [\mathbf{P}^T \dot{\mathbf{x}}] = \operatorname{Div} [\mathbf{P}] \cdot \dot{\mathbf{x}} + \mathbf{P} \cdot \dot{\mathbf{F}}$ into

$$\begin{aligned} \mathcal{P} &= \int_B (\rho_0 \dot{\mathbf{x}} \cdot \mathbf{b} + \operatorname{Div} [\mathbf{P}^T \dot{\mathbf{x}}]) \, dV = \int_B \left[\dot{\mathbf{x}} \cdot \underbrace{(\rho_0 \mathbf{b} + \operatorname{Div} [\mathbf{P}])}_{=\rho_0 \ddot{\mathbf{x}}} + \mathbf{P} \cdot \dot{\mathbf{F}} \right] dV \\ &= \int_B \left[\rho_0 \dot{\mathbf{x}} \cdot \ddot{\mathbf{x}} + \mathbf{P} \cdot \dot{\mathbf{F}} \right] dV, \end{aligned} \quad (3.49)$$

where $\rho_0 \mathbf{b} + \operatorname{div} [\mathbf{P}] = \rho_0 \ddot{\mathbf{x}}$ is the local form of the balance of linear momentum from Eq. (3.37). Finally, thermal energy comprises the inner heat source r per unit reference

volume and the inward heat source \mathbf{q} per time which enters the physical body across the surface $\partial\mathcal{S}$. Converting thermal energy into the reference configuration by including the Gauss divergence theorem, \mathcal{Q} is described by

$$\mathcal{Q} = \int_{\mathcal{S}} r \, dv + \int_{\partial\mathcal{S}} \mathbf{q} \cdot \mathbf{n} \, da = \int_{\mathcal{S}} (r - \operatorname{div}[\mathbf{q}]) \, dv = \int_{\mathcal{B}} (r_0 - \operatorname{Div}[\mathbf{q}_0]) \, dV, \quad (3.50)$$

with the normal vector \mathbf{n} on an infinitesimal area element of the surface $\partial\mathcal{S}$.

Taking all four parts of the balance of energy into account, the final equation over the entire body can be expressed as

$$\begin{aligned} \int_{\mathcal{B}} \dot{e} \rho_0 \, dV + \int_{\mathcal{B}} \rho_0 \dot{\mathbf{x}} \cdot \ddot{\mathbf{x}} \, dV &= \int_{\mathcal{B}} (\dot{\mathbf{x}} \cdot \rho_0 \ddot{\mathbf{x}} + \mathbf{P} \cdot \dot{\mathbf{F}}) \, dV + \int_{\mathcal{B}} (r_0 - \operatorname{Div}[\mathbf{q}_0]) \, dV \\ \int_{\mathcal{B}} \dot{e} \rho_0 \, dV &= \int_{\mathcal{B}} (\mathbf{P} \cdot \dot{\mathbf{F}} + r_0 - \operatorname{Div}[\mathbf{q}_0]) \, dV. \end{aligned} \quad (3.51)$$

This equation is also fulfilled when every material point of the body satisfies the local form

$$\dot{e} \rho_0 = \mathbf{P} \cdot \dot{\mathbf{F}} + r_0 - \operatorname{Div}[\mathbf{q}_0], \quad (3.52)$$

which can also be formulated in respect to the second Piola-Kirchhoff stress \mathbf{S} with $\mathbf{P} \cdot \dot{\mathbf{F}} = \mathbf{F} \mathbf{S} \cdot \dot{\mathbf{F}} = \mathbf{S} \cdot \mathbf{F}^T \dot{\mathbf{F}} = 1/2 \mathbf{S} \cdot \dot{\mathbf{C}}$ resulting in

$$\dot{e} \rho_0 = \frac{1}{2} \mathbf{S} \cdot \dot{\mathbf{C}} + r_0 - \operatorname{Div}[\mathbf{q}_0]. \quad (3.53)$$

3.3.5 Balance of Entropy (Second Law of Thermodynamics)

As fundamental physical observation, it is known that heat is transported exclusively from warmer to colder regions of a system. Furthermore, heat can be produced by mechanical energy and increase the thermal energy of an isolated system, but not the other way around. To satisfy these observations, the entropy of an isolated system cannot decrease over time. In particular, the entropy remains unchanged for an idealized reversible process, but increases for irreversible processes. In consequence, the balance of entropy states that the total production of entropy per time cannot be negative. The time derivative of the entropy $\dot{\mathcal{S}}$ of the physical body can be expressed as

$$\dot{\mathcal{S}} = \int_{\mathcal{S}} \left(\dot{\rho} s + \underbrace{\rho \dot{s} + \rho s \operatorname{div}[\dot{\mathbf{x}}]}_{=0} \right) dv = \int_{\mathcal{S}} \rho \dot{s} \, dv \quad \text{with} \quad \mathcal{S} = \int_{\mathcal{S}} \rho s \, dv, \quad (3.54)$$

where the local form of the balance of mass is applied, and s is the specific entropy per unit reference mass. Including the rate of entropy into the equation, the balance of entropy can be formulated in terms of the Clausius-Duhem inequality as

$$\int_{\mathcal{S}} \rho \dot{s} \, dv \geq \int_{\mathcal{S}} \frac{r}{\theta} \, dv - \int_{\partial\mathcal{S}} \frac{1}{\theta} \mathbf{q} \cdot \mathbf{n} \, da, \quad (3.55)$$

where the first term on the right side is the inner entropy source and the second term is the entropy flux over the surface of the closed system. Furthermore, r is the inner

heat source per unit reference volume and \mathbf{q} is the inward heat source per time which enters the physical body across the surface $\partial\mathcal{S}$ as defined for the thermal energy \mathcal{Q} in the previous section. Using the Gauss divergence theorem, the entropy flux can be transformed into the volumetric form. Consequently, the balance of entropy can be expressed in the local form of the reference configuration as

$$\mathcal{D} = \rho_0 \dot{s} - \frac{r_0}{\theta} + \text{Div} \left[\frac{\mathbf{q}_0}{\theta} \right] \geq 0, \quad (3.56)$$

where \mathcal{D} is defined as the internal dissipation.

For the next step, the balance of energy is again taken into account. Here, the variable for the specific inner energy per unit reference mass e can be split into the stored energy $\tilde{\Psi}$ per unit reference mass and the potential for dissipation by $e = \tilde{\Psi} - \theta s$. This leads to the local form of the balance of energy from Eq. (3.53) as

$$\left(\dot{\tilde{\Psi}} - \dot{\theta} s \right) \rho_0 = \frac{1}{2} \mathbf{S} \cdot \dot{\mathbf{C}} + r_0 - \text{Div}[\mathbf{q}_0], \quad (3.57)$$

where $\dot{\theta} s$ is the time derivative of the term θs . Dividing this equation by the temperature θ , it can be reformulated to

$$-\frac{r_0}{\theta} = \frac{1}{\theta} \left(\frac{1}{2} \mathbf{S} \cdot \dot{\mathbf{C}} - \dot{\tilde{\Psi}} \rho_0 + \dot{\theta} s \rho_0 + \theta \dot{s} \rho_0 - \text{Div}[\mathbf{q}_0] \right). \quad (3.58)$$

Inserting Eq. (3.58) and $\text{Div} \left[\frac{\mathbf{q}_0}{\theta} \right] = 1/\theta \text{Grad}[\theta] \cdot \mathbf{q}_0 + 1/\theta \text{Div}[\mathbf{q}_0]$ into Eq. (3.56) results in

$$\mathcal{D} = \frac{1}{\theta} \left[\frac{1}{2} \mathbf{S} \cdot \dot{\mathbf{C}} - \rho_0 \left(\dot{\tilde{\Psi}} + \dot{\theta} s \right) - \frac{1}{\theta} \text{Grad}[\theta] \cdot \mathbf{q}_0 \right] \geq 0. \quad (3.59)$$

For many applications, it can be assumed that the change of the temperature of the physical body is negligible. Consequently, processes can be approximated to be isothermal which results in a constant temperature $\dot{\theta} = 0$ and no heat flux over the surface of the body $\mathbf{q} = 0$. In this case, the equation can be reduced to

$$\mathcal{D} = \frac{1}{2} \mathbf{S} \cdot \dot{\mathbf{C}} - \dot{\tilde{\Psi}} \geq 0, \quad (3.60)$$

where $\tilde{\Psi}$ is the stored energy per unit reference volume, also known as the free Helmholtz energy or the strain-energy density function. Assuming that the free Helmholtz energy is a function of the right Cauchy-Green tensor \mathbf{C} , the time derivative $\dot{\tilde{\Psi}}$ can be formulated with the chain rule as

$$\dot{\tilde{\Psi}}(\mathbf{C}) = \frac{\partial \tilde{\Psi}}{\partial \mathbf{C}} \cdot \frac{\partial \mathbf{C}}{\partial t} = \frac{\partial \tilde{\Psi}}{\partial \mathbf{C}} \cdot \dot{\mathbf{C}}. \quad (3.61)$$

Inserting this derivative into Eq. (3.60) leads to

$$\left(\frac{1}{2} \mathbf{S} - \frac{\partial \tilde{\Psi}}{\partial \mathbf{C}} \right) \cdot \dot{\mathbf{C}} \geq 0. \quad (3.62)$$

To satisfy any process in which $\dot{\mathbf{C}}$ is arbitrary, the term inside the bracket has to equal zero. This is the standard argument of rational continuum mechanics, also known as Coleman-Noll method, which results in the following constitutive equations for the stresses:

$$\mathbf{S} = 2 \frac{\partial \Psi}{\partial \mathbf{C}}. \quad (3.63)$$

4 Finite Element Method

Based on the balance equations described in the previous chapter, the deformed state of a physical body under surface or volumetric load can be determined. In principal, an analytic solution is feasible for simple mechanical problems. However, more complex problems require a computational approach which enables a reliable approximation of body displacements. Here, the finite element method (FEM) is a robust and adaptable approach and therefore universally applied in the field of engineering. In total, three steps have to be performed to determine the final equations for FEM with regard to finite strain theory. The balance of linear momentum describes the relation between the position of a point in the current configuration and the corresponding stresses and is, therefore, the starting point. In the basic form, it constitutes a complex system of nonlinear partial differential equations. As a first step, the balance of linear momentum is replaced by a weak form which changes the vectorial equation into a scalar form. This enables the solution of problems with discontinuous variations of variables such as changes in the material. Furthermore, the nonlinearity of the equations, which is caused by the nonlinear material behavior and the geometric nonlinearity with large displacements, makes an analytic solution generally improbable. Therefore, the application of an incremental solution technique as the Newton–Raphson method is beneficial which requires a consistent linearization of nonlinear problems. Consequently, as a second step, a linearization of the weak form of the balance of linear momentum is derived. As the final step, the complex geometry of the physical body is discretized into a finite number of elements. These elements are defined by a set of individual points (also known as nodes) and associated connections. The mechanical fields, such as the displacements, can then be interpolated between the nodes by the usage of preselected shape functions. Furthermore, discretizing the body into elements and corresponding shape functions allows to solve volume integrals by Gauss point integration. In the following sections, the three steps to derive the classical finite element method, which is applied in this thesis, are summarized. However, more complex examples can be found in literature, e.g., WRIGGERS [191], ZIENKIEWICZ, TAYLOR, AND FOX [204] and BATHE [11].

4.1 Variational Problem

To determine the displacement field of a deformed body based on a corresponding load, the balance of linear momentum has to be considered, which was derived in the local form as

$$\text{Div}[\mathbf{P}] + \rho_0 [\mathbf{b} - \ddot{\mathbf{x}}] = \mathbf{0}, \quad (4.1)$$

see Section 3.3.2. Furthermore, boundary conditions and initial conditions for motion are necessary to satisfy the equation. Accordingly, the surface of the physical body $\partial\mathcal{B}$ can be decomposed into disjoint parts with

$$\mathbf{u} = \mathbf{u}_{\text{BC}} \quad \text{on} \quad \partial\mathcal{B}_u \quad \text{and} \quad \mathbf{P}\mathbf{N} = \mathbf{T}_{\text{BC}} \quad \text{on} \quad \partial\mathcal{B}_\sigma, \quad (4.2)$$

where the displacements \mathbf{u}_{BC} of the surface part $\partial\mathcal{B}_u$ are Dirichlet boundary conditions and the surface traction \mathbf{T}_{BC} of the surface part $\partial\mathcal{B}_\sigma$ defines Neumann boundary condi-

tions. To enable the approximation of the displacement field \mathbf{u} using FEM, the strong form in Eq. (4.1) is multiplied with the vectorial test function $\delta\mathbf{u}$. This test function $\delta\mathbf{u}$ can be considered as arbitrary virtual change of the displacement \mathbf{u} (variation of \mathbf{u}) independent of the real displacement. Subsequently, the integral over the entire body is formed which leads to the weak form

$$G = \int_{\mathcal{B}} (\text{Div}[\mathbf{P}] + \rho_0 [\mathbf{b} - \ddot{\mathbf{x}}]) \cdot \delta\mathbf{u} \, dV = 0, \quad (4.3)$$

where G is the scalar value of the virtual work. To include the Neumann boundary conditions and separate them from the internal stresses, the divergence $\text{Div}[\mathbf{P}^T \delta\mathbf{u}]$ is used to replace the term $\mathbf{P} : \text{Grad}[\delta\mathbf{u}]$. Furthermore, the Gauss divergence theorem is applied which results in

$$\begin{aligned} G &= \int_{\mathcal{B}} \mathbf{P} : \text{Grad}[\delta\mathbf{u}] \, dV - \int_{\partial\mathcal{B}_\sigma} \mathbf{T}_{\text{BC}} \cdot \delta\mathbf{u} \, dA - \int_{\mathcal{B}} \rho_0 (\mathbf{b} - \ddot{\mathbf{x}}) \cdot \delta\mathbf{u} \, dV \\ &\text{with } \text{Div}[\mathbf{P}^T \delta\mathbf{u}] = \text{Div}[\mathbf{P}] \cdot \delta\mathbf{u} + \mathbf{P} : \text{Grad}[\delta\mathbf{u}] \\ &\text{and } \int_{\mathcal{B}} \text{Div}[\mathbf{P}^T \delta\mathbf{u}] \, dV = \int_{\partial\mathcal{B}_\sigma} \mathbf{P}^T \delta\mathbf{u} \cdot \mathbf{N} \, dA = \int_{\partial\mathcal{B}_\sigma} \mathbf{T}_{\text{BC}} \cdot \delta\mathbf{u} \, dA. \end{aligned} \quad (4.4)$$

From a physical point of view, this formulation of the weak form can be split into the internal virtual energy G^{int} and the external virtual work G^{ext} , corresponding to the virtual displacement $\delta\mathbf{u}$, which leads to

$$\begin{aligned} G &:= G^{\text{int}} - G^{\text{ext}} = 0, \quad \text{with} \\ G^{\text{int}} &= \int_{\mathcal{B}} \mathbf{P} : \text{Grad}[\delta\mathbf{u}] \, dV \quad \text{and} \quad G^{\text{ext}} = \int_{\partial\mathcal{B}_\sigma} \mathbf{T}_{\text{BC}} \cdot \delta\mathbf{u} \, dA + \int_{\mathcal{B}} \rho_0 (\mathbf{b} - \ddot{\mathbf{x}}) \cdot \delta\mathbf{u} \, dV. \end{aligned} \quad (4.5)$$

Subsequently, the inner virtual energy of the weak form of the balance of linear momentum can be transformed into a term which depends on the second Piola-Kirchhoff stress \mathbf{S} . This transformation allows a connection of the equations in this section with later chapters, since \mathbf{S} and the right Cauchy-Green tensor are primarily used for the material modeling of the arterial wall. As a first step, it can be shown that

$$\delta\mathbf{F} = \delta(\text{Grad}[\mathbf{u}] + \mathbf{I}) = \text{Grad}[\delta\mathbf{u}], \quad (4.6)$$

since $\delta\text{Grad}[\mathbf{u}] = \text{Grad}[\delta\mathbf{u}]$ and the second-order identity tensor \mathbf{I} do not change for a virtual variation of $\delta\mathbf{u}$ and, therefore, $\delta\mathbf{I} = \mathbf{0}$. Furthermore, $\mathbf{P} = \mathbf{F}\mathbf{S}$ can be used to exchange the first Piola-Kirchhoff stress tensor \mathbf{P} with a term including the symmetric second Piola-Kirchhoff stress tensor \mathbf{S} . In consequence, $\mathbf{P} : \text{Grad}[\delta\mathbf{u}]$ can be reformulated into

$$\begin{aligned} \mathbf{P} : \text{Grad}[\delta\mathbf{u}] &= \mathbf{P} : \delta\mathbf{F} = \mathbf{F}\mathbf{S} : \delta\mathbf{F} = \mathbf{S} : \mathbf{F}^T \delta\mathbf{F} = \mathbf{S} : \text{sym} [\mathbf{F}^T \delta\mathbf{F}] \\ &= \mathbf{S} : \underbrace{\frac{1}{2} (\mathbf{F}^T \delta\mathbf{F} + \delta\mathbf{F}^T \mathbf{F})}_{=\delta\mathbf{C}} = \mathbf{S} : \frac{1}{2} \delta\mathbf{C}. \end{aligned} \quad (4.7)$$

Consequently, the transformed version of the weak form of the balance of linear momentum is expressed by

$$G = \int_{\mathcal{B}} \mathbf{S} : \frac{1}{2} \delta \mathbf{C} \, dV - \int_{\partial \mathcal{B}_\sigma} \mathbf{T}_{\text{BC}} \cdot \delta \mathbf{u} \, dA - \int_{\mathcal{B}} \rho_0 (\mathbf{b} - \ddot{\mathbf{x}}) \cdot \delta \mathbf{u} \, dV. \quad (4.8)$$

An alternative determination of this equation can be achieved by applying the principle of stationary potential energy where the potential energy of the system Π is obtained by the sum of the internal energy Π^{int} and the external energy Π^{ext} . The unknown deformed configuration can be found when the total potential energy of the system is stationary. This is satisfied when the first variation of Π with respect to the displacement \mathbf{u} is zero which leads to

$$\begin{aligned} \delta \Pi &= \delta \Pi^{\text{int}} + \delta \Pi^{\text{ext}} = 0 \quad \text{with} \\ \delta \Pi^{\text{int}} &= \int_{\mathcal{B}} \mathbf{S} : \frac{1}{2} \delta \mathbf{C} \, dV \quad \text{and} \quad \delta \Pi^{\text{ext}} = - \int_{\partial \mathcal{B}_\sigma} \mathbf{T}_{\text{BC}} \cdot \delta \mathbf{u} \, dA - \int_{\mathcal{B}} \rho_0 (\mathbf{b} - \ddot{\mathbf{x}}) \cdot \delta \mathbf{u} \, dV. \end{aligned} \quad (4.9)$$

4.2 Linearization

As the application of finite strain theory and the nonlinear material behavior increase the difficulty to solve the mechanical problem, the Newton–Raphson method is applied. Based on this method, a linearization of the weak form of the balance of linear momentum is build for a displacement field which is assumed to be close to the real solution. The linearization leads to an update of the displacement field which can be reused in a new linearization. Consequently, this can be performed as an iterative process which converges quadratically as long as it starts close enough to the final solution. To ensure that the assumption for the displacement field is reasonable, the total load is subdivided into load steps as a consequence of which the final value of the load is not applied at once, but increases over time. Accordingly, even simulations for static problems, which are time-independent, are executed by considering a virtual timespan in which the load is raised in every time step. The corresponding linearization $\text{Lin } G$ of the weak form is given by

$$\text{Lin } G = G + \Delta G = 0, \quad (4.10)$$

where ΔG is incremental virtual work which can be considered as the difference of the virtual work G between two consecutive iterative steps $n+1$ and n , such that $(\Delta G)_{n+1} = G_{n+1} - G_n$. Since the virtual work is only dependent on the displacements \mathbf{u} , the term ΔG can also be expressed as

$$\Delta G(\mathbf{u}) := \frac{dG}{d\mathbf{u}} \Delta \mathbf{u}. \quad (4.11)$$

Furthermore, it can be assumed that the Neumann boundary conditions are independent from displacements. Therefore, the incremental virtual work ΔG only bases on

the internal virtual energy G^{int} and can be calculated by applying the product rule such that

$$\Delta G = \Delta G^{\text{int}} = \Delta \left[\int_{\mathcal{B}} \frac{1}{2} \mathbf{S} : \delta \mathbf{C} \, dV \right] = \int_{\mathcal{B}} \frac{1}{2} \Delta \mathbf{S} : \delta \mathbf{C} \, dV + \int_{\mathcal{B}} \frac{1}{2} \mathbf{S} : \Delta \delta \mathbf{C} \, dV. \quad (4.12)$$

According to the definition of ΔG , the increments $\Delta \mathbf{S}$ and $\Delta \delta \mathbf{C}$ are obtained by building the derivation in respect to \mathbf{u} and multiplying by $\Delta \mathbf{u}$. Since the second Piola-Kirchhoff stress tensor \mathbf{S} only depends on \mathbf{u} via the right Cauchy-Green tensor \mathbf{C} , an intermediate step can be performed by

$$\Delta \mathbf{S} = \frac{d\mathbf{S}}{d\mathbf{C}} : \Delta \mathbf{C} = \frac{1}{2} \mathbb{C} : \Delta \mathbf{C} \quad \text{with} \quad \mathbb{C} = 2 \frac{d\mathbf{S}}{d\mathbf{C}}, \quad (4.13)$$

where \mathbb{C} is considered as the tangent modulus. Subsequently, the increment of \mathbf{C} as well as the variation of \mathbf{C} can be expressed by the product rule with regard to the deformation gradient \mathbf{F} such that

$$\begin{aligned} \Delta \mathbf{C} &= \Delta (\mathbf{F}^T \mathbf{F}) = \Delta \mathbf{F}^T \mathbf{F} + \mathbf{F}^T \Delta \mathbf{F} \quad \text{and} \\ \delta \mathbf{C} &= \delta (\mathbf{F}^T \mathbf{F}) = \delta \mathbf{F}^T \mathbf{F} + \mathbf{F}^T \delta \mathbf{F}. \end{aligned} \quad (4.14)$$

Since $\delta \mathbf{F} = \text{Grad}[\delta \mathbf{u}]$ does not depend on the local displacements \mathbf{u} , the increment of the variation of the right Cauchy-Green tensor $\Delta \delta \mathbf{C}$ is built by

$$\Delta \delta \mathbf{C} = \Delta (\delta \mathbf{F}^T \mathbf{F} + \mathbf{F}^T \delta \mathbf{F}) = \delta \mathbf{F}^T \Delta \mathbf{F} + \Delta \mathbf{F}^T \delta \mathbf{F}. \quad (4.15)$$

For the final version of the linearization of G considered in this thesis, inertia and gravity are assumed to be negligible in comparison to acting surface forces. Consequently, ΔG can be formulated as

$$\text{Lin } G = \int_{\mathcal{B}} \mathbf{S} : \frac{1}{2} \delta \mathbf{C} \, dV - \int_{\partial \mathcal{B}_\sigma} \mathbf{T}_{\text{BC}} \cdot \delta \mathbf{u} \, dA + \underbrace{\int_{\mathcal{B}} \frac{1}{2} \delta \mathbf{C} : \mathbb{C} : \frac{1}{2} \Delta \mathbf{C} \, dV}_{=\Delta G_{\text{mat}}^{\text{int}}} + \underbrace{\int_{\mathcal{B}} \mathbf{S} : \frac{1}{2} \Delta \delta \mathbf{C} \, dV}_{=\Delta G_{\text{geo}}^{\text{int}}}, \quad (4.16)$$

where $\Delta G_{\text{mat}}^{\text{int}}$ refers to the material part of the increment ΔG and $\Delta G_{\text{geo}}^{\text{int}}$ to the geometric part.

4.3 Discretization

The main idea of FEM is to subdivide the geometry of the investigated object into a mesh with a finite number of elements. These elements are defined by nodal points. As a result, the infinite number of material points from the continuum mechanical formulation is reduced to a finite number with only nodal values for the unknown displacements of the body. Combining these nodal values with shape functions allows an interpolation of mechanical fields at any point of the element. Several different formulations can be applied for the shape functions. However, linear and quadratic shape functions are primarily used. The quality of the resulting approximation of the geometry and the mechanical fields is highly dependent on the number of elements and the degree of the polynomial (see, e.g., Fig. 4.1). Generally, it can be expected

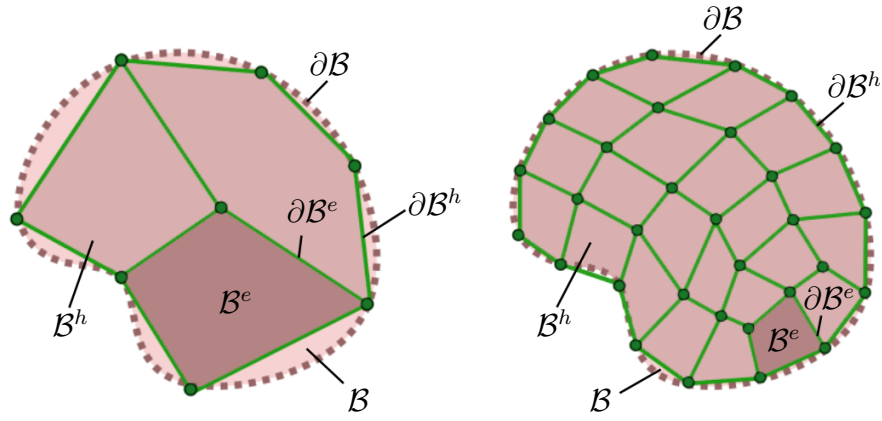


Figure 4.1: Illustration of two examples of finite element approximations \mathcal{B}^h for a two-dimensional body \mathcal{B} . Quality of the approximation increases significantly with the number of elements.

that the accuracy of the mechanical fields computed by a FE simulation increases with a higher number of elements which were generated for the geometry. This property is considered mesh convergence. Nonetheless, certain element types might add an artificial stiffness or show no mesh convergence behavior which was, e.g., identified for tetrahedral elements with linear shape functions. Since the number of elements can increase the calculation time of FE simulations substantially, the desired accuracy of the mechanical problem has to be taken into account to limit the computation resources. In the following paragraphs, the general formulation of the equations for FEM with respect to the discretization of the body is derived. This formulation is independent from the number of elements and assumes polynomial shape functions which allows the application of an isoparametric mapping.

Approximation and Isoparametric Concept The corresponding approximation \mathcal{B}^h of the body \mathcal{B} can be expressed as the union of all elements

$$\mathcal{B} \approx \mathcal{B}^h = \bigcup_{e=1}^{n_{\text{ele}}} \mathcal{B}^e, \quad (4.17)$$

where n_{ele} is the total number of elements. Furthermore, the surface $\partial\mathcal{B}$ of the body \mathcal{B} is approximated by the boundary of the finite element mesh $\partial\mathcal{B}^h$. The position vectors \mathbf{X} and \mathbf{x} for a material point in the reference and current configuration can be approximated as

$$\mathbf{X} \approx \mathbf{X}^h(\boldsymbol{\xi}) = \sum_{I=1}^n N_I(\boldsymbol{\xi}) \mathbf{X}_I \quad \text{and} \quad \mathbf{x} \approx \mathbf{x}^h(\boldsymbol{\xi}) = \sum_{I=1}^n N_I(\boldsymbol{\xi}) \mathbf{x}_I, \quad (4.18)$$

where N_I is the value of a shape function at the position $\boldsymbol{\xi} = [\xi_1 \xi_2 \xi_3]^T$ of the isoparametric element and \mathbf{X}_I as well as \mathbf{x}_I are the nodal positions corresponding to this shape function. As an example for a two-dimensional case, Fig. 4.2 illustrates a quadrilateral element which can be mapped to the isoparametric element. This allows for applying equal shape functions associated with the isoparametric element for every single

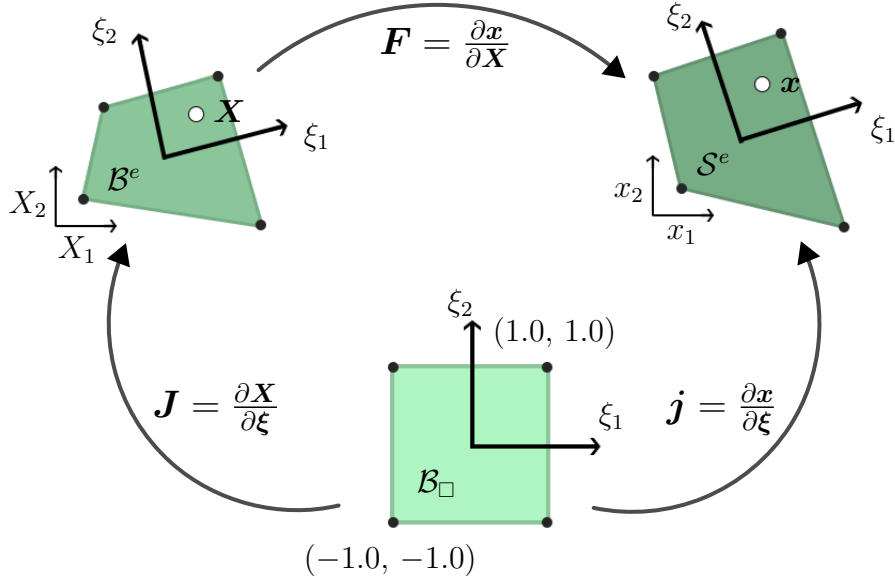


Figure 4.2: Illustration of isoparametric mapping for a quadrilateral element. Shape functions $N_I(\boldsymbol{\xi})$ are efficiently defined for the isoparametric element. Mapping \mathbf{j} and \mathbf{J} between the isoparametric element \mathcal{B}_\square and the reference \mathcal{B}^e or current configuration \mathcal{S}^e of the element enable the application of the shape functions in mechanical equations. Additionally, the location and weight factors of integration points of the isoparametric element are known which allows an approximation of the integral of a function over the volume of the element.

element of the mesh. Shape functions are formulated to equal one at their respective nodes. In addition, the sum of all shape functions at any point of the element equals one. The components of the vector $\boldsymbol{\xi}$ are generally defined on the interval $[-1, 1]$ for the isoparametric element. A transformation between the physical representation of an element and the isoparametric element can be executed by the Jacobi matrices which are defined as

$$\mathbf{J} = \frac{\partial \mathbf{X}}{\partial \boldsymbol{\xi}} \quad \text{and} \quad \mathbf{j} = \frac{\partial \mathbf{x}}{\partial \boldsymbol{\xi}}. \quad (4.19)$$

The displacement vectors at any point of the element are equally approximated as the position vectors. Consequently, the approximation \mathbf{u}^h of the displacement \mathbf{u} and the corresponding mapping of the referential nodal position \mathbf{X}_I to the current nodal position \mathbf{x}_I are formulated as

$$\mathbf{u} \approx \mathbf{u}^h = \sum_{I=1}^n N_I \mathbf{d}_I \quad \text{with} \quad \mathbf{x}_I = \mathbf{X}_I + \mathbf{d}_I, \quad (4.20)$$

where the discretized nodal displacement is denoted as \mathbf{d}_I . Similar to the displacement \mathbf{u} , the variation $\delta \mathbf{u}$ and the increment $\Delta \mathbf{u}$ are defined as

$$\delta \mathbf{u} \approx \delta \mathbf{u}^h = \sum_{I=1}^n N_I \delta \mathbf{d}_I \quad \text{and} \quad \Delta \mathbf{u} \approx \Delta \mathbf{u}^h = \sum_{I=1}^n N_I \Delta \mathbf{d}_I, \quad (4.21)$$

in the discretized form. To improve legibility in the following equations, the superscript \bullet^h for the approximation is subsequently not included anymore.

The gradient of the displacements $\text{Grad}[\mathbf{u}]$ has to be described in the discretized form as

$$\text{Grad}[\mathbf{u}] = \text{Grad} \left[\sum_{I=1}^n N_I \mathbf{d}_I \right] = \sum_{I=1}^n \text{Grad} [N_I] \mathbf{d}_I, \quad (4.22)$$

where the gradient of the shape functions $\text{Grad} [N_I]$ is

$$\text{Grad} [N_I(\boldsymbol{\xi})] = \frac{\partial N_I}{\partial \boldsymbol{\xi}} \frac{\partial \boldsymbol{\xi}}{\partial \mathbf{X}} = \mathbf{J}^{-\text{T}} \frac{\partial N_I}{\partial \boldsymbol{\xi}}. \quad (4.23)$$

To enable the formulation of every coefficient of terms related to the right Cauchy-Green tensor \mathbf{C} , the partial derivative $u_{i,j}$ of a component of \mathbf{u} in direction of X_j is noted here as

$$u_{i,j} = \sum_{I=1}^n (N_I I j)_{,j} = \sum_{I=1}^n N_{I,j} I j \quad \text{with} \quad N_{I,j} = \frac{\partial N_I}{\partial X_j} \quad \text{and} \quad \text{Grad}[\mathbf{u}] = \underbrace{\frac{\partial u_i}{\partial X_j}}_{=u_{i,j}} \mathbf{e}_i \otimes \mathbf{e}_j, \quad (4.24)$$

which can be equally applied for the gradient of $\delta \mathbf{u}$ and $\Delta \mathbf{u}$ such that

$$\delta u_{i,j} = \sum_{I=1}^n N_{I,j} \delta I j \quad \text{and} \quad \Delta u_{i,j} = \sum_{I=1}^n N_{I,j} \Delta I j. \quad (4.25)$$

Accordingly, coefficients of the variation $\delta \mathbf{C}$ in the term $\Delta G_{\text{mat}}^{\text{int}}$ of Eq. (4.16) can be reformulated as

$$\frac{1}{2} \delta C_{ij} = \frac{1}{2} [\delta u_{k,i} F_{kj} + F_{ki} \delta u_{k,j}] \approx \sum_{I=1}^n \frac{1}{2} (N_{I,i} F_{kj} + N_{I,j} F_{ki}) \delta d_{Ik}, \quad (4.26)$$

assuming the transformation $\delta \mathbf{C} = (\text{Grad}[\delta \mathbf{u}])^{\text{T}} \mathbf{F} + \mathbf{F}^{\text{T}} \text{Grad}[\delta \mathbf{u}]$ (see Eq. (4.14)). This shows that the virtual nodal displacement δd_{Ik} can be separated from the rest of the term which will be demonstrated subsequently for all terms of the linearization of the weak form.

Application of Voigt Notation To improve notation of symmetric tensors of second and higher order, the Voigt notation is applied here. As a result, a second-order tensor such as the virtual right Cauchy-Green tensor $\delta \mathbf{C}$ or the second Piola-Kirchhoff stress tensor \mathbf{S} can be expressed as

$$\begin{aligned} \underline{\delta \mathbf{C}} &= [\delta C_{11} \quad \delta C_{22} \quad \delta C_{33} \quad 2 \delta C_{12} \quad 2 \delta C_{23} \quad 2 \delta C_{13}]^{\text{T}} \quad \text{and} \\ \underline{\mathbf{S}} &= [S_{11} \quad S_{22} \quad S_{33} \quad S_{12} \quad S_{23} \quad S_{13}]^{\text{T}}, \end{aligned} \quad (4.27)$$

where the factor 2 in the non-diagonal components of $\delta \mathbf{C}$ has to be added in the Voigt notation for the discretization in later steps but not for \mathbf{S} . Applying the new notation, the components of the virtual right Cauchy-Green tensor $\delta \mathbf{C}$ as well as the related

increment $\Delta \underline{\mathbf{C}}$ can be formulated as

$$\frac{1}{2} \delta \underline{\mathbf{C}} = \sum_{I=1}^n \underline{\mathbf{B}}_I \delta \mathbf{d}_I \quad \text{and} \quad \frac{1}{2} \Delta \underline{\mathbf{C}} = \sum_{I=1}^n \underline{\mathbf{B}}_I \Delta \mathbf{d}_I, \quad (4.28)$$

where the B-matrix to the corresponding node I is

$$\underline{\mathbf{B}}_I = \begin{bmatrix} F_{11}N_{I,1} & F_{21}N_{I,1} & F_{31}N_{I,1} \\ F_{12}N_{I,2} & F_{22}N_{I,2} & F_{32}N_{I,2} \\ F_{13}N_{I,3} & F_{23}N_{I,3} & F_{33}N_{I,3} \\ F_{11}N_{I,2} + F_{12}N_{I,1} & F_{21}N_{I,2} + F_{22}N_{I,1} & F_{31}N_{I,2} + F_{32}N_{I,1} \\ F_{12}N_{I,3} + F_{13}N_{I,2} & F_{22}N_{I,3} + F_{23}N_{I,2} & F_{32}N_{I,3} + F_{33}N_{I,2} \\ F_{11}N_{I,3} + F_{13}N_{I,1} & F_{21}N_{I,3} + F_{23}N_{I,1} & F_{31}N_{I,3} + F_{33}N_{I,1} \end{bmatrix}. \quad (4.29)$$

In consideration of one single element, the virtual and incremental right Cauchy-Green tensor can also be expressed as

$$\frac{1}{2} \delta \underline{\mathbf{C}} = \sum_{I=1}^n \underline{\mathbf{B}}_I \delta \mathbf{d}_I = \underline{\mathbf{B}}^e \delta \mathbf{d}^e \quad \text{and} \quad \frac{1}{2} \Delta \underline{\mathbf{C}} = \sum_{I=1}^n \underline{\mathbf{B}}_I \Delta \mathbf{d}_I = \underline{\mathbf{B}}^e \Delta \mathbf{d}^e. \quad (4.30)$$

The corresponding virtual and incremental displacement vectors in Voigt notation $\delta \mathbf{d}^e$ and $\Delta \mathbf{d}^e$ as well as the B-matrix $\underline{\mathbf{B}}^e$ for the element can be noted as

$$\delta \mathbf{d}^e = \begin{bmatrix} \delta \mathbf{d}_1 \\ \delta \mathbf{d}_2 \\ \vdots \\ \delta \mathbf{d}_n \end{bmatrix}, \quad \Delta \mathbf{d}^e = \begin{bmatrix} \Delta \mathbf{d}_1 \\ \Delta \mathbf{d}_2 \\ \vdots \\ \Delta \mathbf{d}_n \end{bmatrix} \quad \text{and} \quad \underline{\mathbf{B}}^e = [\underline{\mathbf{B}}_1 \quad \underline{\mathbf{B}}_2 \quad \dots \quad \underline{\mathbf{B}}_n]. \quad (4.31)$$

This procedure can also be executed for the virtual and incremental displacements such that

$$\delta \mathbf{u} = \sum_{I=1}^n N_I \delta \mathbf{d}_I = \underline{\mathbf{N}}^e \delta \mathbf{d}^e \quad \text{and} \quad \Delta \mathbf{u} = \sum_{I=1}^n N_I \Delta \mathbf{d}_I = \underline{\mathbf{N}}^e \Delta \mathbf{d}^e \quad (4.32)$$

with the elemental matrix notation of $\underline{\mathbf{N}}^e$ and an associated diagonal matrix of the shape function N_I represented as

$$\underline{\mathbf{N}}^e = [\underline{\mathbf{N}}_1 \quad \underline{\mathbf{N}}_2 \quad \dots \quad \underline{\mathbf{N}}_n] \quad \text{and} \quad \underline{\mathbf{N}}_I = \begin{bmatrix} N_I & 0 & 0 \\ 0 & N_I & 0 \\ 0 & 0 & N_I \end{bmatrix}. \quad (4.33)$$

Discretization of Linearization at Element Based on the formulations so far, the internal virtual energy $G^{e,\text{int}}$ of an element e can be expressed in Voigt notation as

$$G^{e,\text{int}} = \int_{\mathcal{B}^e} \underline{\mathbf{S}} : \frac{1}{2} \delta \underline{\mathbf{C}} \, dV \approx \int_{\mathcal{B}^e} \underline{\mathbf{S}} \cdot \underline{\mathbf{B}}^e \delta \mathbf{d}^e \, dV = \delta \mathbf{d}^{e\text{T}} \int_{\mathcal{B}^e} \underline{\mathbf{B}}^{e\text{T}} \underline{\mathbf{S}} \, dV, \quad (4.34)$$

where the virtual displacement vector $\delta \mathbf{d}^e$ can be moved outside the integral as it is not dependent on the position within the element. This can be executed similarly for the external virtual work $G^{e,\text{ext}}$ of an element e with

$$G^{e,\text{ext}} = \int_{\partial B_e^e} \mathbf{T}_{\text{BC}} \cdot \delta \mathbf{u} \, dA \approx \int_{\partial B_e^e} \mathbf{T}_{\text{BC}} \cdot \underline{\mathbf{N}}^e \delta \mathbf{d}^e \, dA = \delta \mathbf{d}^{e\text{T}} \int_{\partial B_e^e} \underline{\mathbf{N}}^{e\text{T}} \mathbf{T}_{\text{BC}} \, dA. \quad (4.35)$$

For the increment of G , also $\Delta \mathbf{d}^e$ has to be considered. Furthermore, the symmetric fourth-order tensor \mathbb{C} has to be brought into Voigt notation which results in a 6×6 matrix. Consequently, the first term of the increment $\Delta G_{\text{mat}}^{e,\text{int}}$ for an element e can be formulated as

$$\begin{aligned} \Delta G_{\text{mat}}^{e,\text{int}} &= \int_{B^e} \frac{1}{2} \delta \mathbf{C} : \mathbb{C} : \frac{1}{2} \Delta \mathbf{C} \, dV \approx \int_{B^e} (\underline{\mathbf{B}}^e \delta \mathbf{d}^e) \cdot (\underline{\mathbb{C}} \underline{\mathbf{B}}^e \Delta \mathbf{d}^e) \, dV \\ &= \delta \mathbf{d}^{e\text{T}} \int_{B^e} \underline{\mathbf{B}}^{e\text{T}} \underline{\mathbb{C}} \underline{\mathbf{B}}^e \, dV \Delta \mathbf{d}^e, \end{aligned} \quad (4.36)$$

where $\Delta \mathbf{d}^e$ is moved outside the integral. To apply the discretization of the last term of the linearization $\text{Lin } G$ which is termed as $\Delta G_{\text{geo}}^{\text{int}}$ in Eq. (4.16), the expression $\delta \mathbf{F} = \text{Grad}[\delta \mathbf{u}]$ from Eq. (4.6) is applied which can be also used to build $\Delta \mathbf{F} = \text{Grad}[\Delta \mathbf{u}]$. In consequence, the index notation of the coefficients of the term

$$\frac{1}{2} \Delta \delta C_{ij} = \frac{1}{2} (\delta u_{k,i} \Delta u_{k,j} + \Delta u_{k,i} \delta u_{k,j}) = \sum_{I=1}^n \sum_{J=1}^n \delta d_{Ik} N_{I,i} N_{J,j} \Delta d_{Jk} \quad (4.37)$$

can be applied to express $\Delta G_{\text{geo}}^{e,\text{int}}$ for an element e of the body as

$$\begin{aligned} \Delta G_{\text{geo}}^{e,\text{int}} &= \int_{B^e} \mathbf{S} : \frac{1}{2} \Delta \delta \mathbf{C} \, dV \approx \sum_{I=1}^n \sum_{J=1}^n \delta d_{Ik} \int_{B^e} S_{ij} N_{I,i} N_{J,j} \, dV \Delta d_{Jk} \\ &= \delta \mathbf{d}^{e\text{T}} \int_{B^e} \underline{\mathbf{G}}^e \, dV \Delta \mathbf{d}^e. \end{aligned} \quad (4.38)$$

Here, the matrix $\underline{\mathbf{G}}^e$ summarizes the derivatives of the shape functions and the coefficients of the second Piola-Kirchhoff stress tensor \mathbf{S} in the following manner

$$\underline{\mathbf{G}}^e = \begin{bmatrix} \underline{\mathbf{G}}_{11} & \underline{\mathbf{G}}_{12} & \cdots & \underline{\mathbf{G}}_{1n} \\ \underline{\mathbf{G}}_{21} & \underline{\mathbf{G}}_{22} & \cdots & \underline{\mathbf{G}}_{2n} \\ \vdots & \vdots & \ddots & \vdots \\ \underline{\mathbf{G}}_{n1} & \underline{\mathbf{G}}_{n2} & \cdots & \underline{\mathbf{G}}_{nn} \end{bmatrix} \quad \text{with} \quad \underline{\mathbf{G}}_{IJ} = \begin{bmatrix} G_{IJ} & 0 & 0 \\ 0 & G_{IJ} & 0 \\ 0 & 0 & G_{IJ} \end{bmatrix} \quad \text{and} \quad G_{IJ} = S_{ij} N_{I,i} N_{J,j}. \quad (4.39)$$

Elemental Stiffness Matrix and Residuum Based on the separation of the virtual and incremental nodal displacements $\delta \mathbf{d}^e$ and $\Delta \mathbf{d}^e$ at the element e from the rest of the terms, the linearization of the weak form of the balance of linear momentum can also be written in the discretized form as

$$\text{Lin } G^e = \delta \mathbf{d}^{e\text{T}} \mathbf{r}^e + \delta \mathbf{d}^{e\text{T}} \mathbf{K}^e \Delta \mathbf{d}^e \quad (4.40)$$

with the element residual vector

$$\mathbf{r}^e = \int_{\mathcal{B}^e} \underline{\mathbf{B}}^e{}^T \underline{\mathbf{S}} dV - \int_{\partial\mathcal{B}_g^e} \underline{\mathbf{N}}^e{}^T \mathbf{T}_{\text{BC}} dA \quad (4.41)$$

and the element stiffness matrix \mathbf{K}^e as combination of the material and geometric part

$$\mathbf{K}^e = \mathbf{K}^{e,\text{mat}} + \mathbf{K}^{e,\text{geo}} = \int_{\mathcal{B}^e} \underline{\mathbf{B}}^e{}^T \underline{\mathbf{C}} \underline{\mathbf{B}}^e dV + \int_{\mathcal{B}^e} \underline{\mathbf{G}}^e dV. \quad (4.42)$$

Global Expression To express the set of equations for the entire mechanical problem, the virtual and incremental nodal displacements are gathered in global vectors as

$$\delta \mathbf{d} = [\delta \mathbf{d}^1 \quad \delta \mathbf{d}^2 \quad \dots \quad \delta \mathbf{d}^{n_{\text{ele}}}]^T \quad \text{and} \quad \Delta \mathbf{d} = [\Delta \mathbf{d}^1 \quad \Delta \mathbf{d}^2 \quad \dots \quad \Delta \mathbf{d}^{n_{\text{ele}}}]^T. \quad (4.43)$$

According to these global vectors, the residual vectors of the elements as well as the element stiffness matrices are assembled to the global versions \mathbf{r} and \mathbf{K} with

$$\mathbf{r} = \mathbf{A} \mathbf{r}^e \quad \text{and} \quad \mathbf{K} = \mathbf{A} \mathbf{K}^e. \quad (4.44)$$

Consequently, the final version of the discretized weak form can be expressed as

$$\text{Lin } G = \delta \mathbf{d}^T (\mathbf{r} + \mathbf{K} \Delta \mathbf{d}) = 0. \quad (4.45)$$

This equation holds as long as the term in the bracket equals zero and, hence, when the equation

$$\mathbf{K} \Delta \mathbf{d} = -\mathbf{r} \quad (4.46)$$

is satisfied. Since the Newton–Raphson method is performed, the resulting increment $\Delta \mathbf{d}$ is used to update the nodal displacements of the iterative step $n+1$ to $\mathbf{d}_{n+1} = \mathbf{d}_n + \Delta \mathbf{d}_{n+1}$. As described in the beginning of this chapter, the final solution of the mechanical problem is found when the virtual work G equals zero. From a computational point of view, this occurs as soon as the global residual vector \mathbf{r} is lower than a predefined tolerance value in an iterative step.

Gauss Point Integration The calculation of residual vectors and stiffness matrices includes integrals over the volume which can usually not be computed analytically. Therefore, the Gauss point integration is applied which substitutes the actual integral with a sum over a finite number of integration points. These integration points, also known as Gauss points, can be determined for the isoparametric elements. To deliver high accuracy, weighting factors corresponding to every Gauss point are crucial in this approach. Accordingly, the integral of a function $g(\mathbf{X})$ over a brick element e can be

approximated by

$$\begin{aligned} \int_{\mathcal{B}^e} g(\mathbf{X}) dV &= \int_{\mathcal{B}^{\mathbb{B}}} g(\boldsymbol{\xi}) \det[\mathbf{J}(\boldsymbol{\xi})] d\mathbb{B} = \int_{-1}^{+1} \int_{-1}^{+1} \int_{-1}^{+1} g(\boldsymbol{\xi}) \det[\mathbf{J}(\boldsymbol{\xi})] d\boldsymbol{\xi} \\ &\approx \sum_{p=1}^{n_p} g(\boldsymbol{\xi}_p) \det[\mathbf{J}(\boldsymbol{\xi}_p)] w_p, \end{aligned} \quad (4.47)$$

where n_p is the total number of Gauss points and w_p represents the weight factors at the corresponding integration point p . The Jacobi matrix $\mathbf{J}(\boldsymbol{\xi})$ is included for the transition between the referential state of the element and the isoparametric element with parameter space $\mathcal{B}^{\mathbb{B}}$. Values of the function $g(\boldsymbol{\xi}_p)$ and $\mathbf{J}(\boldsymbol{\xi}_p)$ are evaluated at each Gauss point p . In the following chapters, three-dimensional hollow cylinders, which are rotationally symmetric, are used to illustrate the functionality of the proposed material models for muscular arteries. These hollow cylinders are approximated with meshes of quadratic, 20-node brick elements. In consequence, the rotational symmetry of the geometry is maintained by the defined mesh. According shape functions and positions of Gauss points with corresponding weight factors can be found in LAPIDUS AND PINDER [107] (pp. 142-144). In Chapter 10, a more realistic geometry of an artery is investigated. This geometry qualifies by using tetrahedral elements such that quadratic, 10-node tetrahedrons build the corresponding mesh. Information on the corresponding shape functions and Gauss points can be found in WRIGGERS [191] (pp. 120-122).

5 Numerical Modeling of the Contraction of Vascular SMCs

In this chapter, a mechanical model for the contraction of vascular SMCs in combination with the hyperelastic, passive material response is proposed. The formulation of active material model was already published in UHLMANN AND BALZANI [177] and is described in more detail here. To define the active modeling, biochemical reactions in SMCs and their stretch-dependent stimulation are taken into account which were described in Section 2.2. While many intermediate steps of the intracellular reaction chains are known based on numerous experiments, quantification of reactants and products in such intermediate steps along the entire reaction chain is difficult to achieve. That is why obtainable data for the chemomechanical process has to be considered in advance of the definition of the mechanical model. As shown in Section 2.2.4, *in vitro* mechanical experiments for middle cerebral arteries of rats were able to identify the stretch-dependent contraction of SMCs based on measurements of the time-dependent change of the diameter of the arterial wall after an increase of the intravascular pressure [94]. Furthermore, arteries were investigated with the same experimental load protocol, but adjusted chemical environment, in two additional scenarios. In the first scenario, ROCK and PKC inhibitors were added into the surrounding solution of the artery and the following decrease of the arterial contraction evaluated. In the second scenario, the passive material response was investigated by excluding the access of SMCs from Ca^{2+} . While data for the intermediate reactions is not collected, it is possible to identify the major components of the reaction chain: a stretch of GPCRs and mechanosensitive calcium channels of the cell membrane and the resulting contraction of the SMCs based on increased activity of the enzyme MLCK as well as suppressed activity of the enzyme MLCP. Consequently, the proposed mechanical model includes the stretch-dependency of the contraction mechanism. This will be achieved by formulating evolution equations for the activity of MLCK and MLCP which contain the stretch λ of SMCs as a variable. For MLCK in particular, the evolution equation is expressed for rapid change of cytosolic Ca^{2+} after a stretch of the cell. However, this mechanism is modeled in direct connection to the cell stretch and does not include modeling the membrane potential which would require the consideration of other cytosol ions such as potassium and sodium. Since the suppression of the activity of MLCP and the subsequent reactivation are significantly slower than for MLCK, a more complex system of equations is required to capture the time-dependent regulation sufficiently. In consequence, two coupled evolution equations influencing each other are defined.

The first part of this chapter gives a state-of-the-art overview of mechanical modeling of vascular SMCs. This includes chemical as well as the mechanical aspects of modeling. Subsequently, the proposed model is presented. For the active material part, a model of cross-bridge phosphorylation by HAI AND MURPHY [69] is applied as foundation for the chemical description of contractile units. The inclusion of the aforementioned stretch-dependent evolution equations enables the modification of the chemical model as mechanosensitive. Furthermore, a phenomenological approach by MURTADA ET AL. [122] is adjusted for the mechanical description of contractile units. For the passive, hyperelastic material behavior of the arterial wall, a polyconvex model by BALZANI

ET AL. [8] is adopted. In the last part of this chapter, the numerical implementation is presented in detail which includes solutions for the evolution equations as well as the equations for the computation of the second Piola-Kirchhoff stresses and the numerical approximation of the tangent modulus.

5.1 State of the Art: Vascular SMCs

One of the first well-known models for muscle shortening was published by HILL [74]. In this approach, the mechanical behavior and heat production during the shortening of muscles is described as a system of two components which includes a visco-elastic element and a contractile element arranged in series. Accordingly, the mechanical behavior of the elastic part of the material is considered by the visco-elastic element and the contractile part describes the muscle contraction. An extension of this model was described in FUNG [57] which is also known as the three-element Hill muscle model. In addition to the series of the visco-elastic and contractile part of the model, a third component is added parallelly to the series representing the elasticity of the muscle tissue while no muscle contraction occurs. Hill's and Fung's approaches constitute one-dimensional characterizations of the mechanical behavior of the muscle tissue. The foundation for the chemical part of most mechanical smooth muscle model was formulated by HAI AND MURPHY [69]. As presented in Section 2.2, the contraction of SMCs is controlled by contractile units in the cell consisting of actin and myosin filaments (thin and thick filaments). The intensity of the contraction of the contractile units depends on the proportion of myosin heads which are able to perform power strokes. For this purpose, the myosin heads have to be phosphorylated and build so-called cross-bridges to the thin filaments. The model of HAI AND MURPHY [69] describes the transformation of myosin heads by a system of evolution equations making the calculation of the fraction of active myosin heads possible. This kinetic model for cross-bridge phosphorylation is well-accepted and has been applied as chemical component in various chemomechanical models for smooth muscle contraction over the last two decades (see [122], [123], [193], [23], [167]).

In MURTADA ET AL. [122], a phenomenological approach is used to develop a new material model for the contraction of vascular SMCs. For this purpose, the three-element Hill muscle model was applied and combined with the chemical model of HAI AND MURPHY [69]. Furthermore, the model for cross-bridge phosphorylation is defined as dependent on the cytosolic Ca^{2+} concentration. The Ca^{2+} concentration is not formulated as adaptable quantity, but set as input parameter to the model. Correspondingly, the model by MURTADA ET AL. [122] captures the influence of the chemical model on the mechanical behavior of the SMCs reliably (which is considered as the chemical-mechanical coupling here) and is, therefore, adopted for the mechanical description of smooth muscle contraction in this thesis. However, the influence of mechanical quantities on the chemistry (mechanical-chemical coupling), such as the increased inflow of Ca^{2+} from sarcoplasmic reticulum and through the cell membrane when the SMC is stretched, is not included. An extension is required to capture the contractile behavior of muscular arteries sufficiently which will be presented in the following sections of this chapter. In addition, several adjustments for the model of MURTADA ET AL. [122] were published which aimed for an improved mechanical description of the contraction

mechanism. In MURTADA ET AL. [123], the model was extended by the definition of an overlap between myosin and actin filaments. This filament overlap was defined as a function of the cell stretch which influences the degree of active contraction. This approach fits well when skeletal muscles are considered where the overlap of the thin and thick filaments increases directly with the level of muscle shortening based on the structure of their sarcomeres [186] in which long protein filaments of actin and myosin are parallelly arranged. However, this feature is missing in contractile units of SMCs. In a study by LIU ET AL. [113], the length of myosin filaments of SMCs is reported as widely varying and relatively short. Nonetheless, a certain increase of the overlap between myosin and actin can be expected also in SMCs. As described in Section 2.2, in the study by CHITANO ET AL. [32], the concentration of monomeric free myosin in the cytosol of the SMC was measured for different states of muscle stretch. It was found that the concentration of monomeric free myosin decreases in stretched SMCs. While monomeric free myosin has no direct influence on the mechanical behavior of the cell, it is likely that the monomeric myosin is consumed for polymerization which extends the myosin filaments. In consequence, an elongation of the myosin filaments leads to an increase of the overlap between thin and thick filaments. However, the influence of this mechanism on the contraction of SMCs is rarely considered in biology papers which investigate the corresponding intracellular reaction-chains. The consideration of the stretch-dependency of GPCRs is noticeably more dominant. Nonetheless, the model extension, which includes the filament overlap into the mechanical model part, leads to a match between results of numerical simulation and experimental data. In this regard, the definition of the filament overlap is a sufficient extension to include the stretch-dependency of SMCs to fit the observed experiments. Further publications, which take this approach for the modeling of smooth muscle contraction into account, are [72], [124], and [166].

Since it is well-accepted for decades that the cytosolic Ca^{2+} concentration plays an important role during SMCs contraction, numerous publications included this cellular mechanism in their modeling approaches. An early cell model from 2003 is described in YANG ET AL. [193], where an electrochemical model is included which combines a Hodgkin-Huxley-type membrane model [77] with models of the fluid compartment. This model describes a detailed approach to include the inflow and release of Ca^{2+} into the cell, however it requires a detailed amount of experimental data for a reliable fit of the model parameters. An extension of the model for the entire vessel can be found in YANG ET AL. [194]. In BÖL ET AL. [23], a time-dependent calcium function was formulated to investigate the impact of the change of the cytosolic Ca^{2+} on the contraction of the cell. Based on this straightforward approach, numerical simulations included calcium waves without a direct definition of the mechanical-chemical coupling. Another promising approach for the description of the smooth muscle contraction can be found in STÅLHAND ET AL. [167]. Based on a modification of the model for cross-bridge phosphorylation from HAI AND MURPHY [69], the influence of the mechanics on the chemical state of contractile units was taken into account. In particular, this modification included a stretch-dependent formulation of the reaction rates which describe the velocity of the transformation of myosin heads into different chemical states resulting in an enhanced contraction for stretched SMCs. However, the formulations for the reaction rates enabled their values to become negative which is non-physiological. In addition to models for vascular SMCs, the publications by SHAR-

IFIMAJD ET AL. [160] and SEYDEWITZ ET AL. [159] describe the contraction of SMCs in uterus and urinary bladder. These models include the membrane potential for the influx of Ca^{2+} through voltage-gated L-type calcium channels. While this approach coincides with the biological state of the art for the dominant mechanism of Ca^{2+} influx into the SMC, the inhibition of MLCP based on stimulated GPCRs is not included.

An additional model, which is described in YOSIBASH AND PRIEL [196], included the impact of vasoconstrictors onto the contraction of SMCs. The model is based on experimental data from WAGNER AND HUMPHREY [182], who investigated the influence of different concentrations of ET-1 on the contraction. In consequence, the strain-energy density function of the model was defined as dependent on the concentration of ET-1 and the stretch of the SMC. The considered experimental data were matched by results of numerical experiments. A further extension of this model was studied in GILBERT ET AL. [63] which took into account the diffusion of the vasoconstrictor through the tissue. While this modeling approach is promising looking at the inclusion of the impact of vasoconstrictors and vasodilators into the mechanical model, chemical mechanisms which comprise mechanosensitivity are not considered.

For a promising representation of the bio-chemo-mechanical aspect on the cell level, a very recent publication has to be mentioned. In FLANARY AND BAROCAS [55], a detailed connection between extracellular activators and intracellular reaction chains is considered. This includes the production of nitric oxide and ET-1 from the endothelial, stress and agonist activation of angiotensin II receptors of the SMC membrane, stress-activated integrins as well as stretch-sensitive membrane channels. The even more complex signaling network of IRONS AND HUMPHREY [89] was adapted as foundation for this modeling approach. In the subsequent publication of FLANARY ET AL. [56], simulations for three-dimensional geometries were implemented. In the first step, experimental data from WIN ET AL. [187] were obtained to validate the model parameters on the cell-scale. These experiments used traction force microscopy with biaxial load scenarios to investigate the mechanical behavior of single SMCs. In the second step, simulations with entire arterial rings were investigated. To acquire data for comparison, mechanical experiments for the contraction of rings of murine thoracic aortas were performed. In these experiments, two pins were located inside the lumen of the arterial ring which were used to stretch the tissue by increasing the distance between the pins. The resulting contraction force of the arterial ring on the pins was measured and applied to compute the traction stress inside of the tissue. The mechanical data from simulations were comparable to experimental measurements. Consequently, the proposed model is promising for the inclusion of the biochemical reactions towards changes of mechanical quantities into the description of the mechanical behavior of SMCs in the arterial wall. Nonetheless, the contractile behavior of the aorta is significantly less intense than the contraction of muscular arteries with higher proportion of SMCs in the tissue in which the diameter can even decrease as a reaction to an increase of the intravascular pressure during higher body activity. The replication of this mechanical behavior of muscular arteries has not been presented yet.

In summary, the majority of publications merely consider the calcium-dependent part of the intracellular mechanism for the modeling of the contraction of vascular SMCs. The mechanical-chemical coupling of the contraction mechanism, which is well-accepted

in biological publications, is only included in a minority of mechanical models. Furthermore, simulation results, which correspond to the contractile behavior of small or medium-sized muscular arteries, are not represented in any known publication of other research groups. Therefore the following sections describe the proposed model for the contraction of vascular SMCs of this thesis and demonstrate corresponding simulation results for the replication of the contraction of muscular arteries.

5.2 Mechanical Model of the Arterial Wall

For the description of the mechanical behavior of the arterial wall, three components are considered in the model. Next to the active contraction of SMCs, elastin and collagen fibers are included for the passive, hyperelastic material response of the arterial tissue. The active material model is presented in two steps which capture the mechanical-chemical coupling and, subsequently, the chemical-mechanical coupling. Here, the mechanical-chemical coupling is used as a term to describe the dependency of variables of the chemical model on changes of mechanical quantities. Furthermore, the chemical-mechanical coupling corresponds to the impact of the chemical variables on the mechanical response of the SMCs. In consequence, the connection between chemistry and mechanics in the model allows the description of self-regulation of the mechanical response of vascular SMCs in arteries. In the end of this section, the active material model is combined with the passive model part in a strain-energy density function Ψ .

5.2.1 Mechanical-Chemical Coupling

The model by HAI AND MURPHY [69] describes the phosphorylation and regulation of the latch state of myosin heads in contractile units of SMCs and is therefore adopted for the chemical part of the proposed material model. In particular, HAI AND MURPHY [69] classify four functional states for myosin heads: (A) detached and dephosphorylated, (B) detached and phosphorylated, (C) attached and phosphorylated, and (D) attached and dephosphorylated. Myosin heads in state C are able to perform power strokes which lead to a contraction of the cell. Furthermore, reaction rates are defined to describe the transformation of myosin heads from one state into another which includes the phosphorylation of myosin heads (k_1 and k_6), the dephosphorylation of myosin heads (k_2 and k_5), the attachment of myosin heads to an actin filament (k_3), and the detachment of myosin heads from an actin filament (k_4 and k_7). Since only phosphorylated myosin heads can attach to actin filaments, the transformation of myosin heads from state A to state D does not exist. A schematic illustration of the model is shown in Fig. 5.1. The corresponding kinetic model of the four myosin states is described by four ordinary differential equations as the following

$$\begin{bmatrix} \dot{n}_A \\ \dot{n}_B \\ \dot{n}_C \\ \dot{n}_D \end{bmatrix} = \begin{bmatrix} -k_1 & k_2 & 0 & k_7 \\ k_1 & -k_2 - k_3 & k_4 & 0 \\ 0 & k_3 & -k_4 - k_5 & k_6 \\ 0 & 0 & k_5 & -k_6 - k_7 \end{bmatrix} \begin{bmatrix} n_A \\ n_B \\ n_C \\ n_D \end{bmatrix}, \quad (5.1)$$

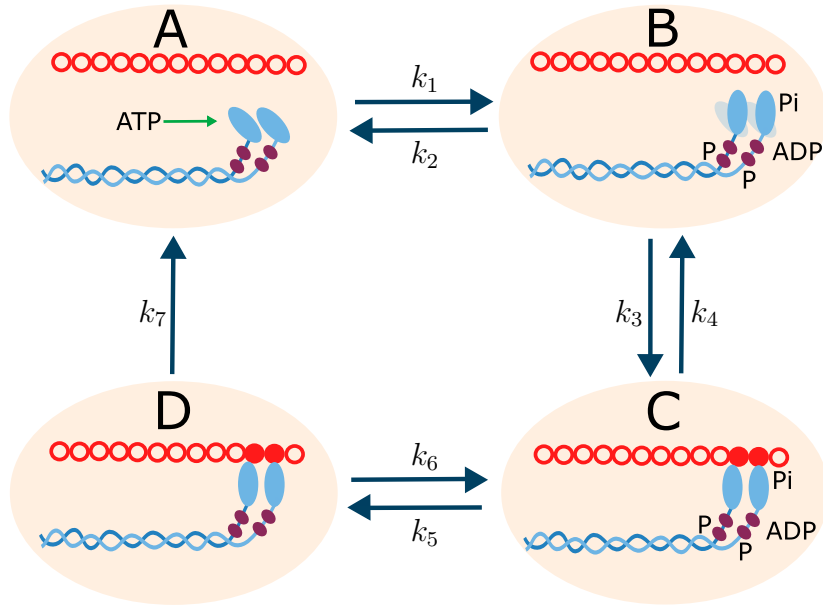


Figure 5.1: Schematic illustration of the model by HAI AND MURPHY [69]. Four function states are defined for myosin heads in SMCs: **A** detached and dephosphorylated, **B** detached and phosphorylated, **C** attached to actin and phosphorylated, and **D** attached to actin and dephosphorylated. Myosin heads can transform from one state to another which is described by the reaction rates k_1 to k_7 .

where the proportions of myosin heads in the respective state are expressed by n_A , n_B , n_C and n_D . As natural constraints for proportions, the following equations have to be satisfied at all times

$$n_A + n_B + n_C + n_D = 1, \quad \text{with } n_A, n_B, n_C, n_D \in [0; 1]. \quad (5.2)$$

Based on the advantageous formulation of the linear system of ordinary differential equations in Eq. (5.1), the constraints are fulfilled at all times as long as the reaction rates are values between 0 and 1. The dependency of the chemical system on the mechanical state of SMCs is applied by the definition of equations for the reaction rates k_1 and k_6 as well as k_2 and k_5 . This does not include the attachment and detachment of myosin heads to/from actin filaments which is considered a steady process. Consequently, the reaction rates k_3 , k_4 and k_7 are constant input parameters for the chemical model.

Based on biological knowledge described in Section 2.2, the contraction of SMCs can be manipulated when the cell membrane is stretched. This stretch λ leads to a stimulation of GPCRs and an additional opening of stretch-sensitive ion channels. In this regard, two different subclasses of GPCRs have to be considered which contain G_q or $G_{12/13}$ proteins at the intracellular side of the membrane receptor. A stimulation of GPCRs with G_q proteins leads primarily to a rapid but brief increase of the cytosolic Ca^{2+} concentration. Based on the interaction of Ca^{2+} with CaM, the activity of the enzyme MLCK increases with the Ca^{2+} inflow from ECM and the sarcoplasmic reticulum which leads to an increase of the phosphorylation of myosin heads. In addition, the stimulation of receptors with $G_{12/13}$ proteins inhibits the enzyme MLCP mainly caused by an increased activity of ROCK. This results in a decreased long-lasting dephosphory-

lation of myosin heads predominant for the additional contraction of SMCs at high body activity. In consequence, the reaction rates for phosphorylation (k_1 and k_6) and dephosphorylation (k_2 and k_5) have to be defined depending on the stretch λ of SMCs. Since SMCs are long in shape and contractile units are oriented in this direction of the cell, λ is considered the stretch in longitudinal direction of the cells. With regard to the following sections, the correct notation of λ would be $\lambda^{(f)}$ to define the stretch in the direction (f). However, since only one single fiber direction is considered in the following equations, the index (f) is skipped to avoid overcomplicating the notation.

Phosphorylation For the phosphorylation of myosin heads, the reaction rates k_1 and k_6 are not directly defined as functions of λ , but include the cytosolic Ca^{2+} concentration. Based on a suggestion in BLUMENTHAL AND STULL [21], k_1 and k_6 are defined as

$$k_{1/6} = \eta \frac{[Ca^{2+}]^2}{[Ca^{2+}]^2 + (Ca_{50})^2}, \quad (5.3)$$

where $[Ca^{2+}]$ constitutes the intracellular Ca^{2+} concentration, Ca_{50} is the half-activation constant and η is a parameter which defines the highest achievable rate for the phosphorylation k_1 and k_6 . As described in Section 2.2.2, the inflow and release of Ca^{2+} is regulated by a complex system of channels in the cell membrane and the sarcoplasmic reticulum which can be activated by stretch, but more importantly, by a change of the membrane potential. To capture all components of the system, an electro-chemical model such as an extended version of the Hodgkin-Huxley-type membrane model [77] is necessary which also involves the ions of potassium, sodium, and chloride. For an adequate description, the necessary system of evolution equations requires a dependency on the membrane stretch of the cell and the activity levels of DAG and PKC as well as a modeling of the concentration of IP_3 . While a reduced version of such a model might be sufficient to include the adjustment of the Ca^{2+} concentration in SMCs, the general mechanism might be already captured by a time-dependent formulation for the Ca^{2+} concentration dependent on the cell stretch λ . Accordingly, the equation for the Ca^{2+} concentration is defined as

$$[Ca^{2+}](\lambda) = \gamma_1 \langle \lambda - \bar{\lambda}_c \rangle^2, \quad (5.4)$$

where γ_1 is a material parameter, the stretch of the SMC in longitudinal direction can be calculated by $\lambda = (I_4^{(f)})^{1/2}$, and the Macaulay brackets are defined as $\langle \bullet \rangle = \frac{1}{2} (\bullet + |\bullet|)$. Note that the fourth invariant $I_4^{(f)}$ is based on the deformation in fiber direction $\mathbf{a}^{(f)}$ as described in Eq. (3.15). Based on the definition in Eq. (5.4), the rapid increase of cytosolic Ca^{2+} concentration is described as instantaneous process when the SMC is stretched. This can be considered sufficient for numerical simulations, since the time frame for the increase of $[Ca^{2+}]$ is under 100 ms. For the considerably slower release of Ca^{2+} , a virtual stretch variable $\bar{\lambda}_c$ is introduced which is changing over time. In this regard, it is assumed that the Ca^{2+} concentration inside the cell will balance at a certain stretch of the SMC to a constant value after enough time. Reaching this constant value of $[Ca^{2+}]$ can be considered the homeostatic state of Ca^{2+} concentration and, therefore, is the target value for $[Ca^{2+}]$. This target value $[Ca^{2+}]_{\text{tar}}(\lambda)$ is defined

as dependent on λ by

$$[Ca^{2+}]_{\text{tar}}(\lambda) = \gamma_3 \frac{\lambda^2}{\lambda^2 + (\lambda_{50,c})^2}, \quad (5.5)$$

where γ_3 is a material parameter and $\lambda_{50,c}$ constitutes the half-activation stretch. The difference between the current Ca^{2+} concentration and the target value can be expressed as $\Delta[Ca^{2+}] = [Ca^{2+}]_{\text{tar}} - [Ca^{2+}]$. As long as the current calcium concentration is not equal to the target value, the virtual stretch variable $\bar{\lambda}_c$ is adjusted in the model. For this purpose, an evolution equation for the time-dependent change of $\bar{\lambda}_c$ is formulated as four-parameter sigmoid function by

$$\dot{\bar{\lambda}}_c(\Delta[Ca^{2+}]) = \dot{\bar{\lambda}}_{c,\min} + \frac{\dot{\bar{\lambda}}_{c,\max} - \dot{\bar{\lambda}}_{c,\min}}{1 + e^{\gamma_2(\Delta[Ca^{2+}] - \tau_c)}}, \quad (5.6)$$

where $\dot{\bar{\lambda}}_{c,\min}$ and $\dot{\bar{\lambda}}_{c,\max}$ constitute the change rate of $\bar{\lambda}_c$ at $\Delta[Ca^{2+}] = -\infty$ and $\Delta[Ca^{2+}] = \infty$, respectively, and γ_2 is a material parameter. The behavior for parameter changes of γ_2 or $\dot{\bar{\lambda}}_{c,\min}$ and $\dot{\bar{\lambda}}_{c,\max}$ is illustrated in Fig. 5.2. Furthermore, the parameter τ_c is set as

$$\tau_c = \ln \left(\frac{\dot{\bar{\lambda}}_{c,\min} - \dot{\bar{\lambda}}_{c,\max}}{\dot{\bar{\lambda}}_{c,\min}} - 1 \right) (-\gamma_2)^{-1}, \quad (5.7)$$

as a consequence of which the change of $\bar{\lambda}_c$ equals zero as long as $\Delta[Ca^{2+}] = 0$. Based on the described set of equations, the activity of MLCK is included in the model by

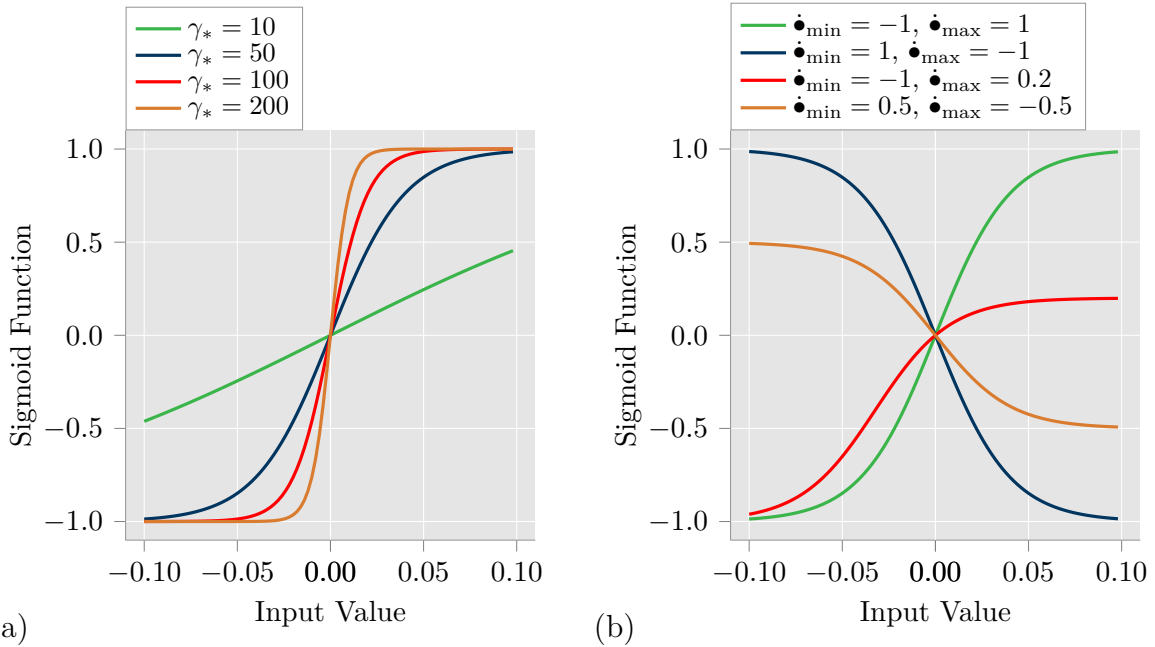


Figure 5.2: Illustration of different sigmoid functions. (a) Impact of changes of the parameter γ_* on sigmoid functions where the function value at $-\infty$ is set to $\dot{\bullet}_{\min} = -1$ and the function value at $+\infty$ to $\dot{\bullet}_{\max} = 1$; * corresponds to the indices 2, 4 and 6, see Eqs. (5.6), (5.8), (5.11). (b) Impact on sigmoid functions $\dot{\bullet}_{\min}$ and $\dot{\bullet}_{\max}$ are changed where $\dot{\bullet}_{\min}$ and $\dot{\bullet}_{\max}$ constitute the change rate of \bullet when the input value is $-\infty$ and $+\infty$, respectively; input value corresponds to $\Delta[Ca^{2+}]$, $\Delta\bar{\lambda}_p$ and $\Delta k_{2/5}$, see Eqs. (5.6), (5.8), (5.11).

a dependency on the cytosolic Ca^{2+} concentration which is stretch-dependent. This mechanism is considered the initial contraction mechanism which protects the tissue of the arterial wall from overstretching.

Dephosphorylation For the description of the change of dephosphorylation, a similar approach is applied. The intracellular reaction chain, which leads from a stimulated GPCR with $\text{G}_{12/13}$ protein to the increased activity of ROCK and phosphorylation of CPI-17 to a decreased activity of the enzyme MLCP, is reduced to a system of equations which formulates a coupling of the stretch of the SMC to a time-dependent change of the dephosphorylation of myosin heads. However, it is more crucial to capture the time-dependency of this process in the model than of the process of phosphorylation. The decrease of dephosphorylation is considerably slower after a stretch of the SMC already. The subsequent recovery process to reach the homeostatic value for the dephosphorylation is even more delayed. In consequence, the time-dependent change of the dephosphorylation is directly defined by an evolution equation as dependent on the longitudinal cell stretch λ . This includes the introduction of a virtual stretch variable $\bar{\lambda}_p$ with difference $\Delta\bar{\lambda}_p = \lambda - \bar{\lambda}_p$ to the current stretch λ . The corresponding evolution equation is described by the four-parameter sigmoid function (see Fig. 5.2) as

$$\dot{k}_{2/5}(\Delta\bar{\lambda}_p, k_{2/5}) = \dot{k}_{2/5, \min} (1 - e^{-\zeta_1 k_{2/5}}) + \frac{\dot{k}_{2/5, \max} - \dot{k}_{2/5, \min}}{1 + e^{\gamma_4(\Delta\bar{\lambda}_p - \tau_p)}}, \quad (5.8)$$

in which the change rate of $k_{2/5}$ at $\Delta\bar{\lambda}_p = -\infty$ and $\Delta\bar{\lambda}_p = +\infty$ is defined by $\dot{k}_{2/5, \min}$ and $\dot{k}_{2/5, \max}$, respectively, and γ_4 is a material parameter. Since the dephosphorylation of myosin heads inside of the SMC cannot be negative, the constraint $e^{-\zeta_1 k_{2/5}}$ with the penalty parameter ζ_1 is included in the evolution equation which ensures that $k_{2/5}$ is always larger than zero. Furthermore, the change of the dephosphorylation is assumed to be zero when $\Delta\bar{\lambda}_p = 0$. For this purpose, the parameter is set to be

$$\tau_p = \ln \left(\frac{\dot{k}_{2/5, \min} - \dot{k}_{2/5, \max}}{\dot{k}_{2/5, \min}} - 1 \right) (-\gamma_4)^{-1}, \quad (5.9)$$

which can be obtained by rearrangement of the condition $\dot{k}_{2/5}(\Delta\bar{\lambda}_p = 0) = 0$. Assuming that the rate of dephosphorylation $k_{2/5}$ reaches a constant value after enough time at a certain stretch of the SMC, the target value $k_{2/5, \text{tar}}$ is introduced as

$$k_{2/5, \text{tar}} = \gamma_6 \left(1 - \frac{\lambda}{\lambda_{50, p} + \lambda} \right), \quad (5.10)$$

with the half-activation stretch $\lambda_{50, p}$ and the material parameter γ_6 . A rapid stretch of the SMC leads to a decrease of $k_{2/5}$ with smaller value than the target value $k_{2/5, \text{tar}}$ at the current stretch λ . For the adjustment of $k_{2/5}$ to the target value $k_{2/5, \text{tar}}$, the virtual stretch variable $\bar{\lambda}_p$ is also defined as evolution equation dependent on the difference between current value of $k_{2/5}$ and the target value $k_{2/5, \text{tar}}$ by $\Delta k_{2/5} = k_{2/5, \text{tar}} - k_{2/5}$. Using the formulation of the four-parameter sigmoid function (see Fig. 5.2), the corre-

sponding evolution equation is expressed as

$$\dot{\bar{\lambda}}_p(\Delta k_{2/5}, \Delta \bar{\lambda}_p) = \dot{\bar{\lambda}}_{p, \min} + \frac{\dot{\bar{\lambda}}_{p, \max} - \dot{\bar{\lambda}}_{p, \min}}{1 + e^{\gamma_5(\Delta k_{2/5} - \tau_k)}} - \dot{\bar{\lambda}}_{p, \max} e^{-\zeta_2(\Delta \bar{\lambda}_p - \Delta \bar{\lambda}_{p, \min})}, \quad (5.11)$$

where $\dot{\bar{\lambda}}_{p, \min}$ and $\dot{\bar{\lambda}}_{p, \max}$ constitute the change rate of $\bar{\lambda}_p$ at $\Delta k_{2/5} = -\infty$ and $\Delta k_{2/5} = \infty$, respectively, and γ_5 is a material parameter. Since the condition $\dot{\bar{\lambda}}_p(\Delta k_{2/5} = 0) = 0$ has to be satisfied, a reformulation of the Eq. (5.11) leads to the following expression for the parameter τ_k such that

$$\tau_k = \ln \left(\frac{\dot{\bar{\lambda}}_{p, \min} - \dot{\bar{\lambda}}_{p, \max}}{\dot{\bar{\lambda}}_{p, \min}} - 1 \right) (-\gamma_5)^{-1}. \quad (5.12)$$

An additional point is addressed in Eq. (5.11) by the last term. The decrease of the dephosphorylation of myosin heads after a stretch of the SMC is long-lasting and recovers very slowly. To include this into the model, the constraint term $\dot{\bar{\lambda}}_{p, \max} e^{-\zeta_2(\Delta \bar{\lambda}_p - \Delta \bar{\lambda}_{p, \min})}$ with the penalty parameter ζ_2 ensures that the difference between the the cell stretch λ and the virtual stretch value $\bar{\lambda}_p$ cannot be larger than the value $\Delta \bar{\lambda}_{p, \min}$. In consequence, the increase of the reaction rates $k_{2/5}$ is notably inhibited in the corresponding evolution equation $\dot{k}_{2/5}(\Delta \bar{\lambda}_p, k_{2/5})$. It has to be noted that this process cannot be validated in the mechanical model since experimental data for the relaxation process of the arterial wall is not available. The corresponding parameter $\Delta \bar{\lambda}_{p, \min}$ is manually adjusted. However, the system of equations enables a sufficient description of the time-dependent change of the dephosphorylation of myosin heads after a stretch of SMCs and a corresponding contraction of the artery which will be shown in the simulation in Section 6.1 and following.

5.2.2 Chemical-Mechanical Coupling

For the modeling of the mechanical part of the active material response, the approach by MURTADA ET AL. [122] is adopted as foundation. In their model, the stretch $\lambda^{(f)} = \lambda_e^{(f)} + \lambda_a^{(f)}$ of SMCs is additively split in an elastic part $\lambda_e^{(f)}$ which constitutes the elongation of the SMCs based on the mechanical load of the arterial wall, and the active part $\lambda_a^{(f)}$ which describes the stretch of the cell based on the active contraction. Since significant elastic strains may be reached, the additive split of the stretch can result in negative values of the active stretch $\lambda_a^{(f)}$ which is non-physical. Therefore, a multiplicative decomposition of the stretch is assumed in this thesis which is more appropriate for the application of finite strain theory and leads to

$$\lambda^{(f)} = \lambda_a^{(f)} \lambda_e^{(f)}, \quad (5.13)$$

where the index (f) denotes the longitudinal direction of the SMCs. This approach coincides with the classical multiplicative splits of the deformation gradient which is applied for materials with plasticity in LEE [109]. For the modeling of the contraction of the SMC, the execution of power stroke from phosphorylated myosin heads inside of the contractile units (which leads to the shortening of the cell) has to be described by a mechanical quantity. This is achieved by introducing the driving stress $P_c^{(f)}$ which

characterizes the potential of the power strokes to contract (shorten) the SMCs of the tissue of the arterial wall. The actual mechanical stress, which is stored inside of the cells of the tissue, is expressed by $P_a^{(f)}$. As long as the driving stress $P_c^{(f)}$ is larger than the mechanical stress $P_a^{(f)}$, the SMCs contract further over time. Contrarily, the cells relax while the active stress $P_a^{(f)}$ is greater than the driving stress $P_c^{(f)}$ which means that the power strokes of the myosin heads cannot hold the current contractile state of the tissue. In correspondence to the relationship between $P_c^{(f)}$ and $P_a^{(f)}$, the active stretch $\lambda_a^{(f)}$ has to be changed over time which is considered the shortening velocity. This shortening velocity can be described by using Hill's equation for tetanized muscle contraction in KATZ [98] which can be better understood in the execution of quick-release experiments in which the shortening velocity of the tissue is investigated for different afterloads. The equation can be expressed as

$$(F + a)(v + b) = (F_0 + a)b, \quad (5.14)$$

where F constitutes the isotonic afterload, F_0 is the isometric force at which the quick-release is performed, v is the muscle shortening, and a and b are fitting parameters for the process. To include the equation in the model, F can be considered the actual stress in the tissue $P_a^{(f)}$, F_0 corresponds to the driving stress $P_c^{(f)}$, and the shortening velocity v is expressed by the time-derivative $\dot{\lambda}_a^{(f)}$. Including a rearrangement of the equation, the evolution equation for the active stretch $\lambda_a^{(f)}$ in direction (f) of the tissue is obtained as

$$\dot{\lambda}_a^{(f)} = \beta_1 \frac{P_a^{(f)} - P_c^{(f)}}{P_a^{(f)} + \beta_2}, \quad (5.15)$$

where the material parameters are described with β_1 and β_2 . As described in Section 3.3.5 for the second law of thermodynamics, the second Piola-Kirchhoff stresses \mathbf{S} of the material can be received from the constitutive equation by building $\mathbf{S} = 2 \partial \Psi / \partial \mathbf{C}$ which is the derivative of the strain-energy density function with respect to the right Cauchy-Green tensor \mathbf{C} . This procedure can be executed similarly for the 1D first Piola-Kirchhoff stress $P_a^{(f)}$ by the derivative $P_a^{(f)} = \partial \Psi_a^{(f)} / \partial \lambda^{(f)}$. In this context, the material behavior of the SMCs is described by the strain-energy density function $\Psi_a^{(f)}$ which is defined as

$$\Psi_a^{(f)} = \frac{\mu_a}{2} \left(n_C^{(f)} + n_D^{(f)} \right) \left(\lambda_e^{(f)} - 1 \right)^2, \quad (5.16)$$

with the material parameter μ_a , the elastic stretch of the SMCs $\lambda_e^{(f)}$, and the proportions of myosin heads in state C and D as $n_C^{(f)}$ and $n_D^{(f)}$. Here, all myosin heads which are attached to the actin filaments are included based on their contribution to the stability of the cells. For the derivative $P_a^{(f)} = \partial \Psi_a^{(f)} / \partial \lambda^{(f)}$, the elastic part of the stretch $\lambda_e^{(f)}$ in Eq. (5.16) has to be substituted with $\lambda_e^{(f)} = \lambda^{(f)} / \lambda_a^{(f)}$. In consequence, the active stress $P_a^{(f)}$ is obtained as

$$P_a^{(f)} = \frac{\mu_a}{\lambda_a^{(f)}} \left(n_C^{(f)} + n_D^{(f)} \right) \left(\lambda_e^{(f)} - 1 \right). \quad (5.17)$$

The driving stress of the SMCs $P_c^{(f)}$ depends only on the myosin heads which are able to perform power strokes. Therefore, only the proportion $n_C^{(f)}$ is included into the

equation which leads to

$$P_c^{(f)} = \kappa n_C^{(f)}, \quad (5.18)$$

where κ constitutes the highest achievable driving stress. Based on the dependency of the active and driving stress $P_c^{(f)}$ and $P_a^{(f)}$ on the chemical state of the myosin head, chemical-mechanical coupling is included.

5.2.3 Inclusion of the Passive Response and Formulation of the Total Strain-Energy Density Function

In the previous sections, the active material model was described in consideration of one fiber direction (f). To obtain the general description of the three-dimensional material behavior of the arterial wall, the passive material behavior is included and the number of fiber directions for SMCs as well as collagen is considered. For hyperelastic, passive material response, the polyconvex model by BALZANI ET AL. [8] is adopted. Based on the three-element Hill muscle model from FUNG [57] which is adopted in MURTADA ET AL. [122] and also included here, the elastic and active material components are understood to act parallelly. In this regard, the coupling between ECM and SMCs is assumed weak. In consequence, an additive split of both material components can be applied to the total strain-energy density function Ψ . The location of the artery and their type influences the specific fiber orientation significantly. Furthermore, the orientation of embedded fibers in soft biological tissues is generally dispersed and, therefore, can be arbitrarily complex. In consequence, a suitable simplification of the fiber direction has to be considered in the mechanical model. In various publications, the fiber direction of SMCs is considered uniquely circumferential which can be an appropriate approximation in small arteries such as resistance arteries, but is less reliable for the description of larger muscular as well as elastic arteries. With regard to collagen fibers, the assumption of two fiber directions in a material point resulted in a successful replication of data from mechanical experiments with numerical simulations. In this regard, two fiber directions for collagen as well as SMCs are considered in the proposed material model which follows similar approaches as can be found in the literature, see [72]. It is assumed that the two fiber families have a weak interaction, which allows a further additive decomposition of the formulation of the strain-energy density function Ψ . Accordingly, the mechanical behavior of the tissue is defined by a strain-energy density function $\Psi(\mathbf{C}, \mathbf{M}^{(f)})$ which can be decomposed as

$$\Psi = \Psi_{p, \text{isot}} + \sum_{f=1}^2 \Psi_{p, \text{ti}}^{(f)} + \sum_{f=1}^2 \Psi_a^{(f)}, \quad (5.19)$$

where $\Psi_{p, \text{isot}}$ describes the isotropic part of the passive material, $\Psi_{p, \text{ti}}^{(f)}$ constitutes the material behavior of collagen fibers in the direction (f) and $\Psi_a^{(f)}$ represents the active material behavior of SMCs oriented in the direction (f). The isotropic energy part $\Psi_{p, \text{isot}}$ constitutes the material behavior of elastin as matrix material which is described in a neo-Hookean formulation that excludes the dependency on I_2 . The resulting equation is expressed as

$$\Psi_{p, \text{isot}} = \alpha_1 \left(I_1 I_3^{-1/3} - 3 \right) + \alpha_2 \left(I_3^{\alpha_3} + I_3^{-\alpha_3} - 2 \right), \quad (5.20)$$

in which the material parameters are restricted to $\alpha_1 > 0$, $\alpha_2 > 0$ and $\alpha_3 > 1$. The invariants I_1 , I_3 , and K_3 for the anisotropic component are defined in Section 3.1 (see Eqs. (3.14), (3.16)). This part of the strain-energy density function includes the penalty function $\alpha_2(I_3^{\alpha_3} + I_3^{-\alpha_3} - 2)$ which punishes deviations from the incompressible state in which $I_3 = 1$. Biological tissue has been considered incompressible for decades and material models are adjusted in various ways to realize this material behavior. However, experimental studies showed that the tissue of the arterial wall is up to 6% compressible, see [197] and [198]. Accordingly, it is sufficient to express the tissue as nearly incompressible as applied here. The material behavior of the collagen fibers is described by

$$\Psi_{\text{p,ti}}^{(f)} = \alpha_4 \left\langle K_3^{(f)} - 2 \right\rangle^{\alpha_5}, \quad (5.21)$$

where the material parameters are assumed to be $\alpha_4 > 0$ and $\alpha_5 > 2$ and the Macaulay brackets are defined as $\langle \bullet \rangle = \frac{1}{2}(\bullet + |\bullet|)$. Based on the application of the invariant K_3 , this definition of the anisotropic material part fulfills the polyconvexity condition [155].

5.3 Numerical Implementation

The proposed model for the mechanical description of the arterial wall was implemented into *FEAP* using a multilevel Newton scheme. In this section, the applied methods to compute solutions for the evolution equations of the model as well as the tangent modulus are explained. Furthermore, the algorithm for the calculation of second Piola-Kirchhoff stresses and the tangent modulus at a material point is described.

A common approach to solve evolution equations relies on using the Euler integration scheme. A usual evolution equation can be expressed as $\dot{y} = f(y(t))$. With regard to the Euler integration scheme, a direct integration of the evolution equation over time is performed such that

$$\int_{t_0}^{t_0+h} \dot{y} dt = \int_{t_0}^{t_0+h} f(y(t)) dt, \quad (5.22)$$

where h is a perturbation from the point in time t_0 . In consideration of the time steps which are applied in the finite element method to enable the convergence of the Newton-Raphson method, the boundaries of the integral in Eq. (5.22) can be exchanged with the times t_n and t_{n+1} . Here, t_n constitutes the last point in time for which the solution of the FE problem is already known and, therefore, also the solution for the variable y_n at the observed material point. The current time is described by t_{n+1} , at which the new solution y_{n+1} has to be found. In consequence, the integrals of Eq. (5.22) can be rewritten to

$$\int_{t_n}^{t_{n+1}} \dot{y} dt = \int_{t_n}^{t_{n+1}} f(y(t)) dt. \quad (5.23)$$

Furthermore, a linear approximation is considered which leads to

$$y_{n+1} - y_n = \hat{f} \Delta t, \quad (5.24)$$

where $\Delta t = t_{n+1} - t_n$ is the size of the time step. In this form, the function $f(y(t))$ is substituted by the term \hat{f} which expresses an approximation of $f(y(t))$ at a certain time point t . The quantity y in function $f(y(t))$ can be replaced by different approaches. The most common versions are the substitution by either y_n or y_{n+1} , which constitute the forward (explicit) and the backward (implicit) Euler integration scheme, respectively. A comparison of the forward and backward Euler method is illustrated in Fig. 5.3. Generally, the application of the forward Euler method is straightforward, since the value y_n at the last time step is already known and, therefore, $\hat{f}_n = f(y_n)$ can be calculated directly to solve the problem. However, the explicit Euler method can lead to stability issues for the numerical solution of the FE problem. Especially in this material model, where several evolution equations are coupled, the application of the explicit Euler method can result in oscillations for the quantities of the chemical model part. Furthermore, the limits, which are set for $k_{2/5}$ and $\bar{\lambda}_p$ in the evolution equations (5.8) and (5.11), can be overstepped when the value of the derivative of the last time step is assumed. Therefore, the evolution equations of the material model are solved by the backward Euler integration scheme, which can be rearranged to

$$0 = y_{n+1} - y_n - \hat{f}_{n+1} \Delta t = g(y_{n+1}), \quad (5.25)$$

where \hat{f}_{n+1} constitutes the approximation of $f(y_{n+1})$ at the current time t_{n+1} . Equation (5.25) lays the foundation to further describe the solution of the evolution equations of the material model. The solution is presented in order of the implementation. An illustration for the solution algorithm is shown in Fig. 5.4 at the end of this chapter.

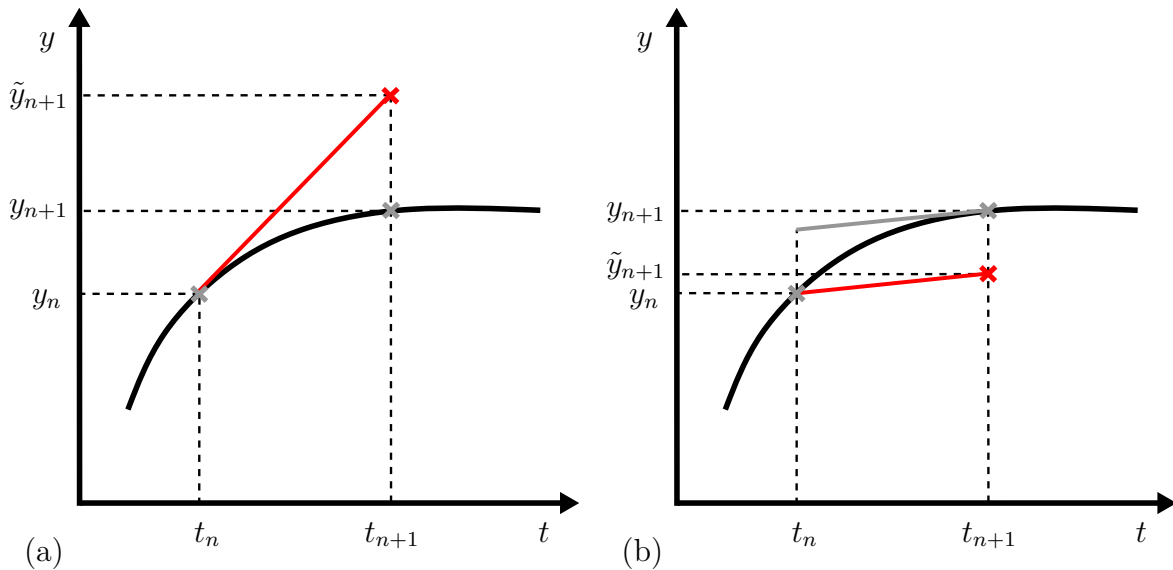


Figure 5.3: Comparison of (a) forward and (b) backward Euler method for the approximation \tilde{y}_{n+1} of the variable y_{n+1} at t_{n+1} . Slope of the function decreases over time. For the forward Euler method, the time-derivative at the last time step is assumed for the linearization. Consequently, the slope is overestimated with forward Euler which results in an overvalued approximation \tilde{y}_{n+1} . On the contrary, the time-derivative at the current time is assumed for the linearization in the backward Euler method which underestimates the slope and leads to an undervalued approximation \tilde{y}_{n+1} .

Numerical Solution for the Phosphorylation The equations, which describe the phosphorylation of the myosin heads, depend on the stretch in longitudinal direction of the cells $\lambda_{n+1}^{(f)}$. The value $\lambda_{n+1}^{(f)}$ can be calculated at the material point from the intermediate solution of the Newton iteration of the global finite element problem. Therefore, the target value $[Ca^{2+}]_{\text{tar}, n+1}^{(f)}$ for the calcium concentration can be obtained directly. Subsequently, the evolution equation for the virtual stretch $\bar{\lambda}_{c, n+1}^{(f)}$ has to be solved by the backward Euler integration scheme. For this purpose, the Newton-Raphson method is applied. In correspondence to Eq. (5.25), the function $g_1(\bar{\lambda}_{c, n+1}^{(f)})$ can be formulated as

$$g_1\left(\bar{\lambda}_{c, n+1}^{(f)}\right) = \bar{\lambda}_{c, n+1}^{(f)} - \bar{\lambda}_{c, n}^{(f)} - \left[\dot{\bar{\lambda}}_{c, \min} + \frac{\dot{\bar{\lambda}}_{c, \max} - \dot{\bar{\lambda}}_{c, \min}}{1 + e^{\gamma_2([Ca^{2+}]_{\text{tar}, n+1}^{(f)} - \gamma_1(\lambda_{n+1}^{(f)} - \bar{\lambda}_{c, n+1}^{(f)})^2 - \tau_c)}} \right] \Delta t = 0. \quad (5.26)$$

In the Newton-Raphson method, this problem is solved iteratively by formulating a linearization of the function $g_1(\bar{\lambda}_{c, n+1}^{(f)})$ at a value for $\bar{\lambda}_{c, n+1}^{(f)}$ which is close to the solution. A new intermediate solution can then be found where this linearization is equal zero. In this context, the linearization can be expressed as

$$0 = g_1\left(\bar{\lambda}_{c, n+1, i}^{(f)}\right) + g_1'\left(\bar{\lambda}_{c, n+1, i}^{(f)}\right) \left[\bar{\lambda}_{c, n+1, i+1}^{(f)} - \bar{\lambda}_{c, n+1, i}^{(f)}\right], \quad (5.27)$$

where the index i corresponds to values for the solution of the last iterative step and $i + 1$ is the notation for the solution of the current step. Furthermore, $g_1'\left(\bar{\lambda}_{c, n+1}^{(f)}\right) = \partial g_1 / \partial \bar{\lambda}_{c, n+1}^{(f)}$ expresses the derivative of the function $g_1\left(\bar{\lambda}_{c, n+1}^{(f)}\right)$ with respect to $\bar{\lambda}_{c, n+1}^{(f)}$ which can be represented as

$$g_1'\left(\bar{\lambda}_{c, n+1}^{(f)}\right) = \frac{1 + 2\gamma_1\langle\lambda_{n+1}^{(f)} - \bar{\lambda}_{c, n+1}^{(f)}\rangle \left(\dot{\bar{\lambda}}_{c, \max} - \dot{\bar{\lambda}}_{c, \min}\right) e^{\gamma_2([Ca^{2+}]_{\text{tar}, n+1}^{(f)} - \gamma_1(\lambda_{n+1}^{(f)} - \bar{\lambda}_{c, n+1}^{(f)})^2 - \tau_c)}}{\left[1 + e^{\gamma_2([Ca^{2+}]_{\text{tar}, n+1}^{(f)} - \gamma_1(\lambda_{n+1}^{(f)} - \bar{\lambda}_{c, n+1}^{(f)})^2 - \tau_c)}\right]^2} \Delta t. \quad (5.28)$$

Accordingly, the solution at the current iteration of the Newton-Raphson method can be obtained by

$$\bar{\lambda}_{c, n+1, i+1}^{(f)} = \bar{\lambda}_{c, n+1, i}^{(f)} - \frac{g_1\left(\bar{\lambda}_{c, n+1, i}^{(f)}\right)}{g_1'\left(\bar{\lambda}_{c, n+1, i}^{(f)}\right)}. \quad (5.29)$$

As a suitable assumption, the initial value $\bar{\lambda}_{c, n+1, 0}^{(f)}$ is set to the known solution of the last time step $\bar{\lambda}_{c, n}^{(f)}$. The application of the Newton-Raphson method is stopped as soon as the absolute value of the difference $\bar{\lambda}_{c, n+1, i+1}^{(f)} - \bar{\lambda}_{c, n+1, i}^{(f)}$ is smaller than a predefined tolerance value. Subsequently, the updated value for the reaction rates $k_{1/6, n+1}$ can be calculated.

Numerical Solution for the Dephosphorylation For the solution of the system of equations which describe the dephosphorylation process of the myosin heads, the application of the backward Euler integration scheme is crucial. The first step constitutes the calculation of the target value of the reaction rates $k_{2/5, \text{tar}, n+1}^{(f)}$ which only depends on the known value of the stretch $\lambda_{n+1}^{(f)}$ in fiber direction. In the next step, the evolution equations (5.8) and (5.11) have to be solved to obtain the new values for the virtual stretch $\bar{\lambda}_{p, n+1}^{(f)}$ and the reaction rates $k_{2/5, n+1}^{(f)}$. The corresponding equations for the backwards Euler method (see Eq. (5.25)) can be expressed as

$$\begin{aligned}
g_2 \left(\bar{\lambda}_{p, n+1}^{(f)}, k_{2/5, n+1}^{(f)} \right) &= k_{2/5, n+1}^{(f)} - k_{2/5, n}^{(f)} \\
&- \left[\dot{k}_{2/5, \min} \left(1 - e^{-\zeta_1 k_{2/5, n+1}^{(f)}} \right) + \frac{\dot{k}_{2/5, \max} - \dot{k}_{2/5, \min}}{1 + e^{\gamma_4 (\lambda_{n+1}^{(f)} - \bar{\lambda}_{p, n+1}^{(f)} - \tau_p)}} \right] \Delta t, \quad \text{and} \\
g_3 \left(k_{2/5, n+1}^{(f)}, \bar{\lambda}_{p, n+1}^{(f)} \right) &= \bar{\lambda}_{p, n+1}^{(f)} - \bar{\lambda}_{p, n}^{(f)} \\
&- \left[\dot{\lambda}_{p, \min} + \dot{\lambda}_{p, \max} e^{-\zeta_2 (\lambda_{n+1}^{(f)} - \bar{\lambda}_{p, n+1}^{(f)} - \Delta \bar{\lambda}_{p, \min})} + \frac{\dot{\lambda}_{p, \max} - \dot{\lambda}_{p, \min}}{1 + e^{\gamma_5 (k_{2/5, \text{tar}, n+1}^{(f)} - k_{2/5, n+1}^{(f)} - \tau_k)}} \right] \Delta t,
\end{aligned} \tag{5.30}$$

which both depend on the unknown values $\bar{\lambda}_{p, n+1}$ and $k_{2/5, n+1}$ at the current time step. Consequently, they are treated as system of equations for the application of the Newton-Raphson method which leads to

$$\mathbf{0} = \begin{bmatrix} g_2 \left(\bar{\lambda}_{p, n+1, i}^{(f)}, k_{2/5, n+1, i}^{(f)} \right) \\ g_3 \left(k_{2/5, n+1, i}^{(f)}, \bar{\lambda}_{p, n+1, i}^{(f)} \right) \end{bmatrix} + \begin{bmatrix} g_2' \left(k_{2/5, n+1, i}^{(f)} \right) & g_2^* \left(\bar{\lambda}_{p, n+1, i}^{(f)} \right) \\ g_3' \left(k_{2/5, n+1, i}^{(f)} \right) & g_3^* \left(\bar{\lambda}_{p, n+1, i}^{(f)} \right) \end{bmatrix} \begin{bmatrix} k_{2/5, n+1, i+1}^{(f)} - k_{2/5, n+1, i}^{(f)} \\ \bar{\lambda}_{p, n+1, i+1}^{(f)} - \bar{\lambda}_{p, n+1, i}^{(f)} \end{bmatrix} \tag{5.31}$$

where the superscript $\bullet' = \partial \bullet / \partial k_{2/5, n+1, i}^{(f)}$ denotes the derivative of the function \bullet with respect to $k_{2/5, n+1, i}^{(f)}$ and the superscript $\bullet^* = \partial \bullet / \partial \bar{\lambda}_{p, n+1, i}^{(f)}$ is the derivative of the function \bullet with respect to $\bar{\lambda}_{p, n+1, i}^{(f)}$. Building these four derivatives results in the following equations

$$\begin{aligned}
g_2' \left(k_{2/5, n+1, i}^{(f)} \right) &= 1 - \dot{k}_{2/5, \min} \zeta_1 e^{-\zeta_1 k_{2/5, n+1}^{(f)}} \Delta t, \\
g_2^* \left(\bar{\lambda}_{p, n+1, i}^{(f)} \right) &= \frac{\left(\dot{k}_{2/5, \max} - \dot{k}_{2/5, \min} \right) \gamma_4 e^{\gamma_4 (\lambda_{n+1}^{(f)} - \bar{\lambda}_{p, n+1}^{(f)} - \tau_p)}}{\left[1 + e^{\gamma_4 (\lambda_{n+1}^{(f)} - \bar{\lambda}_{p, n+1}^{(f)} - \tau_p)} \right]^2} \Delta t, \\
g_3' \left(k_{2/5, n+1, i}^{(f)} \right) &= \frac{\left(\dot{\lambda}_{p, \max} - \dot{\lambda}_{p, \min} \right) \gamma_5 e^{\gamma_5 (k_{2/5, \text{tar}, n+1}^{(f)} - k_{2/5, n+1}^{(f)} - \tau_k)}}{\left[1 + e^{\gamma_5 (k_{2/5, \text{tar}, n+1}^{(f)} - k_{2/5, n+1}^{(f)} - \tau_k)} \right]^2} \Delta t, \quad \text{and} \\
g_3^* \left(\bar{\lambda}_{p, n+1, i}^{(f)} \right) &= 1 - \dot{\lambda}_{p, \max} \zeta_2 e^{-\zeta_2 (\lambda_{n+1}^{(f)} - \bar{\lambda}_{p, n+1}^{(f)} - \Delta \bar{\lambda}_{p, \min})} \Delta t.
\end{aligned} \tag{5.32}$$

An intermediate solution for $k_{2/5, n+1, i+1}^{(f)}$ and $\bar{\lambda}_{p, n+1, i+1}^{(f)}$ in the Newton-Raphson iteration can be obtained by reformulating the system of equations in (5.31) which requires

the formulation of the invariant of the matrix of derivatives such that

$$\begin{bmatrix} k_{2/5,n+1,i+1}^{(f)} \\ \bar{\lambda}_{p,n+1,i+1}^{(f)} \end{bmatrix} = \begin{bmatrix} k_{2/5,n+1,i}^{(f)} \\ \bar{\lambda}_{p,n+1,i}^{(f)} \end{bmatrix} - \begin{bmatrix} g_2' \left(k_{2/5,n+1,i}^{(f)} \right) & g_2^* \left(\bar{\lambda}_{p,n+1,i}^{(f)} \right) \\ g_3' \left(k_{2/5,n+1,i}^{(f)} \right) & g_3^* \left(\bar{\lambda}_{p,n+1,i}^{(f)} \right) \end{bmatrix}^{-1} \begin{bmatrix} g_2 \left(\bar{\lambda}_{p,n+1,i}^{(f)}, k_{2/5,n+1,i}^{(f)} \right) \\ g_3 \left(k_{2/5,n+1,i}^{(f)}, \bar{\lambda}_{p,n+1,i}^{(f)} \right) \end{bmatrix}. \quad (5.33)$$

The iteration is stopped as soon as the absolute value of the improved values $k_{2/5,n+1,i+1}^{(f)}$ and $\bar{\lambda}_{p,n+1,i+1}^{(f)}$ in comparison to the previous iterative step is smaller than a predefined tolerance. The initial values $k_{2/5,n+1,0}^{(f)}$ and $\bar{\lambda}_{p,n+1,0}^{(f)}$ are set to their solution at the last time step n .

Numerical Solution for the Kinetic Model of the Myosin Heads Since the reaction rates $k_{1/6,n+1}^{(f)}$ and $k_{2/5,n+1}^{(f)}$ are obtained, the values of the proportions of the myosin heads in their corresponding state can be calculated. Applying the backward Euler integration scheme to the kinetic model (5.1), which describes the transformation of the myosin heads between four different states by four ordinary differential equations, the following system of equations is obtained

$$\underbrace{\begin{bmatrix} n_{A,n+1}^{(f)} \\ n_{B,n+1}^{(f)} \\ n_{C,n+1}^{(f)} \\ n_{D,n+1}^{(f)} \end{bmatrix}}_{=\mathbf{n}_{n+1}^{(f)}} - \underbrace{\begin{bmatrix} n_{A,n}^{(f)} \\ n_{B,n}^{(f)} \\ n_{C,n}^{(f)} \\ n_{D,n}^{(f)} \end{bmatrix}}_{=\mathbf{n}_n^{(f)}} = \underbrace{\begin{bmatrix} -k_{1,n+1}^{(f)} & k_{2,n+1}^{(f)} & 0 & k_7 \\ k_{1,n+1}^{(f)} & -k_{2,n+1}^{(f)} - k_3 & k_4 & 0 \\ 0 & k_3 & -k_4 - k_{5,n+1}^{(f)} & k_{6,n+1}^{(f)} \\ 0 & 0 & k_{5,n+1}^{(f)} & -k_{6,n+1}^{(f)} - k_7 \end{bmatrix}}_{=\mathbf{K}} \underbrace{\begin{bmatrix} n_{A,n+1}^{(f)} \\ n_{B,n+1}^{(f)} \\ n_{C,n+1}^{(f)} \\ n_{D,n+1}^{(f)} \end{bmatrix}}_{=\mathbf{n}_{n+1}^{(f)}} \Delta t, \quad (5.34)$$

in which the notation for the vectors $\mathbf{n}_{n+1}^{(f)}$ and $\mathbf{n}_n^{(f)}$ as well as for the matrix with reaction rates \mathbf{K} is introduced. This system of equations can be rearranged to receive the values $n_{A,n+1}^{(f)}$, $n_{B,n+1}^{(f)}$, $n_{C,n+1}^{(f)}$ and $n_{D,n+1}^{(f)}$ at the current time t_{n+1} which can be expressed as

$$\mathbf{n}_{n+1}^{(f)} = \mathbf{n}_n^{(f)} [\mathbf{1} - \mathbf{K} \Delta t]^{-1}. \quad (5.35)$$

Here, $\mathbf{1}$ constitutes a 4×4 diagonal matrix with ones as components in the diagonal and $[\bullet]^{-1}$ represents the inverse of the resulting 4×4 matrix. Consequently, the backward Euler method can be solved without iterative solution scheme.

Numerical Solution of the Active Stretch The calculation of the active stretch $\lambda_{a,n+1}^{(f)}$ remains as a last step, before the second Piola-Kirchhoff stresses \mathbf{S} and the tangent modulus \mathbb{C} can be computed for the current time step t_{n+1} . Based on the known value of $n_{C,n+1}^{(f)}$, the value for the driving stress $P_{c,n+1}^{(f)}$ can be obtained directly and inserted into the evolution equation $\dot{\lambda}_a^{(f)}$ from Eq. (5.15). Since the active stress $P_a^{(f)}$ depends on the active stretch $\lambda_a^{(f)}$, a replacement of the quantity $P_{a,n+1}^{(f)}$ in the evolution equation for $\lambda_a^{(f)}$ is required by considering Eq. (5.17). This equation contains the elastic stretch which can be described as $\lambda_{e,n+1}^{(f)} = \lambda_{n+1}^{(f)} / \lambda_{a,n+1}^{(f)}$ (see Eq. (5.13)). According to Eq. (5.25), this leads to the following equation when the backwards Euler

method is applied

$$g_4 \left(\lambda_{a,n+1}^{(f)} \right) = \lambda_{a,n+1}^{(f)} - \lambda_{a,n}^{(f)} - \frac{\mu_a \left(\lambda_{a,n+1}^{(f)} \right)^{-1} \left(n_{C,n+1}^{(f)} + n_{D,n+1}^{(f)} \right) \left(\lambda_{n+1}^{(f)} / \lambda_{a,n+1}^{(f)} - 1 \right) - P_{c,n+1}^{(f)}}{\mu_a \left(\lambda_{a,n+1}^{(f)} \right)^{-1} \left(n_{C,n+1}^{(f)} + n_{D,n+1}^{(f)} \right) \left(\lambda_{n+1}^{(f)} / \lambda_{a,n+1}^{(f)} - 1 \right) + \beta_2} \Delta t. \quad (5.36)$$

As for the other evolution equations, the Newton-Raphson method is used to receive the numerical solution. Following the description for the numerical calculation of $\bar{\lambda}_{c,n+1}^{(f)}$ (see Eq. (5.27) and (5.29)), the current value of the active stretch $\lambda_{a,n+1}^{(f)}$ can be obtained by iteratively solving

$$\lambda_{a,n+1,i+1}^{(f)} = \lambda_{a,n+1,i}^{(f)} - \frac{g_4 \left(\lambda_{a,n+1,i}^{(f)} \right)}{g_4' \left(\lambda_{a,n+1,i}^{(f)} \right)}. \quad (5.37)$$

For the expression of the derivative $g_4' = \partial g_4 / \partial \lambda_{a,n+1}^{(f)}$, the numerator of the fraction in g_4 is defined as u and the denominator is defined as v . The terms u and v as well as their derivatives $\bullet' = \partial \bullet / \partial \lambda_{a,n+1}^{(f)}$ can be formulated as

$$\begin{aligned} u &= \mu_a \left(n_{C,n+1}^{(f)} + n_{D,n+1}^{(f)} \right) \left(\frac{\lambda_{n+1}^{(f)}}{\left(\lambda_{a,n+1}^{(f)} \right)^2} - \frac{1}{\lambda_{a,n+1}^{(f)}} \right) - P_{c,n+1}^{(f)}, \\ v &= \mu_a \left(n_{C,n+1}^{(f)} + n_{D,n+1}^{(f)} \right) \left(\frac{\lambda_{n+1}^{(f)}}{\left(\lambda_{a,n+1}^{(f)} \right)^2} - \frac{1}{\lambda_{a,n+1}^{(f)}} \right) + \beta_2, \quad \text{and} \\ u' &= v' = \mu_a \left(n_{C,n+1}^{(f)} + n_{D,n+1}^{(f)} \right) \left(\frac{-2 \lambda_{n+1}^{(f)}}{\left(\lambda_{a,n+1}^{(f)} \right)^3} + \frac{1}{\left(\lambda_{a,n+1}^{(f)} \right)^2} \right). \end{aligned} \quad (5.38)$$

The corresponding derivative g_4' can be expressed as

$$g_4' = 1 - \beta_1 \frac{u' v - u v'}{v^2} \Delta t. \quad (5.39)$$

One issue in this application of the Newton-Raphson method constitutes the equilibrium between the active stretch $\lambda_a^{(f)}$, the elastic stretch $\lambda_e^{(f)}$ and the total stretch $\lambda^{(f)}$. Since the total stretch $\lambda_{n+1}^{(f)}$ at the current time t_{n+1} is already known, the equilibrium as defined in Eq. (5.13) is not fulfilled anymore as $\lambda_{n+1}^{(f)} \neq \lambda_{a,n}^{(f)} \lambda_{e,n}^{(f)}$. Accordingly, either $\lambda_{a,n}^{(f)}$ or $\lambda_{e,n}^{(f)}$ has to be adjusted to satisfy the equilibrium before the evolution equation $\dot{\lambda}_a^{(f)}$ can be solved to obtain the new value for the current active stretch $\lambda_{a,n+1}^{(f)}$. In this regard, changes from $\lambda_n^{(f)}$ to $\lambda_{n+1}^{(f)}$ are considered to be based on changes of the boundary conditions (displacements; load scenario) or mechanical properties of the model during the time step Δt . This results for the passive material part in adjust-

ments of the stresses. Consequently, the active material part should react equally. Since the active stress $P_a^{(f)}$ depends on the elastic stretch $\lambda_e^{(f)}$, which describes the elongation of the SMCs, and not on the active stretch $\lambda_a^{(f)}$, the adjustment of the stretches is accomplished by defining an intermediate value for the elastic stretch by

$$\lambda_{e,n}^{(f)*} = \frac{\lambda_{n+1}^{(f)}}{\lambda_{a,n}^{(f)}}. \quad (5.40)$$

By applying this approach, the value $\lambda_{a,n}^{(f)}$ from the last time step t_n can be set as first assumption for iterative step $i = 0$ of the Newton-Raphson method. The iterative procedure is stopped as soon as the change of $\lambda_{a,n+1,i+1}^{(f)}$ to the previous iteration is smaller than a tolerance value. Subsequently, the current value of the elastic stretch can be calculated by $\lambda_{e,n+1}^{(f)} = \lambda_{n+1}^{(f)} / \lambda_{a,n+1}^{(f)}$.

Calculation of the second Piola-Kirchhoff stresses The second Piola-Kirchhoff stress tensor \mathbf{S} is calculated based on the derivative of the strain-energy density function Ψ with respect to the right Cauchy-Green tensor \mathbf{C} (see Eq. (3.63)). For this purpose, the chain rule is applied in which the derivative of Ψ with respect to their invariants is multiplied with the derivatives of the corresponding invariant with respect to \mathbf{C} . Consequently, the second Piola-Kirchhoff stresses \mathbf{S} can be expressed as

$$\begin{aligned} \mathbf{S} = 2 \left[\frac{\partial \Psi_{p, \text{isot}}}{\partial I_1} \frac{\partial I_1}{\partial \mathbf{C}} + \frac{\partial \Psi_{p, \text{isot}}}{\partial I_3} \frac{\partial I_3}{\partial \mathbf{C}} \right. \\ \left. + \sum_{f=1}^2 \left(\frac{\partial \Psi_{p, \text{ti}}^{(f)}}{\partial I_1} \frac{\partial I_1}{\partial \mathbf{C}} + \frac{\partial \Psi_{p, \text{ti}}^{(f)}}{\partial I_4^{(f)}} \frac{\partial I_4^{(f)}}{\partial \mathbf{C}} + \frac{\partial \Psi_{p, \text{ti}}^{(f)}}{\partial I_5^{(f)}} \frac{\partial I_5^{(f)}}{\partial \mathbf{C}} \right) + \sum_{f=1}^2 \frac{\partial \Psi_a^{(f)}}{\partial I_4^{(f)}} \frac{\partial I_4^{(f)}}{\partial \mathbf{C}} \right]. \end{aligned} \quad (5.41)$$

The corresponding derivatives of the invariants with respect to the right Cauchy-Green tensor \mathbf{C} can be formulated as

$$\frac{\partial I_1}{\partial \mathbf{C}} = \mathbf{I}, \quad \frac{\partial I_3}{\partial \mathbf{C}} = I_3 \mathbf{C}^{-1}, \quad \frac{\partial I_4^{(f)}}{\partial \mathbf{C}} = \mathbf{M}^{(f)}, \quad \text{and} \quad \frac{\partial I_4^{(f)}}{\partial \mathbf{C}} = \mathbf{C} \mathbf{M}^{(f)} + \mathbf{M}^{(f)} \mathbf{C}. \quad (5.42)$$

Furthermore, the derivatives of the strain-energy density function Ψ with respect to the invariants are obtained for the passive isotropic part as

$$\frac{\partial \Psi_{p, \text{isot}}}{\partial I_1} = \alpha_1 I_3^{-1/3}, \quad \frac{\partial \Psi_{p, \text{isot}}}{\partial I_3} = -\frac{\alpha_1}{3} I_1 I_3^{-4/3} + \alpha_2 (\alpha_3 I_3^{\alpha_3-1} - \alpha_3 I_3^{-\alpha_3-1}). \quad (5.43)$$

Furthermore, the derivative of $\Psi_{p, \text{ti}}^{(f)}$ with respect to the principal invariants can be expressed as

$$\frac{\partial \Psi_{p, \text{ti}}^{(f)}}{\partial I_1} = \alpha_4 \alpha_5 I_4^{(f)} \left\langle K_3^{(f)} - 2 \right\rangle^{\alpha_5-1}, \quad (5.44)$$

and the derivative with respect to the mixed invariants is

$$\frac{\partial \Psi_{p, \text{ti}}^{(f)}}{\partial I_4^{(f)}} = \alpha_4 \alpha_5 I_1 \left\langle K_3^{(f)} - 2 \right\rangle^{\alpha_5-1}, \quad \frac{\partial \Psi_{p, \text{ti}}^{(f)}}{\partial I_5^{(f)}} = -\alpha_4 \alpha_5 \left\langle K_3^{(f)} - 2 \right\rangle^{\alpha_5-1}. \quad (5.45)$$

The active part of the strain-energy density function $\Psi_a^{(f)}$ depends only on the mixed invariant $I_4^{(f)}$. The corresponding derivative can be formulated as

$$\frac{\partial \Psi_a^{(f)}}{\partial I_4^{(f)}} = \frac{\mu_a}{2\lambda_a^{(f)} \lambda^{(f)}} \left(n_C^{(f)} + n_D^{(f)} \right) \left(\frac{\lambda^{(f)}}{\lambda_a^{(f)}} - 1 \right). \quad (5.46)$$

Note that this derivative was performed based on $\lambda^{(f)} = \sqrt{I_4^{(f)}}$.

Calculation of the Tangent Modulus The calculation of the tangent modulus $\mathbb{C} = 2d\mathbf{S}/d\mathbf{C}$ can be obtained by building the derivative of the second Piola-Kirchhoff stress \mathbf{S} with respect to the right Cauchy-Green tensor \mathbf{C} . For the proposed material model, the formulation of the analytic tangent modulus is not straightforward since all evolution equations which depend on the right Cauchy-Green tensor \mathbf{C} via invariants or stretch $\lambda^{(f)}$ have to be considered. Therefore, the tangent modulus is calculated numerically. One approach for the numerical formulation would be the approximation of the derivative by the finite difference scheme which can be expressed for the function $f(x)$ as

$$f'(x) \approx \frac{f(x+h) - f(x)}{h}, \quad (5.47)$$

where h constitutes a perturbation from the point x . This approximation improves mathematically the closer h is to zero. However, in the computational implementation, the rounding error in the term $x+h$ increases the smaller h is. Therefore, the complex-step derivative approximation (CSDA) is applied here which was published by TANAKA ET AL. [172]. In this approach, the perturbation is accomplished along an imaginary axis such that the approximation of the derivative $f'(x)$ can be reformulated as

$$f'(x) \approx \frac{\Im[f(x+ih)]}{h}, \quad (5.48)$$

wherein i constitutes the imaginary unit and, therefore, $i^2 = -1$, and the operator $\Im[\bullet]$ results in the value of the imaginary part of the term \bullet . For the tangent modulus of the material model, this approach leads to the approximation

$$\mathbb{C}_{IJ(K)L} = 2 \frac{\Im \left[\mathbf{S}_{IJ} \left(\mathbf{C} + ih \mathbf{C}_{(K)(L)}^* \right) \right]}{h}. \quad (5.49)$$

Based on the right subsymmetry $\mathbb{C}_{IJ(K)L} = \mathbb{C}_{IJ(L)K}$, six perturbations steps are sufficient to approximate six coefficients of the tangent modulus \mathbb{C} per perturbation.

Correspondingly, the term $\mathbf{C}_{(K)(L)}^*$ can be expressed by Kronecker's deltas δ_{IJ} in Voigt notation such that

$$\mathbf{C}_{(K)(L)}^* = \begin{bmatrix} \delta_{1(K)}\delta_{1(L)} & \delta_{2(K)}\delta_{2(L)} & \delta_{3(K)}\delta_{3(L)} & 0.5\delta_{1(K)}\delta_{2(L)} & 0.5\delta_{2(K)}\delta_{3(L)} & 0.5\delta_{1(K)}\delta_{3(L)} \end{bmatrix}^T. \quad (5.50)$$

As already mentioned in the beginning of this Section, the solution algorithm for the

numerical implementation is illustrated in Fig. 5.4.

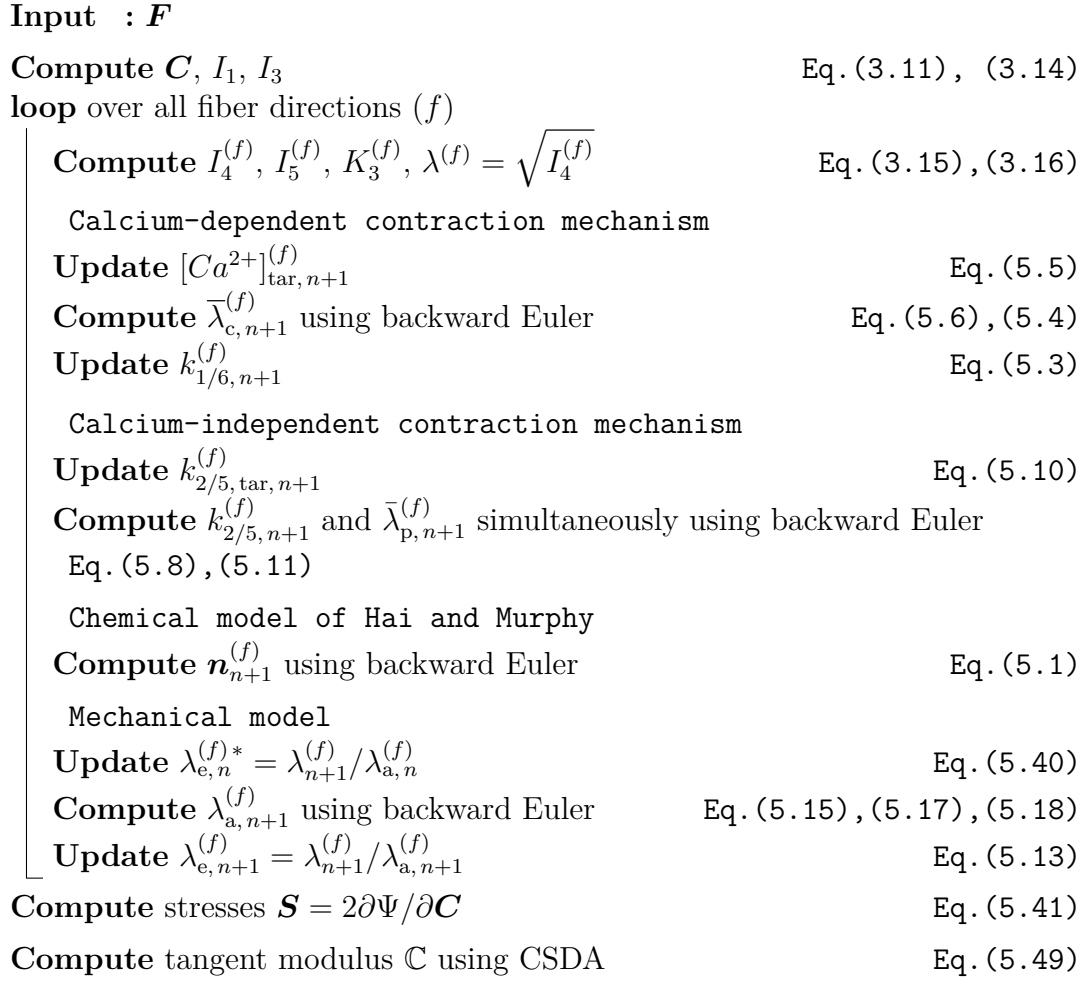


Figure 5.4: Algorithm to calculate the second Piola-Kirchhoff stresses and the tangent modulus at a material point from the proposed material model. All quantities have to be computed for all fiber directions, separately.

6 Numerical Simulation with Active Material Response

In this chapter, the execution of numerical simulations with the proposed material model for the active contraction of SMCs in arterial walls is presented and the results are discussed and analyzed. The analysis and simulation results have been previously published in UHLMANN AND BALZANI [177]. For the validation of the proposed model, the results from the mechanical experiment of JOHNSON ET AL. [94] are replicated with simulations in which all three scenarios of the experiment are considered (see Section 2.2.4). In these simulations, an axial segment of the artery is described as hollow cylinder with suitable geometry. For the inclusion of residual stresses, the mechanical model is not combined with a growth model in this chapter. Instead, the opening angle method is applied which constitutes a straightforward approach to considered circumferential residual stresses [34]. To investigate the mechanical model with validated material parameters, additional simulations are performed in which intravascular pressure waves are applied to an arterial ring. These pressure waves constitute an approach to create a load scenario which is more comparable with the in vivo pulse pressure created by the difference between systolic and diastolic blood pressure. The identical protocol is used in two additional simulations with arterial rings in which the material model is modified to exclude either the activity adjustment of MLCP or even the entire stretch-dependency to the contraction mechanism. The comparison of these three simulation results will demonstrate that the proposed model is advantageous to describe the behavior of muscular arteries which are able to decrease their diameter after an increase of the intravascular pressure.

6.1 Model Parameters: Adjustment and Validation

In the experiments by JOHNSON ET AL. [94], the contraction of a segment of a middle cerebral artery of a rat was investigated. Middle cerebral arteries constitute medium sized muscular arteries. A sequence of intravascular pressure with increasing pressure values was applied to the arterial segment. During this sequence, the adjustment of the outer diameter was measured over time. The corresponding pressure protocol is illustrated in Fig 6.1c. As described in Section 2.2.4, this sequence of intravascular pressure was repeated three times, in which the surrounding Krebs solution was altered to obtain three different mechanical responses:

1. Fully active response,
2. Suppressed contraction by blocking the stretch-dependent inhibition of MLCP,
3. Passive material response.

All three data sets of these experimental scenarios are considered for the validation of the proposed material model. From the three presented results in Section 2.2.4, the data from Fig. 2.6b is taken into account for the validation of the material model. To enable a suitable comparison of the numerical simulations with the experimental data, the experimental setup was replicated in a boundary value problem in *FEAP*. During

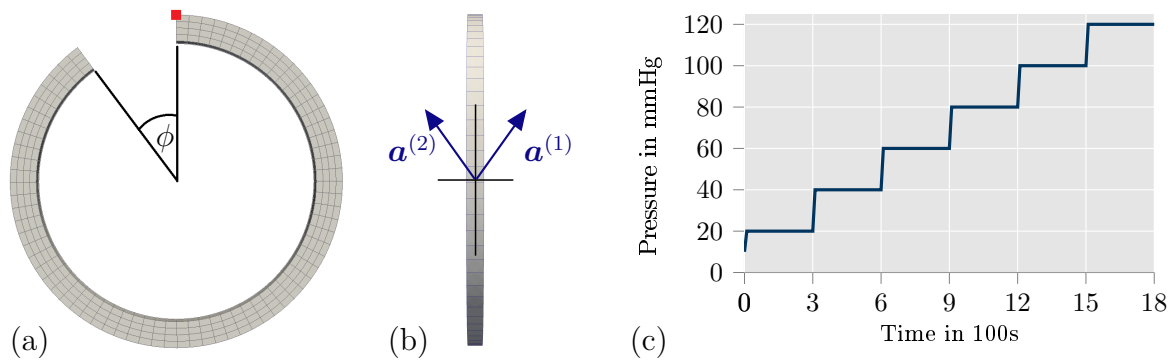


Figure 6.1: Visualization of the mesh with (a) the opening angle to apply residual stresses, (b) the fiber angles in the plane of longitudinal and circumferential direction, and (c) a diagram of the pressure profile, which was used in experimental data and applied for the parameter adjustment of the proposed model. The red square in (a) marks the node which is used in Fig. 6.4 to plot the evolution of mechanical and chemical quantities over time. Illustration is adopted from UHLMANN AND BALZANI [177].

the experiments, the cerebral artery is fixated on the cannulas of the arteriograph with nylon threads which prevents the artery from movement in axial direction. Furthermore, no axial prestretch is applied before the fixation of the artery. In consequence, Dirichlet boundaries at the axial ends of the artery are applied in which the axial displacements are set to zero during the numerical simulations. Moreover, the mesh for the arterial ring includes only one element in longitudinal direction to minimize computation time. With four elements in radial direction and 72 elements in circumferential direction, the mesh consists of 288 quadratic, 20-node brick elements in total. The geometry of the unloaded artery is not described in JOHNSON ET AL. [94]. According to measurements in [58], the ratio between wall thickness and inner radius is 0.21 for middle cerebral arteries of mice which is assumed for the creation of the geometry of the same artery type of rats here. Since residual stresses are applied in simulations of this chapter by the opening angle method [34], the radius of the stress-free geometry is still decreasing during the closure of the arterial ring (see Fig. 6.1a). Therefore, the inner and outer radius of the unloaded and stress-free state of the arterial ring was set to 92 and 112 μm , respectively. For the modeling of the fiber direction, two fiber families are defined in the material model which are oriented in between circumferential and longitudinal direction of the arterial wall (see Fig. 6.1b). The orientation of SMCs is considered equal to the orientation of collagen in the numerical simulations. This assumption bases on a deficiency of data for the actual orientation of SMCs. A frequently used alternative approach for numerical simulations with SMCs constitutes their orientation in circumferential direction which can be regarded as less realistic. Measurements of the fiber directions in larger human arteries by SCHRIEFL ET AL. [153] showed that the orientation of collagen is considerably closer to the circumferential direction at the inner side of the wall than at the outer side. In consequence, the fiber direction is dependent on the radial position inside of the wall here. The corresponding angle between fiber and circumferential direction begins with 10° at the inner side and increases linearly to 40° at the outer side of the arterial wall.

6.1.1 Optimization of the Model Parameters

For the fitting of the parameters of the mechanical model to the experimental data, an optimization was implemented into *Python* which is based on the library *mystic*. The used optimization tool in *mystic* constitutes a mixture of evolution strategy and gradient methods. For every newly generated set of parameters from *mystic*, the *Python* script calls *FEAP* as a subprocess to solve the described boundary value problem with the corresponding parameter set. Based on the parallelization of *mystic*, 40 children parameter sets can be analyzed simultaneously. For the validation of the parameter set, the following objective function is formulated

$$z = \sqrt{\sum_{k=1}^{n_{\text{data}}} \left(\frac{d_{\text{exp},k} - d_{\text{sim},k}}{d_{\text{exp},k}} \right)^2}, \quad (6.1)$$

where $d_{\text{exp},k}$ constitutes the measured, outer diameter from the experimental data at the time t_k , and $d_{\text{sim},k}$ is the outer diameter from the simulation at the same time t_k . The optimal parameter set is found by a minimization of the objective function. To save computational time, the optimization is executed in two sequential steps.

Parameters of the Passive Material Response Since the experiments provide information about the passive material response as separated data set, the material parameters for the passive model part can be fitted first. Here, the opening angle ϕ of the arterial ring is included which leads to six parameters in the first optimization step. The fitted values for the passive material response are listed in Table 1.

Table 1: Optimized passive parameters and opening angle

Parameter	α_1	α_2	α_3	α_4	α_5	ϕ
Value	11.52507 kPa	151.73775 kPa	2.75662	1.27631 kPa	3.08798	38.923°

Parameters of the Active Material Response In the second step of the optimization, the first and second experimental scenario were replicated sequentially in the numerical simulation. Accordingly, the active material response is fitted to the data which include the full activity and the suppressed contraction. For the selected data set, the contraction in the second experimental scenario is decreased by adding $1 \mu\text{m}$ of the ROCK inhibitor Y27632 into the Krebs solution around the arterial segment. The corresponding inhibition of ROCK leads to a significant reduction of the phosphorylation of the enzyme MLCP and, therewith, an increased dephosphorylation of myosin heads (see Section 2.2.3). This process can be formulated by the modification of the reaction rates $k_{2/5}$ which express the rate of dephosphorylation. Here, it is assumed that the amount of ROCK inhibitor Y27632 is sufficient to disable the phosphorylation of the enzyme MLCP and, therefore, results in a constant value for the reaction rates $k_{2/5}$. In consequence, the evolution equations (5.8) and (5.11) are not solved for the second

scenario of the experiment, but an additional parameter $k_{2/5,\text{const}}$ is optimized. To enable adequate numerical simulations, reliable starting values for the time-dependent variable of the proposed model have to be chosen which are labeled as \bullet_{start} . Since the proportions $n_{A,\text{start}}$, $n_{B,\text{start}}$, $n_{C,\text{start}}$ and $n_{D,\text{start}}$ of the myosin heads in their chemical states cannot be predicted for the initial contractile state of the arterial wall prior the beginning of the mechanical experiment, the value $n_{A,\text{start}} = 1$ is assumed for the start of the simulation. Following Eq. (5.2), the values for the remaining three proportions have to be zero. Accordingly, the material is not able to produce an active contraction in the beginning since $n_{C,\text{start}} = 0$. The initial contractile state of the arterial wall is reproduced by applying an intravascular pressure of 10 mmHg over a time of 600 s before the pressure profile starts. The remaining starting values and the chosen material parameters for the proposed model are listed in Table 2. Note that experience gathered from previous optimizations was taken into account to preselect these parameters. Furthermore, data from other publications were considered. In this context, the mechanical parameter $\beta_2 = 26.68$ kPa was adopted from MURTADA ET AL. [123]. All other mechanical parameters were part of the optimization. The constant reaction rate for $k_{2/5}$ in scenario 2 was optimized to be $k_{2/5,\text{const}} = 0.892345\text{s}^{-1}$. The other values of the parameter optimization are shown in Table 3.

Table 2: Chemical material parameters, manually adjusted/set prior to optimization

k_3	k_4	k_7	Ca_{50}	γ_2	γ_3	$\lambda_{50,c}$	$\bar{\lambda}_{c,\text{start}}$	$\lambda_{a,\text{start}}$
0.134s^{-1}	0.00166s^{-1}	0.000066s^{-1}	$0.4\mu\text{M}$	$50\mu\text{M}^{-1}$	$0.9\mu\text{M}$	1.2	1.0	1.0
γ_4	ζ_1	γ_5	ζ_2	$\Delta\bar{\lambda}_{p,\text{min}}$	γ_6	$\lambda_{50,p}$	$\bar{\lambda}_{p,\text{start}}$	$\lambda_{e,\text{start}}$
200	100s	50s	1000	-0.00001	1.5s^{-1}	1.0	1.0	1.0

Table 3: Active mechanical and chemical parameters, optimized

η	γ_1	$\dot{\lambda}_{c,\text{max}}$	$\dot{\lambda}_{c,\text{min}}$	$\dot{k}_{2/5,\text{max}}$	$\dot{k}_{2/5,\text{min}}$
0.1624s^{-1}	$0.5131\mu\text{M}$	0.0443s^{-1}	-0.0443s^{-1}	0.0009735s^{-2}	-0.0010694s^{-2}
$\dot{\lambda}_{p,\text{max}}$	$\dot{\lambda}_{p,\text{min}}$	μ_a	κ	β_1	$k_{2/5,\text{start}}$
0.0000699s^{-1}	-0.0002323s^{-1}	11.857kPa	148.262kPa	0.001006s^{-1}	1.82758s^{-1}

6.1.2 Comparison of Simulation Results and Experimental Data

The data points of the experiments were manually extracted from the diagram of the original paper (see Fig. 2.6b). The marks and graphs in blue, green and red of Fig. 6.2 represent the data of the experiment and the simulation results which applied the optimized parameters. As can be seen, the proposed material model for the active response enables an accurate representation of the experimental data. Nonetheless, it has to be noted that the calculation of the Ca^{2+} concentration was not modified between the first (red) and second (green) scenario of the numerical simulations. According measurements of cytosolic Ca^{2+} concentration are not presented in JOHNSON ET AL. [94]. However, in the paper by JACKSON AND BOERMAN [90], it is shown that Y27632 has

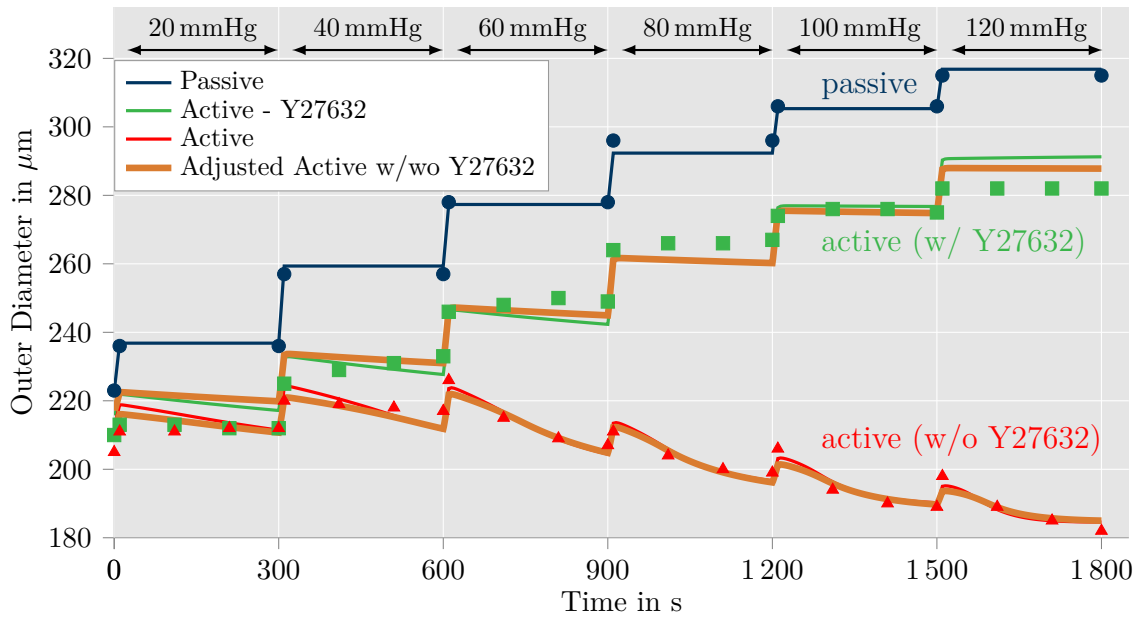


Figure 6.2: Comparison of model response with experimental data from [94] for three different setups: passive response, active response under influence of $1 \mu\text{m}$ Rho kinase inhibitor Y27632 and fully active response. The Rho kinase inhibitor Y27632 is assumed to block the calcium-independent contraction mechanism ($k_{2/5}$ is const.). The results of the model nearly reproduce the experimental data. An adjusted variation of the parameter optimization is illustrated in orange. In this case, the parameter optimization incorporates a decrease of calcium concentration and calcium flow rate while Y27632 influences the artery. The results are almost identical to the original computation. Illustration and data is adopted from UHLMANN AND BALZANI [177].

an impact on the Ca^{2+} inflow which results in a decreased concentration and a decelerated inflow rate. In order to investigate if the proposed material model is able to represent the experiment even when the calcium concentration is changed by the agent in the second scenario, an additional parameter optimization was performed. Based on the diagram in Fig. 7 of JACKSON AND BOERMAN [90], the addition of $1 \mu\text{m}$ of Y27632 into the solution leads to an approximate reduction of the Ca^{2+} concentration by 25%. Furthermore, the reported reduction in number and frequency of calcium waves in Fig. 8a of JACKSON AND BOERMAN [90] is assumed to decrease the inflow rate to 75%. Therefore, the parameter values of γ_1 and γ_3 were reduced to 75% of their original values for the second optimization procedure. The reduction of γ_1 results in a direct decrease of the inflow rate of Ca^{2+} into the cell. The additional lowering of γ_3 decreases the target value of the cytosolic Ca^{2+} concentration at a certain stretch. The fitted set of parameters for the second parameter optimization is listed in Table 7 of the Appendix and the corresponding results are illustrated by the orange graphs in Fig. 6.2. As can be seen, the material parameters of the proposed model can be adjusted in both optimizations to accurately reproduce the experimental data.

To obtain an impression about the validity of the mechanical fields, Fig. 6.3 shows 3D contour plots of the circumferential Cauchy stress at the end of each pressure level during the fully active material response (first scenario; red graph in Fig. 6.2). The circumferential stresses reach values up to 30 kPa at the middle of the artery for an intravascular pressure of 120 mmHg. Stress gradients over the wall thickness are vis-

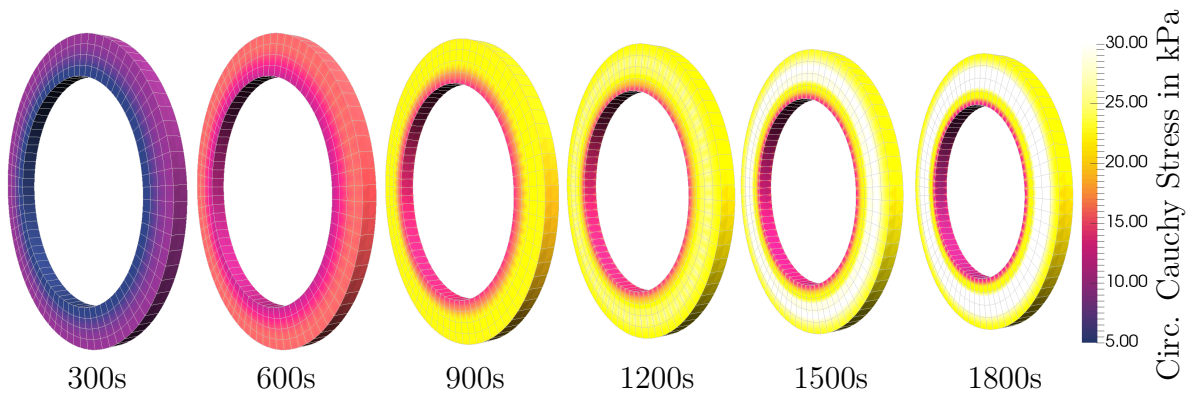


Figure 6.3: Comparison of circumferential Cauchy stresses of the fully active material response of Fig. 6.2 at different times of the pressure profile (see Fig. 6.1c). Stresses increase up to 30 kPa for an intravascular pressure of 120 mmHg. Stress gradients over the wall thickness are significantly reduced at all times due to application of residual stresses. Illustration is adopted from UHLMANN AND BALZANI [177].

ible at all times. While the application of the opening angle method might lead to a reduction of the gradients, it is not sufficiently adequate for the inclusion of residual stresses to describe the mechanical homeostasis of the arterial wall. A corresponding extension of the material model will be described in Chapter 7 to calculate the residual stresses automatically.

Based on the comparison between experimental data and numerical simulations, a reliable representation of the stretch-dependent contraction mechanism can be assumed by the proposed mechanical model which includes the mechanical-chemical coupling of the SMCs. In consequence, the contraction of the arterial wall during an increase of the intravascular pressure can be described. This is not the case for various competitive approaches which include the stretch-dependency directly in the mechanical part of the active material model by considering a dependency of the myosin-actin overlap on the stretch of the cell (see, e.g., [123], [72]). These model approaches are able to describe the stretch-dependent adjustment of the active contraction in elastic or large muscular arteries, where the dominant elasticity of the tissue leads to large deformations of the arterial wall. However, for physiological load scenarios, the active stress of these material models increases only when the cell-stretch increases. This cannot cover the experimental data for medium or small muscular arteries such as the middle cerebral artery. There, initial stretch of the SMCs leads to a decrease of the diameter, which can be associated with an increase of the active stress. In consequence, an inclusion of the stretch-dependency of the chemical quantities such as the activity of MLCP and MLCK seems a considerable improvement to describe the contraction of vascular SMCs. This allows not only for a suitable reproduction of the experimental results, but enables the more direct and biophysically motivated incorporation of further effects on the active response such as the impact of antihypertensive drugs.

6.1.3 Investigation of the Contraction at a Material Point

To further investigate the capability of the proposed model to describe the stretch-dependent intracellular reaction chains, four diagrams in Fig. 6.4 show the evolution of important quantities over time for the fully active material response. The data is pro-

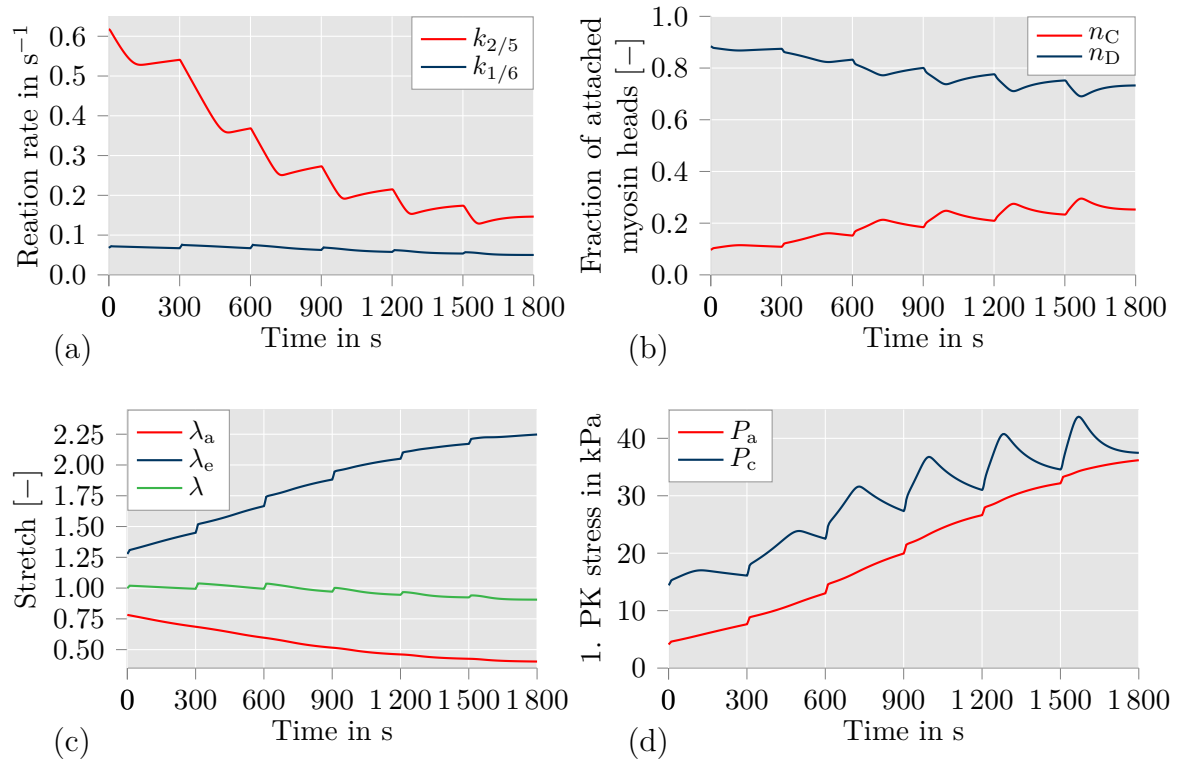


Figure 6.4: Plots of mechanical and chemical quantities over time for the simulation setup with fully active contraction at the marked node in Fig. 6.1b: (a) reaction rates $k_{1/6}$ and $k_{2/5}$; (b) fraction of attached myosin heads n_C and n_D ; (c) active stretch λ_a , elastic stretch λ_e and total stretch λ in fiber direction; (d) active stress P_a and driving stress P_c . Illustration and data is adopted from UHLMANN AND BALZANI [177].

vided for one fiber direction of the marked node in Fig. 6.1b, which is positioned at the outer diameter of the arterial ring. However, since the geometry and the orientation of the fiber angles are symmetric, all quantities are equal in both fiber directions. The evolution of the reaction rates $k_{1/6}$ and $k_{2/5}$ are illustrated in the first diagram. These quantities are considered to correspond to the activity of the enzymes MLCK and MLCP inside of SMCs. The downregulation of $k_{2/5}$ is notably dominant in comparison to the insignificant raise of $k_{1/6}$ after the stretch of the artery based on an increase of the intravascular pressure after every 300 s. This could result from the simultaneous optimization of the first and second scenario of the experiments, in which $k_{2/5}$ is considered as constant due to the ROCK inhibition from Y27632. The difference of the diameter between the passive material response and the suppressed contraction only amounts to around 10% over the entire duration of the experiment (see Fig. 6.2). The minor contraction has to be fitted by the calcium-dependent contraction mechanism. Accordingly, the calcium-independent contraction mechanism had to be predominant to capture the contractile behavior when the entire model is active which can result in a difference of up to 40% between diameter of passive and fully active material. Associated with the time-dependent change of the reaction rates, the proportions of the attached myosin heads n_C and n_D are adjusted as illustrated in Fig. 6.4b. There, n_C reaches a value of 0.25 at the end of the pressure phase with 120 mmHg. Consequently, a considerable increase of n_C is still possible which raises the driving stress P_c proportionally (see Fig. 6.4d) and leads to a higher contraction of the artery.

In Fig. 6.4c, the evolution of the elastic stretch λ_e , the active stretch λ_a , and the total stretch λ are shown. The increase of the elastic stretch λ_e can clearly be identified which constitutes a crucial input parameter to achieve a significant contraction of the arterial wall. At the end of the simulation, λ_e reaches a value as high as 2.25. An additive split of the stretch λ into an active and a passive part would have led to a negative value for the active stretch λ_a which should be considered non-physical. This was prevented by applying the multiplicative decomposition of Eq. (5.13). Furthermore, it can be observed that the elastic stretch λ_e adjusts similarly to the total stretch λ during the increase of the intravascular pressure after every 300s while the active stretch λ_a decreases consistently. This behavior corresponds to the implementation choice as discussed in Section 5.3 in which the changes of the total stretch λ are applied to the intermediate value of the elastic stretch $\lambda_{e,n}^{(f)*}$ (see Eq. (5.40)) before the evolution equation for the active stretch λ_a is solved. In the last diagram, the evolution of the active stress P_a and the driving stress P_c are compared. The decrease of the active stretch λ_a occurs as long as the driving stress P_c is larger than P_a . At the end of the last three pressure steps, both values are almost equal which results in a deceleration of the contraction. The visible decrease of P_c corresponds to the increase of $k_{2/5}$ which is shown in Fig. 6.4a. As the sum of n_C and n_D is nearly constant, the increase of P_a is primarily caused by the decrease of λ_a (which also depends on the difference between P_c and P_a). In consequence, it can be concluded that the evolution of the dephosphorylation is predominant for the contraction of the SMCs in the proposed model which corresponds with the biological state of art (see Section 2.2.3). However, a more distinct impact of the stretch on the calcium concentration and, correspondingly, on the initial increase of the reaction rates $k_{1/6}$ could be expected after an increase of the intravascular pressure. Nonetheless, three contraction mechanisms can be identified in the proposed model:

1. Stretch-dependent increase of Ca^{2+} concentration expressed in $k_{1/6}$,
2. Stretch-dependent suppression of MLCP activity expressed in $k_{2/5}$, and
3. The mechanical reaction of the contracting SMCs via the active stretch λ_a .

All of them should be considered to produce a reliable mechanical response of SMCs in muscular arteries.

6.2 Application of Pressure Waves in an Artery

For the investigation of the ability of the proposed model to describe the active contraction of arterial walls under a load scenario which is more comparable to regular blood, simple intravascular pressure waves were defined. These pressure waves are meant to mimic the idealized heart-beat-like variations of the pressure. As described in Section 2.2 and shown in the experimental data by JOHNSON ET AL. [94], the diameter of medium and smaller muscular arteries decreases when the blood pressure increases based on the contraction of vascular SMCs (see also BLUM ET AL. [20] for in vivo experiments). This functionality enables arteries to build a resistance towards the blood flow while the blood pressure is increased which occurs during high body activity. Based on the location of smaller arteries, the resistance regulates the blood

flow towards inner organs which do not require higher amounts of blood. Instead, the increased volume of oxygen-rich blood, which is pumped into the blood cycle by the heart, is actually reaching the active muscles. In consequence, a reliable mechanical model for the contraction of muscular arteries should be able to provide a comparable decrease of the arterial diameter in numerical simulations in which the pressure waves are increased to mimic the higher body activity.

In the numerical simulations here, the geometry, mesh and Dirichlet boundary conditions of the arterial ring remain as described in Section 6.1. Fig. 6.5a shows the load protocol which is used for the entire simulation and Fig. 6.5b illustrates the applied pressure waves. The load protocol can be separated as follows:

1. Linear increase of constant pressure from 0 mmHg to 80 mmHg (0-1 s),
2. Holding of constant pressure of 80 mmHg (1-2000 s),
3. Application of pressure waves with 120/80 mmHg (2000-3000 s),
4. Linear increase of pressure waves to 180/120 mmHg (3000-3010 s),
5. Application of pressure waves with 180/120 mmHg (3010-3400 s),
6. Linear decrease of pressure waves to 120/80 mmHg (3400-3410 s), and
7. Application of pressure waves with 120/80 mmHg (3410-4200 s).

The pressure values are chosen as suitable values for the blood pressure of rats in low and high activity which have comparable blood pressure to human beings (see, e.g., Table 2 in [185]). Nonetheless, it has to be noted that the measurement of blood pressure is performed in large elastic arteries where the blood pressure can be assumed to be slightly higher than in medium muscular arteries such as the middle cerebral artery of the rat. In BLANCO ET AL. [19], numerical simulations were performed to estimate the blood pressure in different arteries of the human brain. Based on these simulations, a 15% lower blood pressure in the middle cerebral artery than in large elastic arteries can be assumed as reasonable. However, ideal values of 120/80 mmHg and 180/120 mmHg as well as a characteristic approximation of the time-dependent change of the in vivo blood pressure are sufficient to investigate the effect of a more realistic load scenario on the proposed material model.

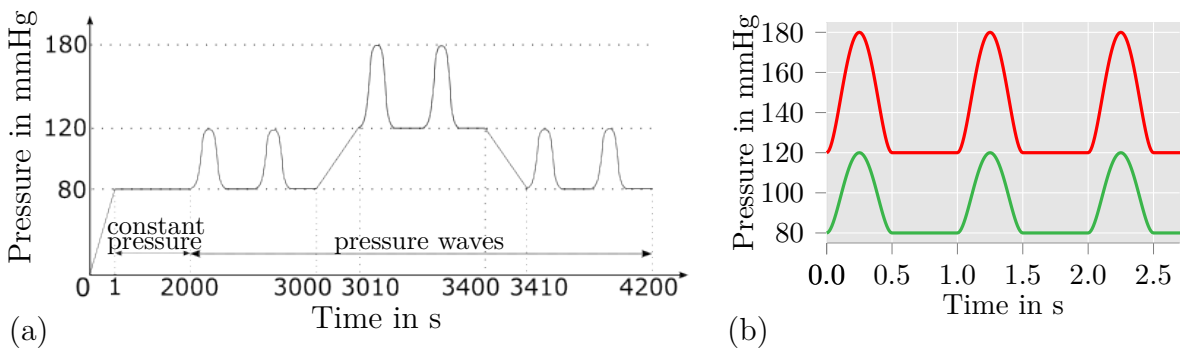


Figure 6.5: (a) Applied load protocol to arterial ring (see results in Fig. 6.6). Note that in time regions where pressure waves are applied (time > 2000 s) a number of one pressure wave per second is considered. (b) Considered intravascular pressure waves: 120/80 mmHg (green), 180/120 mmHg (red). Illustration is adopted from UHLMANN AND BALZANI [177].

To illustrate the results of the numerical simulations, the evolution of the outer diameter of the arterial ring is shown from 2800s to 4200s in Fig. 6.6a. It can be directly recognized that the diameter of the arterial ring is permanently smaller during the application of pressure waves than during the application of constant pressure values (see Fig. 6.2). This feature can be explained by the difference of the load scenario. Due to the frequent change of the pressure during the application of the pressure waves, the stretch-dependency of the chemical model part is repeatedly triggered. In consequence, the diameter of the artery is even smaller during a blood pressure of 120/80 mmHg than for a constant pressure value of 120 mmHg. Furthermore, after roughly 900s of pressure waves with a blood pressure of 120/80 mmHg (at 2900s), the arterial ring shows nearly no change towards the pressure waves anymore. This occurrence is considered repetitive material response towards the pressure waves here. Such a repetitive material response develops again at roughly 3200s in the diagram (for a blood pressure of 180/120 mmHg), and also at approximately 4100s (during the second application of pressure waves with a blood pressure of 120/80 mmHg). This indicates that the proposed model for the contraction of vascular SMCs is able to

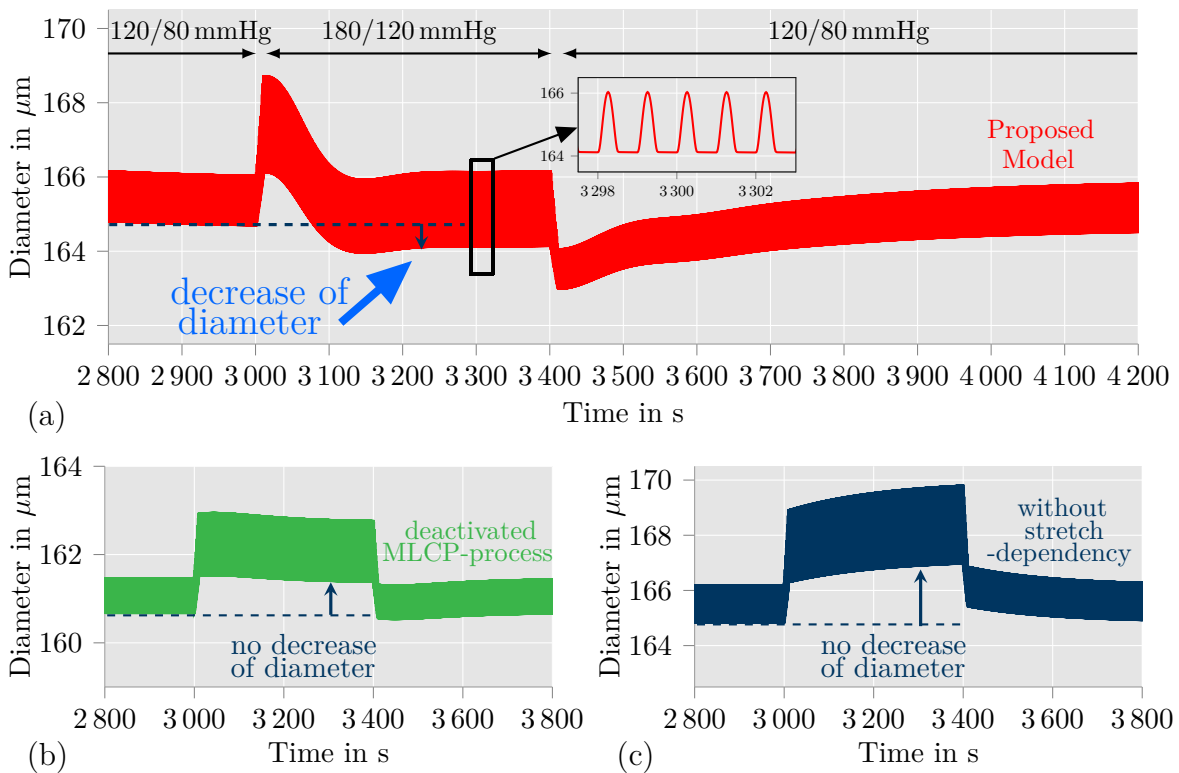


Figure 6.6: Arterial ring under intravascular pressure waves (see Fig 6.5) with different models: (a) proposed model; (b) proposed model without calcium-independent contraction mechanism ($k_{2/5}$ is constant); (c) proposed model without stretch-dependencies of the chemical model ($k_{2/5}$ and $k_{1/6}$ is constant). After an increase of the pressure from 120/80 mmHg to 180/120 mmHg, the application of the proposed model leads to a decrease of the arterial diameter (see (a) between 3100s and 3400s) which is significantly visible for the diastolic blood pressure. The reduced models in (b) and (c) cannot achieve this contractile behavior. Illustration and data is adopted from UHLMANN AND BALZANI [177].

provide a stable, repeatable material response for more complex load scenarios, such as pressure waves on an arterial ring which is represented here. This property of the material model is especially underlined by the similarity of the repetitive material response during the first and second application of pressure waves with a blood pressure of 120/80 mmHg (see before 3000 s and 4200 s in Fig. 6.6a). Another property of the proposed material can be identified by comparing the repetitive material responses for a blood pressure of 120/80 mmHg (see Fig. 6.6a, 2900 s-3000 s) and 180/120 mmHg (see Fig. 6.6a, 3200 s-3400 s). As can be seen, the highest diameters are nearly equal. Furthermore, the minimal diameter is smaller during higher blood pressure. This indicates that the blood flow regulation of muscular arteries can be replicated by the proposed model which can be considered crucial for the investigation of arteries with atherosclerotic plaque as well as for the impact of antihypertensive drugs on the stress distribution in the arterial wall.

Two additional simulations with pressure waves were executed to obtain a comparison to material models which either do not consider a stretch-dependency of the dephosphorylation process of myosin heads or exclude the stretch-dependency of the chemical model part entirely. In the first variation, the reaction rates $k_{2/5}$ were set to a constant value which corresponds to the assumption that the activity of MLCP cannot adjust to mechanical stimulation of the SMC. To receive comparable diameter values, the reaction rates were considered to be $k_{2/5} = 0.03 \text{ s}^{-1}$. In the second variation, also the stretch-dependency of the reaction rates $k_{1/6}$ was eliminated from the proposed model by setting the cytosolic Ca^{2+} concentration to a constant value of $[\text{Ca}^{2+}] = 0.25 \text{ } \mu\text{M}$. In consequence, the second variation is comparable to the model of MURTADA ET AL. [122] which does not consider a mechanical-chemical coupling. As can be seen in Fig 6.6b and 6.6c, both variations adjust notably differently to the blood pressure increase from 120/80 mmHg to 180/120 mmHg at 3000 s. The results for the model without stretch-dependency for $k_{2/5}$ (see Fig. 6.6b, 3000 s-3400 s) show a minor contraction but the diameter of the arterial ring remains significantly higher than at a blood pressure of 120/80 mmHg. The mechanical reaction of the arterial ring with the material model, which excludes the stretch-dependency of the chemical model part (see Fig. 6.6c, 3000 s-3400 s), is more comparable to a viscoelastic material model. The diameter further increases over time which is contrary to an active contraction. In conclusion, the stretch-dependency of the chemical model seems fundamental to describe the contraction of the arterial walls in simulations with heart-beat-like variations of the pressure reliably. In the proposed model, this was achieved by modeling the stretch-dependent stimulation of receptors of the cell membrane which leads to an adjustment of the phosphorylation process of myosin heads.

7 Numerical Modeling for the Automatic Calculation of Residual Stresses

In this chapter, model for the automatic calculation of residual stresses in arterial walls is defined which bases on the consideration of growth processes in the tissue. The corresponding formulation of the anisotropic growth model is already described in UHLMANN AND BALZANI [178]. Further details are considered here. The growth model is founded on the approach of kinematic growth which includes a decomposition of the deformation gradient into a growth part and an elastic part. The growth part of the deformation gradient depends on the evolution of up to three growth factors which describe an anisotropic growth process. As described and shown in Section 2.3.4, the existence of residual stresses can be demonstrated by extracting arteries from the body and dissect them into tissue strips. Based on the residual stresses inside the tissue, these strips deform and show curvatures which can be described by circumferential and axial opening angles. Additionally, the shortening of arteries after extraction displays the existence of a certain mechanical stretch in longitudinal direction which is characterized as axial prestretch. The presence of residual stresses results in an equalization of the stress values over the wall thickness. In consequence, it can be assumed that growth of the tissue maintains a mechanical homeostasis of the arterial wall [48]. The mechanical homeostasis is interpreted as a homogenization of the first and second principal stress in this thesis. For consideration of a hollow cylinder (tube), which is often used as basic geometry for numerical simulation with mechanical models of arterial walls, the direction of the first and second principal stress correspond to the circumferential and axial direction when loaded by an intravascular pressure. Accordingly, the proposed growth model aims to automatically calculate the residual stresses which result in a homogenization of the first and second principal stress (circumferential and axial stress in a hollow cylinder). To acquire a completely automatic calculation, three different aspects have to be considered:

1. The growth directions,
2. The drive of the growth in each direction, and
3. The stopping criterion for the growth process.

For the determination of reliable growth directions, simulations results from the dissertation of ZAHN [202] are taken into account. In this dissertation, Zahn focused on the identification of a mathematically optimal kinematic growth process which included various combinations of growth directions defined as eigenvectors of the elastic part of the Mandel stress. The investigation showed that a combination of growth in radial and axial direction results in a minimal change of the volume during the homogenization of the circumferential and axial stress. For the definition of the drive of the growth, stretches or stresses can be regarded. Based on investigations of growth models in other publications (see [105], [170], [38]), it is significantly advantageous to consider stresses as driving forces. Related to this conclusion, principal stresses are applied as driving forces in the growth model of this thesis. For the drive of the growth in simulations presented here, Zahn's findings are taken into account again where the trace and the second principal Mandel stress of the elastic part were optimal as driving forces.

However, including the definition of a reliable stopping criterion, the elastic part of the Mandel stress seems to be suboptimal as stress quantity. The homogenization of the stresses is evaluated for the Cauchy stresses of the tissue. Since the elastic part of the Mandel stress is not directly proportional to the Cauchy stresses, the stopping criterion cannot be defined as dependent on the elastic part of the Mandel stress at a material point to result in a reliable homogenization of the stresses over the wall thickness. Instead, the Cauchy stress is considered directly as driving force in the proposed model. Since growth models are supposed to replicate the actual growth process of arterial tissue, the stopping criterion cannot be dependent on an evaluation with respect to the entire structural problem of the simulation. Protein synthesis as well as proliferation of cells depend on local stimulation which can be mechanically initiated (see Section 2.3). In consequence, the stopping criterion should be related to a local mechanical quantity. For the proposed model, the evolution of growth factors is defined to reach convergence values for the part of the Cauchy stress which are considered as corresponding driving forces. Accordingly, the velocity of the growth process at a material point decelerates automatically the closer the driving force is to the convergence value. This means that the growth model can remain activated even after a homogenization of the Cauchy stress is already achieved and will not evoke new disturbances in the stress distribution. This is not outright possible with the Mandel stress as driving force of the growth process. Based on this feature, the combination of the proposed growth model with an active material model is applicable, since the growth velocity can be adjusted towards the more sensitive time-dependency of the active material response. Simulation results for a combination of the proposed growth model with the material model for the contraction of vascular SMCs will be demonstrated in Chapter 9.

In the following section, the development of modeling of residual stresses in biological tissue over the last few decades is presented. This is mostly focused on models with kinematic growth and constraint mixture theory, but also analytic approaches as well as biological modeling of the growth process are included. Afterwards, the proposed growth model is described in detail. Since kinematic growth is considered for this model, the corresponding multiplicative split of the deformation gradient and the changes to the balance equations from Section 3.3 are presented. Eventually, the numerical solution for the evolution of the growth factors and the implemented algorithm for the calculation of the material response is presented.

7.1 State of the Art: Residual Stresses

Various approaches can be applied to include residual stresses in the tissue of the arterial wall for mechanical calculations. The most straightforward approach constitutes the replication of the bending in circumferential direction which leads primarily to an equalization of the stresses in circumferential direction. For this approach, the referential state of the geometry contains an opening angle which is closed in an initial bending deformation prior to the application of external load [34]. An application of this method is described in HOLZAPFEL ET AL. [80] where a hollow cylinder is considered as presentation of an idealized geometry of the arterial wall. An extended method for the closure of the artery is formulated in BALZANI ET AL. [9] which allows the inclusion of residual stresses in arbitrary geometries. While the replication of an opening

angle of the arterial wall in circumferential direction involves the crucial part of residual stresses, the opening angle of an extracted tissue strip in axial direction and the axial prestretch of the artery have to be applied as well to acquire a more realistic stress distribution. Such a mathematical approach for an idealized geometry with isotropic material model was defined in HOLZAPFEL [83] considering different deformations for intima, media and adventitia correlating to experimental data from HOLZAPFEL ET AL. [82]. An extension of this mathematical method is presented in SIGAEVA ET AL. [162] which involves an anisotropic material model. However, two issues have to be considered when residual stresses are applied by replicating the deformations from extracted arterial tissue. First, the observed deformations represent only the general structural material behavior due to the residual stresses. The exact values of residual stresses at a material point cannot be determined. Accordingly, these methods are simple approaches to improve the quality of the mechanical fields, but remain inaccurate for the detailed description of the stress distribution. Secondly, the experimental data is limited. Experiments are generally performed for elastic arteries and represent only a current state of the geometry which is considerably changing over the life span of a human being (see Figure 2.12 in Section 2.3.4). In consequence, the opening angles and the axial prestretch can only be assumed or have to be optimized when experimental data is not available which is primarily the case for muscular arteries.

There are various approaches which include residual stresses in numerical simulations without a growth model, see, e.g., SCHRÖDER AND BRINKHUES [154], POLZER ET AL. [141], JOLDES ET AL. [95], UREVC ET AL. [180], and AHAMED ET AL. [2]. However, this state of the art is rather focused on the development of growth models, which (once implemented) allow a fast application to any type of geometry, calculate residual stresses directly at the material points, and, therefore, can be associated with the regular growth processes in biological tissue. Before a deeper insight into growth models is given, the distinction between growth and remodeling of the tissue has to be explained. In this thesis, the term growth is applied to volume or mass changes of the tissue while the term remodeling refers to adjustments of material properties such as the fiber direction of collagen or SMCs. In consequence, remodeling processes are not considered in the proposed growth model. However, both processes play a certain role in healing processes of biological tissue and are, therefore, not always that clearly distinguished in other publications.

Over the last decade, several papers summarized the variety of growth and remodeling models (see, e.g., AMBROSI ET AL. [5], CYRON AND HUMPHREY [39], CYRON ET AL. [41], SAEZ [150], KUHL [104] and [119]). In general, two different theories are widely accepted as foundation for new growth models: the kinematic growth theory and the constrained mixture model. Subsequently, the difference, advantages and disadvantages of both growth theories are discussed separately.

Kinematic Growth The foundation for the kinematic growth model was laid in 1994 by RODRIGUEZ ET AL. [148]. There, the deformation gradient is defined as decomposition of a growth part and an elastic part. In this concept, only the elastic part is taken into account as deformations which lead to mechanical stresses inside the tissue. The growth part can be expressed by scalar growth factors which can be transformed

into isotropic, uniaxial (in most cases radial) or anisotropic growth of the tissue. As long as the constraints to the neighboring points are not considered, the growth part cannot lead to any stresses in the material point. This state of the material is considered as intermediate configuration. The creation of a kinematic growth model can be accomplished straightforwardly by defining the growth factors, corresponding growth directions and considering the decomposition of the deformation gradient. Accordingly, the kinematic growth represents the perfect model type to investigate the efficiency of certain growth directions and the different quantities which can be considered as drive for the growth. However, in such models, growth is treated for all components of the material model equally. As shown in Section 2.3, the synthesis of elastin and collagen as well as the proliferation of SMCs is based on different processes. Even if the application of a kinematic growth model results in a perfect homogenization of the stress distribution, the final growth state constitutes an approximation which contributes to the improvement of mechanical simulations, but does not distinguish between growth processes of different components of the tissue.

A first model with kinematic growth is formulated in TABER AND HUMPHREY [170] which aimed for the replication of circumferential opening angles of the arterial wall and a homogenization of the circumferential stresses. The arterial ring was not only cut in axial direction to obtain the circumferential opening angle, but also in circumferential direction to receive an inner and an outer ring. The investigation showed, that the stresses, and not stretches, correlate well with growth in arteries. In LUBARDA AND HOGER [114], the mathematical formulation within the framework of finite deformation continuum thermodynamics for solids with growing mass is published. There, isotropic, transversely isotropic as well as orthotropic biomaterials are considered for stress-driven growth which still constitutes a reliable source for the generation of new models. Based on changes of mass during the growth process, the material has to consider changes of volume or/and changes of density. A comparison between density preservation and volume preservation during isotropic growth is presented in HIMPEL ET AL. [75] which considers the trace of the Mandel stress as driving force. This growth model was applied to geometries of patient-specific arteries in KUHL ET AL. [106]. A comparison of stress-driven isotropic, stretch-driven transversely isotropic and stress-driven transversely isotropic growth is shown by GÖKTEPE ET AL. [65] for the consideration of cardiac dilation and wall thickening. The resulting growth of the heart walls is comparable to growth which could be caused by diseases. However, in the model, growth is primarily defined to stop when the growth factors reach a predefined maximal value which occurs as long as the trace of the elastic part of the Mandel stress is larger than a critical value. Therefore, the growth model should not be considered a reliable replication of the mechanical drive for growth processes, but a suitable representation of anisotropic growth. The same definition for the growth factor was used in SÁEZ ET AL. [169] where growth in radial direction is applied to a patient-specific artery under hypertension. The simulation results show that a reduction of maximal stress values is acquired. The difference between maximal and minimal stress values over the wall thickness remains considerably large. In consequence, the growth models mentioned so far might be applicable to approximate volume changes of biological tissue, especially when diseases are considered. However, the results might not lead to a homogenization of the stress distribution.

A more promising method for the homogenization of the stresses is described in LIU ET AL. [112] where anisotropic growth is formulated for the radial and circumferen-

tial direction. The principal Cauchy stresses are used as driving forces for the growth process. The simulation results demonstrate a sufficient homogenization of the stress distribution. However, the driving forces are evaluated for the entire structure after each time step which cannot take place in biological tissue. In consequence, the method represents a suitable engineering approach to approximate residual stresses, but is not based on realistic growth processes which depend only on local events. Furthermore, axial growth is clearly visible in experimental data and should be considered in a reliable growth model.

Different combinations of anisotropic growth and remodeling of the fiber direction of collagen are presented in ZAHN AND BALZANI [203]. While this model adopts the elastic part of the Mandel stress as driving force from previous publications, a manual stop of the growth process at distinct times results in a considerable adjustment of the stresses over the wall thickness. In addition, the impact of an axial prestretch of the geometry prior to the growth process was investigated which appears to be necessary for reasonable results with this model for growth and remodeling. A more detailed analysis for more combinations of growth directions and driving forces is presented in the doctoral thesis of ZAHN [202]. In this investigation, an optimization of growth parameters was executed to obtain a homogenization of stresses after a distinct runtime of the growth and remodeling process. For this purpose, the objective function included stress values and volumetric change of the resulting geometry to evaluate the quality of the growth process. As a result, a combination of growth in radial and axial direction was considered optimal. In consequence, these growth directions and their corresponding driving forces are considered for the simulations in this chapter. It has to be noted that the applied optimization procedure for the stress distribution allowed a reduction of the axial stresses to zero which was achieved in the optimal scenario. Since the remodeling process for the fiber direction of collagen fibers is defined to depend on the principal values of stresses, the final fiber directions were entirely in circumferential direction over the wall thickness. This implies that a homogenization and reduction of stresses by an optimization of the growth procedure might not be combinable with a remodeling model which is based on principal stresses. Therefore, the definition of fiber directions is based on experimental data in this thesis.

Constrained Mixture Model Contrary to the kinematic growth model, the constrained mixture model separates not only different material parts such as elastin, collagen and SMCs, but includes a separation between constituents which were deposited at different times. Therefore, the stress-free configuration is different for each of the considered constituents of the constrained mixture model and requires an individual calculation for the mechanical response. In consequence, the constrained mixture model is advantageous for the inclusion of different growth processes of different types of tissue components and enables the consideration of old and newly grown components which experience different stretch states at the same material point. However, for the original form of this modeling approach which was described in 2002 by HUMPHREY AND RAJAGOPAL [87] the tracking of different configurations of all constituents is notably expensive and requires a well-organized history management of time-dependent parameters. Therefore, simplifications for the constrained mixture model were suggested in some publications which lead to a significant reduction of the computational time. In the variation by FAMAIEY ET AL. [52], a limitation of the number of constituents

is assumed where older components of the arterial tissue are degenerating over time. In consequence, these components are substituted over time by newly grown tissue. This variation was applied in numerical simulations which predicted the adaptation of a pulmonary autograft over an extended period. The simulation results corresponded to data obtained in experiments with sheep. In another approach by CYRON ET AL. [40], the method of the kinematic growth theory was considered. For a fixed number of different mechanical constituents, the deformation gradients are homogenized into one elastic and one growth part. With this concept, growing tissue is not represented by new components but by changes of the growth part of the deformation gradient. A numerical investigation of arteries with this growth model was performed in BRAEU ET AL. [25]. There, elastin degradation was applied which can be considered representative for aging elastic arteries. The geometry is described by a hollow cylinder. In the numerical simulations, gain parameters (growth parameters) were varied which resulted either in maintaining the geometry shape by substituting elastin with collagen or building an aneurysm.

GIERIG ET AL. [62] use the constrained mixture theory in a more biologically motivated growth model. This biological growth model is based on the previous publication of the authors (GIERIG ET AL. [61]) where the growth of the tissue is formulated depending on the activity of matrix metalloproteinase and concentration of growth factors. Damage of the tissue is applied by overstretching which results in growth of collagen fibers. In the expansion of the model [62], growth of SMCs (contractile and synthetic), fibroblasts as well as myofibroblasts is included. The growth model was applied on idealized tissue patches to observe the resulting growth behavior which included the adjustment of matrix metalloproteinase and growth factors stimulated by tissue damage. A more detailed description of the model can be found in the doctoral thesis of GIERIG [60] which also includes simulations with arteries represented by hollow cylinders. While this biological growth model constitutes a promising approach to formulate a time-wise realistic growth process which allows suitable predictions for patient-specific arteries, the considered mechanical model needs to be expanded to achieve reliable results. So far, only the passive material response is included and the material behavior is exclusively adjusted for growth of collagen. An inclusion of the mechanical behavior of vascular SMCs, which are considered during growth and are distinguished in different phenotypes, could enable time-wise realistic numerical simulations.

7.2 Multiplicative Decomposition of the Deformation Gradient for Inclusion of Growth Processes

According to the kinematic growth model by RODRIGUEZ ET AL. [148], the deformation of a body can be separated into a growth part and an elastic part which are considered in the deformation gradient \mathbf{F} by a multiplicative decomposition. This decomposition is expressed as

$$\mathbf{F} = \mathbf{F}_e \mathbf{F}_g, \quad (7.1)$$

where \mathbf{F}_g constitutes the growth part of the deformation gradient and \mathbf{F}_e is the elastic part. In this context, the intermediate configuration \mathcal{B}_i is defined as the state in which each material point can grow independently of the neighboring points. The material is

considered stress-free in this intermediate configuration as the mechanical constraints to the environment of a material point are not applied. In consequence, the compatibility condition $\nabla \times \mathbf{F} = \mathbf{0}$ is not satisfied. Fig. 7.1 illustrates the relationship between the intermediate configuration and the reference as well as current configuration. The application of the elastic part $\mathbf{F}_e = \mathbf{F}\mathbf{F}_g^{-1}$ ensures the compatibility of the deformation gradients \mathbf{F} at all material points in the current configuration \mathcal{S} . This elastic part is associated with the deformation part which leads to a mechanical response of the material. Therefore, the corresponding strain-energy density function $\Psi(\mathbf{C}_e) = \Psi(\mathbf{C}, \mathbf{F}_g)$ is formulated as dependent on the elastic part of the right Cauchy-Green tensor \mathbf{C}_e which can be obtained by

$$\mathbf{C}_e = \mathbf{F}_e^T \mathbf{F}_e = (\mathbf{F}\mathbf{F}_g^{-1})^T \mathbf{F}\mathbf{F}_g^{-1} = \mathbf{F}_g^{-T} \mathbf{F}^T \mathbf{F}\mathbf{F}_g^{-1} = \mathbf{F}_g^{-T} \mathbf{C}\mathbf{F}_g^{-1}. \quad (7.2)$$

As expressed for the entire volume change from \mathcal{B} to \mathcal{S} in Eq. (3.5), the Jacobians of the growth part and the elastic part can be formulated as

$$J_g = \det[\mathbf{F}_g] \quad \text{and} \quad J_e = \det[\mathbf{F}_e], \quad (7.3)$$

which leads to $J = \det[\mathbf{F}]$ by a sequential application. Furthermore, the time derivative of the Jacobians \dot{J}_g and \dot{J}_e can be build equally to \dot{J} in Eq. (3.20) by applying the chain rule such that

$$\begin{aligned} \dot{j}_g &= \frac{\partial J_g}{\partial \mathbf{F}_g} \cdot \frac{\partial \mathbf{F}_g}{\partial t} = J_g \mathbf{F}_g^{-T} \cdot \dot{\mathbf{F}}_g = J_g \dot{\mathbf{F}}_g \cdot \mathbf{F}_g^{-T} = J_g \text{tr}[\dot{\mathbf{F}}_g \mathbf{F}_g^{-1}] = J_g \text{tr}[\mathbf{l}_g] \quad \text{and} \\ \dot{j}_e &= \frac{\partial J_e}{\partial \mathbf{F}_e} \cdot \frac{\partial \mathbf{F}_e}{\partial t} = J_e \mathbf{F}_e^{-T} \cdot \dot{\mathbf{F}}_e = J_e \text{tr}[\mathbf{F}_e^{-1} \dot{\mathbf{F}}_e] = J_e \text{tr}[\mathbf{l}_e], \end{aligned} \quad (7.4)$$

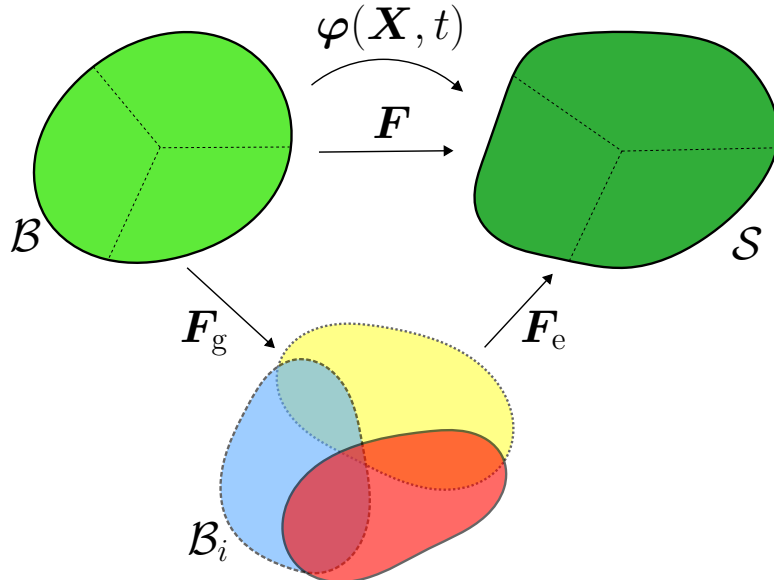


Figure 7.1: Schematic representation of the multiplicative decomposition of the deformation gradient \mathbf{F} in a growth part \mathbf{F}_g and an elastic part \mathbf{F}_e . In the intermediate configuration \mathcal{B}_i , growth is applied to material points, but no stresses are generated. In this context, the mechanical constraints to the environment of a material point is not applied in this configuration.

where $\mathbf{l}_g = \dot{\mathbf{F}}_g \mathbf{F}_g^{-1}$ and $\mathbf{l}_e = \mathbf{F}_e^{-1} \dot{\mathbf{F}}_e$ represent the growth velocity gradient and the elastic velocity gradient, respectively (see [75]).

7.2.1 Adjustment of Balance Equations for Growing Systems

The growth process of the physical body has to be accounted for in the Balance Equations (discussed in Section 3.3) as presented briefly in the following paragraphs.

Balance of Mass Growth results in a volumetric change of the physical body which corresponds to a change of mass. Therefore, the balance of mass has to be extended by the term r_g which is the mass source per time and unit volume in the current configuration (see [114]). This results in the following changes for the continuity equation of Eq. (3.30)

$$\dot{\rho} + \rho \operatorname{div}[\dot{\mathbf{x}}] = r_g = \frac{R_g^0}{J}, \quad (7.5)$$

which can be transformed to the intermediate configuration as

$$\dot{\rho}_i + \rho_i \operatorname{tr}[\mathbf{l}_g] = \frac{R_g^0}{J_g}. \quad (7.6)$$

However, for the growth processes of the body, it is assumed that the structure of the grown tissue is equal to the structure of the pre-existing tissue of the arterial wall. In consequence, densities do not change during the growth process and, hence, $\rho_i = \rho_0$ which is considered density preservation. Accordingly, the change of mass of the growing body is directly proportional to the change of volume. This means in particular that the mass change of an element is directly connected to the growth part of the deformation gradient \mathbf{F}_g and the evolution of the Jacobian J_g (see [75]) which leads to

$$R_g^0 = \rho_0 J_g \operatorname{tr}[\mathbf{l}_g] = \rho_0 \dot{J}_g. \quad (7.7)$$

Balance of Linear Momentum As shown for the local form of the balance of mass in Eq. (7.5) which considers growth, the corresponding change of mass of the body is expressed by the term r_g . Consequently, the second term of Eq. (3.32) for the time derivative of the linear momentum does not equal zero and $\dot{\mathbf{p}}$ has to be expressed as

$$\dot{\mathbf{p}} = \int_{\mathcal{B}} \rho \ddot{\mathbf{x}} J \, dV + \int_{\mathcal{B}} \underbrace{(\dot{\rho} + \rho \operatorname{div}[\dot{\mathbf{x}}])}_{=r_g} \dot{\mathbf{x}} J \, dV = \int_{\mathcal{B}} \rho \ddot{\mathbf{x}} J \, dV + \int_{\mathcal{B}} r_g \dot{\mathbf{x}} J \, dV. \quad (7.8)$$

However, the grown mass of the body has to be regarded for the acting body forces as well [114] by adding the forces \mathbf{f}_v into Eq. (3.34) such that

$$\mathbf{f} = \mathbf{f}_b + \mathbf{f}_t + \underbrace{\int_{\mathcal{S}} r_g \dot{\mathbf{x}} \, dv}_{\mathbf{f}_v} = \mathbf{f}_b + \mathbf{f}_t + \int_{\mathcal{B}} r_g \dot{\mathbf{x}} J \, dV. \quad (7.9)$$

Therefore, the derivative of the linear momentum as well as the body forces are equally altered by the grown mass and, consequently, the growth process does not affect the

balance of linear momentum.

Balance of Angular Momentum The change of mass from the growth process results in additional terms for the derivative of the angular momentum $\dot{\mathbf{h}}$ of the physical body and are also included in the resulting moment \mathbf{M} based on volumetric forces acting on the new mass. Therefore, the new forms of $\dot{\mathbf{h}}$ and \mathbf{M} can be expressed as

$$\begin{aligned} \dot{\mathbf{h}} &= \int_S (\rho \mathbf{x} \times \ddot{\mathbf{x}} + r_g \mathbf{x} \times \dot{\mathbf{x}}) dv \quad \text{and} \\ \mathbf{M} &= \int_S (\rho \mathbf{x} \times \mathbf{b}(\mathbf{x}, t) + \mathbf{x} \times \operatorname{div} [\boldsymbol{\sigma}^T] + \mathbf{I} \cdot \times \boldsymbol{\sigma}^T + r_g \mathbf{x} \times \dot{\mathbf{x}}) dv, \end{aligned} \tag{7.10}$$

with the mass source per time and unit volume r_g . Accordingly, the balance of angular momentum with $\dot{\mathbf{h}} - \mathbf{M} = \mathbf{0}$ results in

$$\begin{aligned} \dot{\mathbf{h}} - \mathbf{M} &= \int_S \left[\mathbf{x} \times \underbrace{(\rho \ddot{\mathbf{x}} - \rho \mathbf{b} - \operatorname{div} [\boldsymbol{\sigma}^T])}_{=0} - \mathbf{I} \cdot \times \boldsymbol{\sigma}^T + r_g \mathbf{x} \times \dot{\mathbf{x}} - r_g \mathbf{x} \times \dot{\mathbf{x}} \right] dv \\ &= \int_S \mathbf{I} \cdot \times \boldsymbol{\sigma}^T dv = \mathbf{0}, \end{aligned} \tag{7.11}$$

which is equal to the form without growth process. Consequently, the Cauchy stress tensor $\boldsymbol{\sigma}$ and the second Piola-Kirchhoff stress tensor \mathbf{S} are also symmetric when the growth process is included.

Balance of Energy Concerning the energy of the physical body, the time derivatives of the inner energy $\dot{\mathcal{E}}$ as well as the time derivative of the kinetic energy $\dot{\mathcal{K}}$ obtain an additional term in which the grown mass is considered. The corresponding equations for both parts of the balance of energy can be expressed as

$$\begin{aligned} \mathcal{E} &= \int_B (R_g^0 e + \dot{e} \rho_0) dV \\ \text{and } \mathcal{K} &= \int_B \left(\frac{1}{2} R_g^0 \dot{\mathbf{x}} \cdot \dot{\mathbf{x}} + \rho_0 \dot{\mathbf{x}} \cdot \ddot{\mathbf{x}} \right) dV. \end{aligned} \tag{7.12}$$

According to ZAHN [202] who follows LUBARDA AND HOGER [114], the additional term of the external energy acting on the physical body with regard to different mass is described by \mathcal{G} with

$$\mathcal{G} = \int_B \left[R_g^0 \left(\frac{1}{2} \dot{\mathbf{x}} \cdot \dot{\mathbf{x}} + e \right) \right] dV. \tag{7.13}$$

Accordingly, the total equation for the balance of energy changes to $\dot{\mathcal{E}} + \dot{\mathcal{K}} = \mathcal{P} + \mathcal{Q} + \mathcal{G}$. Since the new terms of $\dot{\mathcal{E}}$ and $\dot{\mathcal{K}}$ are equal to \mathcal{G} , the local form of the balance of energy in Eq. (3.53) remains unchanged with regard to the growing mass.

Balance of Entropy As mentioned, in the beginning of Section 7.2, the strain energy density function Ψ is defined as dependent on the elastic part of the right Cauchy-Green tensor \mathbf{C}_e . Since the elastic part of the right Cauchy-Green tensor can also

be expressed as $\mathbf{C}_e = \mathbf{F}_g^{-T} \mathbf{C} \mathbf{F}_g^{-1}$, the strain energy density function Ψ can also be transformed depending on the right Cauchy-Green tensor \mathbf{C} and the growth part of the deformation gradient \mathbf{F}_g which is necessary for the formulation of the Coleman-Noll method. Accordingly, the time derivative $\dot{\Psi}(\mathbf{C}, \mathbf{F}_g)$ can be expressed as

$$\dot{\Psi}(\mathbf{C}, \mathbf{F}_g) = \frac{\partial \Psi}{\partial \mathbf{C}} \cdot \underbrace{\frac{\partial \mathbf{C}}{\partial t}}_{=\dot{\mathbf{C}}} + \frac{\partial \Psi}{\partial \mathbf{F}_g} \cdot \underbrace{\frac{\partial \mathbf{F}_g}{\partial t}}_{=\dot{\mathbf{F}}_g}. \quad (7.14)$$

Considering the system to be isothermal and that the density of the material is preserved during the growth process then, according to Eq. (3.60), the balance of entropy can be formulated as

$$\mathcal{D} = \left[\frac{1}{2} \mathbf{S} - \frac{\partial \Psi}{\partial \mathbf{C}} \right] \cdot \dot{\mathbf{C}} - \frac{\partial \Psi}{\partial \mathbf{F}_g} \cdot \dot{\mathbf{F}}_g \geq 0. \quad (7.15)$$

The derivative of Ψ with respect to \mathbf{F}_g can be build by applying the chain rule with \mathbf{C}_e and including the corresponding substitution which was determined in Eq. (7.2). This results in

$$\frac{\partial \Psi}{\partial \mathbf{F}_g} = \underbrace{\frac{\partial \Psi}{\partial \mathbf{C}_e}}_{=\frac{1}{2} \mathbf{S}_e} \cdot \frac{\partial \mathbf{C}_e}{\partial \mathbf{F}_g} = \frac{1}{2} \mathbf{S}_e \cdot \frac{\partial (\mathbf{F}_g^{-T} \mathbf{C} \mathbf{F}_g^{-1})}{\partial \mathbf{F}_g} = \mathbf{C}_e \mathbf{S}_e \mathbf{F}_g^{-T}, \quad (7.16)$$

which contains the elastic part of the second Piola-Kirchhoff stresses \mathbf{S}_e . This equation is derived in more detail in ZAHN [202] (pp. 40, 152-153). Taking this derivative into account, the right term of Eq. (7.15) can be transformed further into

$$(\mathbf{C}_e \mathbf{S}_e \mathbf{F}_g^{-T}) \cdot \dot{\mathbf{F}}_g = (\mathbf{C}_e \mathbf{S}_e \mathbf{F}_g^{-T}) \cdot (\mathbf{l}_g \mathbf{F}_g) = \mathbf{C}_e \mathbf{S}_e \cdot \mathbf{l}_g \quad (7.17)$$

which leads to the final form of Eq. (7.15) with

$$\mathcal{D} = \left[\frac{1}{2} \mathbf{S} - \frac{\partial \Psi}{\partial \mathbf{C}} \right] \cdot \dot{\mathbf{C}} - \mathbf{C}_e \mathbf{S}_e \cdot \mathbf{l}_g \geq 0. \quad (7.18)$$

Accordingly, the elastic part of the Mandel stress $\boldsymbol{\Sigma}_e = \mathbf{C}_e \mathbf{S}_e$ is energetically conjugated to the growth part of the velocity gradient \mathbf{l}_g and, therefore, is assumed to be the corresponding driving force for the growth process of the tissue in several growth models. However, with this assumption, the homogenization of the stresses is difficult to achieve without controlling either the exact run-time of the growth model or taking the entire structure of the artery into account to evaluate the state of the stress distribution. An exemplary simulation with such a growth model is shown in Section 8.4 (see Fig. 8.8).

7.3 Anisotropic, Kinematic Growth Model based on Cauchy Stresses as Driving Force

In this section, a new kinematic growth model is introduced which is based on the simple idea that the homeostatic stress level in axial and circumferential direction can

be predefined as distinct values dependent on the Cauchy stress. Accordingly, these values constitute the convergence values for the driving force of the growth evolution. Motivated by the growth model in ZAHN AND BALZANI [203] and ZAHN [202], the combination of up to three growth scenarios is considered which take into account the eigenvectors of the Cauchy stress as growth directions. Correspondingly, the growth part of the deformation gradient \mathbf{F}_g can be multiplicatively split into three separate parts which can be written as

$$\mathbf{F}_g = \mathbf{F}_g^{(3)} \mathbf{F}_g^{(2)} \mathbf{F}_g^{(1)}, \quad (7.19)$$

where the parts $\mathbf{F}_g^{(1)}$, $\mathbf{F}_g^{(2)}$ and $\mathbf{F}_g^{(3)}$ represent the adjustment of the deformation gradient based on growth in the direction of the first, second and third eigenvector $\mathbf{n}^{(a)}$ of the Cauchy stress tensor with $a = 1, 2, 3$, respectively. Since eigenvectors are linearly independent based on their respective perpendicularity, the growth tensors $\mathbf{F}_g^{(a)}$ in Eq. (7.19) are commutative. In detail, the parts of \mathbf{F}_g are defined as

$$\mathbf{F}_g^{(a)} = \mathbf{I} + (\vartheta^{(a)} - 1) \mathbf{n}^{(a)} \otimes \mathbf{n}^{(a)}, \quad (7.20)$$

where $\vartheta^{(a)}$ constitutes the growth factor in the particular direction. Based on this definition, the parts $\mathbf{F}_g^{(a)}$ are always symmetric. The time-wise evolution of the growth factors $\vartheta^{(a)}$ is controlled by a set of evolution equations which depend on the Cauchy stress as driving force $\phi^{(a)}(\boldsymbol{\sigma})$. While in total three evolution equations can be formulated to describe the change of $\vartheta^{(a)}$ in the three different growth directions, in this chapter, only evolution equations for $\vartheta^{(2)}$ and $\vartheta^{(3)}$ are considered. This choice is based on the optimization results from ZAHN [202] where the lowest growth volume was reached during the homogenization of the stresses over the wall-thickness for growth in direction of the second and third principal stress. Since, in this optimization, the geometry of the arterial wall was represented by a hollow cylinder, the second and third eigenvector of the stress tensor are oriented in axial and radial direction. The identification of growth in these two directions as optimal procedure can be explained conceptually by visualizing the load scenario of an arterial wall. To represent the blood flow through the arterial wall in a numerical simulation with regard only to the solid structure, the mechanical load of the blood on the artery is replicated by an application of surface pressure on the inner side of the wall. Based on the primary orientation of the collagen fibers and SMCs in circumferential direction and the associated mechanical behavior of the tissue, the intravascular pressure leads to high stress values in circumferential direction. Accordingly, the stresses in circumferential direction can be considered as primarily force-controlled. In addition, it is known that axial prestretch exists in arterial walls which results generally in a displacement-controlled increase of the stress in axial direction. From a conceptual point of view, the displacement-controlled stresses in axial direction can be reduced by growth into this direction (which is the direction of the second principal stress). For force-controlled stresses, the lowering of the stress values is achieved by an increase of the surface area withstanding the applied load. In consequence, growth in radial direction has to be added for an effective adjustment of the circumferential stresses (which is the direction of the third principal stress). Therefore, only growth in the directions of $\mathbf{n}^{(2)}$ and $\mathbf{n}^{(3)}$ are applied in this chapter. The corresponding evolution equations for $\vartheta^{(2)}$ and $\vartheta^{(3)}$ are defined

as

$$\dot{\vartheta}^{(a)} = \kappa_{\vartheta}^{(a)} (\phi^{(a)} - \phi_{\text{con}}^{(a)}) \quad \text{with} \quad a = 2, 3, \quad (7.21)$$

where $\phi_{\text{con}}^{(a)}$ constitutes the value which the driving force $\phi^{(a)}$ converges to during the growth process and $\kappa_{\vartheta}^{(a)}$ is the material parameter which represents the maximal growth velocity. To define the correct scalar values with respect to the Cauchy stress $\boldsymbol{\sigma}$ as driving forces $\phi^{(a)}$, the concept for the explanation of the growth direction is taken into account again. The growth induced by $\mathbf{F}_g^{(2)}$ is supposed to adjust the displacement-controlled part of the stresses in axial direction. Therefore, the second principal Cauchy stress σ_{II} is applied for the driving force of growth in the direction of $\mathbf{n}^{(2)}$ which represents the stresses in axial direction for an idealized geometry of the arterial wall. The determination of an appropriate driving force for growth in the direction of the third principal stress is more complicated. The growth process applied by $\mathbf{F}_g^{(3)}$ is considered to reduce primarily the force-controlled stresses in direction of the first principal stress (stresses in circumferential direction). However, it does not seem credible that the biological tissue can sense stresses in one direction (circumferential) and reacts by growing into a perpendicular direction (radial). Corresponding to the driving force, which was used for the optimal growth process in ZAHN [202], $\phi^{(3)}(\boldsymbol{\sigma})$ is defined as the isotropic stress value of the Cauchy stress tensor $\boldsymbol{\sigma}$. In consequence, the driving forces $\phi^{(2)}(\boldsymbol{\sigma})$ and $\phi^{(3)}(\boldsymbol{\sigma})$ can be expressed by the equations

$$\phi^{(2)}(\boldsymbol{\sigma}) = \boldsymbol{\sigma} : (\mathbf{n}^{(2)} \otimes \mathbf{n}^{(2)}) \quad \text{and} \quad \phi^{(3)}(\boldsymbol{\sigma}) = \boldsymbol{\sigma} : \mathbf{I}, \quad (7.22)$$

where \mathbf{I} is the second order unit tensor and $\mathbf{n}^{(2)}$ is the second eigenvector of the Cauchy stress tensor. Accordingly, $\phi^{(2)}(\boldsymbol{\sigma})$ equals the second principal Cauchy stress σ_{II} .

7.3.1 Calculation of Stresses and Tangent Modulus

For the simulations in this chapter, only the hyperelastic, passive material response of the arterial wall is applied which leads to the following strain-energy density function

$$\Psi(\mathbf{C}_e) = \Psi_{\text{p, isot}}(\mathbf{C}_e) + \sum_{f=1}^2 \Psi_{\text{p, ti}}^{(f)}(\mathbf{C}_e). \quad (7.23)$$

Since Ψ only depends on the elastic part of the right Cauchy-Green tensor \mathbf{C}_e in simulations which include the kinematic growth model, the corresponding invariants of Eqs. (3.14) and (3.15) have to be adjusted to

$$\begin{aligned} I_1 &= \text{tr}[\mathbf{C}_e], & I_3 &= \det[\mathbf{C}_e], \\ I_4^{(f)} &= \mathbf{C}_e \cdot \mathbf{M}^{(f)}, & \text{and} & \quad I_5^{(f)} = [\mathbf{C}_e]^2 \cdot \mathbf{M}^{(f)}. \end{aligned} \quad (7.24)$$

The isotropic part $\Psi_{\text{p, isot}}$ and the anisotropic part $\Psi_{\text{p, ti}}^{(f)}$ remain as described in Eqs. (5.20) and (5.21), though applying the adjusted invariants. Based on the strain-energy density function, the elastic part of the second Piola-Kirchhoff stress \mathbf{S}_e can be determined. Subsequently, a pull back operation can be applied to obtain the second

Piola-Kirchhoff stress \mathbf{S} which can be expressed as

$$\mathbf{S} = \mathbf{F}_g^{-1} \mathbf{S}_e \mathbf{F}_g^{-T} \quad \text{with} \quad \mathbf{S}_e = 2 \frac{\partial \Psi}{\partial \mathbf{C}_e}. \quad (7.25)$$

Furthermore, the total derivative of the second Piola-Kirchhoff stress \mathbf{S} with respect to the right Cauchy-Green tensor \mathbf{C} results in the tangent modulus \mathbb{C} which is formulated as

$$\mathbb{C} = \underbrace{2 \frac{\partial \mathbf{S}}{\partial \mathbf{C}}}_{\mathbb{C}^e} + 2 \underbrace{\sum_{a=2}^3 \frac{\partial \mathbf{S}}{\partial \vartheta^{(a)}} \otimes \frac{\partial \vartheta^{(a)}}{\partial \mathbf{C}}}_{\mathbb{C}^g}, \quad (7.26)$$

where the elastic part and the growth part are labeled as \mathbb{C}^e and \mathbb{C}^g , respectively. Similar to the determination of \mathbf{S} , the elastic part of the tangent modulus in the intermediate configuration \mathbb{C}_i^e has to be build first and, subsequently, pulled back into the reference configuration to obtain the elastic part \mathbb{C}^e . The according equations are

$$\mathbb{C}^e = (\mathbf{F}_g^{-1} \boxtimes \mathbf{F}_g^{-1}) : \mathbb{C}_i^e : (\mathbf{F}_g^{-T} \boxtimes \mathbf{F}_g^{-T}) \quad \text{with} \quad \mathbb{C}_i^e := 2 \frac{\partial \mathbf{S}_e}{\partial \mathbf{C}_e}, \quad (7.27)$$

where the operator \boxtimes constitutes a form of a dyadic product between two second order tensors which leads to the following fourth order tensor in index notation $A_{ij} \mathbf{e}_i \otimes \mathbf{e}_j \boxtimes B_{kl} \mathbf{e}_k \otimes \mathbf{e}_l = A_{ik} B_{jl} \mathbf{e}_i \otimes \mathbf{e}_j \otimes \mathbf{e}_k \otimes \mathbf{e}_l$. The growth part of the tangent modulus \mathbb{C}^g depends on the derivative of the growth factors $\vartheta^{(a)}$ with respect to \mathbf{C} . Accordingly, this derivative results only in a second order tensor with non-zero coefficients, if the growth factor $\vartheta^{(a)}$ depends on the right Cauchy-Green tensor \mathbf{C} . This is only the case when the evolution equation of the growth factor $\vartheta^{(a)}$ is solved by an implicit procedure such as the backward Euler integration scheme. However, the proposed kinematic growth model is primarily applied to automatically calculate the residual stresses which enable reliable mechanical simulations with realistic stress distributions. The temporal evolution of the residual stresses during the application of the growth model does not matter in particular. The final result for the residual stresses does not depend on the time step width Δt or even on the values chosen for the growth velocity parameters $\kappa_y^{(a)}$ as long as Δt is small enough to allow a robust and stable simulation. This property of the kinematic growth model is demonstrated in simulations in Section 8.4 (see Fig. 8.9a). Therefore, the application of the forward Euler integration scheme is sufficient for the evolution equation (7.21) which not only allows a straightforward implementation of the growth model, but also results in $\partial \vartheta^{(a)} / \partial \mathbf{C} = \mathbf{0}$ and, consequently, $\mathbb{C} = \mathbb{C}^e$.

7.4 Numerical Implementation

The proposed kinematic growth model was implemented into *FEAP*. Hence, the growth model can be combined later (see Chapter 9) with the active material model which was described in Chapter 5. As mentioned above, the evolution equations for the growth factors $\vartheta^{(a)}$ in Eq. (7.21) are solved with a forward Euler integration scheme. This implies that the function for the new value $\vartheta_{n+1}^{(a)}$ at the current time t_{n+1} does not depend on the new value $\vartheta_{n+1}^{(a)}$ itself. According to the description of the backward Euler integration scheme in Eq. (5.25) of Section 5.3, the general formulation for the

forward Euler method can be transformed to the solution

$$y_{n+1} = y_n + f(y_n(t_n)) \Delta t, \quad (7.28)$$

where y_{n+1} and y_n are the values of the current and last time step, the function $f(y_n(t_n))$ is the evolution equation which depends on the last time step and the time step width is expressed as $\Delta t = t_{n+1} - t_n$. Applying this equation to calculate the growth factor $\vartheta_{n+1}^{(a)}$ results in

$$\vartheta_{n+1}^{(a)} = \vartheta_n^{(a)} + \kappa_{\vartheta}^{(a)} (\phi_n^{(a)} - \phi_{\text{con}}^{(a)}) \Delta t, \quad (7.29)$$

where the Cauchy stresses $\boldsymbol{\sigma}_n$ of the last time step t_n are considered. Since the Cauchy stresses $\boldsymbol{\sigma}_n$ are already known at the end of the last time step and no other variables are necessary to compute $\vartheta^{(a)}$, the updating of $\vartheta_n^{(a)}$ to $\vartheta_{n+1}^{(a)}$ is already executed at the end of time step t_n . This is an usual procedure for the implementation of the explicit Euler method. An updating of $\vartheta^{(a)}$ at the beginning of the current time step t_{n+1} would require to numerically store $\boldsymbol{\sigma}_n$ as a history parameter.

Fig. 7.2 illustrates the implemented algorithm for the growth model. The algorithm to compute the second Piola-Kirchhoff stresses \boldsymbol{S}_{n+1} and the tangent modulus \mathbb{C}_{n+1} begins with a calculation of the current growth part of the deformation gradient $\boldsymbol{F}_{g,n+1}$ which can then be used to obtain the elastic part of the right Cauchy-Green tensor $\boldsymbol{C}_{e,n+1}$. Subsequently, the elastic part of the second Piola-Kirchhoff stresses $\boldsymbol{S}_{e,n+1}$ can be calculated analytically by using the passive parts of Eqs. (5.41), (5.42) and (5.43) (where \boldsymbol{C} has to be substituted with \boldsymbol{C}_e). The elastic part of the tangent modulus in the inter-

Input	: \boldsymbol{F}	
Compute	\boldsymbol{C}	Eq. (3.11)
Compute	$\boldsymbol{F}_{g,n+1}^{(1)}(\vartheta_{n+1}^{(1)})$, $\boldsymbol{F}_{g,n+1}^{(2)}(\vartheta_{n+1}^{(2)})$, $\boldsymbol{F}_{g,n+1}^{(3)}(\vartheta_{n+1}^{(3)})$	Eq. (7.20)
Compute	$\boldsymbol{F}_{g,n+1}$, $\boldsymbol{C}_{e,n+1}$	Eq. (7.19), (7.2)
Compute	$I_1(\boldsymbol{C}_{e,n+1})$, $I_3(\boldsymbol{C}_{e,n+1})$	Eq. (7.24)
loop	over all fiber directions (f)	
Compute	$I_4^{(f)}(\boldsymbol{C}_{e,n+1})$, $I_5^{(f)}(\boldsymbol{C}_{e,n+1})$, $K_3^{(f)}(\boldsymbol{C}_{e,n+1})$	Eq. (7.24)
Compute	elastic stresses $\boldsymbol{S}_{e,n+1}$	Eq. (5.41)
Compute	stresses \boldsymbol{S}_{n+1} , $\boldsymbol{\sigma}_{n+1}$	Eq. (7.25), (3.25)
Compute	driving forces $\phi_{n+2}^{(1)}(\boldsymbol{\sigma})$, $\phi_{n+2}^{(2)}(\boldsymbol{\sigma})$, $\phi_{n+2}^{(3)}(\boldsymbol{\sigma})$	Eq. (7.22)
Update	$\vartheta_{n+2}^{(1)}$, $\vartheta_{n+2}^{(2)}$, $\vartheta_{n+2}^{(3)}$	Eq. (7.21)
Compute	tangent modulus \mathbb{C}_{n+1} using CSDA	Eq. (5.49)

Figure 7.2: Algorithm to calculate the second Piola-Kirchhoff stress tensor \boldsymbol{S}_{n+1} and the tangent modulus \mathbb{C}_{n+1} at the current time t_{n+1} as well as the update of the growth factors $\phi_{n+2}^{(a)}$ for the next time step t_{n+2} at a material point.

mediate configuration \mathbb{C}_i^e is obtained by performing CSDA as described in the end of Section 5.3 (see [172]). The pullback operations (see Eqs. (7.25) and (7.27)) then lead to the final coefficients of the second Piola-Kirchhoff stresses \mathbf{S}_{n+1} and the tangent modulus \mathbb{C}_{n+1} . Note that the elastic part of the tangent modulus \mathbb{C}^e equals the full tangent modulus \mathbb{C} since $\partial\vartheta^{(a)}/\partial\mathbf{C} = \mathbf{0}$. As described above, the update of $\vartheta^{(a)}$ is performed afterwards which (correctly labeled) leads to the growth factor $\vartheta_{n+2}^{(a)}$ for the next time step t_{n+2} .

8 Numerical Investigation of Growth Model and Optimization: Passive Response

For the numerical investigation of the proposed kinematic growth model in this chapter only the passive material response is considered. To obtain a general insight into the deformations and opening angles of dissected geometry parts which grew based on the growth model, predefined fields for the growth factors $\vartheta^{(a)}$ in single grow direction are defined and applied to halves of a hollow cylinder or a geometry which represents an axial strip of the hollow cylinder. While growth in direction of the first principal stress (circumferential) is not included in the growth model defined in Chapter 7, it is included in this investigation.

A crucial issue in the application of growth models is constituted by the volumetric change of the geometry. To describe the mechanical behavior of a distinct artery, the parameters of the mechanical model as well as the geometry of the arterial wall have to correspond to measurements from experiments. To match the final state of the resulting geometry, the volumetric change during the growth process has to be predicted and the referential state of the geometry has to be determined accordingly. This is difficult to achieve manually and, therefore, an optimization procedure is applied here. The objective function of the optimization leads to an adjustment of the inner and outer radii of the final version of the geometry to measurements by GANNON ET AL. [58]. Furthermore, the optimization procedure includes a fitting of the material parameters to match the mechanical behavior of the final geometry to experimental data from JOHNSON ET AL. [94] which were already used for the validation of the material model of the smooth muscle contraction in Chapter 6. For the parameter of the growth model, it is aimed for a minimal change over the entire arterial wall during the growth process.

In addition to the formulation of this optimization procedure and its results, the time-dependent evolution of the Cauchy stresses is presented for simulations which considered different growth velocities. The results demonstrate that convergence values of Cauchy stresses are always reached after a sufficiently long run-time of the proposed growth model and that they are not changing afterwards. A comparable simulation is performed with the growth model considering the elastic part of the Mandel stress as driving forces. In this simulation, a homogenization of the stresses is achieved at a distinct run-time, but it leads to further growth which disturbs the stress distribution afterwards. Subsequently, results for various additional optimizations are presented in which the fiber directions, the stretch or the growth in axial direction are changed for the numerical simulations. The results demonstrate the capability of the combination of the proposed growth model with the optimization procedure which can be applied to different artery types.

8.1 Principal Deformations of Arterial Rings based on Predefined Fields for the Growth Factors

As discussed in Section 7.1, the results of simulations with new growth models are often validated by comparing the change of the geometry from the referential state to the final state after growth to data gained in experiments in which real arteries were dissected. Results from such experiments were presented and analyzed in Section 2.3.4. Accordingly, the final state of the arterial ring after application of the growth model can be investigated for the circumferential and axial opening angles and the axial prestretch. While it can be assumed that the axial prestretch directly depends on the displacement of the artery in vivo in longitudinal direction and is adjusted by growth in this direction, it is more difficult to predict the changes of the opening angles from growth in different directions. Therefore, results from simulations with different geometries are presented in which a field for one of the growth factors $\vartheta^{(a)}$ is predefined. Accordingly, the growth process of the evolution equation in (7.21) is not applied. In these simulations, the geometry is load-free and, consequently, equals the load scenario of arterial tissue in experiments. Furthermore, the material model is assumed to be isotropic with $\alpha_1 = 12 \text{ kPa}$, $\alpha_2 = 100 \text{ kPa}$ and $\alpha_3 = 2$.

Growth in Radial Direction To illustrate the deformation of the geometry, a mesh for one half of a hollow cylinder was created which contains $1 \times 4 \times 48$ 20-node quadratic brick elements in axial, radial and circumferential direction. To allow a free deformation, only one open ending of the half ring was fixated in circumferential direction with Dirichlet boundary condition. Furthermore, nodes at one axial side of the half ring cannot move in axial direction. Nodes at the other side of the half ring are linked in axial direction which allows them only to move together at the exact same distance. For the final state of the growth factor $\vartheta^{(\text{rad})}$, the value is linearly distributed over the wall thickness from the value $\vartheta_{\text{in}}^{(\text{rad})}$ at the inner side of the wall to the value $\vartheta_{\text{out}}^{(\text{rad})}$ at the outer side. During the simulation, the growth factor $\vartheta^{(\text{rad})}$ of each integration point is developing from 1.0 to the predefined value over a time span of one second. This leads to an adjustment of the growth part of the deformation gradient $\mathbf{F}_g^{(3)} = \mathbf{I} + (\vartheta^{(\text{rad})} - 1) \mathbf{n}^{(3)} \otimes \mathbf{n}^{(3)}$ with $\mathbf{n}^{(3)}$ as unit vector in radial direction. In total, four simulations with different fields for the growth factor $\vartheta^{(\text{rad})}$ were performed with

- (a) $\vartheta_{\text{in}}^{(\text{rad})} = 1.0$ at the inner side and $\vartheta_{\text{out}}^{(\text{rad})} = 0.8$ at the outer side,
- (b) $\vartheta_{\text{in}}^{(\text{rad})} = 0.8$ at the inner side and $\vartheta_{\text{out}}^{(\text{rad})} = 1.0$ at the outer side,
- (c) $\vartheta_{\text{in}}^{(\text{rad})} = 1.2$ at the inner side and $\vartheta_{\text{out}}^{(\text{rad})} = 1.0$ at the outer side, and
- (d) $\vartheta_{\text{in}}^{(\text{rad})} = 1.0$ at the inner side and $\vartheta_{\text{out}}^{(\text{rad})} = 1.2$ at the outer side.

Accordingly, volumetric change is negative in the simulations (a) and (b), and positive in simulations (c) and (d). Furthermore, the gradient of the growth factors over the wall thickness is negative in (a) and (c), and positive in (b) and (d). The resulting deformations of geometries are illustrated in Fig. 8.1. Surprisingly, geometries in the

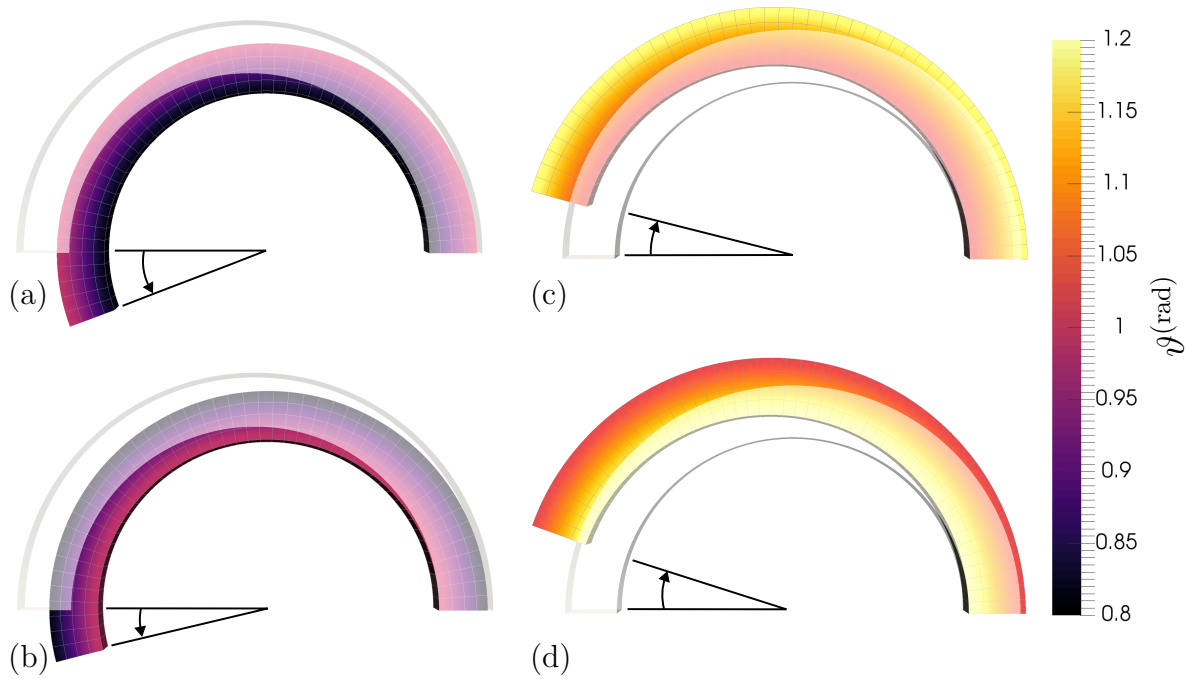


Figure 8.1: Illustration of bending of half of an arterial ring after growth in radial direction with predefined field for growth factor $\vartheta^{(\text{rad})}$. Growth factor linearly changes over the wall thickness with (a) $\vartheta_{\text{in}}^{(\text{rad})} = 1.0$ and $\vartheta_{\text{out}}^{(\text{rad})} = 0.8$; (b) $\vartheta_{\text{in}}^{(\text{rad})} = 0.8$ and $\vartheta_{\text{out}}^{(\text{rad})} = 1.0$; (c) $\vartheta_{\text{in}}^{(\text{rad})} = 1.2$ and $\vartheta_{\text{out}}^{(\text{rad})} = 1.0$; (d) $\vartheta_{\text{in}}^{(\text{rad})} = 1.0$ and $\vartheta_{\text{out}}^{(\text{rad})} = 1.2$. The parameters $\vartheta_{\text{in}}^{(\text{rad})}$ and $\vartheta_{\text{out}}^{(\text{rad})}$ label the growth factors at the inner and outer side, respectively. Arterial ring opens for positive volumetric change (see (c) and (d)), and closes for negative volumetric change, (see (a) and (b)). The gradient of the growth factor over the wall thickness has only quantitative influence over the opening angle.

simulations (a) and (b) show a closing of the arterial ring while geometry in the simulations (c) and (d) open. This means that the direction of the bending of the arterial ring for growth in radial direction does not depend on the gradient of the growth factor but on the volumetric change. This is probably connected to the nearly incompressible material behavior of the arterial tissue which is considered by the material parameters α_2 and α_3 of the isotropic material model. However, the homogenization of the stresses in circumferential direction depends on the gradient of the growth factor and not necessarily on the volumetric change as can be seen in the results of simulations in this and the following chapter (see, e.g., Fig. 8.6 and 9.2). Therefore, growth models with growth in radial direction can hardly be validated by the corresponding opening angle in circumferential direction in simulations to the opening angle of arteries measured in experiments. When growth in radial direction is considered, the opening angle in circumferential direction only indicates to which degree the volumetric change is adequate. An evaluation of the stress distribution over the wall thickness is crucial to estimate the accuracy of the growth process.

Growth in Circumferential Direction For the representation of the deformation after growth in circumferential direction, the same mesh for half of an arterial ring was used as for the radial growth with $1 \times 4 \times 48$ 20-node quadratic brick elements in axial, radial and circumferential direction, respectively. Dirichlet boundary conditions are also defined equally. The linear distribution of the growth factor $\vartheta^{(\text{cir})}$ over the wall

thickness is defined in two versions with

- (a) $\vartheta_{\text{in}}^{(\text{cir})} = 1.0$ at the inner side and $\vartheta_{\text{out}}^{(\text{cir})} = 0.8$ at the outer side and
- (b) $\vartheta_{\text{in}}^{(\text{cir})} = 0.8$ at the inner side and $\vartheta_{\text{out}}^{(\text{cir})} = 1.0$ at the outer side.

In consequence, the growth part of the deformation gradient adjusts at the integration point with $\mathbf{F}_g^{(1)} = \mathbf{I} + (\vartheta^{(\text{cir})} - 1) \mathbf{n}^{(1)} \otimes \mathbf{n}^{(1)}$, where $\mathbf{n}^{(1)}$ represents a unit vector in circumferential direction. The deformations of the geometry with different fields for the growth factor are illustrated in Fig. 8.2. As can be seen, the arterial ring opens when the growth factor is larger at the inner side $\vartheta_{\text{in}}^{(\text{cir})}$ than at the outer side of the wall $\vartheta_{\text{out}}^{(\text{cir})}$ (see Fig. 8.2a). A closing of the ring can be seen when $\vartheta_{\text{in}}^{(\text{cir})} < \vartheta_{\text{out}}^{(\text{cir})}$ (see Fig. 8.2b). The deformation of the arterial rings is similar for fields of the growth factor $\vartheta^{(\text{cir})}$ with comparable gradients over the wall thickness, but varying volumetric changes and, hence, was not further illustrated here. It should be emphasized that bending is significantly higher for equal values of the growth factor $\vartheta^{(\text{cir})}$ than of the growth factor $\vartheta^{(\text{rad})}$ (compare Fig. 8.1). As shown in the experimental results for aging arteries in Section 2.3.4, the circumferential growth seems to be minor in comparison to the radial growth of elastic arteries. However, since the opening angle changes significantly on circumferential growth, an accurate relation between the age-dependent growth in radial and circumferential direction is considerably difficult to estimate from experimental data.

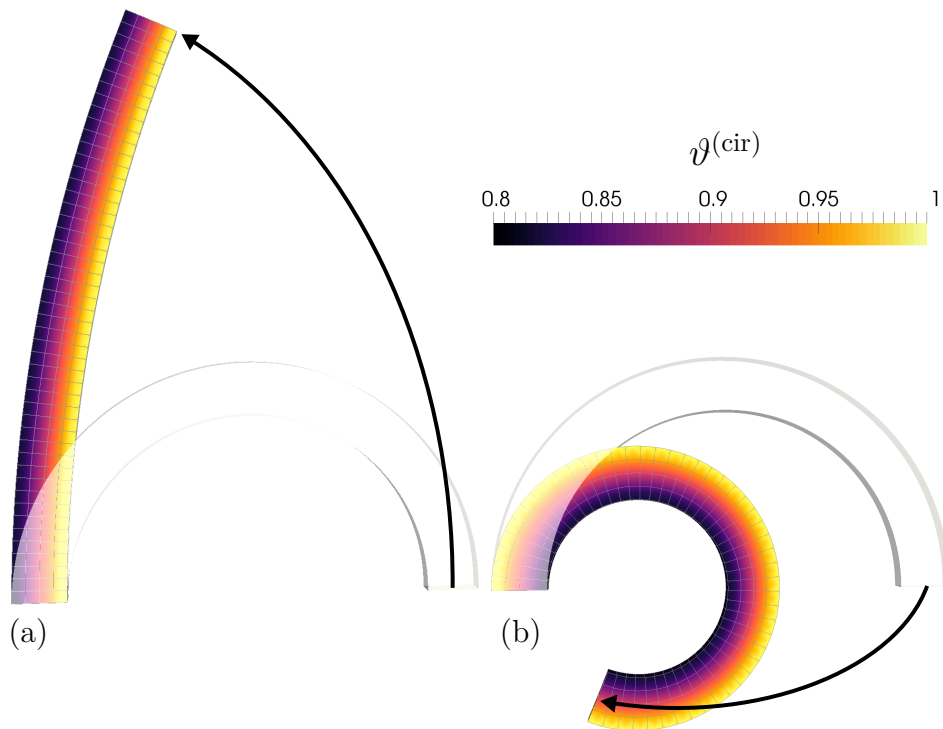


Figure 8.2: Illustration of the bending of half of an arterial ring after growth in circumferential direction with predefined field for growth factor $\vartheta^{(\text{cir})}$. Growth factor linearly changes over the wall thickness with (a) $\vartheta_{\text{in}}^{(\text{cir})} = 1.0$ and $\vartheta_{\text{out}}^{(\text{cir})} = 0.8$; and (b) $\vartheta_{\text{in}}^{(\text{cir})} = 0.8$ and $\vartheta_{\text{out}}^{(\text{cir})} = 1.0$. The parameters $\vartheta_{\text{in}}^{(\text{cir})}$ and $\vartheta_{\text{out}}^{(\text{cir})}$ label the growth factors at the inner and outer side, respectively. Arterial ring significantly opens in case (a) and closes in case (b).

Growth in Axial Direction For the investigation of bending of an axial tissue strip of the arterial wall, the mesh of this strip was defined by $20 \times 4 \times 4$ 20-node quadratic brick elements in axial, radial and circumferential direction, respectively. The mesh is curved in circumferential direction and elements are equal in size to the elements in the meshes for growth in radial and circumferential direction. Accordingly, the 4 elements in circumferential direction represent $1/24$ of an arterial ring. One axial side of the tissue strip is fixated in axial direction by corresponding Dirichlet boundary conditions. In addition, one circumferential side of the tissue strip is fixated in circumferential direction. The growth factor $\vartheta^{(\text{ax})}$ is again linearly distributed over the wall thickness. Two different scenarios were investigated in simulations with

- (a) $\vartheta_{\text{in}}^{(\text{ax})} = 1.0$ at the inner side and $\vartheta_{\text{out}}^{(\text{ax})} = 0.8$ at the outer side and
- (b) $\vartheta_{\text{in}}^{(\text{ax})} = 0.8$ at the inner side and $\vartheta_{\text{out}}^{(\text{ax})} = 1.0$ at the outer side.

The growth part of the deformation gradient is adjusted accordingly with $\mathbf{F}_g^{(2)} = \mathbf{I} + (\vartheta^{(\text{ax})} - 1) \mathbf{n}^{(2)} \otimes \mathbf{n}^{(2)}$, where $\mathbf{n}^{(2)}$ represents a unit vector in circumferential direction. Bending of the tissue strips is illustrated in Fig. 8.3. As could be expected, the geometry bends to the outside when the growth factor $\vartheta^{(\text{ax})}$ is smaller at the outside (see Fig. 8.3a) which corresponds to the experimental opening angles in axial direction. Accordingly, the tissue strip bends to the inside when $\vartheta_{\text{in}}^{(\text{ax})} < \vartheta_{\text{out}}^{(\text{ax})}$ (see Fig. 8.3b). It can be concluded that the opening angle in axial direction of elastic arteries can be represented by growth in axial direction which results from fields of the growth factor $\vartheta^{(\text{ax})}$ comparable to case (a).

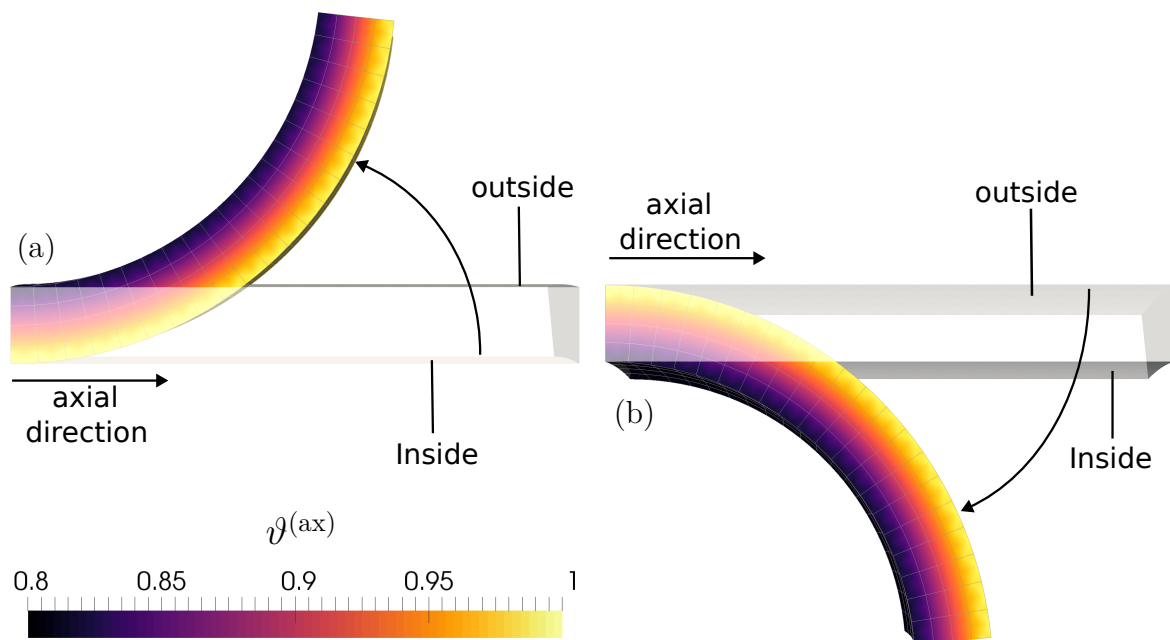


Figure 8.3: Illustration of the bending of an arterial tissue strip after growth in axial direction with predefined field for growth factor $\vartheta^{(\text{ax})}$. Growth factor linearly changes over the wall thickness with (a) $\vartheta_{\text{in}}^{(\text{ax})} = 1.0$ and $\vartheta_{\text{out}}^{(\text{ax})} = 0.8$; and (b) $\vartheta_{\text{in}}^{(\text{ax})} = 0.8$ and $\vartheta_{\text{out}}^{(\text{ax})} = 1.0$. The parameters $\vartheta_{\text{in}}^{(\text{ax})}$ and $\vartheta_{\text{out}}^{(\text{ax})}$ label the growth factors at the inner and outer side, respectively. Arterial tissue strip bends to the outside in case (a) and to the inside in case (b).

8.2 Formulation of Optimization Procedure to Obtain Accurate Geometry and Material Behavior

For a realistic description of the structural problem of an arterial wall with a finite element simulation, several aspects have to be taken into account. As a first step, a reliable material model was proposed in Chapter 5 with the ability to replicate the contractile behavior of vascular SMCs in an arterial wall as demonstrated in results of simulations in Chapter 6. Secondly, the novel kinematic growth model can be applied to automatically calculate residual stresses which result in a homogenization of the stress distribution over the wall thickness. However, as described earlier, this growth process changes the geometry of the arterial wall unpredictably. Therefore, an optimization procedure is described in this section which results in an accurate geometry after the growth process is completed. Furthermore, this optimization considers the fitting of the material parameters. To evaluate the mechanical behavior of the arterial wall, experimental data is required which describes the deformation process of the tissue under a certain loading scenario. The arterial tissue comprises residual stresses which are often not taken into account in simulations used to replicate experimental data. Accordingly, resulting material parameters of these fitting attempts are inadequate. An increase of the accuracy is achieved by applying the growth model to receive residual stresses first, before the replication of the mechanical experiments is performed with numerical simulations. In consequence, this order is applied in the simulations which are used in the optimization procedure. An additional aspect which has to be taken into account to describe the structural problem accurately, is the determination of the parameter values of the growth model which lead to residual stresses. For this purpose, experimental data for the deformation of dissected arteries as presented in Section 2.3.4 could be considered. However, such data can only be found for some artery types and is especially rare for muscular arteries. In addition, it was demonstrated in Section 8.1 that the opening angles of dissected arteries are difficult to interpret to obtain meaningful estimations for the parameter values of the growth model. Therefore, a different approach is considered here. In a material model, which does not consider growth, the parameters are fitted for the entire structure, assuming that elastin, collagen and SMCs behave equally at every material point. This assumption does not remain true when a kinematic growth model is applied since the strain-energy density function of the material model only depends on the elastic part of the deformation gradient \mathbf{F}_e . The more a growth factor $\vartheta^{(a)}$ differs from its original value of 1.0, the higher is the impact of the growth part of the deformation gradient $\mathbf{F}_g^{(a)}$ on \mathbf{F}_e (see Eq. (7.1)). Therefore, it is a central goal to minimize the impact of the growth model on the material model while, nonetheless, reliable residual stresses are predicted. For the prediction of reliable residual stresses in circumferential direction, the minimization corresponds to a minimization of the change of the growth factors $\vartheta^{(3)}$ (radial direction). This can be achieved by an optimization of the convergence value $\phi_{\text{con}}^{(3)}$ to which the driving force $\phi^{(3)}$ converges to during the growth process at the material point. In summary, the optimization procedure is implemented to establish three specific aspects to improve the accuracy of the structural description of the arterial wall:

1. Minimize the change of the growth factor $\vartheta^{(3)}$ during the growth process,
2. Match the resulting geometry after growth to experimental measurements, and

3. Replicate mechanical experimental data with numerical simulations by fitting the material parameters after the growth process is finished.

Due to this application, only two aspects remain to acquire an adequate structural problem: a reliable assumption of the orientation of the collagen fibers and SMCs as well as the determination of a reasonable convergence value $\phi_{\text{con}}^{(2)}$ for growth in axial direction. The application of a remodeling process for the adjustment of the fiber directions could be considered. However, the final direction of the fibers usually depends on the values of the principal stresses. In this thesis, the values of the principal stresses are predefined in the kinematic growth model. In consequence, the application of the remodeling process would simply lead to an adjustment of the fiber directions to an orientation which was predefined in the growth model already. In fact, it is questionable if the resulting fiber direction would be adequate for the corresponding artery. Therefore, the orientation of collagen and SMCs from experimental data is taken into account for the simulations in this thesis. Furthermore, the convergence value $\phi_{\text{con}}^{(2)}$ is predefined for every optimization to obtain reasonable axial prestretch for the arterial ring. Subsequently, details about the numerical simulations including choice of parameters and the objective function are described.

Geometry and Predefined Parameters The geometry of the arterial ring is described by a hollow cylinder with $1 \times 4 \times 96$ 20-node quadratic brick elements in all simulations of this chapter as well as Chapters 9 and 11. An example for the corresponding geometry is illustrated in Fig. 8.4a. Due to results from simulations in previous publications, the mechanical contribution of the adventitia can be neglected (see, e.g., [179]). Therefore, only the media is taken into account for simulations in this thesis. For a reliable result from the growth model, the convergence values $\phi_{\text{con}}^{(2)}$ and $\phi_{\text{con}}^{(3)}$ of the growth method have to be selected appropriately. This requires consideration of the load scenario which the investigated artery experiences in vivo. For the mechanical modeling of the arterial wall, the same experimental data from JOHNSON ET AL. [94] are taken into account as used in Chapter 6 for the validation of the active material model. Accordingly, the artery in the simulations is considered a

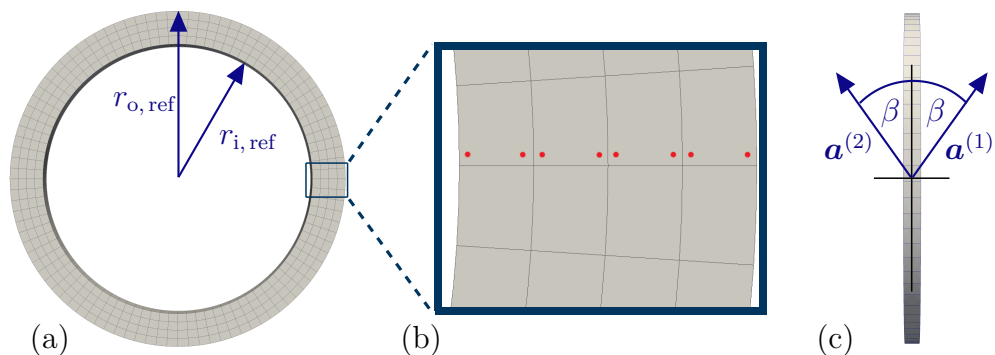


Figure 8.4: Detailed visualization of the mesh of the arterial ring. (a) The mesh in the referential state with the inner and outer radii, $r_{i, \text{ref}}$ and $r_{o, \text{ref}}$. (b) A magnified cutout of the wall with marks at the positions of the Gauss points which were used to illustrate results in Figs. 8.6, 8.8, 8.9, 8.10, 9.2, C.1 and C.2. (c) The fiber vectors $\mathbf{a}^{(1)}$ and $\mathbf{a}^{(2)}$ and the corresponding fiber angle β illustrated in the plane of longitudinal and circumferential direction. Illustration is adopted from UHLMANN AND BALZANI [178].

middle cerebral artery of a rat. A blood pressure of 100/60 mmHg can be assumed for a healthy rat at rest (see, e.g., [134]). Regarding the activity of the rat over the day, a static pressure value of 120 mmHg constitutes a realistic mean value for the dynamically changing blood pressure. Since the middle cerebral artery is located in the brain of the rat and, therefore, protected from additional displacements caused by body movement, dynamical changes of the axial stretch have not to be accounted for in numerical simulations. Instead, a constant value for the axial prestretch is sufficient which was identified as a value of 1.1 in experimental investigations of the middle cerebral artery of a rat (see [15]). This value will be considered in the optimization which includes the active material response in Chapter 9 and fits the structural problem of the artery most reliably. However, in this chapter, the combination of the growth model and optimization procedure is supposed to be tested to its limits. For larger arteries of aged humans (such as aorta, superficial femoral artery or iliac artery), in vivo axial prestretches lower than 1.0 were measured (see [92], [85], [157], [164]). To imply this shortening of the artery after the in situ cut also in numerical simulations, the most expensive (but still considerable) numerical scenario is tested in which the axial stress is decreased to a convergence value of $\phi_{\text{con}}^{(2)} = 0$ kPa. For this scenario, large values for the growth factor $\vartheta^{(2)}$ are required which lead to an expansion of the arterial ring in axial direction. This might lead to an axial prestretch lower than 1.0. To which degree an additional displacement of the artery in axial direction influences this part of the growth model is presented in Section 8.5. For the first example of the optimization (see Section 8.3), the axial displacements of the nodes at the axial ends of the arterial ring are set to zero.

Minimal Change of Radial Growth Factor For the minimization of the change of $\vartheta^{(3)}$ over the wall thickness, first simulations with $\phi_{\text{con}}^{(3)} = \bar{\sigma}_{\text{tr}}$ already showed promising results. There, $\bar{\sigma}_{\text{tr}}$ is the mean value of the trace of the Cauchy stresses $\text{tr}(\boldsymbol{\sigma})$ over the wall thickness for the loaded geometry without growth. Therefore, the convergence value $\phi_{\text{con}}^{(3)}$ is defined as the multiplication of this mean value $\bar{\sigma}_{\text{tr}}$ with a factor w_{min} . The factor w_{min} constitutes the first parameter of the optimization which leads to a minimization of the change of $\vartheta^{(3)}$. Since the minimization of the change of $\vartheta^{(3)}$ can be interpreted as minimization of the volumetric change from $\mathbf{F}_g^{(3)}$, w_{min} can be considered a volumetric minimizer. The corresponding equations for the calculation of $\phi_{\text{con}}^{(3)}$ can be written as

$$\phi_{\text{con}}^{(3)} = w_{\text{min}} \bar{\sigma}_{\text{tr}} \quad \text{with} \quad \bar{\sigma}_{\text{tr}} = \frac{1}{n_{\text{gp}}} \sum_{g=1}^{n_{\text{gp}}} \text{tr}(\boldsymbol{\sigma})_g, \quad (8.1)$$

where $\text{tr}(\boldsymbol{\sigma})_g$ is the trace of the Cauchy stress at the Gauss point g . To acquire a reliable evaluation of $\bar{\sigma}_{\text{tr}}$, eight Gauss points were chosen which have the same position in axial direction and build an exact line from the inside to the outside of the arterial wall (see illustration in Fig. 8.4b).

Match Final Geometry to Measurements To match the final state of the geometry, after the growth process is finished, to realistic measurements of an artery, data by GANNON ET AL. [58] is taken into account (see Table 1 in the original publication). There, the ratio between wall thickness and outer radius of a middle cerebral artery of

a mouse was measured to be 0.21. It is assumed that this ratio is similar for the same artery type of the rat. During the measurement, an intravascular pressure of 15 mmHg was applied to the arterial wall. Furthermore, the solution around the artery contained no Ca^{2+} which leads to a deactivation of the contraction of vascular SMCs. To optimize the final state of the geometry, the inner and outer radius of the reference configuration of the arterial ring $r_{i,\text{ref}}$ and $r_{o,\text{ref}}$ are used as optimization parameters (see Fig.8.4a). According to the experimental setup, the final state of the geometry (after growth) is loaded by an intravascular pressure of 15 mmHg. Furthermore, only the passive material response is applied.

Fitting of Material Parameters As mentioned above, the material parameters are fitted by replicating the experimental data from JOHNSON ET AL. [94] with results from numerical simulations. A detailed description of these experiments can be found in Sections 2.2.4. In summary, a segment of a middle cerebral artery was investigated for the temporal adjustment of the outer diameter during the application of different values of intravascular pressure over a time of 300 s. There, Krebs solution around the artery was varied which results in an adjustments of the material response. In consequence, the fully active material response, a suppressed active material response and the passive material response of the arterial ring were obtained. In this chapter, only the experimental data for the passive material response is considered. The fully active and suppressed form is taken into account in the next chapter. For the replication of the data with FE simulations, the optimization used the material parameters α_1 , α_4 and α_5 as optimization parameters which describe the general mechanical behavior of elastin and collagen fibers. The additional parameters α_2 and α_3 , which control that the arterial tissue is nearly incompressible, are set prior the optimization to 100 kPa and 2, respectively.

Description of Optimization Procedure A schema of the optimization can be found in Fig. 8.5. Overall, the optimization adjusts six different parameters, namely, the volumetric minimizer w_{min} , the inner and outer radii $r_{i,\text{ref}}$ and $r_{o,\text{ref}}$, and the material parameters α_1 , α_4 and α_5 (see left box of Fig. 8.5). Equally to the fitting of the material parameters in Chapter 6, the optimization was implemented in *Python* by utilizing the library *mystic* which applies a mixture of evolution strategy and gradient method. Based on the parallelization of *mystic* and the used hardware, 40 children parameter sets were tested at the same time. To evaluate a new set of parameters, *FEAP* is called inside the *Python* script to run three sequential boundary value problems which adopt the new parameters. These simulations are executed in the following order (see also middle box in Fig. 8.5): 2(a) the growth process of the artery, 2(b) the check of the wall thickness at an intravascular pressure of 15 mmHg, and 2(c) the replication of the mechanical experiments from [94]. Since the simulations 2(b) and 2(c) have to imply the resulting geometry after growth, the final values of the growth factors $\vartheta^{(a)}$ are exported for every single Gauss point at the end of simulation 2(a). Subsequently, these values of the growth factors $\vartheta^{(a)}$ are defined as target values in the simulations 2(b) and 2(c). Over a time span of one second, the growth factors are linearly increased from their starting value of 1.0 to the final values from simulation 2(a).

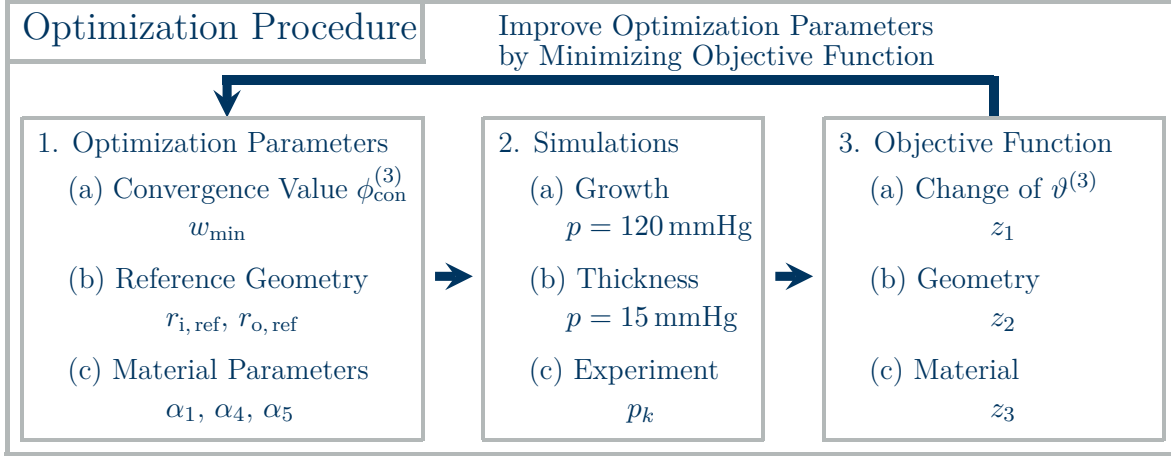


Figure 8.5: Schematic representation of the optimization procedure which is based on evolution and gradient method. Three steps are presented which result in an evaluation of a parameter set: 1. Creation of new sample of parameters based on data from earlier generations, 2.(a) Execution of growth process, 2.(b) Checking the wall thickness of the resulting geometry, 2.(c) Reproduction of mechanical experiments with simulation, and 3. Evaluating the sample based on the objective function. Illustration is adopted from UHLMANN AND BALZANI [178].

Objective Function According to the three aspects of the optimization, three different parts are defined for the objective function (see right box of Fig. 8.5). The corresponding equation with $z = z_1 + z_2 + z_3$ is formulated as

$$z = \underbrace{0.035 \sqrt{\frac{1}{n_{\text{gp}}} \sum_{g=1}^{n_{\text{gp}}} \left(\vartheta_g^{(3)} - 1 \right)^2}}_{z_1} + \underbrace{\sqrt{\left(\frac{r_{o,15} - r_{i,15}}{r_{o,15}} - 0.21 \right)^2}}_{z_2} + \underbrace{\sqrt{\frac{1}{n_{\text{data}}} \sum_{k=1}^{n_{\text{data}}} \left(\frac{d_{\text{exp},k} - d_{\text{sim},k}}{d_{\text{exp},k}} \right)^2}}_{z_3}. \quad (8.2)$$

In the first term z_1 , the change of the growth factors $\vartheta^{(3)}$ from its starting value of 1.0 is evaluated for every Gauss point g (for position of the Gauss points, see Fig. 8.4c). Here, the prefactor of 0.035 is required to balance the influence of the first part z_1 to the second and third part of the optimization process. In the second term z_2 , the inner and outer radii of the resulting version of the geometry after growth at an intravascular pressure of 15 mmHg is described by $r_{o,15}$ and $r_{i,15}$, respectively. In consequence, the ratio between the wall thickness and the outer radius is calculated which is optimal for a value of 0.21. In the last term z_3 , the parameter $d_{\text{exp},k}$ constitutes the measured outer diameter from the experiments while the arterial ring was loaded with an intravascular pressure of p_k (see Fig. 2.6b) where n_{data} is the total number of different pressure values. In the simulations of this chapter, only the passive material response is considered. The parameter $d_{\text{sim},k}$ is the outer diameter of the arterial ring in simulation 2(c) at the intravascular pressure p_k . The additive split of the three parts of the objective function enables an evaluation of the fitting of the mechanical experiments without significant influence of the respective other parts. This advantage is crucial when certain parameters or boundary conditions are varied such as the fiber direction of collagen and SMCs or the convergence value $\phi_{\text{con}}^{(2)}$. Such variations of the simulation might have a considerable impact on the part z_1 of the objective function. However, due to the additive split of the objective function, the quality of the fitting

of the material parameter in part z_3 remains comparable for different variations.

8.3 Results for First Application of Optimization

Including the information about the optimization procedure from the previous section, which comprises the description of the mesh, the geometry, certain boundary conditions, and the determination of values for material as well as growth model parameters, the results of the first application of this optimization is presented here. As mentioned above, the axial displacement of the nodes of the arterial ring is set to zero. Based on the load scenario with intravascular pressure and the symmetry of the geometry, displacements in circumferential direction are not expected. In consequence, the nodes of the arterial ring will only react by radial displacements to the load scenario. In the simulations for the optimization presented here, the orientation of the collagen fibers is determined by considering measurements from FINLAY ET AL. [54], where the fibers of arteries in the human brain were investigated. The angles between the fiber orientation and the circumferential direction of the arterial wall reached values up to 13° . Comparable to the simulations in Chapter 6, the corresponding angle β between circumferential and longitudinal direction is defined as a gradient over the wall thickness which starts with 10° at the inner side and ends with 20° at the other side of the arterial wall (see Fig. 8.4c). Since larger (and especially elastic) arteries comprise fibers with considerably higher angle, the impact of a variation of β on the optimization procedure and the new kinematic growth model is investigated in Section 8.5. In all simulations of the different optimizations of this chapter, the growth velocity factors are chosen to be $\kappa_{\vartheta}^{(2)} = 10^{-4}(\text{s} \cdot \text{kPa})^{-1}$ and $\kappa_{\vartheta}^{(3)} = 10^{-4}(\text{s} \cdot \text{kPa})^{-1}$. However, these growth velocity factors could be chosen arbitrarily and the final result for stress distribution and the corresponding residual stresses would not differ as long as the run-time of the growth model is sufficiently long (see Fig. 8.9 in Section 8.4).

The results of the optimization with regard to the stresses and the accuracy of the material behavior are illustrated in Fig. 8.6 and 8.7, respectively. Fig. 8.6a and b show the distribution of the Cauchy stresses $\sigma^{(\text{ax})}$ and $\sigma^{(\text{cir})}$ in axial and circumferential direction as well as the driving forces $\phi^{(2)}$ and $\phi^{(3)}$ before (dashed lines) and after (solid lines) the growth process is applied. The Cauchy stress in direction of the second eigenvector $\sigma_{\text{gr}}^{(\text{ax})}$ (axial direction) and the corresponding driving force $\phi_{\text{gr}}^{(2)}$ reach the predefined value of 0 kPa. The minimization of the change of growth factor $\vartheta^{(3)}$ (see objective function z_2) lead to a value of 139.71 kPa for the convergence value of the driving force $\phi_{\text{con}}^{(3)}$. Accordingly, this value was reached over the entire wall thickness (see $\vartheta_{\text{gr}}^{(3)}$ in Fig. 8.6b). Consequently, the proposed kinematic growth model achieves its purpose to equalize the driving forces over the entire wall. However, the graph, which displays the distribution of the first principal stress $\sigma_{\text{gr}}^{(\text{cir})}$ (circumferential direction) in Fig. 8.6a, comprises a positive gradient. This is a result of the definition of the driving force $\phi^{(3)}$ as the trace of the Cauchy stresses at the material point which also involves the stresses in radial direction. Based on the boundary value problem, the radial stresses are equal to the intravascular pressure at the inner side of the wall (which was 120 mmHg during the growth process) and zero at the outer side of the wall. In consequence, the gradient of the radial stress over the wall thickness will

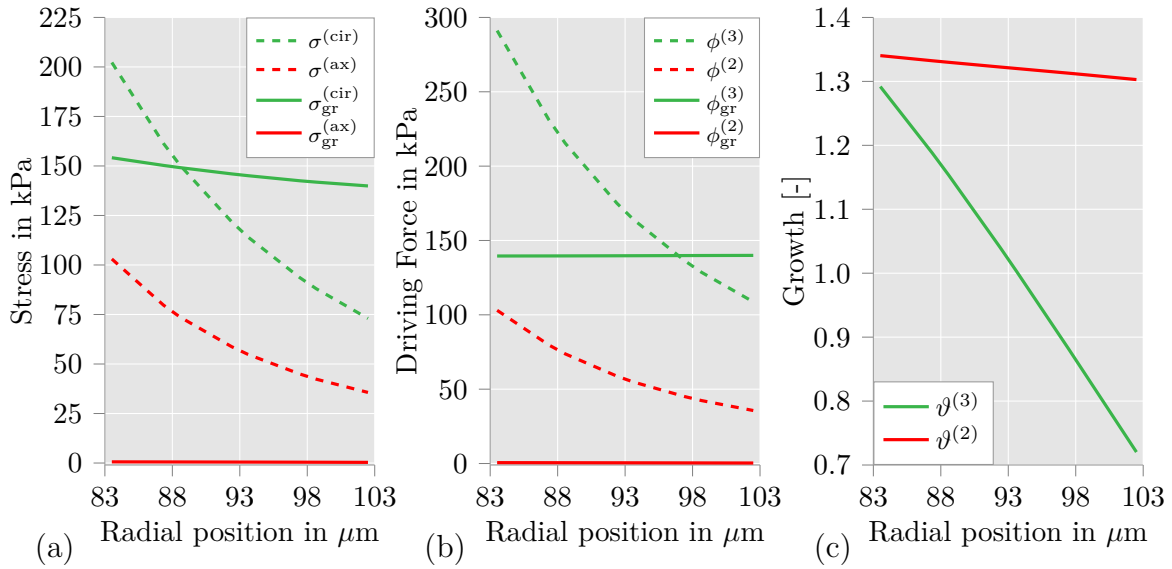


Figure 8.6: Distribution of (a) Cauchy stresses $\sigma^{(\text{ax})}$ and $\sigma^{(\text{cir})}$, (b) driving forces $\phi^{(2)}$ and $\phi^{(3)}$, and (c) growth values $\vartheta^{(2)}$ and $\vartheta^{(3)}$ in circumferential (green) and axial (red) direction over the wall thickness. Artery is loaded with an intravascular pressure of 120 mmHg. Dashed lines show results before growth, solid lines show results after growth. Gradient of the stresses over the wall thickness is significantly lower after growth. Illustration is adopted from UHLMANN AND BALZANI [178].

always be negative. When the driving forces $\phi_{\text{gr}}^{(2)}$ and $\phi_{\text{gr}}^{(3)}$ are equal over the entire wall thickness after the growth process is stopped, the circumferential stresses $\sigma_{\text{gr}}^{(\text{cir})}$ have to show a gradient with opposed sign to the radial stresses. In the application of the optimization procedure with simulations which consider only the passive material response, this gradient could still be accepted. However, the growth model is adjusted for simulations with active response in Chapter 9 where the stress values are notably smaller in circumferential direction, but equal in radial direction.

The final state of the growth factors $\vartheta^{(2)}$ and $\vartheta^{(3)}$ over the wall thickness is illustrated in Fig. 8.6c. As the growth in axial direction is not restricted in the optimization procedure, a value of 1.35 at the inner side and 1.3 at the outer side of the wall is reached for the growth value $\vartheta^{(2)}$ which is predominantly responsible for the reduction of the axial stresses $\sigma_{\text{gr}}^{(\text{ax})}$ to 0 kPa. The increase of the growth factor $\vartheta^{(2)}$ to these values over the entire wall thickness corresponds with a growth (extension) of the artery in longitudinal direction. Accordingly, the resulting axial prestretch of the arterial ring after growth is lower than a value of 1.0 which was aimed for in the simulation here by setting $\phi_{\text{con}}^{(2)} = 0$ kPa. The growth factor $\vartheta^{(3)}$ shows a value of 1.3 at the inner side and 0.7 at the outer side of the arterial wall. This shows that the minimization of the change of $\vartheta^{(3)}$ from the starting value 1.0 was successful. The inner and outer radii $r_{i,\text{ref}}$ and $r_{o,\text{ref}}$ of the arterial wall in the reference configuration were optimized to the values of 82.91 μm and 103.11 μm . This leads to a ratio between wall thickness and outer radius of 0.209997 at an intravascular pressure of 15 mmHg (simulation 2(b)) which nearly equals to the target value of 0.21 in the optimization.

The accuracy of the fitted material parameters of the arterial tissue can be estimated from the graph in Fig. 8.7a. There, the evolution of the outer diameter of the arterial

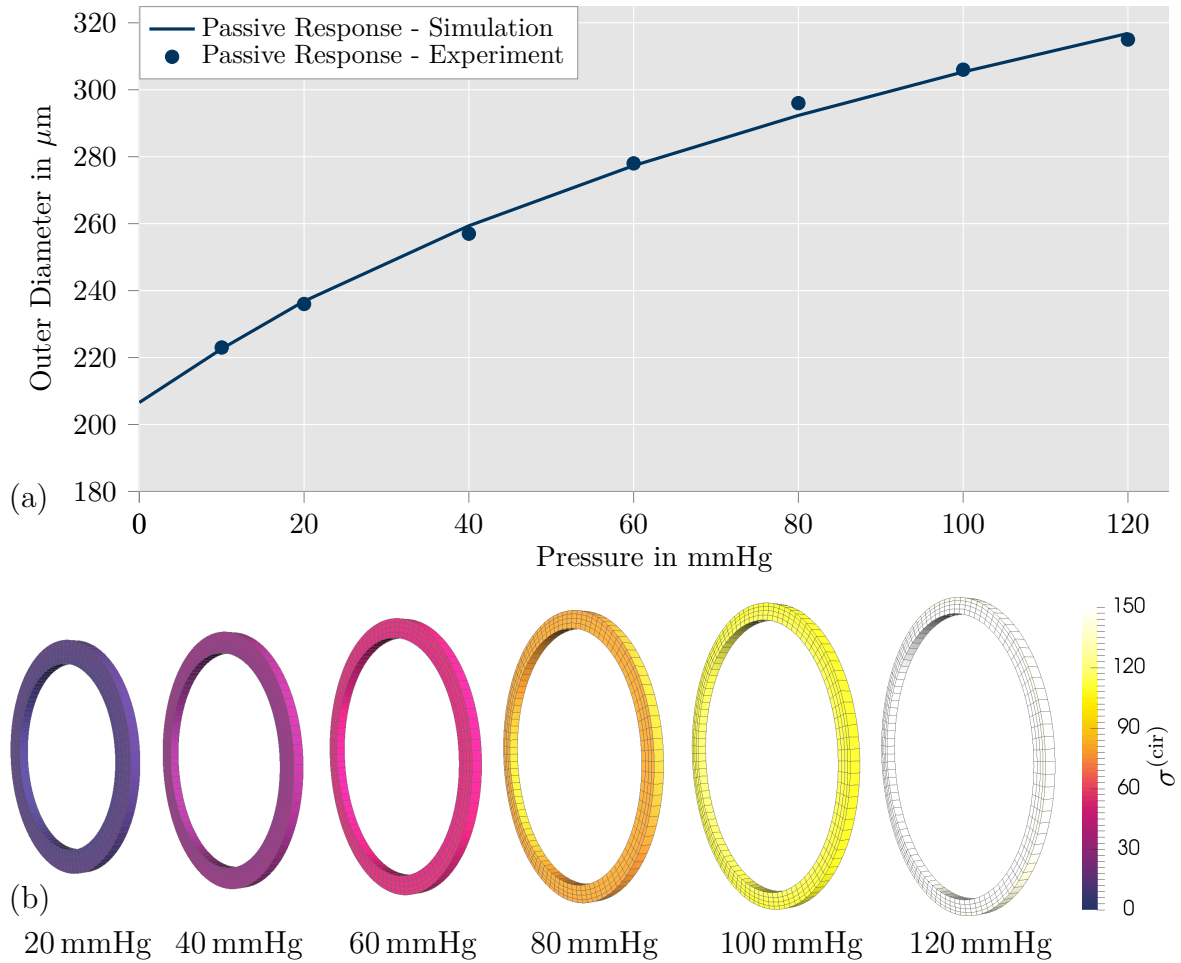


Figure 8.7: Illustration of (a) the comparison of the outer diameter of the arterial wall in simulations after growth (solid line) and corresponding experimental data from [94] (dots), and (b) the comparison of circumferential Cauchy stresses $\sigma^{(cir)}$ of the passive material response at different times of the pressure profile. The simulation results of the model nearly correspond with the experimental data. Stresses show a homeostatic distribution. Note that the stresses reach unrealistic high values. This is caused by the application of a high intravascular pressure on a muscular artery while the active response is deactivated. Illustration is adopted from UHLMANN AND BALZANI [178].

wall for increasing intravascular pressure values is shown for the simulation 2(c) and the corresponding measurements of the experiment. As can be seen, the data between simulation and experiment corresponds in the range of 0 mmHg to 120 mmHg for the intravascular pressure which demonstrates the efficiency of the optimization procedure. Furthermore, the resulting homogenization of the circumferential stresses is illustrated in Fig. 8.7b, where contour plots of the 3D arterial ring are shown for different values of the intravascular pressure. It should be noted that the stress values in the simulations here are unrealistically high. This is associated with the reduction of the material behavior to its passive part. As can be seen in the evolution of the diameter in the experiments (see Fig. 2.6), the contraction of the SMCs has a substantial influence on the material behavior of the tissue. The arterial tissue is stretched by a factor of 1.5 and higher when Ca^{2+} is excluded from the Krebs solution (which results in a deactivation of the SMCs). This stretch is considerably higher than in a physiological state of the artery and a certain damage of the tissue can be expected. However, the damage

of the tissue is not recorded or does not occur during the experiments and, therefore, cannot be considered in the material model. An inclusion of a damage model would lead to stiffer passive material in the undamaged state.

8.4 Homogenization of Stresses is Independent from exact Run-Time for Proposed Growth Model

The homogenization of the stress distribution over the wall thickness, as shown in the previous section for the proposed kinematic growth model, was already achieved by application of other growth models. One example is constituted by the previous version of the growth model of this thesis (see ZAHN [202]) which depends on the elastic part of the Mandel stress $\Sigma_e = \mathbf{C}_e \mathbf{S}_e$ as driving force. As established in Section 7.2.1, the elastic part of the Mandel stress is energetically conjugated to the growth part of the velocity gradient \mathbf{l}_g and, therefore, the application of Σ_e as driving force is founded on thermodynamic considerations. However, the dependency of the growth process on Σ_e does not allow the integration of an automatic stopping of the growth process at the material point when the stresses are homogeneous. In simulations with this model, which resulted in equal stresses over the wall thickness of the arterial ring, the exact run-time of the growth model was predefined and the parameters were optimized for this scenario. The new kinematic growth model of this thesis does not have this restriction and leads automatically to reasonable residual stresses after a sufficiently long run-time. This property is especially important, when the material model considers an additional active material part such as the contraction of SMCs. Since the growth process applied by the growth model is only abstractly time-dependent, which means that the final result for the residual stresses is of interest, but not the exact development over time, the growth velocity can be freely adjusted. This adjustment of the growth velocity does not influence the final results after an infinite run-time of the growth model. In the following, the described properties of the proposed growth model are shown through results from simulations. Furthermore, a comparable optimization of the structural problem as shown in the previous section was applied to the growth model of ZAHN [202] which uses the elastic part of the Mandel stress as driving force. To prevent misunderstandings in the following text, the two growth models are distinguished here as:

- Model **A**: kinematic growth model of this thesis ($\boldsymbol{\sigma}$ as driving force) and
- Model **B**: kinematic growth model by ZAHN [202] (Σ_e as driving force).

The main difference between model A and model B is the formulation of the evolution equation for the growth factors $\vartheta^{(a)}$ (see Eq. (7.21) for model A). These evolution equations are briefly explained for model B in Appendix B.

Based on the definition of the evolution equations in model B, the growth factors $\vartheta^{(a)}$ only increase during the growth process. Values of $\vartheta^{(a)}$ lower than 1.0 are not possible. Therefore, the prefactor in z_1 of the objective function in Eq. (8.2) would have to be reevaluated to enable a reasonable balance between the three parts z_1 , z_2 and z_3 . However, for the comparison of model A and B, the fitting of the material parameters to experimental data and a reliable geometry of the arterial wall are sufficient for model

B to display the differences. Accordingly, the first part of the objective function z_1 is not considered for model B. Furthermore, there are no convergence values in the evolution equations for the growth factor of model B (see Eq. (B.1)). Therefore, the optimization parameter w_{\min} is not considered (see 1(a) in Fig. 8.5). Instead, the minimization of the absolute values of the gradient for the stresses over the wall thickness is applied. For this purpose, the optimization stopped the growth process of model B when the deviation of the stresses increased. For the evaluation of the deviation of the stresses, the same eight Gauss points as in the optimization of model A were used which are marked in Fig. 8.4b. To enable the optimization, the parameters $\vartheta_{(2)}^+$, $\vartheta_{(3)}^+$, $\kappa_{\vartheta, (2)}^+$ and $\kappa_{\vartheta, (3)}^+$ are included in the list of optimization parameters. In Fig. 8.8a, the resulting stress distribution for the optimized parameters of model B are shown. The corresponding values of the growth factors are illustrated in Fig. 8.8b. The final values of the optimized parameters are listed in Table 8 in the Appendix B. The stresses $\sigma_{\text{gr}}^{(\text{ax})}$ and $\sigma_{\text{gr}}^{(\text{cir})}$ (first and second principal Cauchy stress) are homogenized over the wall after an optimal growth time (solid lines). This time point was used to evaluate the quality of the optimized material parameters. The corresponding simulation results match the experimental data which can be seen in Fig. B.1 of Appendix B. Furthermore, the optimization leads to a value of 0.20995 for the ratio between wall thickness and the outer radius at an intravascular pressure of 15 kPa which is nearly equal to the target value of 0.21. Without stopping the growth process, when the deviation of the stresses increase, the growth process would continue as long as the evolution equation for the growth factors does not equal zero. Based on its definition, the evolution equation in model B can only equal zero when the growth factors $\vartheta^{(a)}$ reach their maximal val-

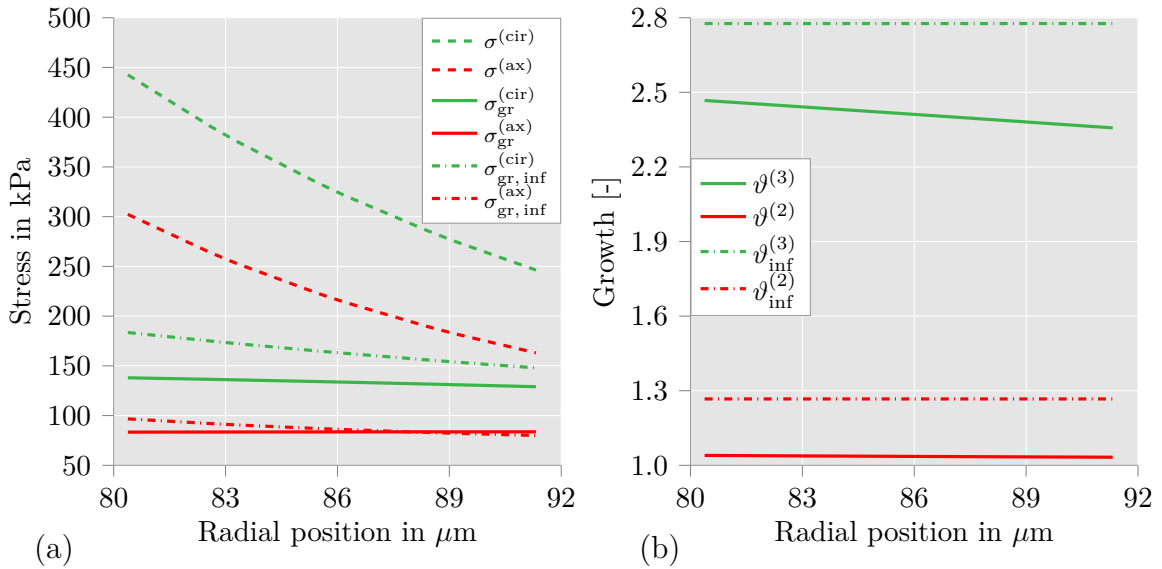


Figure 8.8: Distribution of (a) Cauchy stresses $\sigma^{(\text{ax})}$ and $\sigma^{(\text{cir})}$, and (b) growth values $\vartheta^{(2)}$ and $\vartheta^{(3)}$ in circumferential (green) and axial (red) direction over the wall thickness for the passive material response with application of growth model B which is based on the elastic part of the Mandel stress Σ_e (see [202]). Artery is loaded with an intravascular pressure of 120 mmHg. Dashed lines show results before growth, solid lines show results after optimal time for growth, dashed-dotted lines show results after infinite time of growth. Gradient of the stresses is significantly decreased for the optimal growth time. Gradient increases afterwards and reaches the depicted values after infinite time. Illustration is adopted from UHLMANN AND BALZANI [178].

ues $\vartheta_{(2)}^+$ and $\vartheta_{(3)}^+$ which occurs after a longer run-time. The resulting stress distribution for the case of $\vartheta_{(2)} = \vartheta_{(2)}^+$ and $\vartheta_{(3)} = \vartheta_{(3)}^+$ are illustrated by the dashed-dotted lines in Fig. 8.8. As can be seen, the stresses in circumferential direction are generally larger for this case than after the perfect run-time for the growth process (solid lines) and show a difference of 40 kPa between the inner side and the outer side of the arterial wall which is a notably worse result. A smaller difference of around 20 kPa over the wall thickness can be seen for the stresses in axial direction.

An additional comparison between model A and B is shown in Fig. 8.9 where graphs illustrate the evolution of the circumferential and axial stress of the Gauss point at the inner side of the arterial wall (compare Fig. 8.4b). To demonstrate the property of

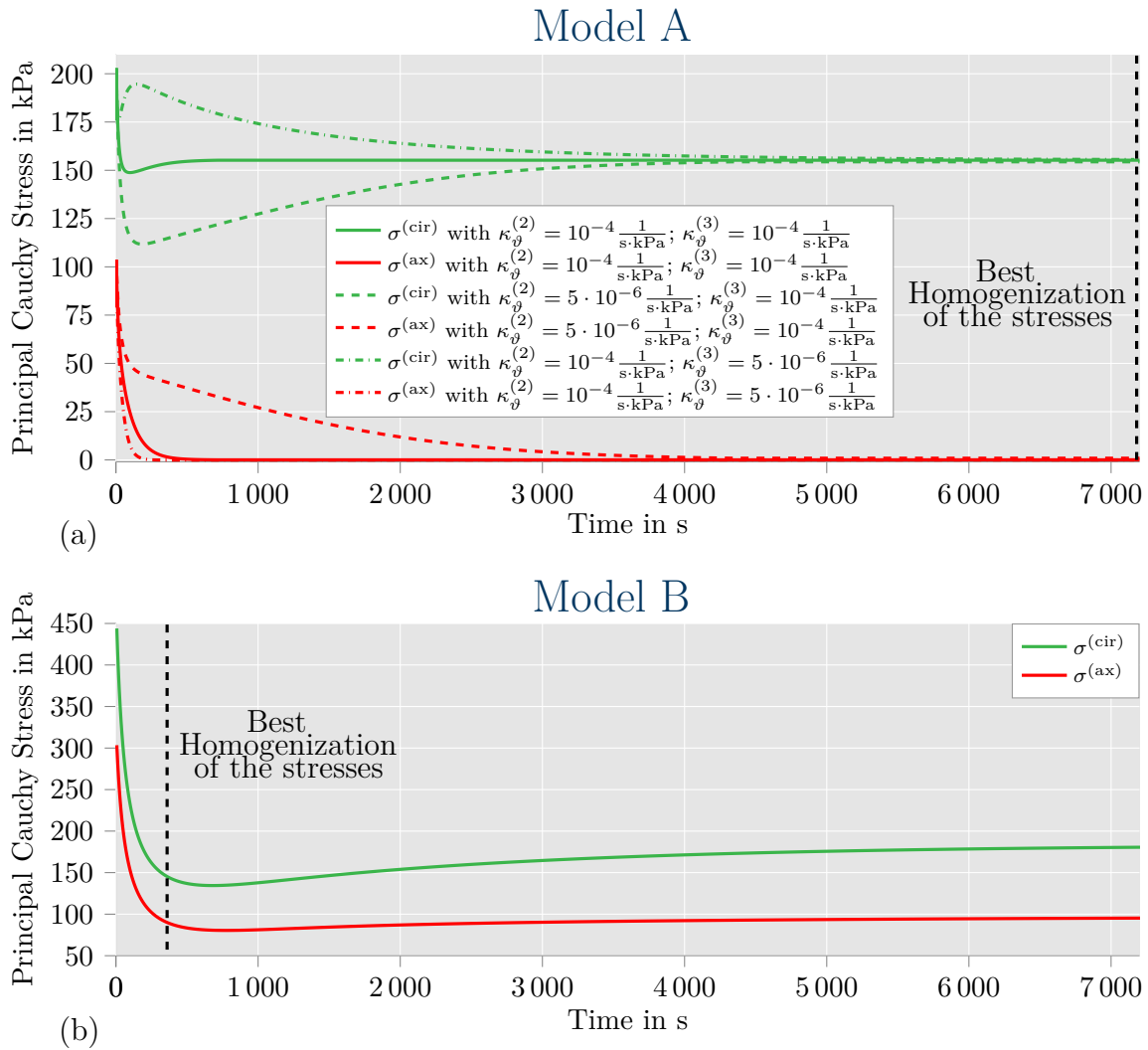


Figure 8.9: Comparison of the time-wise evolution of the stress in axial and circumferential direction at the innermost Gauss point (marked in Figure 8.4). (a) Variation of the values of the growth velocity factors $\kappa_{\vartheta}^{(2)}$ and $\kappa_{\vartheta}^{(3)}$ in growth model A. The graphs show that variations of the growth velocity factors have no impact on the final value of the stresses. (b) For growth model B which depends on the elastic part of the Mandel stress Σ_e as driving force. Homeostatic stress distribution is reached at 360s run time of the growth process. However, growth model B does not converge to this state. Accordingly, a combination with additional active processes such as the contraction of SMCs is challenging. Illustration is adopted from UHLMANN AND BALZANI [178].

the growth model A to be independent from an exact run-time for a reliable homogenization of the stress distribution, different results are displayed which used variations for the growth velocities $\kappa_g^{(2)}$ and $\kappa_g^{(3)}$. There, the values of $\kappa_g^{(2)} = 10^{-4}(\text{s} \cdot \text{kPa})^{-1}$ and $\kappa_g^{(3)} = 10^{-4}(\text{s} \cdot \text{kPa})^{-1}$ (solid lines) represent the evolution for the optimized solution of Section 8.3. In the other two examples, one of the growth velocity parameters $\kappa_g^{(2)}$ (dashed lines) or $\kappa_g^{(3)}$ (dashed-dotted lines) was reduced by a factor of 20. As can be seen, the graphs differ significantly during the first 3000 s of the growth process. However, the final results are equal after a sufficiently long run-time. Moreover, stress distributions over the wall thickness (see Fig. 8.6a) as well as the values of the growth factors (see Fig. 8.6c) and the replication of experimental results (see Fig. 8.7a) are equal in all three variations for the growth velocity parameters. In comparison to these results, the evolution of the stresses at the same Gauss point for model B is shown in Fig. 8.9b. There, the optimal state for the stress distribution is reached after a run-time of 360 s (see distribution in Fig. 8.8). However, the stress still changes significantly afterwards since model B does not provide a stop to the growth process at the material point when a homogenization of the stress distribution is accomplished. Therefore, a qualitatively accurate coupling of model B with another active material process is difficult to achieve.

8.5 Efficiency of Optimization: Variation of Fiber Direction or Axial Growth Conditions

As discussed in Section 8.2, only the fiber direction of collagen (and later also SMCs) and the convergence value $\phi_{\text{con}}^{(2)}$ for the growth process in direction of the second principal stress have to be predefined before the optimization of the structural problem can be started. Since different types of arteries contain different collagen and SMC orientations and experience also different axial prestretches, it should be possible to consider these variations in the combination of optimization procedure and application of the growth model. Therefore, several additional optimization procedures were performed to display the efficiency of the procedure defined in the previous sections. In addition to the variation of the fiber angle β or the convergence value $\phi_{\text{con}}^{(2)}$, also the Dirichlet boundary conditions are adjusted by stretching the arterial ring in axial direction to up to 40% before the growth process is started. Accordingly, the axial stretch value λ_{ax} should not be confused with the in vivo axial prestretch of an artery which constitutes the axial stretch of the artery with residual stresses in the unloaded state. The final results of the optimization parameters and the corresponding values of the three different parts of the objective function z_1 , z_2 and z_3 are listed in Table 4. There, the fiber orientation can be defined by a constant value of the angle β or with linear distribution over the wall thickness. The linear distribution is expressed as $\beta = 10^\circ - 30^\circ$ where the first value (10°) is the value at the inner side of the wall and the second value (30°) is the value at the outer side of the wall. As can be seen in Table 4, the final values of the objective functions are comparable for any variation of the simulation. Only minor outliers can be detected. In the optimization with $\phi_{\text{con}}^{(2)} = 50 \text{ kPa}$, the value of 0.000232 for the second part of the objective function z_2 could be seen as considerably large. However, the corresponding ratio between wall thickness and outer radius constitutes still a value of 0.2098 and, hence, does not differ significantly from the target value of 0.21.

Table 4: Final values of the optimization parameters and the corresponding values of the objective functions z_1 , z_2 and z_3 for variations of the angle of the collagen fibers β , the axial stretch λ_{ax} or the convergence value of the growth factor $\phi_{\text{con}}^{(2)}$. The standard case refers to the first application of the optimization which is presented in Section 8.3.

Variation	Optimization Parameters						Objective Function		
	α_1	α_4	α_5	$r_{o,\text{ref}}$	$r_{i,\text{ref}}$	w_{min}	z_1	z_2	z_3
Standard Case	2.79 kPa	9.90 kPa	2.99	103.11 μm	82.91 μm	0.77	0.00645	2.74e-06	0.00494
$\beta = 10^\circ - 30^\circ$	3.08 kPa	10.48 kPa	3.08	102.44 μm	81.84 μm	0.783	0.00868	8.51e-06	0.00658
$\beta = 10^\circ - 40^\circ$	2.83 kPa	19.87 kPa	2.54	108.44 μm	87.54 μm	0.857	0.01371	3.47e-05	0.00632
$\beta = 30^\circ$	3.62 kPa	14.51 kPa	3.13	96.95 μm	77.50 μm	0.776	0.00535	8.75e-05	0.00460
$\beta = 45^\circ$	3.76 kPa	39.86 kPa	2.76	88.64 μm	69.99 μm	0.915	0.00529	9.53e-06	0.00476
$\lambda_{\text{ax}} = 1.1$	2.79 kPa	11.46 kPa	3.10	102.98 μm	83.24 μm	0.799	0.00552	9.31e-05	0.00652
$\lambda_{\text{ax}} = 1.2$	2.38 kPa	14.89 kPa	3.00	105.17 μm	85.19 μm	0.895	0.00583	7.94e-05	0.00614
$\lambda_{\text{ax}} = 1.3$	1.75 kPa	19.83 kPa	2.92	107.22 μm	87.48 μm	0.986	0.00607	7.18e-06	0.00584
$\lambda_{\text{ax}} = 1.4$	1.56 kPa	25.077 kPa	2.85	108.39 μm	89.36 μm	1.079	0.00619	9.54e-05	0.00557
$\phi_{\text{con}}^{(2)} = 10 \text{ kPa}$	1.28 kPa	14.02 kPa	2.56	107.04 μm	87.04 μm	0.852	0.00634	8.84e-05	0.00540
$\phi_{\text{con}}^{(2)} = 20 \text{ kPa}$	1.52 kPa	10.71 kPa	2.52	105.82 μm	84.50 μm	0.937	0.00663	3.54e-05	0.00554
$\phi_{\text{con}}^{(2)} = 30 \text{ kPa}$	1.56 kPa	8.61 kPa	2.54	103.83 μm	82.29 μm	0.959	0.00639	2.59e-05	0.00581
$\phi_{\text{con}}^{(2)} = 40 \text{ kPa}$	3.11 kPa	5.47 kPa	2.66	101.01 μm	78.53 μm	0.984	0.00607	7.11e-05	0.00637
$\phi_{\text{con}}^{(2)} = 50 \text{ kPa}$	4.93 kPa	3.56 kPa	2.75	101.09 μm	77.17 μm	1.009	0.00572	0.000232	0.00656

In addition, the optimizations with the fiber angles of $\beta = 10^\circ - 30^\circ$ and $\beta = 10^\circ - 40^\circ$ could be identified as outliers, since the values of objective function z_2 are up to 2.5 times higher than in other cases. However, this part of the objective function minimizes the change of the growth factors $\vartheta^{(3)}$. A linear increase of the fiber angle over the wall thickness leads to a stiffer material behavior in circumferential direction at the inner side as compared to the outer side of the wall. Since the stresses are already larger at the inner side of the wall (see, e.g., $\sigma^{(\text{cir})}$ in Fig. 8.6a), the difference between the growth factor $\vartheta^{(3)}$ at the inner and outer side of the wall has to increase even further with this distribution of the fiber angle. This leads to an automatic increase of the value of z_1 . The quality of the fitting of the material parameters (see z_3 in Table 4) is adequate in every optimization.

For a more detailed illustration of the simulation results, the distribution of Cauchy stresses $\sigma^{(\text{ax})}$ and $\sigma^{(\text{cir})}$, the driving forces $\phi^{(2)}$ and $\phi^{(3)}$, and the growth factors $\vartheta^{(2)}$ and $\vartheta^{(3)}$ are displayed in Fig. 8.10 for the variation of the fiber orientation. Illustrations in the same manner can be found in Fig. C.1 for a varying axial stretch λ_{ax} and in Fig. C.2 for the variation of the driving force $\phi_{\text{con}}^{(2)}$ in Appendix C. Since the optimized values for the radii in the reference configuration, $r_{i,\text{ref}}$ and $r_{o,\text{ref}}$, are different for every optimization, the positions over the wall thickness are displayed as relative values where 0.0 represents the inner side of the wall and 1.0 the outer side of the wall. As described before, it can be seen in Fig. 8.10d that the values of growth factors $\vartheta^{(3)}$ differ more from the start value of 1.0 in the case of $\beta = 10^\circ - 30^\circ$ and $\beta = 10^\circ - 40^\circ$. This underlines the larger value of the objective function z_1 in these cases.

An important feature of the optimization procedure can be recognized in Fig. 8.10a, b and c. The stress distribution over the wall thickness is basically equal for every single

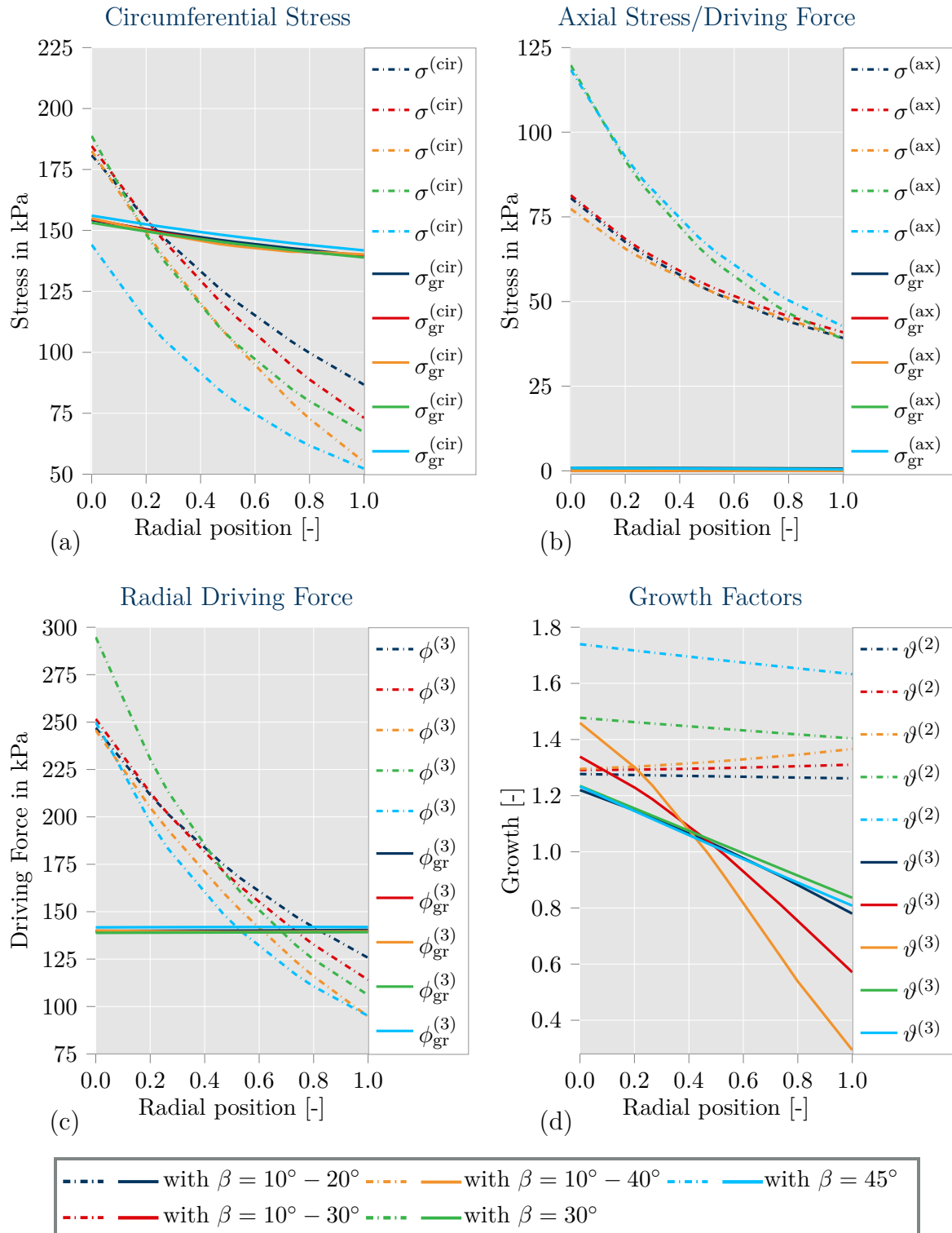
Variation of Collagen Fiber Angle β 

Figure 8.10: Comparison of results from optimizations with different angles β for the collagen fibers. Distribution of the (a) circumferential Cauchy stress $\sigma^{(cir)}$, (b) the axial stress/-driving force $\sigma^{(ax)}/\phi^{(2)}$, (c) the radial driving force $\phi^{(3)}$ which directly influences the stresses in circumferential direction, and (d) the growth factors $\vartheta^{(2)}$ (axial) and $\vartheta^{(3)}$ (radial). Note that $\beta = 10^\circ - 20^\circ$ describes a gradient of the angle over the wall thickness with $\beta = 10^\circ$ at the inner side and $\beta = 20^\circ$ at the outer side of the arterial wall. Since the optimization of $r_{i,ref}$ and $r_{o,ref}$ does not lead to equal values for a variation of the fiber angle, the diagrams show relative values for the position of the Gauss points. Optimizations show convincing results for any assumption of the fiber angle β . Illustration is adopted from UHLMANN AND BALZANI [178].

case of the variation of the fiber direction. While this result has to be expected for the stresses in axial direction $\sigma_{\text{gr}}^{(\text{ax})}$, since all stresses are reduced to the convergence value of $\phi_{\text{con}}^{(2)} = 0$ kPa, the similarity of the stresses in circumferential direction could be seen as surprising. However, it seems that the combination of homogenization of the stress distribution over the wall thickness by a kinematic growth model with an optimization of the reference geometry and a fitting of the material parameters to experimental data is sufficient to make the result in this loading scenario independent from the fiber orientation. Note that Fig. 8.10 illustrates only the loading scenario with an intravascular pressure of 120 mmHg. This result underlines also that the combination of this growth model with a remodeling process for the fiber orientation is counterproductive as long as the remodeling process completely depends on the values of the stresses at the material point in a static load scenario. Since the stress distribution does not change for predefined differences in the fiber orientation, it will also not change for an adjusting fiber direction from such a remodeling process. In consequence, the final fiber direction of the remodeling process is basically predefined by the final stress values which are here defined by the convergence values $\phi_{\text{con}}^{(2)}$ and $\phi_{\text{con}}^{(3)}$. Therefore, an experimental determination of the fiber directions is preferable.

Altogether, the optimization results are convincing. The stress distributions for the variation of the convergence value in axial direction $\phi_{\text{con}}^{(2)}$ and the axial stretch before growth λ_{ax} are reliable as well. In consequence, the described optimization procedure can be used for all types of arteries. As soon as the fiber orientation of collagen and SMCs as well as the axial prestretch is known for the considered artery, the optimization provides an accurate mechanical description of the arterial wall. This will be shown for the inclusion of the active response for a middle cerebral artery of a rat in the next chapter.

9 Combination of Growth and Active Response for Optimal Structural Problem

The combination of the growth model with an active material process as the contraction of SMCs is not straightforward. A kinematic growth model is applied to obtain residual stresses. For this process, the growth factors depending on stresses (or stretches) at the material point. In case of the contraction of vascular SMCs, the mechanism is stretch-dependent. Accordingly, both, the growth and contraction process, are affected by the current state of the mechanical fields and change these mechanical fields simultaneously. This leads to a high interaction between the models for growth and smooth muscle contraction. Therefore, the independency of the growth model from an exact run-time is beneficial. As shown in Section 8.4, the growth velocity parameter of the evolution equations of the growth factors can be freely adjusted. Consequently, the more sensitive process of the smooth muscle contraction can be treated as the dominant active process which runs in real time and the growth process can be run as slow as necessary to enable a robust and stable numerical simulation. Adjustments of biological tissue by growth takes place over a time frame of (at least) hours, but rather weeks, months or even years. Since these time spans cannot be considered in numerical simulations as the time step width has to be kept under one second for a realistic material response of the vascular SMCs, the time-dependency of the growth process is treated abstractly. In addition to the combination of both processes in numerical simulations, the growth model will be adjusted to obtain more realistic stress distributions for the first principal Cauchy stress which is oriented in circumferential direction for the considered geometry of a hollow cylinder. This adjustment will also include growth in circumferential direction which can be observed in experimental data, but was excluded in the previous chapters. For the combination of both active model processes, the optimization of the structural problem is applied. There, a fourth part of the objective function will be added which leads to an adjustment of the geometry to correspond to measurements of the axial prestretch for the considered artery type.

9.1 Adjustment of the Growth Model

As shown and discussed in Section 8.3, a certain gradient remains for the distribution of the circumferential stresses over the wall thickness after the proposed growth model was applied. This is associated with the definition of the driving force $\phi^{(3)}$ which considers the trace of the Cauchy stresses and, therewith, the stresses in radial direction (third principal Cauchy stress). This leads to a difference of 16 kPa between the circumferential stress at the inner side of the wall and the outer side which corresponds to the load scenario of 120 mmHg (16 kPa) for the intravascular pressure. Since the stresses in this direction decrease from around 150 kPa to 30 kPa when the active material response is involved, a radial stress of 16 kPa is more notable and, hence, the growth model has to be adjusted. Resulting data for the application of the growth model as described in Chapter 7 are illustrated in Fig. D.1 of Appendix D. Accordingly, the driving force $\phi^{(3)}$ should not depend on the third principal stress. Instead, a new definition is introduced here where only the first and second principal stress (circum-

ferential and axial direction) are considered for the calculation of the driving force at the material point. In addition, the growth model will be adjusted to correspond more accurately with observations made in experiments as shown in Section 2.3.4. There, a growth in circumferential direction can be identified for aging large arteries although growth in this direction is considerably less recognizable than growth in radial or axial direction of the arterial wall. However, the growth process in arterial tissue is three dimensional. Accordingly, the growth model is adjusted to apply growth in all three directions. In consequence, the same evolution equation as for the second and third growth factor, $\vartheta^{(2)}$ and $\vartheta^{(3)}$, is now applied to the first growth factor $\vartheta^{(1)}$. This leads to a change of Eq. (7.21) to

$$\dot{\vartheta}^{(a)} = \kappa_{\vartheta}^{(a)} (\phi^{(a)} - \phi_{\text{con}}^{(a)}) \quad \text{with } a = 1, 2, 3. \quad (9.1)$$

As described above, the driving force $\phi^{(3)}$ does not include the third principal Cauchy stress anymore. Furthermore, the driving force $\phi^{(1)}$ for the first growth factor $\vartheta^{(1)}$ is defined as the first principal Cauchy stress. This results in the following formulation of the driving forces

$$\phi^{(1/2)}(\boldsymbol{\sigma}) = \boldsymbol{\sigma} : (\mathbf{n}^{(1/2)} \otimes \mathbf{n}^{(1/2)}) \quad \text{and} \quad \phi^{(3)}(\boldsymbol{\sigma}) = \phi^{(1)} + \phi^{(2)}, \quad (9.2)$$

which substitutes Eq. (7.22) from the growth model described in Chapter 7.

9.2 Adjustment of the Optimization Procedure

Corresponding to the adjustment of the growth model, the convergence value for the driving force $\phi_{\text{con}}^{(3)}$ is calculated based on stresses over the wall thickness (see Gauss points in Fig. 8.4b) in circumferential and radial direction before the growth process is started. Accordingly, the equation can be formulated as

$$\phi_{\text{con}}^{(3)} = w_{\min} \bar{\sigma}_{I/II} \quad \text{with} \quad \bar{\sigma}_{I/II} = \frac{1}{n_{\text{gp}}} \sum_{g=1}^{n_{\text{gp}}} (\sigma_{I,g} + \sigma_{II,g}), \quad (9.3)$$

where $\sigma_{I,g}$ and $\sigma_{II,g}$ constitute the first and second principal Cauchy stress at the Gauss point g , and w_{\min} is considered the volumetric minimizer (see Eq. (8.1)). Furthermore, the optimization procedure is extended with a fourth part of the objective function. There, the axial prestretch of the arterial wall is evaluated which is assumed to be optimal with a value of 1.1 for a middle cerebral artery of a rat (adopted from BELL ET AL. [15]). To test the axial prestretch of the arterial wall, an additional simulation labeled as 2(d) is executed in which only one side of the geometry is held in axial direction by Dirichlet boundary conditions. Accordingly, the other side of the arterial ring can experience displacements while the values of the growth factors from the end of simulation 2(a) are applied over a time span of one second (equal to simulations 2(b) and 2(c), see Section 8.2). The nodes of the moving side are linked in their displacement in axial direction. Furthermore, in this simulation 2(d), no intravascular pressure is considered and the active material response is deactivated which corresponds to the scenario for the artery in the experiment. The associated extension of the objective

function is expressed as

$$z_4 = 0.1 \sqrt{\left(\frac{1}{\lambda_{\text{ax}}} - 1.1\right)^2}, \quad (9.4)$$

where λ_{ax} is the axial stretch of the artery in the simulation 2(d) after full values of the growth factors $\vartheta^{(a)}$ are reached. Accordingly, the axial prestretch of the artery can be calculated by $\lambda_{\text{ax, pre}} = \lambda_{\text{ax}}^{-1}$. Then, z_4 is added to Eq. (8.2) which results in $z = z_1 + z_2 + z_3 + z_4$. To achieve the optimum for the axial prestretch, the convergence value $\phi_{\text{con}}^{(2)}$ for the driving force $\phi^{(2)}$ is added as optimization parameter. For the convergence value $\phi_{\text{con}}^{(1)}$, the difference between $\phi_{\text{con}}^{(3)}$ and $\phi_{\text{con}}^{(2)}$ is build which leads to

$$\phi_{\text{con}}^{(1)} = \phi_{\text{con}}^{(3)} - \phi_{\text{con}}^{(2)}. \quad (9.5)$$

The corresponding adjustments of the optimization procedure are applied to its schematic representation which is illustrated in Fig. 9.1.

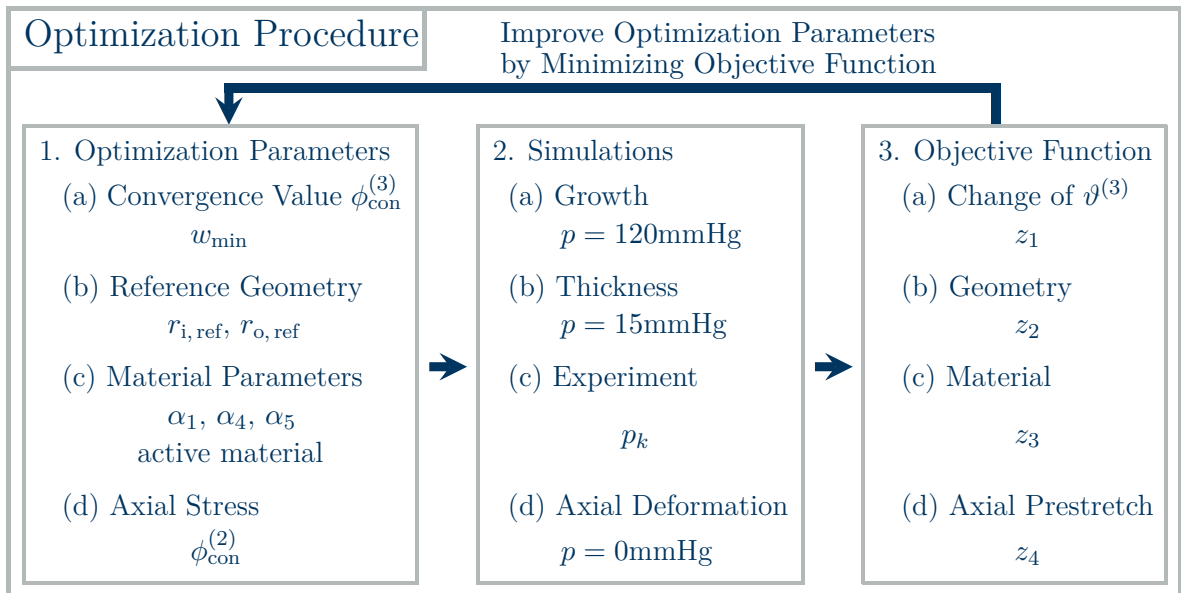


Figure 9.1: Schematic representation of the optimization procedure which is based on evolution and gradient method. Three steps are presented which result in an evaluation of a parameter set: 1. Creation of new sample of parameters based on data from earlier generations, 2.(a) Execution of growth process, 2.(b) Checking the wall thickness of the resulting geometry, 2.(c) Reproduction of mechanical experiments with simulation, 2.(d) Checking the axial prestretch of the arterial ring, and 3. Evaluating the sample based on the objective function. The label active material in 1(c) refers to the optimization parameters which were also used in Chapter 6 (see Table 2).

9.3 Optimization of the Structural Problem with Inclusion of the Active Material Response

The described optimization of the structural problem (see Section 8.2 for the basic form and the previous Section 9.2 for the extension) is now applied to an arterial ring

which includes the active material response as formulated in Chapter 5. As applied in the first example with passive material response, the orientation of the collagen fibers and the SMCs is defined by the angle $\beta = 10^\circ - 20^\circ$ which is based on measurements by FINLAY ET AL. [54]. Since the active material model is used during the application of the growth model at an intravascular pressure of 120 mmHg, the active, stretch-dependent material part has to reach a certain steady state for the load scenario first. This is reached by applying the same simulation protocol as used for the fitting of the parameters of the fully active material in simulations presented in Chapter 6. Accordingly, the arterial ring is set under an intravascular pressure of 10 mmHg over a time of 600 s at the beginning of simulation 2(a). Afterwards, the pressure is increased stepwise to values of 20, 40, 60, 80, 100 and 120 mmHg where every pressure level is held over a time span of 300 s (see Fig. 6.1c). At the end of these 1800 s, the extended version of the growth model is activated and residual stresses are calculated. The interaction between active response and growth process can be controlled by the values of the growth velocity factors which are chosen to be $\kappa_{\vartheta}^{(1)} = 10^{-5}(\text{s} \cdot \text{kPa})^{-1}$, $\kappa_{\vartheta}^{(2)} = 10^{-4}(\text{s} \cdot \text{kPa})^{-1}$ and $\kappa_{\vartheta}^{(3)} = 10^{-4}(\text{s} \cdot \text{kPa})^{-1}$. As a consequence, the active material response reacts significantly faster on growth-induced changes of the stretch in fiber direction of the SMCs than the growth factors evolve over time. It should be noted that simulations in which the value of the growth velocity factor $\kappa_{\vartheta}^{(1)}$ is extending a certain ratio to the growth velocity factor $\kappa_{\vartheta}^{(3)}$, the convergence value cannot be reached and infinite growth in circumferential direction occurs. While growth in radial direction increases the area which withstands the load in circumferential direction, the growth process in circumferential direction itself rather leads to a direct adjustment of the circumferential stretch. For the simulations in this thesis, this results in a reduction of the stretch at the inner side of the wall and an increase of the stretch at the outer side of the wall and, therefore, an equalization of the stresses. However, this growth behavior can also lead to an increase of the inner radius of the arterial ring. In consequence, the area on which the intravascular pressure is applied increases and, therewith, the load on the arterial ring. Accordingly, as the stresses over the wall are raised, growth in circumferential direction is further stimulated leading to an infinite growth process. During testing of the combination of growth and active response, a growth velocity value of $\kappa_{\vartheta}^{(3)} = 10^{-4}(\text{s} \cdot \text{kPa})^{-1}$ showed reliable stability for the simulations with the original version of the growth model described in Chapter 7 (see, e.g., Fig. D.1 of the Appendix D). Simulations with the adjusted version of the growth model did not result in infinite growth, if the growth velocity factor $\kappa_{\vartheta}^{(3)}$ had a value lower than $3 \cdot 10^{-5}(\text{s} \cdot \text{kPa})^{-1}$. The value of $\kappa_{\vartheta}^{(1)} = 10^{-5}(\text{s} \cdot \text{kPa})^{-1}$ was chosen, because the combination of parameters reached the convergences values $\phi_{\text{con}}^{(a)}$ the fastest. Simulation 2(b) is executed in the same manner as described in Section 8.2. For simulation 2(c), the final growth factors of simulation 2(a) are applied over a time span of one second in the beginning. Afterwards, the three different scenarios of the experiment of JOHNSON ET AL. [94] are applied which consider the fully active material response, the suppressed active material response, and the passive material response of a middle cerebral artery of a rat (compare Section 6.1). Accordingly, z_3 of the objective function includes the adjustment of the outer diameter over time from simulations of all three scenarios as well as the corresponding experimental data. To include the active material response in the optimization, the material parameters were treated the same way as in Chapter 6. Accordingly, the values of the predefined parameters are listed in

Table 2. The parameters listed in Table 3 are included in the optimization procedure as optimization parameters here. The label active material in 1(c) of the left box of Fig. 9.1 refers to these optimization parameters.

The results of the homogenization of the stress distribution over the wall thickness are illustrated in Fig. 9.2. There, the Cauchy stresses $\sigma^{(\text{ax})}$ and $\sigma^{(\text{cir})}$ in axial and circumferential direction before (dashed) and after (solid) application of the growth process are shown in Fig. 9.2a and the corresponding growth factors $\vartheta^{(a)}$ in Fig. 9.2b. Note that the stresses $\sigma^{(\text{cir})}$ and $\sigma^{(\text{ax})}$ equal the driving forces $\phi^{(1)}$ and $\phi^{(2)}$, respectively. Therefore, the driving forces are not displayed in the results of the growth process. The optimization identified a value of 27.46 kPa for the driving force in circumferential direction $\phi_{\text{con}}^{(1)}$. In displayed results, the circumferential stress reaches a value of 28.1 kPa at the inner side of the wall and 26.8 kPa at the outer side of the wall. The remaining difference between the stresses and the convergence value $\phi_{\text{con}}^{(1)}$ is caused by interaction between growth and active response. An inclusion of the growth velocity factors in the optimization could lead to a further improvement of the results. However, homogenization of the stresses is qualitatively sufficient in this state. The stresses in axial direction reached values between 1.45 kPa and 1.85 kPa over the entire wall thickness. This minor stress value is enough to reach an axial prestretch of $\lambda_{\text{ax, pre}} = 1.105$. Focusing on the results in Fig. 9.2a in more detail, it can be seen that the stresses have higher values at the outer side of the artery than at the inner side of the artery before growth which contrasts the distribution of the stresses when only the passive material part is applied (compare Fig. 8.6a). This difference is caused by the contraction of the SMCs which can lead to a reduction of the outer diameter of the arterial ring in comparison to the reference configuration. In consequence, the stretch at the outer side of the wall

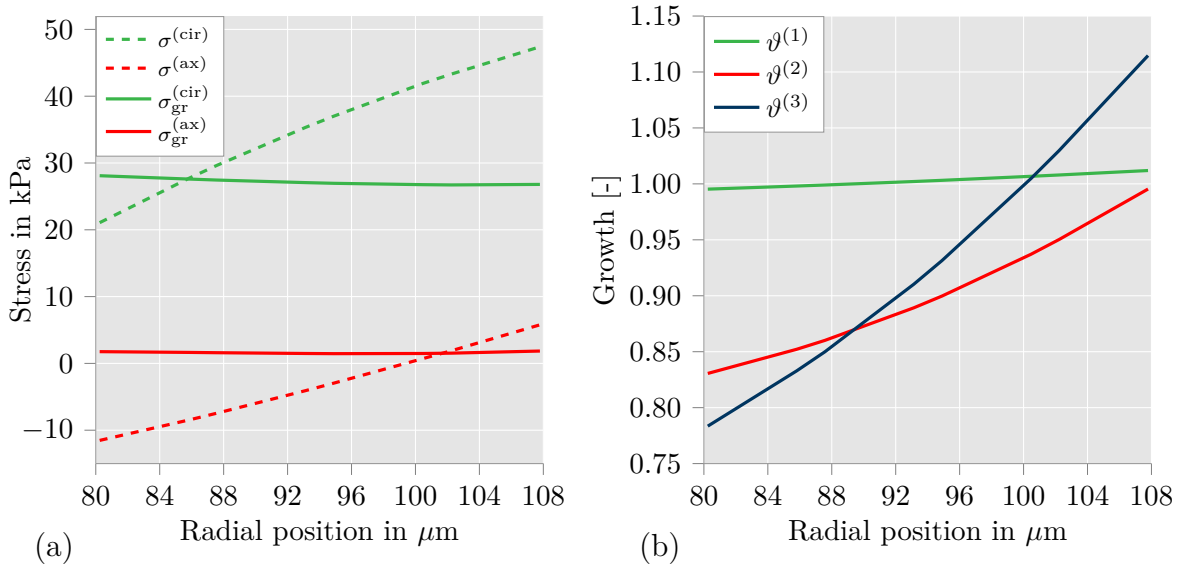


Figure 9.2: Distribution of (a) Cauchy stresses and driving forces $\sigma^{(\text{cir})} = \phi^{(1)}$ and $\sigma^{(\text{ax})} = \phi^{(2)}$ (b) growth values $\vartheta^{(1)}$, $\vartheta^{(2)}$ and $\vartheta^{(3)}$ in circumferential (green), axial (red) and radial (blue) direction over the wall thickness for the fully active material model. Artery is loaded with an intravascular pressure of 120 mmHg. Dashed lines show results before growth, solid lines show results after growth. The new growth method also generates a homeostatic stress distribution when smooth muscle contraction is included. Illustration is adopted from UHLMANN AND BALZANI [178].

is higher than the stretch at the inner side which is contrary to the results with passive material response. This effect can also be identified in the distribution of the growth factors in Fig. 9.2b. The corresponding graphs show a positive gradient which was negative before (see Fig. 8.6c). This result underlines the importance of the combination of growth and active response when middle or small muscular arteries are considered. Residual stresses should not be estimated by the results of simulated growth processes only considering passive material response. Such a procedure would rather increase the difference between the stresses over the wall thickness and lead to a reduction of the accuracy of the mechanical fields in comparison to not considering residual stresses at all.

The final values of the optimization parameters are listed in Table 5. Based on the inner and outer radii, $r_{i,\text{ref}} = 79.36 \mu\text{m}$ and $r_{o,\text{ref}} = 108.67 \mu\text{m}$, in the reference configuration, the final value of the ratio between wall thickness and outer radius was 0.216. This differs notably more from the target value of 0.21 than in the previous optimizations. However, the number of objectives of the optimization expanded especially with regard to the fitting of the material behavior which has a certain impact on the quality of the results. The comparison between the material model and the experimental data is illustrated in Fig. 9.3. The quality of the graphs for the fully active and the suppressed active material response (red and green) are comparable to the results in which growth was not considered. In contrast, simulation results for passive material response show notable gaps in comparison to the experimental data in the range of 20 to 80 mmHg which was not the case without inclusion of the growth model in Chapter 6 (see Fig. 6.2). This can be connected to the setup of the corresponding optimizations. Without the growth process involved, it was possible to optimize the parameters of the passive and active material response separately. In the optimization here, parameters for the growth model as well as the material parameters for both material parts were fitted simultaneously. In consequence, the quality of the results is not equal in both optimizations. Furthermore, growth in circumferential and axial direction can lead to a considerable increase of elastic stretches of collagen fibers (calculated from the elastic part of the deformation gradient \mathbf{F}_e). As a result, all three parameters (α_1 , α_4 and α_5) are smaller here than in the parameter fitting without growth. Moreover, the difference in growth over the wall thickness influences the stress-strain behavior of the passive material response at the material points differently and might result in

Table 5: Final values of the optimization parameters for inclusion of active response

α_1	α_4	α_5	$r_{o,\text{ref}}$	$r_{i,\text{ref}}$	w_{\min}
6.69kPa	1.1kPa	2.38	108.67 μm	79.36 μm	0.884
η	γ_1	$\dot{\lambda}_{c,\text{max}}$	$\dot{\lambda}_{c,\text{min}}$	$\dot{k}_{2/5,\text{max}}$	$\dot{k}_{2/5,\text{min}}$
0.1349s ⁻¹	0.3095 μM	0.0471s ⁻¹	-0.0471s ⁻¹	0.000569s ⁻²	-0.001004s ⁻²
$\dot{\lambda}_{p,\text{max}}$	$\dot{\lambda}_{p,\text{min}}$	μ_a	κ	β_1	$k_{2/5,\text{start}}$
0.000094s ⁻¹	-0.000108s ⁻¹	29.04kPa	104.09kPa	0.00069s ⁻¹	1.9088s ⁻¹

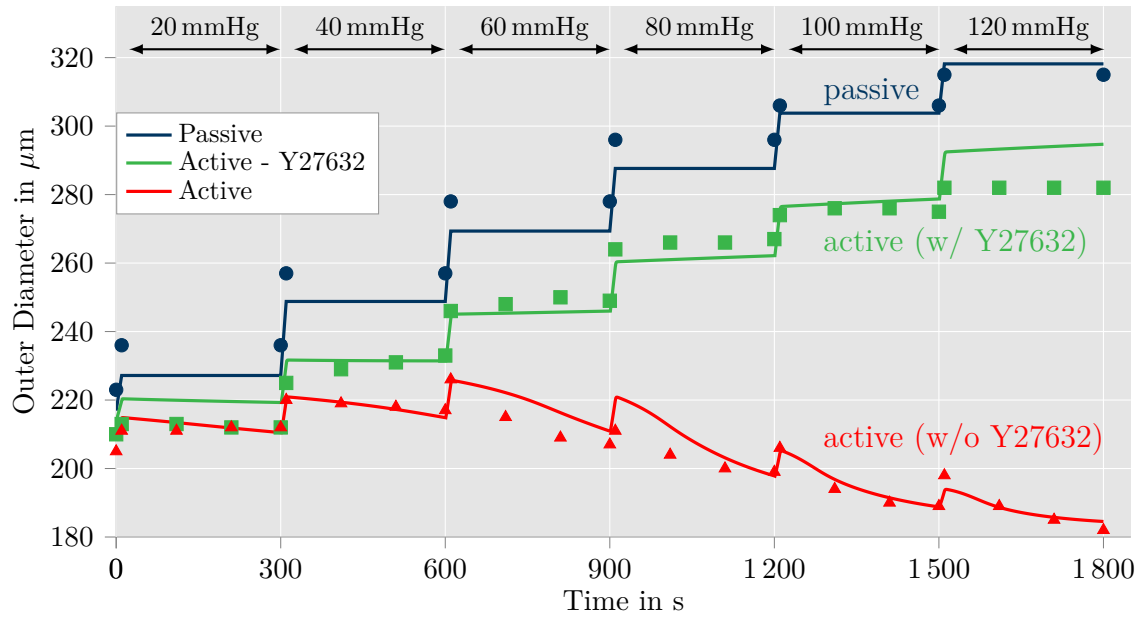


Figure 9.3: Comparison of the outer diameter of the arterial wall in simulations after growth (solid lines) with experimental data from [94] (marks) for three different setups: passive response, active response under influence of $1 \mu\text{M}$ Rho kinase inhibitor Y27632, and fully active response (see material model in Chapter 5). The results for the fully active model nearly correspond with experimental data. The graph for the passive material model shows larger differences to the experimental data compared to the passive material model which was fitted without growth (see Fig. 6.2). The growth procedure aims for homeostatic stresses during the contraction of SMCs which decreases the accuracy of the fitting of the passive material response. Illustration is adopted from UHLMANN AND BALZANI [178].

difficulties to describe the non-linearity of the passive material response adequately. However, the simulation results here include not only a homogeneous stress distribution over the entire wall, but also an optimal reference geometry and an accurate axial prestretch of the arterial ring in addition. Qualitatively comparable results from mechanical simulations of muscular arteries are not known from published literature. The applied optimization procedure enables a reliable combination of the modeling of tissue growth and active material processes. This constitutes a promising foundation to apply mechanical simulations to patient-specific arteries for the improvement of diagnostic and treatment.

10 Combination of Growth and Active Contraction in Realistic Geometry

To establish the capacity of the model for active material response and novel kinematic growth model, so far, only hollow cylinders were used in simulations which constitutes an idealized geometry with rotational symmetry. In this chapter, the results of a numerical simulation are demonstrated which took a more realistic geometry of an artery segment into account. In this simulation, both model parts are combined in a comparable manner as shown in Chapter 9. However, the implemented optimization procedure for an optimal description of the structural problem is not explored here any further in order to possibly enable an application to more realistic geometries. Nonetheless, the final results from simulations presented in Section 9.3 are considered. In the following sections, creation of the finite element mesh, determination of a realistic fiber orientation and the protocol for the simulation are described. This includes a consideration of the growth direction and orientation of the eigenvectors of the Cauchy stress. Furthermore, the homogenization of stress distribution in the geometry is displayed and the quality of the results is analyzed.

10.1 Creation of Finite Element Mesh and Determination of Realistic Fiber Orientation

The creation of a patient-specific geometry of an arterial segment is not straightforward. Imaging methods such as MRI, CT, or ultrasound can be used to obtain images of larger arteries such as the aorta. However, even for such large arteries, the quality of the created geometries is restricted to the resolution of the applied imaging method. Furthermore, the different layers of the arterial wall cannot be identified in these images which makes the determination of the boundary between media and adventitia difficult. Another technique to generate images of an artery is angiography which is a minimally invasive diagnostic procedure, primarily used to detect vessel closure. Based on images from 3D rotational angiography, the geometry of the lumen of smaller arteries can be generated as described in PICCINELLI ET AL. [140]. These geometries have a high quality, but information about the structure of the arterial wall is missing. This issue can be solved by considering data from measurements of ex vivo arteries which can be adopted to assume the wall thickness of the arterial wall. In the following paragraph, this concept is used to create the geometry and finite element mesh of a more realistic geometry of an artery segment.

Creation of Geometry and FE Mesh For the creation of the finite element mesh for the numerical simulation, data was adopted from the case ID C0001 at [136]. There, the geometry for the inner side of internal carotid arteries of a human is provided in STL-format. Furthermore, the centerline of the lumen is described by a series of points. To obtain a 3D geometry of the arterial wall, the outer side of the artery is generated in a *Python* script. In this script, the geometry of the inner side is copied. Afterwards, the minimal distance of every node of this copy to the centerline of the lumen is calculated.

This distance is increased by a factor which corresponds to the ratio between inner and outer radius of the arterial wall. Associated with the simulations shown in previous chapters, the value for this factor is based on measurements of the middle cerebral artery in GANNON ET AL. [58]. Accordingly, a value of 1.2658 was chosen to express the relation of $(r_{o, \text{ref}} - r_{i, \text{ref}})/r_{o, \text{ref}} = 0.21$ for the inner and outer radii $r_{o, \text{ref}}$ and $r_{i, \text{ref}}$ in the referential state. Afterwards, the STL-file with inner and outer side of the arterial wall is edited in the software *Meshmixer* to create the boundaries of the geometry in axial direction. Based on this final version of the geometry, the finite element mesh is generated in *Gmsh* which is illustrated in Fig. 10.1a. This mesh consists of 7,065 quadratic, 10-node tetrahedral elements. Naturally, the size of the geometry is comparable to the internal carotid artery of a human and not the middle cerebral artery of a rat. The size of the geometry could be adjusted by multiplying the location vector of every node of the mesh by the same factor. However, an adjustment of the size is unnecessary. The values of stretches or stresses at a material point are equal for both geometries, since only an intravascular pressure is considered for the load of the artery which reflects the adjustment of size.

Orientation of Collagen Fibers and SMCs An angle of $\beta = 15^\circ$ is applied to describe the orientation of collagen and SMCs at a material point. There, β describes the angle between fiber direction and first eigenvector of the Cauchy stress in the plane defined by its first and second eigenvector. In contrast to the hollow cylinder, first and second eigenvector of the Cauchy stress cannot be directly associated with circumferential and axial direction in the realistic geometry. Furthermore, the direction of the eigenvectors is influenced by the loading scenario and the material behavior which naturally depends on the orientation of collagen fibers and SMCs itself. Therefore, the direction of the fibers is determined in a two-step procedure in which only the passive material response is included and a model for the fiber reorientation is applied. In the corresponding two simulations, displacements in axial direction are prevented on both axial ends of the artery segment by the formulation of associated Dirichlet boundary conditions. Furthermore, several nodes are held in circumferential direction

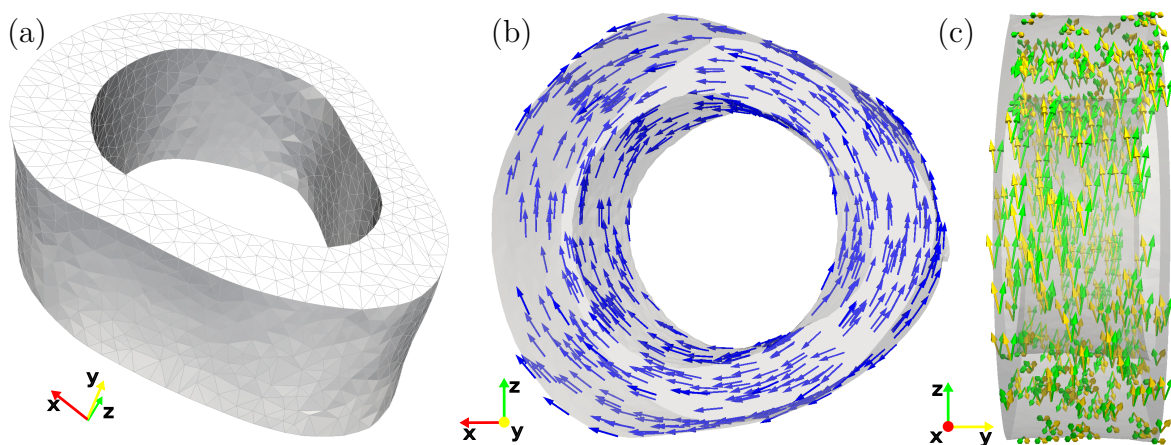


Figure 10.1: Illustration of (a) finite element mesh for realistic geometry of an artery segment in unloaded and stress-free state, (b) first eigenvectors of Cauchy stress at the end of fiber reorientation and (c) final orientation of collagen and SMCs.

to stop rotations during the simulations. Since an intravascular pressure of 120 mmHg is assumed a reasonable load scenario for the growth process, this pressure value is also considered to determine the fiber direction. In the first simulation, this pressure is applied while only the isotropic part $\Psi_{p, \text{isot}}$ of the strain-energy density function is used for the material behavior of the artery segment (compare Eqs. (5.19) and (5.20)). At the end of the simulation, three eigenvectors of the Cauchy stress are saved for all 77,715 Gauss points of the mesh. Subsequently, the initial direction of the collagen fibers is calculated based on these eigenvectors in the beginning of the second simulation. Accordingly, at this point the material behavior includes the passive anisotropic part $\Psi_{p, \text{ti}}^{(f)}$ (see Eq. (5.21)) which describes the material response of the collagen fibers. After the intravascular pressure of 120 mmHg is applied, fiber reorientation is started. The model for reorientation is adopted from ZAHN [202] where it was labeled as model for continuous reorientation (see pp. 87-90). The reorientation model is controlled by the time-dependent minimization of the angle $\eta^{(f)}$ between the current fiber direction $\mathbf{a}^{(f)}$ and a target fiber direction $\mathbf{A}_{\text{targ}}^{(f)}$. Note that the notation for the angle η as well as the target fiber direction \mathbf{A}_{targ} matches the notation in ZAHN [202] to enable a simple comparison. However, the difference between first and second fiber direction was introduced as the superscript (f) in Section 3.1 of this thesis and, therefore, is used again in the formulation here. The evolution equation for the angle $\eta^{(f)}$ is expressed as

$$\dot{\eta}^{(f)} = -\frac{k_{\eta}^{+} (\eta^{(f)})^2}{(\eta^{(f)})^2 + m_{\eta}^{+}}, \quad (10.1)$$

where k_{η}^{+} and m_{η}^{+} are parameters and the angle $\eta^{(f)}$ is expressed in radian. The difference between the current fiber direction $\mathbf{a}^{(f)}$ and target fiber direction $\mathbf{A}_{\text{targ}}^{(f)}$ is calculated by

$$\eta^{(f)} = \arccos \left(\mathbf{a}^{(f)} \cdot \mathbf{A}_{\text{targ}}^{(f)} \right). \quad (10.2)$$

The target fiber directions $\mathbf{A}_{\text{targ}}^{(f)}$ with $f = 1, 2$ are defined as described above which leads to the expressions

$$\mathbf{A}_{\text{targ}}^{(1)} = \cos(15^{\circ}) \mathbf{n}^{(1)} + \sin(15^{\circ}) \mathbf{n}^{(2)} \quad \text{and} \quad \mathbf{A}_{\text{targ}}^{(2)} = \cos(-15^{\circ}) \mathbf{n}^{(1)} + \sin(-15^{\circ}) \mathbf{n}^{(2)}, \quad (10.3)$$

where $\mathbf{n}^{(1)}$ and $\mathbf{n}^{(2)}$ constitute the first and second eigenvectors of the Cauchy stress. The evolution equation (10.1) is solved by the forward Euler integration scheme. Since reorientation of fiber direction $\mathbf{a}^{(f)}$ results in an adjustment of orientation of the eigenvectors, the target fiber orientation changes from time step to time step. Accordingly, the time step width Δt as well as the parameters of the evolution equation k_{η}^{+} and m_{η}^{+} have to be chosen carefully to enable a convergence of $\mathbf{a}^{(f)}$ to the target fiber direction $\bar{\mathbf{A}}_{\text{targ}}^{(f)}$ and avoid oscillations for the angle $\eta^{(f)}$ in the process. The values of $k_{\eta}^{+} = 0.2$ and $m_{\eta}^{+} = 0.5$ with the time step width $\Delta t = 0.05$ s were sufficient for this purpose.

The results for the determination of the fiber orientation are illustrated in Fig. 10.1b and c. In Fig. 10.1b, the first eigenvector of the Cauchy stress is shown in the cross section area. The number of illustrated vectors is reduced to 700 to make the overview comprehensible. As can be seen, vectors are oriented in the direction which can be considered as circumferential at the corresponding material point. Furthermore, the final orientation of the fibers is displayed in Fig. 10.1c in which the artery is rotated

by an angle of 90° . The angle between first and second direction of collagen fibers at a material point is 30° which can be identified in the illustration. Consequently, the two step procedure was successful to determine a reliable direction for collagen and SMCs. It should be noted that a minor change of the direction of the eigenvectors of the Cauchy stress can be expected when the contraction of SMCs is considered in the material model. However, since collagen fibers and SMCs are defined to be oriented in the same directions, this adjustment of the eigenvectors is assumed to be negligible.

10.2 Consideration of Growth Directions and Adjustments of Growth Model

Before the growth model is activated, the steady state of the contraction of the active material model is reached for an intravascular pressure of 120 mmHg. It has to be noted that the application of the active material response leads to a considerable contraction which reduces the outer diameter to a smaller value than in the referential state. As a consequence, stresses can reach negative values which was already demonstrated for the stresses in axial direction over the wall thickness in Fig. 9.2. This change of the sign of the axial stresses did not change the order of the principal stresses in the simulations with a hollow cylinder in Chapter 9. However, for the more realistic geometry, the stresses in axial as well as circumferential direction can reach values lower than -16 kPa which represents the lowest possible value of the stresses in radial direction for an intravascular pressure of 120 mmHg. Since the order of eigenvalues is defined by the size of their values, it is not guaranteed that the first and second eigenvectors of the Cauchy stress are oriented in the circumferential and axial direction, respectively. This would lead to a considerable problem for the growth model. There, the growth factors $\vartheta^{(1)}$, $\vartheta^{(2)}$ and $\vartheta^{(3)}$ are considered to result in a directional adjustment of the tissue which can be identified as growth in circumferential, axial and radial direction, respectively. If the three directions are not comparable at every material point of the artery segment, the stresses will not be homogenized appropriately.

Growth Direction With regard to the described problem, orientation of all eigenvectors of the Cauchy stress is checked at the Gauss point before the growth process is started. Depending on their primary orientation, these eigenvectors are recognized as directed in circumferential, axial or radial direction and, consequently, considered as $\mathbf{n}^{(\text{cir})}$, $\mathbf{n}^{(\text{ax})}$ and $\mathbf{n}^{(\text{rad})}$. In the same manner, the corresponding principal Cauchy stresses are labeled as $\sigma^{(\text{cir})}$, $\sigma^{(\text{ax})}$ and $\sigma^{(\text{rad})}$ in this chapter. Accordingly, the driving forces $\phi^{(a)}$ in Eq. (9.2) as well as the growth parts of the deformation gradient $\mathbf{F}_g^{(a)}$ in Eq. (7.20) are not calculated based on the eigenvectors of the Cauchy stress $\mathbf{n}^{(1)}$, $\mathbf{n}^{(2)}$ and $\mathbf{n}^{(3)}$, but access $\mathbf{n}^{(\text{cir})}$, $\mathbf{n}^{(\text{ax})}$ and $\mathbf{n}^{(\text{rad})}$. This leads to the following adjustments

$$\begin{aligned} \mathbf{F}_g^{(1)} &= \mathbf{I} + (\vartheta^{(1)} - 1) \mathbf{n}^{(\text{cir})} \otimes \mathbf{n}^{(\text{cir})}, & \mathbf{F}_g^{(2)} &= \mathbf{I} + (\vartheta^{(2)} - 1) \mathbf{n}^{(\text{ax})} \otimes \mathbf{n}^{(\text{ax})}, \\ \mathbf{F}_g^{(3)} &= \mathbf{I} + (\vartheta^{(3)} - 1) \mathbf{n}^{(\text{rad})} \otimes \mathbf{n}^{(\text{rad})}, & & \\ \phi^{(1)}(\boldsymbol{\sigma}) &= \boldsymbol{\sigma} : (\mathbf{n}^{(\text{cir})} \otimes \mathbf{n}^{(\text{cir})}) & \text{and} & \phi^{(2)}(\boldsymbol{\sigma}) = \boldsymbol{\sigma} : (\mathbf{n}^{(\text{ax})} \otimes \mathbf{n}^{(\text{ax})}). \end{aligned} \quad (10.4)$$

Convergence Values To establish a reliable growth process, convergence values for the driving forces $\phi_{\text{con}}^{(a)}$ should be determined with regard to the new geometry. Since this geometry is not rotationally symmetric, consideration of the stress distribution over the wall thickness is not reliable for the calculation of $\phi_{\text{con}}^{(3)}$. Accordingly, a new concept is applied in which the mean value of the Cauchy stresses $\sigma^{(\text{cir})}$ and $\sigma^{(\text{ax})}$ is calculated by taking the stress values of all Gauss points into account. As described in the end of Section 4.3, weights of the Gauss points are not equal. Furthermore, the volume of the element should be considered to obtain an adequate estimation of the mean value of a principal stress. Therefore, the weighting factors w_p as well as the volume of the corresponding element V_p^{ele} are used in the calculation. The mean value of the Cauchy stress in circumferential direction is calculated by

$$\sigma_{\text{mean}}^{(\text{cir})} = \frac{\sum_{p=1}^{n_p} \sigma_p^{(\text{cir})} w_p V_p^{\text{ele}}}{\sum_{p=1}^{n_p} w_p V_p^{\text{ele}}} \quad \text{and} \quad \sigma_{\text{mean}}^{(\text{ax})} = \frac{\sum_{p=1}^{n_p} \sigma_p^{(\text{ax})} w_p V_p^{\text{ele}}}{\sum_{p=1}^{n_p} w_p V_p^{\text{ele}}} \quad \text{with} \quad (10.5)$$

$$\sigma_p^{(\text{cir})} = \boldsymbol{\sigma}_p : (\mathbf{n}_p^{(\text{cir})} \otimes \mathbf{n}_p^{(\text{cir})}) \quad \text{and} \quad \sigma_p^{(\text{ax})} = \boldsymbol{\sigma}_p : (\mathbf{n}_p^{(\text{ax})} \otimes \mathbf{n}_p^{(\text{ax})}) ,$$

where n_p is the total number of Gauss points, $\boldsymbol{\sigma}_p$ is the Cauchy stress at the Gauss point p and V_p^{ele} constitutes the volume of the element which the Gauss point p belongs to. Accordingly, the convergence value $\phi_{\text{con}}^{(3)}$ is calculated as

$$\phi_{\text{con}}^{(3)} = w_{\text{min}} (\sigma_{\text{mean}}^{(\text{cir})} + \sigma_{\text{mean}}^{(\text{ax})}) , \quad (10.6)$$

where the value of the parameter w_{min} is adopted from the optimization of the previous chapter as 0.884. For the determination of the convergence value $\phi_{\text{con}}^{(2)}$, it is assumed that $\phi_{\text{con}}^{(3)}$ and $\phi_{\text{con}}^{(2)}$ have the same ratio as in the optimal state in Chapter 9. The remaining convergence value is still calculated as $\phi_{\text{con}}^{(1)} = \phi_{\text{con}}^{(3)} - \phi_{\text{con}}^{(2)}$.

10.3 Execution of the Simulation

For the combination of growth and active material response, the same simulation protocol as described in Chapter 9 is applied. This includes a step-wise increase of the intravascular pressure from 10 mmHg to 120 mmHg where every pressure level is held over a time span of 300 s which leads to a steady state for the contraction of the artery segment at a load of 120 mmHg before the growth model is activated. Furthermore, the final values of the optimization parameters, which are listed in Table 5, are applied in the simulation. These parameters were also used in the reorientation of the fiber vectors. Values for the remaining parameters of the active material response are given in Table 2. Final values of the Cauchy stresses $\sigma^{(\text{cir})}$ and $\sigma^{(\text{ax})}$ are illustrated in a 3D contour plot in Fig. 10.2a and c. As can be seen, stresses in circumferential direction $\sigma^{(\text{cir})}$ show values lower than 0 kPa in some areas of the inner side of the wall. High stress of up to 110 kPa can be seen in the same area of the wall at the outer side. The stresses in axial direction $\sigma^{(\text{ax})}$ show comparable differences at the same location of the artery segment and are primarily negative which is equal to the simulation results in the previous chapter. One possible cause for stress differences could be the Dirichlet boundary conditions which restrict the movement at particular points, but enable more deformations at other locations. Different boundary conditions would probably lead to

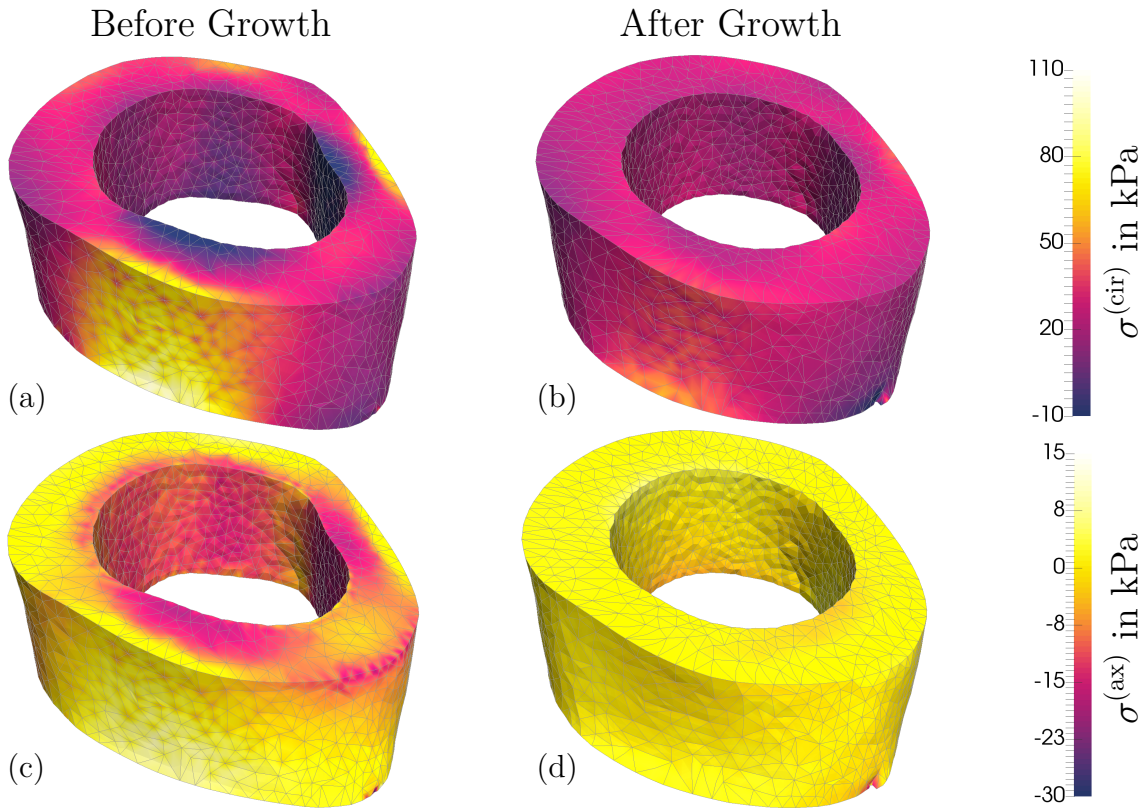


Figure 10.2: Contour plots of circumferential Cauchy stresses $\sigma^{(\text{cir})}$ (a) before activation of growth model and (b) after growth, as well as axial Cauchy stresses $\sigma^{(\text{ax})}$ (c) before activation of growth model and (d) after growth. The growth process homogenized the stresses considerably. Especially the stresses in axial direction are nearly the same over the entire geometry.

a lower difference of the stresses. However, the large gradient of the stresses over the wall thickness constitutes an appropriate example to investigate the capability of the growth model.

For the growth process, the same values for the growth velocity were considered as in Chapter 9 with $\kappa_{\vartheta}^{(1)} = 10^{-5}(\text{s} \cdot \text{kPa})^{-1}$, $\kappa_{\vartheta}^{(2)} = 10^{-4}(\text{s} \cdot \text{kPa})^{-1}$ and $\kappa_{\vartheta}^{(3)} = 10^{-4}(\text{s} \cdot \text{kPa})^{-1}$. The final distribution of the stresses $\sigma^{(\text{cir})}$ and $\sigma^{(\text{ax})}$ is displayed in Fig. 10.2b and d. This result was obtained after a run-time of 244s of the growth process. The contour plot displays a considerable adjustment of the stresses over the entire geometry. The stresses $\sigma^{(\text{ax})}$ are nearly equal over the entire geometry. The areas with the highest difference of the stresses $\sigma^{(\text{cir})}$ before growth show a considerable reduction, but certain differences remain along the wall. A local outlier can be detected at the bottom right edge where a node was restricted in movement due to the corresponding Dirichlet boundary condition in circumferential direction. Overall, a longer run-time of the growth process might lead to improvement, in particular for $\sigma^{(\text{cir})}$. However, the global Newton–Raphson method for the FE problem showed issues in the convergence after the 244s of the growth process. These issues are probably connected to the differences in the growth factors $\vartheta^{(a)}$ over the wall thickness which are illustrated in Fig. 10.3. Especially the growth factor $\vartheta^{(3)}$ reached values higher than 2.0 and lower than 0.45 which results in a significant change in the local material behavior. Also the changes

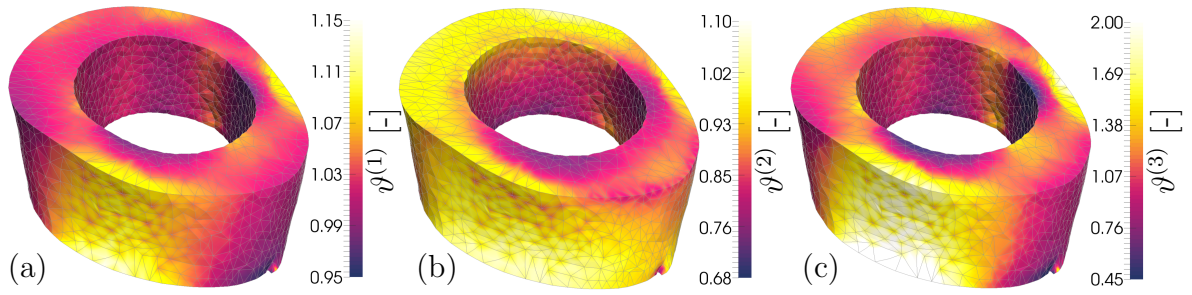


Figure 10.3: Contour plots of the growth factors (a) $\vartheta^{(1)}$, (b) $\vartheta^{(2)}$, and (c) $\vartheta^{(3)}$ at the end of the growth process. Major difference of the stresses occurred before the growth process was activated, which results in significant changes of the growth factors $\vartheta^{(a)}$ from their starting value of 1.0. Especially growth factor $\vartheta^{(3)}$ for growth in radial direction reached considerable differences over the wall thickness.

of the growth factors $\vartheta^{(1)}$ and $\vartheta^{(2)}$ are notably larger than in the simulations with a hollow cylinder (see Fig. 9.2). A possible improvement for the global Newton–Raphson method could be achieved by solving the evolution equations for the growth factors with an implicit method (see Eq. (7.21)). This adjustment has a notable impact on the determination of the tangent modulus, since the growth part \mathbb{C}^g has to be calculated as well. Therefore, implementation of the growth model in FE software with automatic differentiation would be preferable. Nonetheless, the obtained results constitute a notable accomplishment which is further underlined by Fig. 10.4.

Histograms for Cauchy Stresses at the Gauss Points

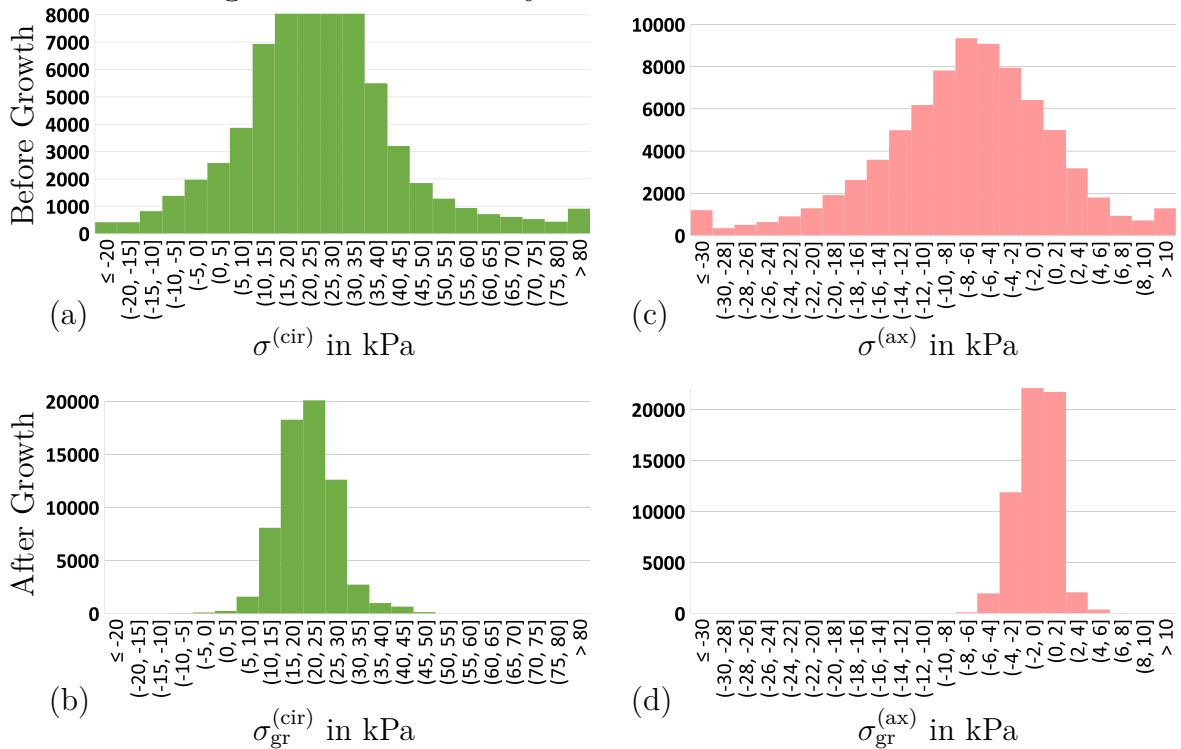


Figure 10.4: Histograms for values of Cauchy stresses at the Gauss points in circumferential direction (a) before growth and (b) after growth, as well as in axial direction (c) before growth and (d) after growth. The growth procedure realizes a significant homogenization of the stresses.

To display the improvement of the stresses $\sigma^{(\text{cir})}$ and $\sigma^{(\text{ax})}$ in more detail, the histograms in Fig. 10.4 show the distributions of these stresses over all 77,715 Gauss points of the mesh before and after the growth process. As illustrated in Fig. 10.4a and c, the difference between the stresses is immense before residual stresses are included. Roughly 10% of Gauss points exhibit values higher than 50 kPa for $\sigma^{(\text{cir})}$ and approximately 7% reach values lower than 0 kPa. Furthermore, more than 80% of the Gauss points have a negative stress value in axial direction which guarantees an axial compression of the artery segment. The convergence value for growth in radial direction was calculated to be $\phi_{\text{con}}^{(3)} = 22.63$ kPa. In consequence, the convergence value for growth in circumferential direction is $\phi_{\text{con}}^{(1)} = 21.35$ kPa which leads to the convergence value $\phi_{\text{con}}^{(1)} = 1.28$ kPa for growth in axial direction. After the growth process, 99% of the displayed stress values are positive in circumferential direction (see Fig. 10.4b) and the majority of values lies between 15 kPa and 30 kPa. A proportion of 95% of the Gauss points display stress between -4 kPa and 2 kPa (see Fig. 10.4d). In conclusion, the combination of the proposed kinematic growth model and the model for the active material response can be applied to more realistic geometries to establish a stretch-dependent contraction mechanism with a reliable description of the mechanical fields over the entire arterial wall.

11 Outlook: Separated Growth for Different Parts of Material

In Chapter 9, it was demonstrated that combining growth model and model for active response can result in adequate descriptions of the mechanical fields in an idealized geometry as long as certain conditions such as the axial prestretch and the fiber orientations are comparable to the physiological state. Furthermore, a considerable homogenization of the stresses was achieved for the application of these models in simulations with a more realistic geometry. Nonetheless, the most essential disadvantage of kinematic growth models is the missing separation of the material constituents which do not grow equally in the arterial tissue as was described in Section 2.3. This disadvantage might be insignificant as long as only young and healthy arteries are considered whose tissue experienced no damage so far. However, especially when patient-specific arteries are mechanically modeled and change of geometry and mechanical fields should be predicted for upcoming years by numerical simulations, differences in growth processes of collagen, elastin, SMCs, and possibly even fibroblasts result in crucial variations of the mechanical behavior for every constituent. In particular newly grown collagen fibers are responsible for the stability of damaged tissue. Therefore, a further extension of the kinematic growth model is suggested in this chapter which considers a separated growth process for collagen fibers. This approach has a certain similarity to the homogenized constraint mixture model by CYRON ET AL. [40] where the complexity of the constraint mixture model is simplified by combining constituents (such as collagen fibers in one direction) and applying only one growth part of the deformation gradient.

Subsequently, the adjustment of the growth model is briefly explained and the definition of the new convergence values for the driving forces is discussed. Afterwards, results are shown and analyzed for the application of the optimization procedure from Chapter 9 with the extended version of the growth model.

11.1 Additive Split of Material Model and Separated Growth

The strain-energy density function Ψ of the material model is separated into one part for the collagen fibers Ψ_{col} and one part for elastin and the contraction of SMCs Ψ_{act} . Based on this separation, the version of the kinematic growth model from Section 9.1 can be applied individually to each part. In consequence, the growth parts of the deformation gradients, $\mathbf{F}_{\text{g,act}}$ and $\mathbf{F}_{\text{g,col}}$, are different and lead to different elastic parts $\mathbf{F}_{\text{e,act}}$ and $\mathbf{F}_{\text{e,col}}$ (see Eq. (7.1)). Accordingly, the strain-energy density functions are expressed as

$$\Psi_{\text{act}}(\mathbf{C}_{\text{e,act}}) = \Psi_{\text{p,isot}}(\mathbf{C}_{\text{e,act}}) + \sum_{f=1}^2 \Psi_{\text{a}}^{(f)}(\mathbf{C}_{\text{e,act}}) \quad \text{and} \quad \Psi_{\text{col}}(\mathbf{C}_{\text{e,col}}) = \sum_{f=1}^2 \Psi_{\text{p,ti}}^{(f)}(\mathbf{C}_{\text{e,col}}),$$

$$\text{with } \mathbf{C}_{\text{e,act}} = \mathbf{F}_{\text{g,act}}^{-\text{T}} \mathbf{C} \mathbf{F}_{\text{g,act}}^{-1} \quad \text{and} \quad \mathbf{C}_{\text{e,col}} = \mathbf{F}_{\text{g,col}}^{-\text{T}} \mathbf{C} \mathbf{F}_{\text{g,col}}^{-1},$$
(11.1)

where $\mathbf{C}_{e, \text{act}}$ and $\mathbf{C}_{e, \text{col}}$ are the elastic parts of the right Cauchy-Green tensor of the active and the collagen part of the material, respectively. The second Piola-Kirchhoff stress tensor \mathbf{S} and the tangent modulus \mathbb{C} can be calculated as additive split which is formulated as

$$\mathbf{S} = \mathbf{S}_{\text{act}} + \mathbf{S}_{\text{col}} \quad \text{and} \quad \mathbb{C} = \mathbb{C}_{\text{act}} + \mathbb{C}_{\text{col}}. \quad (11.2)$$

Accordingly, each part of \mathbf{S} and \mathbb{C} is defined as described in Section 7.3.1 which results in

$$\begin{aligned} \mathbf{S}_{\text{act}} &= 2\mathbf{F}_{g, \text{act}}^{-1} \frac{\partial \Psi_{\text{act}}}{\partial \mathbf{C}_{e, \text{act}}} \mathbf{F}_{g, \text{act}}^{-\text{T}}, & \mathbf{S}_{\text{col}} &= 2\mathbf{F}_{g, \text{col}}^{-1} \frac{\partial \Psi_{\text{col}}}{\partial \mathbf{C}_{e, \text{col}}} \mathbf{F}_{g, \text{col}}^{-\text{T}}, \\ \mathbb{C}_{\text{act}} &= 2 \left(\mathbf{F}_{g, \text{act}}^{-1} \boxtimes \mathbf{F}_{g, \text{act}}^{-1} \right) : \frac{\partial \mathbf{S}_{e, \text{act}}}{\partial \mathbf{C}_{e, \text{act}}} : \left(\mathbf{F}_{g, \text{act}}^{-\text{T}} \boxtimes \mathbf{F}_{g, \text{act}}^{-\text{T}} \right) \quad \text{and} \\ \mathbb{C}_{\text{col}} &= 2 \left(\mathbf{F}_{g, \text{col}}^{-1} \boxtimes \mathbf{F}_{g, \text{col}}^{-1} \right) : \frac{\partial \mathbf{S}_{e, \text{col}}}{\partial \mathbf{C}_{e, \text{col}}} : \left(\mathbf{F}_{g, \text{col}}^{-\text{T}} \boxtimes \mathbf{F}_{g, \text{col}}^{-\text{T}} \right). \end{aligned} \quad (11.3)$$

Growth directions for both growth processes remain the eigenvectors $\mathbf{n}^{(a)}$ of the total Cauchy stresses $\boldsymbol{\sigma}$. In consequence, the growth parts of the deformation gradient $\mathbf{F}_{g, \text{act}}$ and $\mathbf{F}_{g, \text{col}}$ are only distinguished by considering different growth factors which are labeled as $\vartheta_{\text{act}}^{(a)}$ and $\vartheta_{\text{col}}^{(a)}$ (see Eq. (7.20)). Evolution equations of these growth factors are defined as expressed in Eq. (9.1) which results in

$$\dot{\vartheta}_{\text{act}}^{(a)} = \kappa_{\vartheta}^{(a)} \left(\phi_{\text{act}}^{(a)} - \phi_{\text{con, act}}^{(a)} \right) \quad \text{and} \quad \dot{\vartheta}_{\text{col}}^{(a)} = \kappa_{\vartheta}^{(a)} \left(\phi_{\text{col}}^{(a)} - \phi_{\text{con, col}}^{(a)} \right) \quad \text{with} \quad a = 1, 2, 3, \quad (11.4)$$

and with different driving forces, $\phi_{\text{act}}^{(a)}$ and $\phi_{\text{col}}^{(a)}$, and corresponding convergence values, $\phi_{\text{con, act}}^{(a)}$ and $\phi_{\text{con, col}}^{(a)}$. Determination of convergence values is discussed in the following section. Equations for the driving forces remain as defined in Eq. (9.2) but depend only on the Cauchy stresses corresponding to their material part $\boldsymbol{\sigma}_{\text{act}}$ and $\boldsymbol{\sigma}_{\text{col}}$, which leads to the formulation

$$\begin{aligned} \phi_{\text{act}}^{(1/2)}(\boldsymbol{\sigma}_{\text{act}}) &= \boldsymbol{\sigma}_{\text{act}} : \left(\mathbf{n}^{(1/2)} \otimes \mathbf{n}^{(1/2)} \right), & \phi_{\text{col}}^{(1/2)}(\boldsymbol{\sigma}_{\text{col}}) &= \boldsymbol{\sigma}_{\text{col}} : \left(\mathbf{n}^{(1/2)} \otimes \mathbf{n}^{(1/2)} \right), \\ \phi_{\text{act}}^{(3)} &= \phi_{\text{act}}^{(1)} + \phi_{\text{act}}^{(2)} \quad \text{and} \quad \phi_{\text{col}}^{(3)} &= \phi_{\text{col}}^{(1)} + \phi_{\text{col}}^{(2)}. \end{aligned} \quad (11.5)$$

The Cauchy stresses $\boldsymbol{\sigma}_{\text{act}}$ and $\boldsymbol{\sigma}_{\text{col}}$ are calculated as

$$\boldsymbol{\sigma}_{\text{act}} = \frac{1}{J} \mathbf{F} \mathbf{S}_{\text{act}} \mathbf{F}^{\text{T}} \quad \text{and} \quad \boldsymbol{\sigma}_{\text{col}} = \frac{1}{J} \mathbf{F} \mathbf{S}_{\text{col}} \mathbf{F}^{\text{T}}, \quad (11.6)$$

where J is the determinant of \mathbf{F} (see Eq. (3.5)).

It should be noted that a further separation of the material model into one part for elastin and another part for the SMCs could be considered. However, the SMCs are the dominant constituent of the mechanical model and are only defined in two directions without dependency on isotropic invariants of the right Cauchy-Green tensor. In test simulations with a further separation, the global Newton–Raphson method showed convergence problems when the growth part of the deformation gradients were significantly different for elastin and SMCs. Therefore, Ψ_{act} includes elastin as the isotropic material behavior of the tissue. To enable a further separation, the strain-energy density function of the SMCs could be changed to be dependent on isotropic

invariants of the right Cauchy-Green tensor such as formulated for the strain-energy density function $\Psi_{p,ti}^{(f)}$ of the collagen fibers [8].

11.2 Optimization with Inclusion of Active Material Response

The same optimization procedure as formulated in Chapter 9 is executed here for the separated growth of collagen. The only change is applied for the objective function z_1 (see Eq. (8.2)) which is only taking the growth factors $\phi_{act}^{(3)}$ of the active material into account. Accordingly, the objective function z_1 is expressed as

$$z_1 = 0.035 \sqrt{\frac{1}{n_{gp}} \sum_{g=1}^{n_{gp}} \left(\vartheta_{act,g}^{(3)} - 1 \right)^2}. \quad (11.7)$$

As a last uncertain aspect, the values of $\phi_{con,act}^{(a)}$ and $\phi_{con,col}^{(a)}$ have to be defined. The ratio between the values $\phi_{con,act}^{(a)}$ and $\phi_{con,col}^{(a)}$ indicates to which extend the corresponding material parts contribute to the material response at the considered load scenario of an intravascular pressure of 120 mmHg. Since a muscular artery is considered (middle cerebral artery of a rat), SMCs constitute the dominant fraction of the tissue and a substantial contraction is obtained at this load scenario. Hence, the convergence values of the active material part should be significantly larger than the convergences value of the material part for collagen. In the middle cerebral artery of a rat, the collagen fibers are expected to protect the tissue from overstretching when the intravascular pressure increases rapidly, but experience no notable load as long as the rat is not active. Considering these circumstances, the convergence values of the stresses of the collagen part are assumed to present 10% of the total stress. Accordingly, $\phi_{con,act}^{(1)}$ and $\phi_{con,act}^{(2)}$ represent 90% of the total stress in corresponding directions. While the convergence values for growth in the direction of the first eigenvector are optimized by the objective function z_1 , the convergence values for growth in direction of the second eigenvector are optimized to approach an axial prestretch of 1.1 for the arterial ring (see objective function z_4 in Eq. (9.4)). While the growth model is active, the same growth velocity factors are applied as in Chapter 9 with $\kappa_{\vartheta}^{(1)} = 10^{-5}(\text{s} \cdot \text{kPa})^{-1}$, $\kappa_{\vartheta}^{(2)} = 10^{-4}(\text{s} \cdot \text{kPa})^{-1}$ and $\kappa_{\vartheta}^{(3)} = 10^{-4}(\text{s} \cdot \text{kPa})^{-1}$. These are equally applied for the active part and the collagen part of the material.

The final results of the optimization parameters are listed in Table 6. The distribution of the stresses in circumferential and axial direction over the entire wall as well as corresponding growth factors are illustrated in Fig. 11.1. The stresses of active part and collagen part of the material are independently homogenized in circumferential and axial direction. However, homogenization was reached before the stresses equal the convergence values which is associated with the stopping criterion for the growth process in the optimization procedure. These values were determined as $\phi_{con,act}^{(1)} = 30.46 \text{ kPa}$ and $\phi_{con,col}^{(1)} = 3.38 \text{ kPa}$ for growth in circumferential direction, and $\phi_{con,act}^{(2)} = 2.22 \text{ kPa}$ and $\phi_{con,col}^{(2)} = 0.25 \text{ kPa}$ in axial direction. In consequence, the stresses $\sigma_{act,gr}^{(cir)}$ are

Table 6: Final values of the optimization parameters for inclusion of active response and separated growth of collagen

α_1	α_4	α_5	$r_{o, \text{ref}}$	$r_{i, \text{ref}}$	w_{min}
7.16kPa	1.04kPa	3.26	106.35 μm	81.82 μm	0.865
η	γ_1	$\dot{\lambda}_{c, \text{max}}$	$\dot{\lambda}_{c, \text{min}}$	$\dot{k}_{2/5, \text{max}}$	$\dot{k}_{2/5, \text{min}}$
0.1357s ⁻¹	0.3074 μM	0.0482s ⁻¹	-0.0482s ⁻¹	0.000576s ⁻²	-0.001012s ⁻²
$\dot{\lambda}_{p, \text{max}}$	$\dot{\lambda}_{p, \text{min}}$	μ_a	κ	β_1	$k_{2/5, \text{start}}$
0.000097s ⁻¹	-0.000103s ⁻¹	33.47kPa	107.81kPa	0.00078s ⁻¹	1.7168s ⁻¹

roughly 1 kPa too large while $\sigma_{\text{col, gr}}^{(\text{cir})}$ is 1 kPa too small. The resulting stresses in axial direction show opposing differences with an average value of 1.1 kPa for $\sigma_{\text{act, gr}}^{(\text{ax})}$ and an average value of 0.88 kPa for $\sigma_{\text{col, gr}}^{(\text{ax})}$. This means that stresses are not split with proportions of 90% and 10% for active and collagen part. The differences can be explained by the growth process of collagen fibers. The material model of the collagen fibers does not contribute to the stresses before growth (see Fig. 11.1c). Therefore, all growth factors $\vartheta_{\text{col}}^{(a)}$ decrease in the beginning of the growth process which establishes an increase of the elastic stretch. Eventually, the stresses in axial direction are larger than the convergence values which results in a rise of $\vartheta_{\text{col}}^{(2)}$ as can be seen in the final distribution in Fig. 11.1d. An increase of the growth velocity factors of the collagen part could avoid this inaccuracy.

The quality of the fitting of the material parameters can be estimated from the diagram in Fig. 11.2. There, the fully active (red) and suppressed active (green) parts are comparably precise as the results for the optimization in Chapter 9 (see Fig. 9.3). However, the graph for the passive material response shows even further gaps to the experimental data than before. This is probably induced by the individual growth of the collagen fibers. Especially the growth factor $\vartheta_{\text{col}}^{(3)}$, which expresses growth in radial direction, is significantly reduced for the separated growth in comparison to a process without separation (see blue graph in Fig. 9.3b). The average of $\vartheta_{\text{col}}^{(3)}$ is roughly 0.8 which is comparably smaller than the average of 0.93 for $\vartheta^{(3)}$ in the earlier optimization. This leads to a further elastic stretch of the the collagen fibers due to their individual growth process and a corresponding contribution to the stresses in the contracted state at 120 mmHg. The increased elastic stretch is also notable when only the passive material response is considered which results in a higher stiffness of the arterial ring. As a consequence, the passive material parameters would have to be decreased to reach the experimental data. However, the convergence values $\phi_{\text{con, col}}^{(a)}$ for growth of the collagen fibers enforce a 10% participation to the stresses at the contracted state of the artery which would simply result in a further reduction of the growth factors $\vartheta_{\text{col}}^{(a)}$, if the material parameters were decreased. A reduction of $\vartheta_{\text{col}}^{(a)}$ rises the elastic stretches even more. Accordingly, the optimal fitting of the passive material parameters seems difficult to

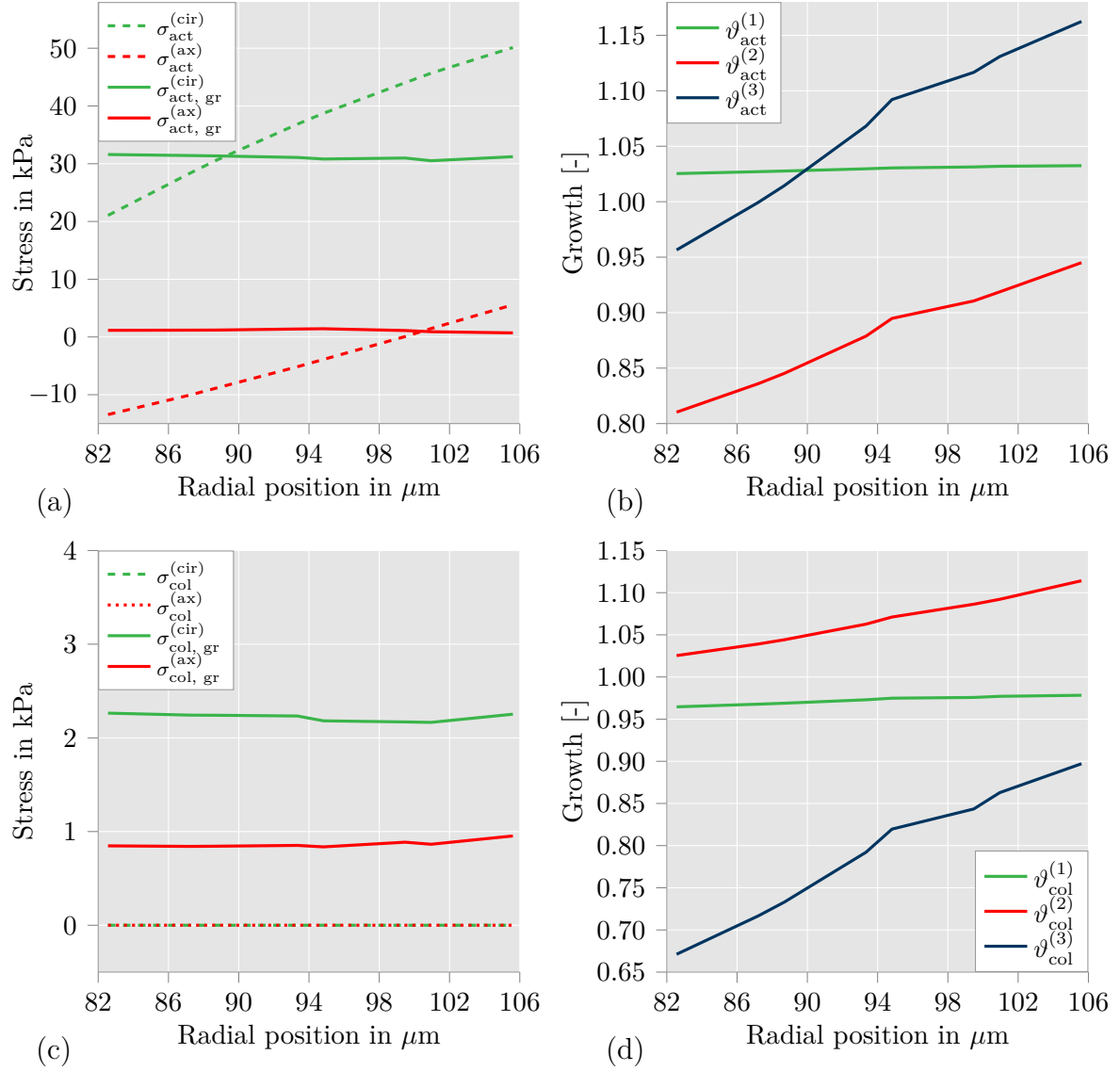


Figure 11.1: Distribution of (a) Cauchy stresses and driving forces $\sigma_{\text{act}}^{(\text{cir})} = \phi_{\text{act}}^{(1)}$ and $\sigma_{\text{act}}^{(\text{ax})} = \phi_{\text{act}}^{(2)}$ for active material as well as (c) $\sigma_{\text{col}}^{(\text{cir})} = \phi_{\text{col}}^{(1)}$ and $\sigma_{\text{col}}^{(\text{ax})} = \phi_{\text{col}}^{(2)}$ for material of collagen fibers. Furthermore, distribution of corresponding growth values (b) $\vartheta_{\text{act}}^{(1)}$, $\vartheta_{\text{act}}^{(2)}$ and $\vartheta_{\text{act}}^{(3)}$, as well as (d) $\vartheta_{\text{col}}^{(1)}$, $\vartheta_{\text{col}}^{(2)}$ and $\vartheta_{\text{col}}^{(3)}$. Dashed/dotted lines show results before growth, solid lines show results after growth. Artery is loaded with an intravascular pressure of 120 mmHg. Stresses are homogenized for both parts of the material in circumferential and axial direction. Separated growth of collagen lead to considerable decrease of growth factors $\vartheta_{\text{col}}^{(3)}$ to applied circumferential stresses.

achieve. Based on the stiffer material response, only an axial prestretch of 1.05 was reached (target value is 1.1). However, it is possible that the middle cerebral artery of the rat was overstretched during the experiment without Ca^{2+} in the Krebs solution around the artery. This overstretch would induce damage which is not considered here. Without tissue damage, an arterial ring would remain stiffer. Corresponding experimental data could be matched more accurately by the numerical simulations with optimized material parameters.

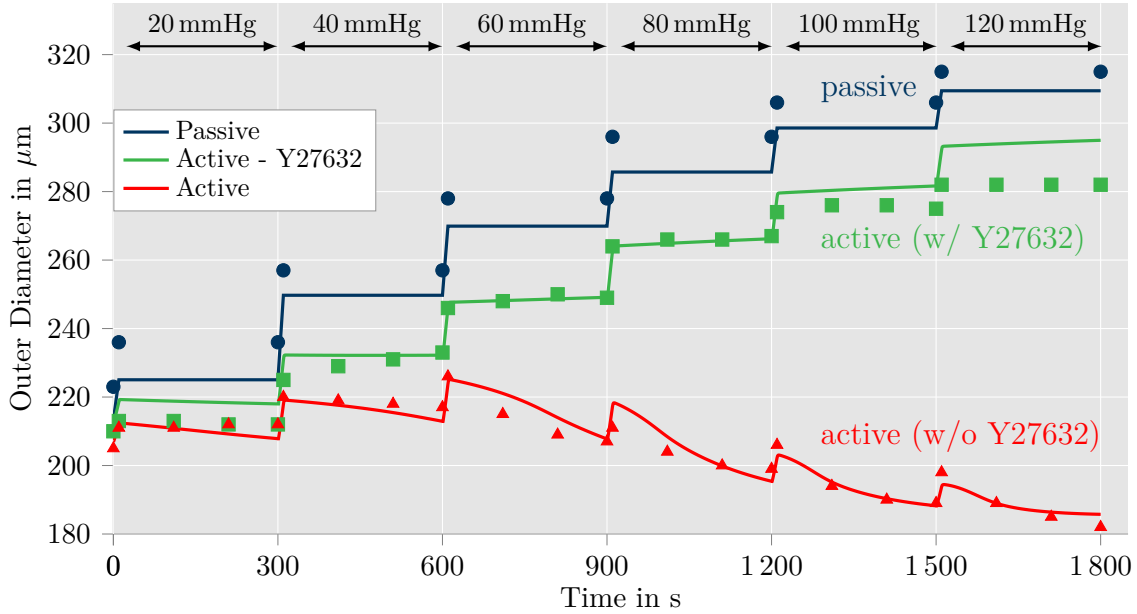


Figure 11.2: Comparison of the outer diameter of the arterial wall in simulations (solid lines) with experimental data from [94] (marks) for three different setups: passive response, active response under influence of $1\mu\text{M}$ Rho kinase inhibitor Y27632, and fully active response (see material model in Chapter 5). The results for the fully active model nearly correspond with experimental data. The graph for the passive material model shows larger differences to the experimental data in comparison to the fit without growth (see Fig. 6.2) and without separated growth for collagen fibers (see Fig. 8.7). Passive material response is stiffer with separated growth process. Accordingly, parameter fitting is more difficult.

Another effect of the stiffer passive material is the rise of the stresses in comparison to the results in Chapter 9. The geometry is fitted to obtain a ratio of 0.21 between outer diameter and wall thickness at an intravascular pressure of 15 mmHg while only the passive material response is applied. A ratio of 0.2104 was reached here. When only the passive material response is considered, the arterial ring is stretched in circumferential direction and decreases the wall thickness correspondingly while loaded. In consequence, a stiffer passive material leads to a lower circumferential stretch and a decreased reduction of the wall thickness which results in a lower wall thickness of the arterial ring in the referential state and, therefore, also in the contracted state. Accordingly, the stresses have to rise in the contracted state of the arterial wall.

In summary, the separation of the material model into two parts and a corresponding separation of their growth generates minor issues in the optimization procedure which decrease the accuracy of the structural problem. However, collagen fibers did not participate notably to the material response when the arterial ring was contracted without separated growth process in Chapter 9. Furthermore, consideration of individual growth for collagen, SMCs and potentially also elastin provides the possibility to model growth after damage of the arterial tissue. During the cure of the tissue, the material behavior of every constituent changes which was described in more detail in Section 2.3. Especially growth of collagen and SMCs contribute to the healing process, which differ in their proportions depending on the type of the artery. In consequence, the common version of the kinematic growth model would not be sufficient to pre-

dict the changes of the material in a diseased artery appropriately, since not only the proportions between collagen and SMCs growth are not adjustable, but also an equal growth of elastin is considered.

12 Conclusion and Outlook

This thesis focuses on the mechanical modeling of muscular arteries which, in contrast to elastic arteries, can reduce their diameter after an increase of blood pressure during higher body activity. This characteristic of arteries is known as Bayliss-effect. A novel model for the contraction of vascular SMCs was formulated considering the activity of MLCK and MLCP which is influenced by the stretch-dependent stimulation of GCPRs. Furthermore, this active material model was combined with a new kinematic growth model to include reliable residual stresses. While an inclusion of residual stresses improves the quality of the mechanical fields considerably, the applied growth model leads to an unpredictable volumetric change of the geometry and changes in the material behavior. The application of an optimization procedure enabled a reliable description of a middle cerebral artery of a rat. In the following paragraphs, the advantages, limitations, and possible expansions of the active material model as well as growth model are described separately.

Contraction of vascular SMCs The proposed active material model of the arterial wall included the stretch-dependent stimulation of biochemical processes in vascular SMCs for the first time which is currently also taken into account in other models as in FLANARY ET AL. [56]. The inclusion of the mechanical-chemical as well as chemical-mechanical coupling allowed the replication of the contraction of a middle cerebral artery of a rat in numerical simulations. Similar simulation results for small or medium-sized muscular arteries are not presented in any known publication of other research groups. In further simulations, the contractile behavior of the model was investigated by applying time-dependent intravascular pressure waves on the arterial wall which is a simplified approach to replicate the pulse pressure in the physiological state of the artery. An increase of the pressure in simulations resulted in a contraction of the artery which corresponds to the Bayliss-effect. Two further variations of the model were used in the same simulation scenario. While the first variation excluded only the stretch-dependent activity of MLCP, the second variation did not consider any mechanosensitivity of the chemical model part. Simulation results for both variations indicate that the mechanical-chemical coupling of the model is crucial to describe the contraction of muscular arteries reliably.

One disadvantage of the proposed material model is the necessity to fit the material parameters with a numerical optimization. The parameters of the model are not directly connected to distinct biochemical reactions. The set of equations in the model rather describes the general relationship between extracellular mechanical stimuli and the eventual effect on the myosin heads of the contractile units. While the fitted set of material parameters can be applied to obtain simulation results replicating the considered experimental data from JOHNSON ET AL. [94] sufficiently, it is unclear how many parameters have to be changed to describe the contraction of other artery types. The model by FLANARY ET AL. [56] offers a more detailed description of the intracellular reaction chains which might enable a straightforward adaptation of the model parameters to characterize the mechanical behavior of different artery types. However, a more detailed model also leads to an increased number of parameters. Comprehensive experiments are required to determine the values of these parameters. If such a

detailed model is able to replicate the contraction of muscular arteries in the current state of experiments remains unclear.

To apply numerical simulations to patient-specific arteries, it should be possible to consider diseased arteries with arteriosclerosis. An expansion of the material model for plaque components could be achieved by making use of NOBLE ET AL. [127]. Furthermore, the effect of antihypertensive drugs on the material model should be included. For this purpose, the proposed model for smooth muscle contraction provides sufficient access to involve CCBs (calcium channel blockers) and ARBs (angiotensin II receptor blocker) which react directly with the cell membrane. The blocking of calcium channels by CCBs can be expressed in the model by influencing the parameters of the calcium function and the corresponding target value. One exemplary adjustment of the proposed active material model to consider CCBs is published in BALZANI ET AL. [10]. For the inclusion of ARBs, the effect of blocked GCPRs on the model has to be realized. This could be achieved by reducing the stretch-sensitivity of the model part for mechanical-chemical coupling. In addition, vasoconstrictors and vasodilators from the autonomic nervous system or endothelial cells influence the contractility of vascular SMCs in vivo. The impact could be considered by an extension of the material model as described in YOSIBASH AND PRIEL [196]. However, the number of vasoconstrictors and vasodilators is considerable and should be reduced to a minimum.

As a last point, the interaction of the blood as a fluid with the arterial wall might be relevant when the mechanosensitivity of biochemical reactions is considered. The simulations in this thesis took only intravascular pressure into account which is applied perpendicularly to the inner side of the arterial wall. However, the blood flow leads also to wall shear stress (WSS) which plays a crucial role in vascular physiology and pathology. Especially when endothelial cells and the production of NO or ET-1 is included, their stimulation by WSS must be considered. This can only be realized by simulations with fluid-structure interaction.

Tissue Growth and Optimization of Structure Description The novel kinematic growth model is based on the simple idea to apply the principal Cauchy stresses as driving forces for an anisotropic growth process. This concept allows a minimization of the number of parameters to the growth velocities and the convergence values of the driving force in the corresponding growth direction. The growth directions are identified by the eigenvectors of the Cauchy stress which enables a commutative application. Simulations with idealized geometry and passive material response demonstrated that the target value of the driving forces is reached at every material point independent from predefined values of the growth velocities. Accordingly, the novel kinematic growth model constitutes a simple tool to include residual stresses in mechanical simulations of arteries but also other hollow organs such as urinary bladder or uterus.

The simulation results with passive material response showed also that the radial Cauchy stress should not be included in the driving forces. Radial stresses are strongly dependent on the boundary conditions of the simulation. In the simulations of this thesis, the radial stress at the inner side of the arterial ring is predefined by the applied intravascular pressure and the radial stress at the outer side is zero. Accordingly, the gradient of the radial stress over the wall thickness influences the results of the growth process when included in the driving forces.

Since the quality of the residual stresses is nearly independent from the values of the growth velocities, the combination of the growth model with the active material is straightforward. The time-dependency of the active material response is considered as predominant while the velocity of the growth model is adjusted to enable a reliable execution of the numerical simulation. While the definition of growth in radial and longitudinal direction is sufficient to reach homogeneous stress distributions in circumferential and axial direction of the arterial ring, experimental data indicates that growth is a three-dimensional process. Therefore, growth in circumferential direction is added to the growth model in the simulations with active material response. The results of simulations with combination of both models showed nearly equal circumferential and axial Cauchy stresses over the entire wall of the arterial ring. The potential of the combination was further underlined in a simulation with a more realistic geometry of an artery segment. There, the first principal Cauchy stress reached values between -20 kPa and 110 kPa before growth. After growth, the stresses were primarily adjusted to values between 10 kPa and 30 kPa.

Three disadvantages of the proposed growth model have to be noted: Firstly, it is necessary to define the convergence of the driving forces before the growth model is activated in the simulation. Secondly, the growth process changes the volume of the geometry which leads to an unpredictable shape of the resulting geometry after homogenization of the stresses. Thirdly, the application of the growth model changes the stress-strain behavior of the material model which might not match experimental data. The disadvantages were overcome by performing an optimization procedure for simulations with an idealized geometry of the arterial ring. As a result, the final version of the geometry matched measurements of a middle cerebral artery of a rat and the material parameters as well as the convergence values of the driving forces were automatically determined to match experimental data from JOHNSON ET AL. [94] with a homogenized stress distribution in axial and circumferential direction. Furthermore, the axial prestretch was optimized to correspond to experimental data for the residual stress. In consequence, the execution of the optimization results in a reliable representation of a healthy muscular artery for mechanical investigations.

Several aspects have to be considered to enable the prediction of tissue growth with the proposed growth model. Firstly, in the presented simulations, the growth model applied only one scalar for the convergence of the driving forces. However, tissue growth is initiated by mechanical stimulation which, e.g., releases TGF- β and leads to transitions of fibroblasts into myofibroblasts or a phenotype change of SMCs into synthetic states. It can be assumed that a certain stretch/stress of the tissue has to be reached before the growth process starts. In a similar way, the degeneration of tissue might not occur before the mechanical stretch/stress falls below a certain value. Accordingly, instead of a scalar, an interval could be defined for the convergence of the driving forces which represents the described limits of the tissue growth.

Secondly, the proposed model was defined to homogenize the stresses in axial and circumferential direction (first and second principal Cauchy stress). However, experimental data of large arteries such as TA, PA, and SFA indicate that the axial prestretch decreases significantly over the lifespan which should lead to a reduction of the stresses in this direction. Therefore, it might be possible that the stresses in axial direction are less relevant for the stimulation of tissue growth in aging arteries. Furthermore, the experimental data show that aging arteries grow considerably in radial and axial direction but only slightly in circumferential direction. If the axial stress does not

play a role in the stimulation of the growth process, the first principal Cauchy stress could be uniquely considered as driving force for growth in all directions. In addition, the amount of tissue growth in each direction could be governed by choosing different values for the growth velocities (high growth velocity in radial and axial direction; low growth velocity in circumferential direction). However, this approach should only be considered for the prediction of tissue growth in aging arteries. For healthy arteries in young humans, the described optimization procedure of this thesis leads to a reliable mechanical description of the arterial wall.

Thirdly, the growth of elastin, collagen, SMCs and other components of the tissue differs. An adjustment of the growth model is presented for separated growth of collagen fibers. This approach does not only allow an improved description of the mechanical fields of collagen fibers, but should also be considered for the prediction of tissue growth in diseased or damaged arteries. However, such an extension of growth model can only be achieved by determining the differences between the growth velocities of each component.

There are plenty of possibilities to improve the mechanical modeling of muscular arteries and accomplish simulations with patient-specific geometries. Although the general knowledge about body functions and intracellular reactions is extensive, the realization of model improvements might be limited to the attainable experimental data. However, the results of this thesis have shown that the missing quantification of biochemical reaction chains can be overcome by a simplified description of the reaction chains themselves. With a progress of biochemical experiments and novel modeling approaches, mechanical simulations of muscular arteries might be applied to improve medical diagnostics and treatment of patients with CVDs in the near future.

A Optimized Parameters for Adjusted, Active Case

Table 7: Active mechanical and chemical parameters with suppressed concentration and flow rate of calcium when SMCs are under the influence of Y27632 (see results in orange in Fig. 6.2), optimized

η	γ_1	$\dot{\lambda}_{c, \max}$	$\dot{\lambda}_{c, \min}$	$\dot{k}_{2/5, \max}$	$\dot{k}_{2/5, \min}$
0.1905s^{-1}	$0.5833\mu\text{M}$	0.05s^{-1}	-0.05s^{-1}	0.0018301s^{-2}	-0.0010865s^{-2}
$\dot{\lambda}_{p, \max}$	$\dot{\lambda}_{p, \min}$	μ_a	κ	β_1	$k_{2/5, \text{start}}$
0.00003983s^{-1}	-0.00035s^{-1}	24.153kPa	160.799kPa	0.000525s^{-1}	1.30029s^{-1}

B Previous Growth Model with Elastic Part of Mandel Stress as Driving Force

The main difference between the new growth model (model A) and the previous version (model B) consists in the definition of the evolution equations for the growth factors $\vartheta^{(a)}$. The evolution equation for model B is defined as

$$\dot{\vartheta}^{(a)} = \kappa_{\vartheta^{(a)}}^+ \left[\frac{\vartheta_{(a)}^+ - \vartheta^{(a)}}{\vartheta_{(a)}^+ - 1} \right]^{m_{\vartheta^{(a)}}^+} \phi^{(a)}, \quad (\text{B.1})$$

where $\vartheta^{(a)}$ is the growth factor, $\vartheta_{(a)}^+$ is the maximal value for the growth factor, $\kappa_{\vartheta^{(a)}}^+$ is the growth velocity factor, and $\phi^{(a)}$ is the driving force. The value of the exponent $m_{\vartheta^{(a)}}^+$ can be chosen as e.g. three or five, but was set to one here. The driving force $\phi^{(a)}$ is defined as dependent on the elastic part of the Mandel stress $\Sigma_e = \mathbf{C}_e \mathbf{S}_e$. As described in Section 7.3 for model A, growth is only considered in the direction of the second and third eigenvectors. While in model A the eigenvectors $\mathbf{n}^{(a)}$ of the Cauchy stresses were used, here the eigenvectors of Σ_e are applied. However, for the consideration of an arterial ring which is modeled as hollow cylinder, these directions do not differ, but point into axial and radial direction. Also comparable to the driving forces in model A, these are defined as the following for model B

$$\phi^{(2)}(\Sigma_e) = \Sigma_e : (\mathbf{n}^{(2)} \otimes \mathbf{n}^{(2)}) \quad \text{and} \quad \phi^{(3)}(\Sigma_e) = \Sigma_e : \mathbf{I}. \quad (\text{B.2})$$

More details about investigation of this growth model can be found in [203] and [202]. Note that a case differentiation is used in the original publication to decide which evolution equation is used for the growth factor. However, in the simulations shown here, the driving forces are always positive and, hence, the straightforward application of Eq. (B.1) is sufficient.

In Fig. B.1, the fitting of the material parameters towards the experimental data for

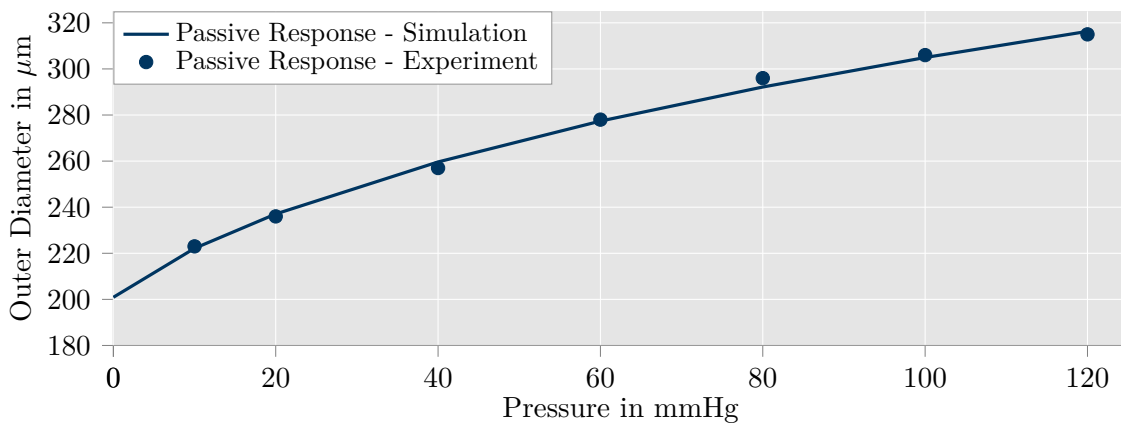


Figure B.1: Comparison of simulation results for the passive response of the arterial wall (solid line) with experimental data from [94] (dots) for the consideration of the previous growth model (model B) in the optimization. The results of the model nearly correspond with the experimental data. Illustration is adopted from UHLMANN AND BALZANI [178].

the passive response of the arterial wall in [94] is shown. Furthermore, the final values for the optimization parameters can be seen in Table 8.

Table 8: Final values of the optimization parameters for model B

Parameter	α_1	α_4	α_5	$\vartheta_{(2)}^+$	$\vartheta_{(3)}^+$	$\kappa_{\vartheta,(2)}^+$	$\kappa_{\vartheta,(3)}^+$
Value	2.97kPa	4.77kPa	2.55kPa	1.27	2.78	$4.95 \cdot 10^{-7} \text{s}^{-1}$	$4.35 \cdot 10^{-4} \text{s}^{-1}$

C Numerical Investigation of Optimization: Axial Stretch and Growth Factor

Variation of Axial Stretch λ_{ax}

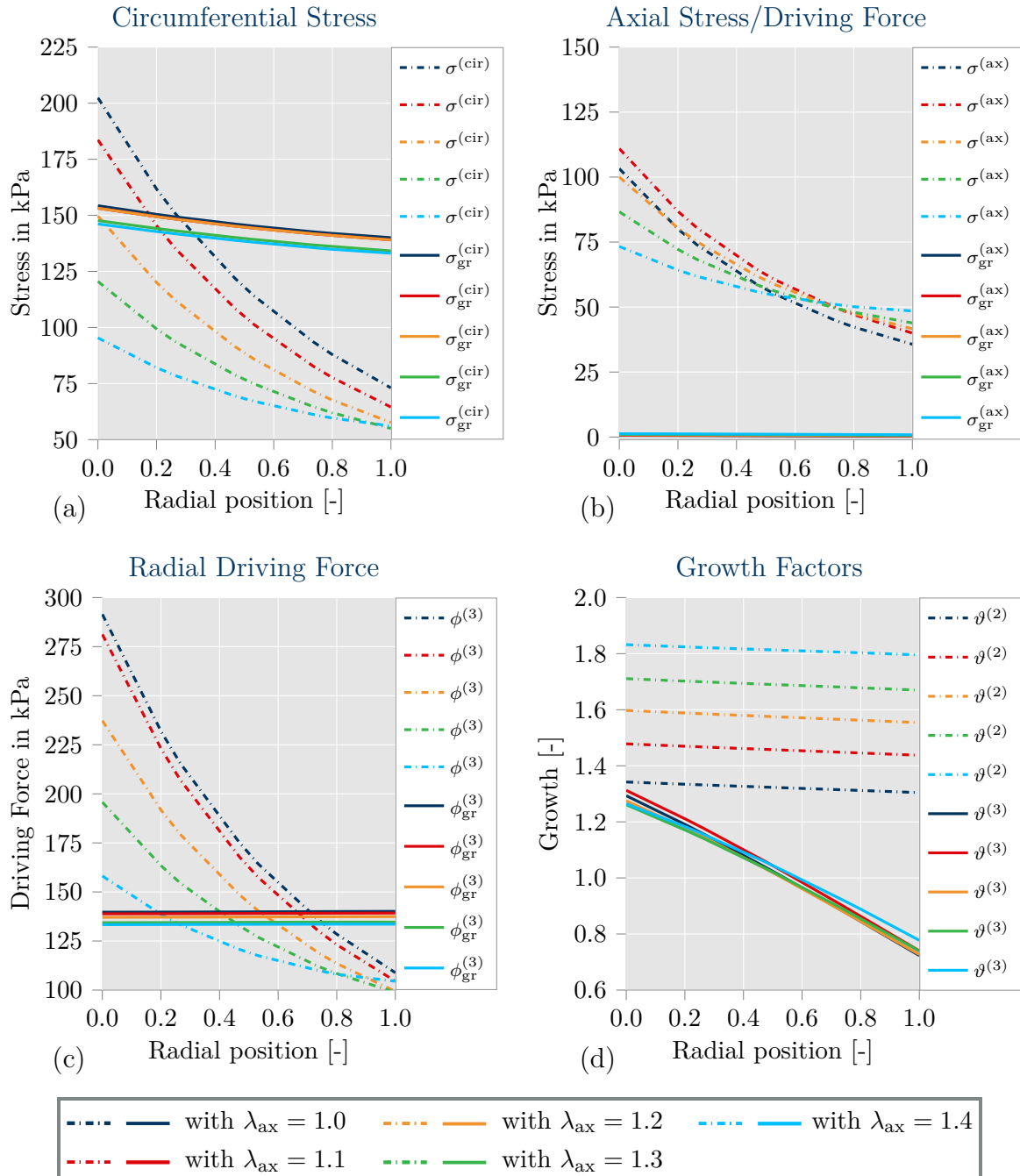


Figure C.1: Comparison of results from optimizations with different axial stretches λ_{ax} as boundary condition. Distribution of the (a) circumferential Cauchy stress $\sigma^{(cir)}$, (b) the axial stress/driving force $\sigma^{(ax)}/\phi^{(2)}$, (c) the radial driving force $\phi^{(3)}$ which directly influences the stresses in circumferential direction, and (d) the growth factors $\vartheta^{(2)}$ (axial) and $\vartheta^{(3)}$ (radial). Since the optimization of $r_{i,ref}$ and $r_{o,ref}$ does not lead to equal values for a variation of the fiber angle, the diagrams show relative values for the position of the Gauss points. Optimizations show convincing results for any value of the axial stretch λ_{ax} . Illustration is adopted from UHLMANN AND BALZANI [178].

Variation of Growth Convergence Value $\phi_{\text{con}}^{(2)}$

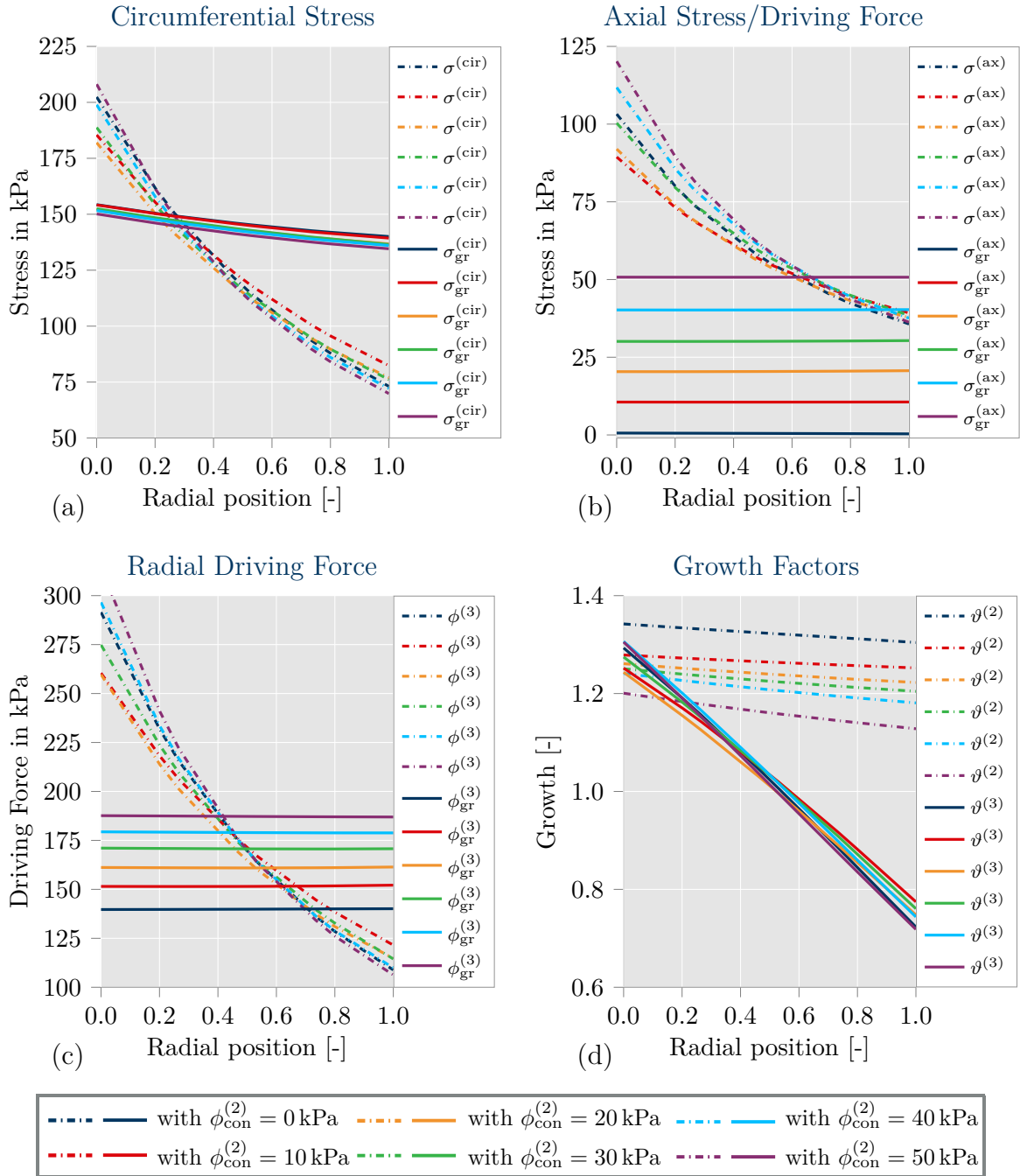


Figure C.2: Comparison of results from optimizations with different convergence values $\phi_{\text{con}}^{(2)}$ for the driving force $\phi^{(2)}$. Distribution of the (a) circumferential Cauchy stress $\sigma^{(\text{cir})}$, (b) the axial stress/driving force $\sigma^{(\text{ax})} / \phi^{(2)}$, (c) the radial driving force $\phi^{(3)}$ which directly influences the stresses in circumferential direction, and (d) the growth factors $\vartheta^{(2)}$ (axial) and $\vartheta^{(3)}$ (radial). Since the optimization of $r_{i,\text{ref}}$ and $r_{o,\text{ref}}$ does not lead to equal values for a variation of the fiber angle, the diagrams show relative values for the position of the Gauss points. Optimizations show convincing results for any convergence values $\phi_{\text{con}}^{(2)}$. Illustration is adopted from UHLMANN AND BALZANI [178].

D Growth with Active Response and Trace of Cauchy Stress as Driving Force

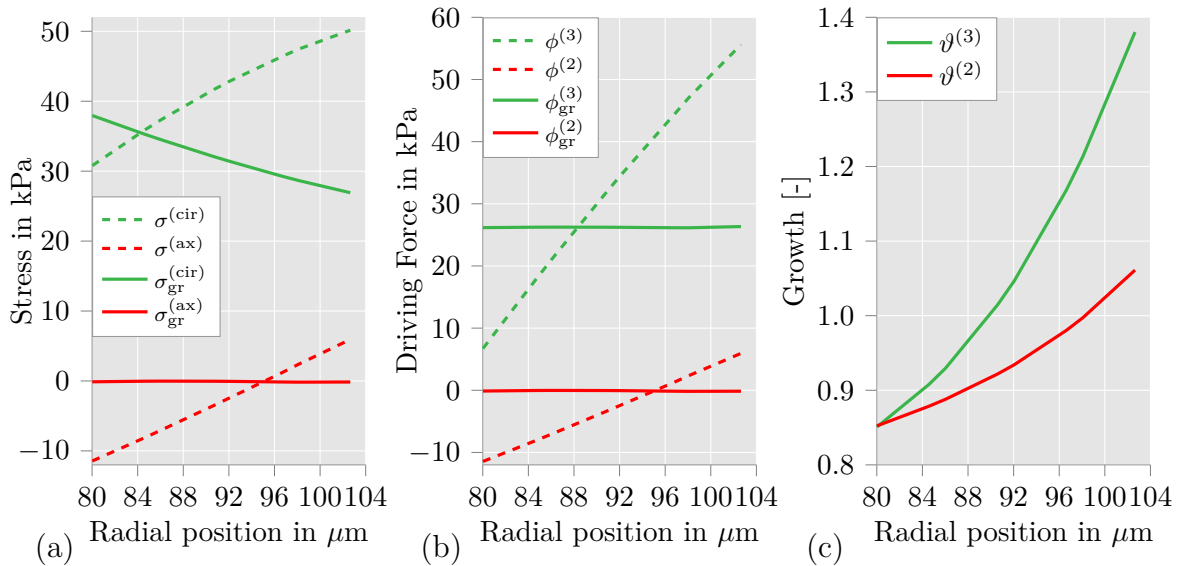


Figure D.1: Distribution of (a) Cauchy stresses $\sigma^{(\text{ax})}$ and $\sigma^{(\text{cir})}$, (b) driving forces $\phi^{(2)}$ and $\phi^{(3)}$, and (c) growth values $\vartheta^{(2)}$ and $\vartheta^{(3)}$ in circumferential (green) and axial (red) direction over the wall thickness for the fully active material model. Artery is loaded with an intravascular pressure of 120 mmHg. Dashed lines show results before growth, solid lines show results after growth. The new growth method also generates a homeostatic stress distribution for $\sigma^{(\text{ax})}$ when smooth muscle contraction is activated. Contrarily, $\sigma^{(\text{cir})}$ shows a significant gradient over the wall thickness caused by $\text{tr}(\sigma)$ as driving force $\phi^{(3)}$. Growth model from Chapter 7 was applied here which excludes growth in circumferential direction and applied trace of Cauchy stress as driving force for growth in radial direction. Illustration is adopted from UHLMANN AND BALZANI [178].

List of Figures

1.1	Death rates by cause in Europe	1
1.2	Usage of antihypertensive drugs in GB	2
2.1	Structure of a common arterial wall	9
2.2	Experimental data for passive material response of media and adventitia	11
2.3	Structure of SMC and function of contractile units	16
2.4	Regulation of intracellular calcium concentration in vascular SMCs . .	17
2.5	Schematic illustration of signal transduction pathways from stimulated receptors	19
2.6	Experimental data for active and passive material response of middle cerebral arteries of rats	22
2.7	Wall thickening of rats aorta at different systolic blood pressure	23
2.8	Schematic illustration of elastin synthesis	25
2.9	Synthesis and maturation scheme of collagen I	26
2.10	Phenotypes of vascular SMCs	27
2.11	Illustration of the transition of fibroblasts into myofibroblasts	31
2.12	Age-dependent growth of large human arteries	33
3.1	Motion of a body from the reference configuration \mathcal{B} into the current configuration \mathcal{S}	36
3.2	Deformation of infinitesimal line element $d\mathbf{X}$, area element dA and volume element dV	37
4.1	Examples of finite element approximation	51
4.2	Illustration of isoparametric mapping for a quadrilateral element	52
5.1	Schematic illustration of the model by Hai and Murphy	64
5.2	Illustration of different sigmoid functions	66
5.3	Comparison of forward and backward Euler method	72
5.4	Algorithm for the implementation of the active material model	79
6.1	Mesh of arterial ring, fiber directions and pressure profile	82
6.2	Comparison of three versions of the material model to experimental data	85
6.3	Contour plot of circumferential stresses	86
6.4	Plots of mechanical and chemical quantities over time for active material model	87
6.5	Load protocol for simulations with pressure waves	89
6.6	Change of outer diameter of arterial ring under pressure waves and comparison to model variations	90
7.1	Schematic representation of the multiplicative decomposition of the de- formation gradient	99
7.2	Algorithm for the implementation of the growth model	106
8.1	Bending of arterial ring after growth in radial direction	111
8.2	Bending of arterial ring after growth in circumferential direction	112
8.3	Bending of arterial strip after growth in axial direction	113
8.4	Mesh of arterial ring, Gauss points and fiber directions	115
8.5	Schematic representation of the optimization procedure	118
8.6	Results for optimized simulation after growth - passive response	120
8.7	Comparison of passive material model after growth to experimental data and contour plots of circumferential stresses	121

8.8	Results of optimized simulation after growth with former model	123
8.9	Time-wise evolution of stress at material point	124
8.10	Comparison of results for optimized simulations with different fiber angles	127
9.1	Schematic representation of the adjusted optimization procedure for inclusion of active material response	131
9.2	Results for optimized simulation after growth - active response	133
9.3	Comparison of three versions of material model after growth to experimental data	135
10.1	Mesh of realistic arterial segment and results of fiber reorientation . . .	138
10.2	Stress distribution in realistic arterial segment before and after growth	142
10.3	Distribution of growth factors in realistic arterial segment	143
10.4	Histograms for values of Cauchy stresses at Gauss points	143
11.1	Results for optimized simulation after separated growth of collagen and active material	149
11.2	Comparison of three versions of material model after separated growth to experimental data	150
B.1	Comparison of passive material response after growth with former model to experimental data	158
C.1	Comparison of results for optimized simulations with different axial stretch	160
C.2	Comparison of results for optimized simulations with different axial convergence values	161
D.1	Results for simulation after growth with trace of Cauchy stress as driving force - active response	162

List of Tables

1	Optimized passive parameters and opening angle	83
2	Chemical material parameters, manually adjusted/set prior to optimization	84
3	Active mechanical and chemical parameters, optimized	84
4	Final values of the optimization parameters and the corresponding values of the objective functions for variations of the angle of the collagen fibers, the axial stretch or the convergence value of the growth factor	126
5	Final values of the optimization parameters for inclusion of active response	134
6	Final values of the optimization parameters for inclusion of active response and separated growth of collagen	148
7	Active mechanical and chemical parameters with suppressed concentration and flow rate of calcium when SMCs are under the influence of Y27632	157
8	Final values of the optimization parameters for model B	159

List of Acronyms

ACEI	angiotensin-converting enzyme inhibitor
ARB	Angiotensin II receptor blocker
ATP	adenosine triphosphate
BB	beta blocker
CaM	calmodulin
CCB	calcium channel blocker
cGMP	cyclic guanosine monophosphate
CGRP	calcitonin gene-related peptide
CPI-17	C-kinase potentiated protein phosphatase-1 inhibitor
CSDA	complex-step derivative approximation
CVD	cardiovascular disease
DAG	diacylglycerol
EBP	elastin-binding protein
ECM	extracellular matrix
ER	endoplasmic reticulum
ET-1	endothelin-1
FEM	finite element method
G_{12/13}	G proteins which activate GEF for RhoA small GTP-binding protein
GEF	guanine nucleotide exchange factor
GPCR	G protein-coupled receptor
G_q	G proteins which activate phospholipase C- β enzyme
GTP	guanosine triphosphate
IP₃	inositol 1,4,5-trisphosphate
KLF2	Krüppel-like factor 2
KLF4	Krüppel-like factor 4
LAP	latency associated peptide
LDL	low-density lipoprotein
LLC	large latent complex
LTCC	voltage-gated L-type calcium channel
MHC	myosin heavy chain
MLC	myosin light chain
MLCK	myosin light-chain kinase
MLCP	myosin light-chain phosphatase
MSC	mesenchymal stem cell
MYPT1	myosin phosphatase target subunit 1
NO	nitric oxide
PA	popliteal artery
PDGF-BB	platelet-derived growth factor BB
PKC	protein kinase C
RER	rough endoplasmic reticulum
RNA	ribonucleic acid
mRNA	mature messenger RNA
ROCK	Rho-associated coiled-coil kinase
RyR	ryanodine receptor
SER	smooth endoplasmic reticulum

SFA	superficial femoral artery
SMC	smooth muscle cell
SR	sarcoplasmic reticulum
TA	thoracic aorta
TGF-β	transforming growth factor β
TRPC	transient receptor potential channel
UPR	unfolding protein response
WSS	wall shear stress

References

- [1] Scintica. <https://scintica.com/product/cell-and-isolated-tissue/pressure-arteriography/> [Accessed: 04 July 2024].
- [2] AHAMED, T., DORFMANN, L., AND OGDEN, R. Modelling of residually stressed materials with application to AAA. *J Mech Behav Biomed*, 61:221–234, 2016.
- [3] ALTENBACH, H. *Kontinuumsmechanik: Einführung in die materialunabhängigen und materialabhängigen Gleichungen*. Springer Vieweg, 4. Aufl. edition, 2018.
- [4] AMBERG, G. C., AND NAVEDO, M. F. Calcium dynamics in vascular smooth muscle. In *Microcirculation*, volume 20, pages 281–289. John Wiley & Sons Ltd., 2013.
- [5] AMBROSI, D., BEN AMAR, M., CYRON, C. J., DESIMONE, A., GORIELY, A., HUMPHREY, J. D., AND KUHL, E. Growth and remodelling of living tissues: perspectives, challenges and opportunities. *J R Soc Interface*, 16:20190233, 2019.
- [6] AN, S. J., BOYD, R., WANG, Y., QIU, X., AND WANG, H. D. Endothelin-1 expression in vascular adventitial fibroblasts. *Am J Physiol Heart Circ Physiol*, 290(2):H700–H708, 2006.
- [7] BALL, J. M. Convexity conditions and existence theorems in nonlinear elasticity. *Arch Ration Mech Anal*, 63:337–403, 1977.
- [8] BALZANI, D., NEFF, P., SCHRÖDER, J., AND HOLZAPFEL, G. A polyconvex framework for soft biological tissues. Adjustment to experimental data. *Int J Solids Struct*, 43(20):6052–6070, 2006.
- [9] BALZANI, D., SCHRÖDER, J., AND GROSS, D. Numerical Simulation of Residual Stresses in Arterial Walls. *Comput Mater Sci*, 39:117–123, 2007.
- [10] BALZANI, D., HEINLEIN, A., KLAWONN, A., KNEPPER, J., NURANI RAMESH, S., RHEINBACH, O., SASSMANNSHAUSEN, L., AND UHLMANN, K. A computational framework for pharmaco-mechanical interactions in arterial walls using parallel monolithic domain decomposition methods. *GAMM-Mitteilungen*, 47(1):e202370002, 2024.
- [11] BATHE, K. *Finite-Elemente-Methoden*. Springer, Berlin, Heidelberg, 2002.
- [12] BAYLISS, W. On the local reactions of the arterial wall to changes of internal pressure. *J Physiol*, 28:220–231, 1902.
- [13] BAŞAR, Y., AND WEICHERT, D. *Nonlinear Continuum Mechanics of Solids: Fundamental Mathematical and Physical Concepts*. Springer, 1 edition, 2000.
- [14] BEDNAREK, M. L., SPEICH, J. E., MINER, A. S., AND RATZ, P. H. Active tension adaptation at a shortened arterial muscle length: inhibition by cytochalasin-D. *Am J Physiol Heart Circ Physiol*, 300(4):H1166–H1173, 2011.

- [15] BELL, E. D., KUNJIR, R. S., AND MONSON, K. L. Biaxial and failure properties of passive rat middle cerebral arteries. *J Biomech*, 46:91–96, 2013.
- [16] BERNARD I. LEVY, A. T. *Biology of the Arterial Wall*. Basic Science for the Cardiologist. Springer, 1st edition, 1999.
- [17] BHATTACHARYYA, M., KARANDUR, D., AND KURIYAN, J. Structural Insights into the Regulation of Ca^{2+} /Calmodulin-Dependent Protein Kinase II (CaMKII). *Cold Spring Harb Perspect Biol*, 12(6):a035147, 2020.
- [18] BILLAUD, M., LOHMAN, A. W., JOHNSTONE, S. R., BIWER, L. A., MUTCHLER, S., AND ISAKSON, B. E. Regulation of Cellular Communication by Signaling Microdomains in the Blood Vessel Wall. *Pharmacol Rev*, 66(2):513–569, 2014.
- [19] BLANCO, P. J., MÜLLER, L. O., AND SPENCE, J. D. Blood pressure gradients in cerebral arteries: a clue to pathogenesis of cerebral small vessel disease. *Stroke and Vascular Neurology*, 2(3):108–117, 2017.
- [20] BLUM, M., BACHMANN, K., WINTZER, D., RIEMER, T., VILSER, W., AND STROBEL, J. Noninvasive measurement of the Bayliss effect in retinal autoregulation. *Graefes Arch Clin Exp Ophthalmol*, 237:296–300, 1999.
- [21] BLUMENTHAL, D. K., AND STULL, J. T. Activation of Skeletal Muscle Myosin Light Chain Kinase by Calcium(2+) and Calmodulin. *Biochemistry*, 19:5608–5614, 1980.
- [22] BOEHLER, J. P. *Introduction to the Invariant Formulation of Anisotropic Constitutive Equations*, pages 13–30. Springer Vienna, Vienna, 1987.
- [23] BÖL, M., SCHMITZ, A., NOWAK, G., AND SIEBERT, T. A three-dimensional chemo-mechanical continuum model for smooth muscle contraction. *J Mech Behav Biomed Mater*, 13:215–229, 2012.
- [24] BRAAKMAN, I., AND BULLEID, N. J. Protein Folding and Modification in the Mammalian Endoplasmic Reticulum. *Annu Rev Biochem*, 80:71–99, 2011.
- [25] BRAEU, F. A., SEITZ, A., AYDIN, R. C., AND CYRON, C. J. Homogenized constrained mixture models for anisotropic volumetric growth and remodeling. *Biomech Model Mechan*, 16:889, 2017.
- [26] BURKE, R. M., VILLAR, K. N. B., AND SMALL, E. M. Fibroblast contributions to ischemic cardiac remodeling. *Cell Signal*, 77:109824, 2021.
- [27] CASTIGLIONI, S., MONTI, M., VETTORE, A., ARNABOLDI, L., CANAVESI, M., CORSINI, A., AND BELLOSTA, S. ABCA1 and HDL₃ are required to modulate smooth muscle cells phenotypic switch after cholesterol loading. *Atherosclerosis*, 266:8–15, 2017.
- [28] CAÑADAS, V., VILACOSTA, I., BRUNA, I., AND FUSTER, V. Marfan syndrome. Part 1: pathophysiology and diagnosis. *Nat Rev Cardiol*, 7:256–265, 2010.

-
- [29] CHAPLIN, R., THACH, L., HOLLENBERG, M. D., CAO, Y., LITTLE, P. J., AND KAMATO, D. Insights into cellular signalling by G protein coupled receptor transactivation of cell surface protein kinase receptors. *J Cell Commun Signal*, 11:117–125, 2017.
- [30] CHATTOPADHYAY, A., KWARTLER, C. S., KAW, K., LI, Y., KAW, A., CHEN, J., LEMAIRE, S. A., SHEN, Y. H., AND MILEWICZ, D. M. Cholesterol-Induced Phenotypic Modulation of Smooth Muscle Cells to Macrophage/Fibroblast-like Cells Is Driven by an Unfolded Protein Response. *Arterioscler Thromb Vasc Biol*, 41(1):302–316, 2021.
- [31] CHEN, P.-Y., QIN, L., LI, G., MALAGON-LOPEZ, J., WANG, Z., BERGAYA, S., GUJJA, S., CAULK, A. W., MURTADA, S.-I., ZHANG, X., ZHUANG, Z. W., RAO, D. A., WANG, G., TOBIASOVA, Z., JIANG, B., MONTGOMERY, R. R., SUN, L., SUN, H., FISHER, E. A., GULCHER, J. R., FERNANDEZ-HERNANDO, C., HUMPHREY, J. D., TELLIDES, G., CHITTENDEN, T. W., AND SIMONS, M. Smooth Muscle Cell Reprogramming in Aortic Aneurysms. *Cell Stem Cell*, 26(4):524–557, 2020.
- [32] CHITANO, P., WANG, L., TIN, G. Y. Y., IKEBE, M., PARÉ, P. D., AND SEOW, C. Y. Smooth muscle function and myosin polymerization. *J Cell Sci*, 130:2468–2480, 2017.
- [33] CHRISTENSEN, K. L., AND MULVANY, M. J. Location of Resistance Arteries. *J Vasc Res*, 38(1):1–12, 2001.
- [34] CHUONG, C. J., AND FUNG, Y.-C. On Residual Stresses in Arteries. *J Biomech Eng*, 108:189–192, 1986.
- [35] COEN, M., GABBIANI, G., BOCHATON-PIALLAT, M.-L., AND CHEN, Y. E. Myofibroblast-Mediated Adventitial Remodeling. *Arterioscler Thromb Vasc Biol*, 31(11):2391–2396, 2011.
- [36] COLE, W. C., AND WELSH, D. G. Role of myosin light chain kinase and myosin light chain phosphatase in the resistance arterial myogenic response to intravascular pressure. *Arch Biochem Biophys*, 510:160–173, 2011.
- [37] COLE, W. C., GORDON, G. R., AND BRAUN, A. P. *Cellular and Ionic Mechanisms of Arterial Vasomotion*, pages 297–312. Springer Singapore, Singapore, 2019.
- [38] COMELLAS, E., CARRIERO, A., GIORGI, M., PEREIRA, A., AND SHEFELBINE, S. Chapter 2 - Modeling the Influence of Mechanics on Biological Growth. In *Numerical Methods and Advanced Simulation in Biomechanics and Biological Processes*, pages 17–35. Academic Press, 2018.
- [39] CYRON, C., AND HUMPHREY, J. Growth and remodeling of load-bearing biological soft tissues. *Meccanica*, 52:645–664, 2017.
- [40] CYRON, C. J., AYDIN, R. C., AND HUMPHREY, J. D. A homogenized constrained mixture (and mechanical analog) model for growth and remodeling of soft tissue. *Biomech Model Mechan*, 15:1389–1403, 2016.

- [41] CYRON, C. J., WILSON, J. S., AND HUMPHREY, J. D. Chapter 4 - Constitutive Formulations for Soft Tissue Growth and Remodeling. In *Biomechanics of Living Organs*, volume 1 of *Translational Epigenetics*, pages 79–100. Academic Press, Oxford, 2017.
- [42] DABRAVOLSKI, S. A., SUKHORUKOV, V. N., KALMYKOV, V. A., GRECHKO, A. V., SHAKHPAZYAN, N. K., AND OREKHOV, A. N. The Role of KLF2 in the Regulation of Atherosclerosis Development and Potential Use of KLF2-Targeted Therapy. *Biomedicines*, 10(2):254, 2022.
- [43] DEATON, R. A., GAN, Q., AND OWENS, G. K. Sp1-dependent activation of KLF4 is required for PDGF-BB-induced phenotypic modulation of smooth muscle. *Am J Physiol Heart Circ Physiol*, 296(4):H1027–H1037, 2009.
- [44] DIMOPOULOS, G. J., SEMBA, S., KITAZAWA, K., ETO, M., AND KITAZAWA, T. Ca^{2+} -Dependent Rapid Ca^{2+} Sensitization of Contraction in Arterial Smooth Muscle. *Circ Res*, 100(1):121–129, 2007.
- [45] DURHAM, A. L., SPEER, M. Y., SCATENA, M., GIACHELLI, C. M., AND SHANAHAN, C. M. Role of smooth muscle cells in vascular calcification: implications in atherosclerosis and arterial stiffness. *Cardiovasc Res*, 114(4):590–600, 2018.
- [46] D'URSO, M., AND KURNIAWAN, N. A. Mechanical and Physical Regulation of Fibroblast–Myofibroblast Transition: From Cellular Mechanoresponse to Tissue Pathology. *Front Bioeng Biotechnol*, 8, 2020.
- [47] ECKERSLEY, A., MELODY, K. T., PILKINGTON, S., GRIFFITHS, C. E., WATSON, R. E., O'CUALAIN, R., BALDOCK, C., KNIGHT, D., AND SHERRATT, M. J. Structural and compositional diversity of fibrillin microfibrils in human tissues. *J Biol Chem*, 293(14):5117–5133, 2018.
- [48] EICHINGER, J. F., HAEUSEL, L. J., PAUKNER, D., AYDIN, R. C., HUMPHREY, J. D., AND CYRON, C. J. Mechanical homeostasis in tissue equivalents: a review. *Biomech Model Mechanobiol*, 20:833–850, 2021.
- [49] EL-YAZBI, A. F., ABD-ELRAHMAN, K. S., AND MORENO-DOMINGUEZ, A. PKC-mediated cerebral vasoconstriction: Role of myosin light chain phosphorylation versus actin cytoskeleton reorganization. *Biochem Pharmacol*, 95(4):263–278, 2015.
- [50] ERBEL, R., AND EGGBRECHT, H. Aortic dimensions and the risk of dissection. *Heart*, 92(1):137–142, 2006.
- [51] ETO, M., AND KITAZAWA, T. Diversity and plasticity in signaling pathways that regulate smooth muscle responsiveness: Paradigms and paradoxes for the myosin phosphatase, the master regulator of smooth muscle contraction. *J Smooth Muscle Res*, 53:1–19, 2017.
- [52] FAMAHEY, N., VASTMANS, J., FEHERVARY, H., MAES, L., VANDERVEKEN, E., REGA, F., MOUSAVI, S. J., AND AVRIL, S. Numerical simulation of arterial remodeling in pulmonary autografts. *Z Angew Meth Mech*, 98:2239–2257, 2018.

-
- [53] FAN, Y., LU, H., LIANG, W., HU, W., ZHANG, J., AND CHEN, Y. E. Krüppel-like factors and vascular wall homeostasis. *J Mol Cell Biol*, 9(5):352–363, 2017.
- [54] FINLAY, H. M., MCCULLOUGH, L., AND CANHAM, P. B. Three-Dimensional Collagen Organization of Human Brain Arteries at Different Transmural Pressures. *J Vasc Res*, 32:301–312, 1995.
- [55] FLANARY, S. M., AND BAROCAS, V. H. A structural bio-chemo-mechanical model for vascular smooth muscle cell traction force microscopy. *Biomech Model Mechanobiol*, 22:1221–1238, 2023.
- [56] FLANARY, S. M., JO, S., RAVICHANDRAN, R., ALEJANDRO, E. U., AND BAROCAS, V. H. A computational bridge between traction force microscopy and tissue contraction. *J Appl Phys*, 134(7):074901, 2023.
- [57] FUNG, Y. C. Mathematical representation of the mechanical properties of the heart muscle. *J Biomech*, 269:381–404, 1970.
- [58] GANNON, K. P., VANLANDINGHAM, L. G., JERNIGAN, N. L., GRIFONI, S. C., HAMILTON, G., AND DRUMMOND, H. A. Impaired pressure-induced constriction in mouse middle cerebral arteries of ASIC2 knockout mice. *Am J Physiol Heart Circ Physiol*, 294:H1793–H1803, 2008.
- [59] GAO, Y. *Biology of Vascular Smooth Muscle: Vasoconstriction and Dilatation*. Springer, 2nd edition, 2022.
- [60] GIERIG, M. The Mechano-Chemo-Biology of Arterial Growth and Remodeling: A Continuum Modeling Framework for Tissue Response to Damage. *PhD thesis*, Gottfried Wilhelm Leibniz Universität Hannover, 2023.
- [61] GIERIG, M., WRIGGERS, P., AND MARINO, M. Computational model of damage-induced growth in soft biological tissues considering the mechanobiology of healing. *Biomech Model Mechanobiol*, 20:1297–1315, 2021.
- [62] GIERIG, M., WRIGGERS, P., AND MARINO, M. Arterial tissues and their inflammatory response to collagen damage: A continuum in silico model coupling nonlinear mechanics, molecular pathways, and cell behavior. *Comput Biol Med*, 158:106811, 2023.
- [63] GILBERT, R. R., GRAFENHORST, M., HARTMANN, S., AND YOSIBASH, Z. Simulating the temporal change of the active response of arteries by finite elements with high-order time-integrators. *Comput Mech*, 64:1669–1684, 2019.
- [64] GIUDICI, A., KHIR, A. W., SZAFRON, J. M., AND SPRONCK, B. From Uniaxial Testing of Isolated Layers to a Tri-Layered Arterial Wall: A Novel Constitutive Modelling Framework. *Ann Biomed Eng*, 49:2454–2467, 2021.
- [65] GÖKTEPE, S., ABILEZ, O. J., AND KUHL, E. A generic approach towards finite growth with examples of athlete’s heart, cardiac dilation, and cardiac wall thickening. *J Mech Phys Solids*, 58:1661–1680, 2010.

- [66] GOPALAN, C., AND KIRK, E. Chapter 8 - Blood pressure, hypertension, and exercise. In GOPALAN, C., AND KIRK, E., editors, *Biology of Cardiovascular and Metabolic Diseases*, pages 141–156. Academic Press, 2022.
- [67] GOUMANS, M.-J., AND TEN DIJKE, P. TGF- β Signaling in Control of Cardiovascular Function. *Cold Spring Harb Perspect Biol*, 10(2):a022210, 2018.
- [68] GUNNAL, S. A., FAROOQUI, M. S., AND WABALE, R. N. Study of Middle Cerebral Artery in Human Cadaveric Brain. *Ann Indian Acad Neurol*, 22(2): 187–194, 2019.
- [69] HAI, C. M., AND MURPHY, R. A. Cross-bridge phosphorylation and regulation of latch state in smooth muscle. *Am J Physiol*, 254:C99–106, 1988.
- [70] HALL, C. N., REYNELL, C., GESSLEIN, B., HAMILTON, N. B., MISHRA, A., SUTHERLAND, B. A., O’FARRELL, F. M., BUCHAN, A. M., LAURITZEN, M., AND ATTWELL, D. Capillary pericytes regulate cerebral blood flow in health and disease. *Nature*, 508:55–60, 2014.
- [71] HARRAZ, O. F., HILL-EUBANKS, D., AND NELSON, M. T. PIP₂: A critical regulator of vascular ion channels hiding in plain sight. *Proc Natl Acad Sci USA*, 117(34):20378–20389, 2020.
- [72] HASPINGER, D. C., MURTADA, S. I., NIESTRAWKA, J. A., AND HOLZAPFEL, G. A. Numerical analyses of the interrelation between extracellular smooth muscle orientation and intracellular filament overlap in the human abdominal aorta. *Z Angew Math Mech*, 98:2198–2221, 2018.
- [73] HAYASH, K., STERGIOPULOS, N., MEISTER, J.-J., GREENWALD, S. E., AND RACHEV, A. Techniques in the Determination of the Mechanical Properties and Constitutive Laws of Arterial Walls. In *Biomechanical Systems: Techniques and Applications, Volume II: Cardiovascular Techniques*, chapter 6, pages 1–61. CRC Press, 2001.
- [74] HILL, A. V. The heat of shortening and the dynamic constants of muscle. *Proc R Soc Lond B*, 126:136–195, 1938.
- [75] HIMPEL, G., KUHL, E., MENZEL, A., AND STEINMANN, P. Computational modelling of isotropic multiplicative growth. *Comput Model Eng Sci*, 8:119–134, 2005.
- [76] HINZ, B. The extracellular matrix and transforming growth factor- β 1: Tale of a strained relationship. *Matrix Biol*, 47:54–65, 2015.
- [77] HODGKIN, A. L., AND HUXLEY, A. F. A quantitative description of membrane current and its application to conduction and excitation in nerve. *J Physiol*, 117 (4):500–544, 1952.
- [78] HOLZAPFEL, G. *Nonlinear Solid Mechanics: A Continuum Approach for Engineering*. Wiley, 2000.
- [79] HOLZAPFEL, G. *Collagen in Arterial Walls: Biomechanical Aspects*, pages 285–324. Springer US, Boston, MA, 2008.

-
- [80] HOLZAPFEL, G. A., GASSER, T. C., AND OGDEN, R. W. A New Constitutive Framework for Arterial Wall Mechanics and a Comparative Study of Material Models. *J Elast*, 61, 2000.
- [81] HOLZAPFEL, G. A., SOMMER, G., GASSER, C. T., AND REGITNIG, P. Determination of layer-specific mechanical properties of human coronary arteries with nonatherosclerotic intimal thickening and related constitutive modeling. *Am J Physiol Heart Circ Physiol*, 289(5):H2048–H2058, 2005.
- [82] HOLZAPFEL, G. A., SOMMER, G., AUER, M., REGITNIG, P., AND OGDEN, R. W. Layer-Specific 3D Residual Deformations of Human Aortas with Non-Atherosclerotic Intimal Thickening. *Ann Biomed Eng*, 35:530–545, 2007.
- [83] HOLZAPFEL, G. A.; OGDEN, R. W. Modelling the layer-specific three-dimensional residual stresses in arteries, with an application to the human aorta. *J R Soc Interface*, 7, 2010.
- [84] HONG, F., BRIZENDINE, R. K., CARTER, M. S., ALCALA, D. B., BROWN, A. E., CHATTIN, A. M., HALDEMAN, B. D., WALSH, M. P., FACEMYER, K. C., BAKER, J. E., AND CREMO, C. R. Diffusion of myosin light chain kinase on actin: A mechanism to enhance myosin phosphorylation rates in smooth muscle. *J Gen Physiol*, 146(4):267–280, 2015.
- [85] HORNY, L., ADAMEK, T., GULTOVA, E., ZITNY, R., VESELY, J., CHLUP, H., AND KONVICKOVA, S. Correlations between age, prestrain, diameter and atherosclerosis in the male abdominal aorta. *J Mech Behav Biomed*, 4:2128–2132, 2011.
- [86] HUMPHREY, J. D. *Cardiovascular Solid Mechanics. Cells, Tissues, and Organs*. New York: Springer Science+Business Media., 2002.
- [87] HUMPHREY, J. D., AND RAJAGOPAL, K. R. A constrained mixture model for growth and remodeling of soft tissues. *Math Mod Meth Appl S*, 12:407, 2002.
- [88] INTENGAN, H. D., AND SCHIFFRIN, E. L. Structure and Mechanical Properties of Resistance Arteries in Hypertension. *Hypertension*, 36:312–318, 2000.
- [89] IRONS, L., AND HUMPHREY, J. D. Cell signaling model for arterial mechanobiology. *PLoS Comput Biol*, 16(8):1–22, 2020.
- [90] JACKSON, W. F., AND BOERMAN, E. M. Regional heterogeneity in the mechanisms of myogenic tone in hamster arterioles. *Am J Physiol Heart Circ Physiol*, 313:H667–H675, 2017.
- [91] JADIDI, M., RAZIAN, S. A., ANTTILA, E., DOAN, T., ADAMSON, J., PIPINOS, M., AND KAMENSKIY, A. Comparison of morphometric, structural, mechanical, and physiologic characteristics of human superficial femoral and popliteal arteries. *Acta Biomater*, 121:431–443, 2021.
- [92] JADIDI, M., RAZIAN, S. A., HABIBNEZHAD, M. AND ANTTILA, E., AND KAMENSKIY, A. Mechanical, structural, and physiologic differences in human elastic and muscular arteries of different ages: Comparison of the descending thoracic aorta to the superficial femoral artery. *Acta Biomater*, 119:268–283, 2021.

-
- [93] JIAO, T., PLATT, R. W., DOUROS, A., AND FILION, K. B. Prescription Patterns for the Use of Antihypertensive Drugs for Primary Prevention Among Patients With Hypertension in the United Kingdom. *Am J Hypertens*, 35(1): 42–53, 2021.
- [94] JOHNSON, R. P., EL-YAZBI, A. F., TAKEYA, K., WALSH, E. J., WALSH, M. P., AND COLE, W. C. Ca^{2+} sensitization via phosphorylation of myosin phosphatase targeting subunit at threonine-855 by Rho kinase contributes to the arterial myogenic response. *J Physiol*, 587.11:2537–2553, 2009.
- [95] JOLDES, G. R., NOBLE, C., POLZER, S., TAYLOR, Z. A., WITTEK, A., AND MILLER, K. A simple method of incorporating the effect of the Uniform Stress Hypothesis in arterial wall stress computations. *Acta Bioeng Biomech*, 20:59–67, 2018.
- [96] JUSTYNA A. NIESTRAWKA, D. C. H., AND HOLZAPFEL, G. A. The influence of fiber dispersion on the mechanical response of aortic tissues in health and disease: a computational study. *Comput Method Biomec*, 21(2):99–112, 2018.
- [97] KARAKI, H. Historical techniques: Cytosolic Ca^{2+} and contraction in smooth muscle. *Trends Pharmacol Sci*, 25(7):388–393, 2004.
- [98] KATZ, B. The relation between force and speed in muscular contraction. *J Physiol*, 96:45–64, 1939.
- [99] KLESCHYOV, A. L., MULLER, B., SCHOTT, C., AND STOCLET, J. C. Role of adventitial nitric oxide in vascular hyporeactivity induced by lipopolysaccharide in rat aorta. *Br J Pharmacol*, 124(4):623–6, 1998.
- [100] KOLEDOVA, V. V., AND KHALIL, R. A. Ca^{2+} , Calmodulin, and Cyclins in Vascular Smooth Muscle Cell Cycle. *Circ Res*, 98(10):1240–1243, 2006.
- [101] KOZEL, B. A., AND MECHAM, R. P. Elastic fiber ultrastructure and assembly. *Matrix Biol*, 84:31–40, 2019.
- [102] KRÄMER, M. S. Characterization of CNP-induced cGMP signaling in the gastrointestinal tract and its role in colonic smooth muscle relaxation. *PhD thesis*, Eberhard Karls Universität Tübingen, 2022.
- [103] KRÜGER-GENGE, A., BLOCKI, A., FRANKE, R.-P., AND JUNG, F. Vascular Endothelial Cell Biology: An Update. *Int J Mol Sci*, 20(18):4411, 2019.
- [104] KUHL, E. Growing matter: a review of growth in living systems. *J Mech Behav Biomed Mater*, 29:529–543, 2014.
- [105] KUHL, E., AND HOLZAPFEL, G. A. A continuum model for remodeling in living structures. *J Mater Sci*, 42:8811–8823, 2007.
- [106] KUHL, E., MAAS, R., HIMPEL, G., AND MENZEL, A. Computational modeling of arterial wall growth. *Biomech Model Mechanobiol*, 6:321–331, 2007.
- [107] LAPIDUS, L., AND PINDER, G. F. *Numerical Solution of Partial Differential Equations in Science and Engineering*. John Wiley & Sons, Inc., 1999.

-
- [108] LAWSON, J. S. Multiple Infectious Agents and the Origins of Atherosclerotic Coronary Artery Disease. *Front Cardiovasc Med*, 3, 2016.
- [109] LEE, E. Elasto-Plastic Deformation at Finite Strains. *J Appl Mech*, 36:1–6, 1969.
- [110] LEHNERS, M., DOBROWINSKI, H., FEIL, S., AND FEIL, R. cGMP Signaling and Vascular Smooth Muscle Cell Plasticity. *J Cardiovasc Dev Dis*, 5(2):20, 2018.
- [111] LELOUP, A. J. A., VAN HOVE, C. E., HEYKERS, A., SCHRIJVERS, D. M., DE MEYER, G. R. Y., AND FRANSEN, P. Elastic and Muscular Arteries Differ in Structure, Basal NO Production and Voltage-Gated Ca^{2+} -Channels. *Front Physiol*, 6, 2015.
- [112] LIU, H., ZHANG, M., LIU, M., MARTIN, C., CAI, Z., AND SUN, W. Finite element simulation of three dimensional residual stress in the aortic wall using an anisotropic tissue growth model. *J Mech Behav Biomed*, 92, 2019.
- [113] LIU, J. C.-Y., ROTTLER, J., WANG, L., ZHANG, J., PASCOE, C. D., LAN, B., NORRIS, B. A., HERRERA, A. M., PARÉ, P. D., AND SEOW, C. Y. Myosin filaments in smoothmuscle cells do not have a constant length. *J Physiol*, 591:5867–5878, 2013.
- [114] LUBARDA, V. A., AND HOGER, A. On the mechanics of solids with a growing mass. *IJSS*, 39:4627–4664, 2002.
- [115] MACDONALD, A. J., AND WALSH, P. M. Regulation of Smooth Muscle Myosin Light Chain Phosphatase by Multisite Phosphorylation of the Myosin Targeting Subunit, MYPT1. *Cardiovasc Hematol Disord Drug Targets*, 18(1):4–13, 2018.
- [116] MACRAE, R. A., MILLER, K., AND DOYLE, B. J. Methods in Mechanical Testing of Arterial Tissue: A Review. *Strain*, 52(5):380–399, 2016.
- [117] MATSUMOTO, T., AND HAYASHI, K. *Response of Arterial Wall to Hypertension and Residual Stress*, pages 93–119. Springer Japan, Tokyo, 1996a.
- [118] MATSUMOTO, T., AND HAYASHI, K. Stress and Strain Distribution in Hypertensive and Normotensive Rat Aorta Considering Residual Strain. *J Biomech Eng*, 118(1):62–73, 1996b.
- [119] MENZEL, A., AND KUHL, E. Frontiers in growth and remodeling. *Mech Res Commun*, 42:1–14, 2012.
- [120] MUHL, L., GENOVÉ, G., LEPTIDIS, S., LIU, J., HE, L., MOCCI, G., SUN, Y., GUSTAFSSON, S., BUYANDELGER, B., CHIVUKULA, I. V., SEGERSTOLPE, A., RASCHPERGER, E. HANSSON, E. M., BJÖRKEGREN, J. L. M., PENG, X.-R., VANLANDEWIJCK, M., LENDAHL, U., AND BETSHOLTZ, C. Single-cell analysis uncovers fibroblast heterogeneity and criteria for fibroblast and mural cell identification and discrimination. *Nat Commun*, 11:3953, 2020.
- [121] MURPHY, S. J., AND WERRING, D. J. Stroke: causes and clinical features. *Medicine*, 48(9):561–566, 2020.

-
- [122] MURTADA, S., KROON, M., AND HOLZAPFEL, G. A. A calcium-driven mechanochemical model for prediction of force generation in smooth muscle. *Biomech Model Mechanobiol*, 9:749–762, 2010a.
- [123] MURTADA, S., ARNER, A., AND HOLZAPFEL, G. A. Experiments and mechanochemical modeling of smooth muscle contraction: significance of filament overlap. *J Theor Biol*, 21:176–186, 2012.
- [124] MURTADA, S. I., HUMPHREY, J. D., AND HOLZAPFEL, G. A. Multiscale and Multiaxial Mechanics of Vascular Smooth Muscle. *Biophys J*, 113:714–727, 2017.
- [125] NAGY, J. A., BENJAMIN, L., ZENG, H., DVORAK, A. M., AND DVORAK, H. F. Vascular permeability, vascular hyperpermeability and angiogenesis. *Angiogenesis*, 11(2):109–119, 2008.
- [126] NGUYEN, E. K., KOVAL, O. M., NOBLE, P., BROADHURST, K., ALLAMARGOT, C., WU, M., STRACK, S., THIEL, W. H., AND GRUMBACH, I. M. CaMKII (Ca²⁺/Calmodulin-Dependent Kinase II) in Mitochondria of Smooth Muscle Cells Controls Mitochondrial Mobility, Migration, and Neointima Formation. *Arterioscler Thromb Vasc Biol*, 38(6):1333–1345, 2018.
- [127] NOBLE, C., CARLSON, K. D., NEUMANN, E., DRAGOMIR-DAESCU, D., ERDEMIR, A., LERMAN, A., AND YOUNG, M. Patient specific characterization of artery and plaque material properties in peripheral artery disease. *J Mech Behav Biomed*, 101:103453, 2020.
- [128] NOOM, A., SAWITZKI, B., KNAUS, P., AND DUDA, G. N. A two-way street – cellular metabolism and myofibroblast contraction. *NPJ Regen Med*, 9(15), 2024.
- [129] OISHI, Y., AND MANABE, I. Macrophages in inflammation, repair and regeneration. *Int Immunol*, 30(11):511–528, 2018.
- [130] ONURSAL, C., DICK, E., ANGELIDIS, I., SCHILLER, H. B., AND STAAB-WEIJNITZ, C. A. Collagen Biosynthesis, Processing, and Maturation in Lung Ageing. *Front Med*, 8, 2021.
- [131] OSOL, G., BREKKE, J. F., MCELROY-YAGGY, K., AND GOKINA, N. I. Myogenic tone, reactivity, and forced dilatation: a three-phase model of in vitro arterial myogenic behavior. *Am J Physiol Heart Circ Physiol*, 283(6):H2260–H2267, 2002.
- [132] OZSVAR, J., YANG, C., CAIN, S. A., BALDOCK, C., TARAKANOVA, A., AND WEISS, A. S. Tropoelastin and Elastin Assembly. *Front Bioeng Biotechnol*, 9: 643110, 2021.
- [133] O’CONNELL, M. K., MURTHY, S., PHAN, S., XU, C., BUCHANAN, J., SPILKER, R., DALMAN, R. L., ZARINS, C. K., DENK, W., AND TAYLOR, C. A. The Three-Dimensional Micro- and Nanostructure of the Aortic Medial Lamellar Unit Measured Using 3D Confocal & Electron Microscopy Imaging. *Matrix Biol*, 27(3):171–181, 2008.

-
- [134] PARASURAMAN, S., AND RAVEENDRAN, R. Measurement of invasive blood pressure in rats. *J Pharmacol Pharmacother*, 3(2):172–177, 2012.
- [135] PARRY, R., MAJEED, K., PIXLEY, F., HILLIS, G. S., FRANCIS, R. J., AND SCHULTZ, C. J. Unravelling the role of macrophages in cardiovascular inflammation through imaging: a state-of-the-art review. *Eur Heart J*, 23:e504–e525, 2022.
- [136] PASSERINI, T., PICCINELLI, M., VENEZIANI, A., AND ANTIGA, L. AneuriskWeb, 2012-2013. <http://ecm2.mathcs.emory.edu/aneuriskweb/repository> [Accessed: 11 March 2024].
- [137] PEDROZA, A. J., TASHIMA, Y., SHAD, R., CHENG, P., WIRKA, R., CHUROVICH, S., NAKAMURA, K., YOKOYAMA, N., CUI, J. Z., IOSEF, C., HIESINGER, W., QUERTERMOUS, T., AND FISCHBEIN, M. P. Single Cell Transcriptomic Profiling of Vascular Smooth Muscle Cell Phenotype Modulation in Marfan Syndrome Aortic Aneurysm. *Arterioscler Thromb Vasc Biol*, 40(9):2195–2211, 2020.
- [138] PEREIRA DA SILVA, E. A., MARTÍN-ARAGÓN BAUDEL, M., NAVEDO, M. F., AND NIEVES-CINTRÓN, M. Ion channel molecular complexes in vascular smooth muscle. *Front Psychol*, 13, 2022.
- [139] PETROV, V. V., FAGARD, R. H., AND LIJNEN, P. J. Stimulation of Collagen Production by Transforming Growth Factor- β_1 During Differentiation of Cardiac Fibroblasts to Myofibroblasts. *Hypertension*, 39(2):258–263, 2002.
- [140] PICCINELLI, M., VENEZIANI, A., STEINMAN, D. A., REMUZZI, A., AND ANTIGA, L. A Framework for Geometric Analysis of Vascular Structures: Application to Cerebral Aneurysms. *IEEE Trans Med Imaging*, 28, 2009.
- [141] POLZER, S., BURSA, J., GASSER, T. C., STAFFA, R., AND VLACHOVSKY, R. A Numerical Implementation to Predict Residual Strains from the Homogeneous Stress Hypothesis with Application to Abdominal Aortic Aneurysms. *Ann Biomed Eng*, 41:1516–1527, 2013.
- [142] POZNYAK, A. V., NIKIFOROV, N. G., STARODUBOVA, A. V., POPKOVA, T. V., AND OREKHOV, A. N. Macrophages and Foam Cells: Brief Overview of Their Role, Linkage, and Targeting Potential in Atherosclerosis. *Biomedicines*, 9(9):1221, 2021.
- [143] PRAKRIYA, M., AND LEWIS, R. S. Store-Operated Calcium Channels. *Physiol Rev*, 95(4):1383–1436, 2015.
- [144] QIAO, Y.-N., HE, W.-Q., CHEN, C.-P., ZHANG, C.-H., ZHAO, W., WANG, P., ZHANG, L., WU, Y.-Z., YANG, X., PENG, Y.-J., GAO, J.-M., KAMM, K. E., STULL, J. T., AND ZHU, M.-S. Myosin Phosphatase Target Subunit 1 (MYPT1) Regulates the Contraction and Relaxation of Vascular Smooth Muscle and Maintains Blood Pressure. *J Biol Chem*, 289(32):22512–22523, 2014.
- [145] RATZ, P. H. *Mechanics of Vascular Smooth Muscle*, pages 111–168. John Wiley & Sons, Ltd, 2015.

-
- [146] RINGVOLD, H., AND KHALIL, R. Chapter Six - Protein Kinase C as Regulator of Vascular Smooth Muscle Function and Potential Target in Vascular Disorders. In KHALIL, R. A., editor, *Vasc Pharmacol*, volume 78 of *Advances in Pharmacology*, pages 203–301. Academic Press, 2017.
- [147] ROBERTSON, I. B., AND RIFKIN, D. B. Unchaining the beast; insights from structural and evolutionary studies on TGF β secretion, sequestration, and activation. *Cytokine Growth Factor Rev*, 24(4):355–372, 2013.
- [148] RODRIGUEZ, E. K., HOGER, A., AND MCCULLOCH, A. D. Stress-dependent finite growth in soft elastic tissues. *J Biomech*, 27:455–467, 1994.
- [149] RÜEGG, J. C. *Smooth Muscle*, pages 895–910. Springer Berlin Heidelberg, 1996.
- [150] SAEZ, P. On the Theories and Numerics of Continuum Models for Adaptation Processes in Biological Tissues. *Arch Computat Methods Eng*, 23:301–322, 2016.
- [151] SANDOW, S. L., GZIK, D. J., AND LEE, R. M. K. W. Arterial internal elastic lamina holes: relationship to function? *J Anat*, 214:258–266, 2009.
- [152] SCHRIEFL, A. J., REINISCH, A. J., SANKARAN, S., PIERCE, D. M., AND HOLZAPFEL, G. A. Quantitative assessment of collagen fibre orientations from two-dimensional images of soft biological tissues. *J R Soc Interface*, 9:3081–3093, 2012.
- [153] SCHRIEFL, A. J., ZEINDLINGER, G., PIERCE, D. M., REGITNIG, P., AND HOLZAPFEL, G. A. Determination of the layer-specific distributed collagen fibre orientations in human thoracic and abdominal aortas and common iliac arteries. *J R Soc Interface*, 9:1275–1286, 2012.
- [154] SCHRÖDER, J., AND BRINKHUES, S. A novel scheme for the approximation of residual stresses in arterial walls. *Arch Appl Mech*, 84, 2014.
- [155] SCHRÖDER, J., AND NEFF, P. Invariant formulation of hyperelastic transverse isotropy based on polyconvex free energy functions. *Int J Solids Struct*, 40: 401–445, 2003.
- [156] SCHRÖDER, M., AND KAUFMAN, R. J. ER stress and the unfolded protein response. *Mutat Res-Fund Mol M*, 569(1):29–63, 2005.
- [157] SCHULZE-BAUER, C. A. J., MÖRTH, C., AND HOLZAPFEL, G. A. Passive Biaxial Mechanical Response of Aged Human Iliac Arteries. *J Biomech Eng*, 125: 395–406, 2003.
- [158] SERINI, G., AND GABBIANI, G. Modulation of α -smooth muscle actin expression in fibroblasts by transforming growth factor- β isoforms: an in vivo and in vitro study. *Wound Repair Regen*, 4(2):278–287, 1996.
- [159] SEYDEWITZ, R., MENZEL, R., SIEBER, T., AND BÖL, M. Three-dimensional mechano-electrochemical model for smooth muscle contraction of the urinary bladder. *J Mech Behav Biomed Mater*, 75:128–146, 2017.

-
- [160] SHARIFIMAJD, B., THORE, C.-J., AND STÅLHAND, J. Simulating uterine contraction by using an electro-chemo-mechanical model. *Biomech Model Mechanobiol*, 15:497–510, 2016.
- [161] SHENG, Y., AND ZHU, L. The crosstalk between autonomic nervous system and blood vessels. *Int J Physiol Pathophysiol Pharmacol*, 10(1):17–28, 2018.
- [162] SIGAEVA, T., SOMMER, G., HOLZAPFEL, G. A., AND DI MARTINO, E. S. Anisotropic residual stresses in arteries. *J R Soc Interface*, 16, 2019.
- [163] SOMMER, G., REGITNIG, P., KÖLTRINGER, L., AND HOLZAPFEL, G. A. Biaxial mechanical properties of intact and layer-dissected human carotid arteries at physiological and suprphysiological loadings. *Am J Physiol Heart Circ Physiol*, 298(3):H898–H912, 2010.
- [164] SOMMER, G., REGITNIG, P., KÖLTRINGER, L., AND HOLZAPFEL, G. A. Biaxial mechanical properties of intact and layer-dissected human carotid arteries at physiological and suprphysiological loadings. *Am J Physiol Heart Circ Physiol*, 298:H898–H912, 2010.
- [165] STORCH, U., SCHNITZLER, M. M. Y., AND GUDERMANN, T. G protein-mediated stretch reception. *Am J Physiol Heart Circ Physiol*, 302(6):H1241–H1249, 2012.
- [166] STÅLHAND, J., AND HOLZAPFEL, G. A. Length adaptation of smooth muscle contractile filaments in response to sustained activation. *J Theor Biol*, 397:13–21, 2016.
- [167] STÅLHAND, J., KLARBRING, A., AND HOLZAPFEL, G. A. A mechanochemical 3D continuum model for smooth muscle contraction under finite strains. *J Theor Biol*, 268:120–130, 2011.
- [168] SUN, J., QIAO, Y.-N., TAO, T., ZHAO, W., WEI, L.-S., LI, Y.-Q., WANG, W., WANG, Y., ZHOU, Y.-W., ZHENG, Y.-Y., CHEN, X., PAN, H.-C., ZHANG, X.-N., AND ZHU, M.-S. Distinct Roles of Smooth Muscle and Non-muscle Myosin Light Chain-Mediated Smooth Muscle Contraction. *Front Physiol*, 11, 2020.
- [169] SÁEZ, P., PEÑA, E., MARTÍNEZ, M., AND KUHL, E. Computational modeling of hypertensive growth in the human carotid artery. *Comput Mech*, 53:1183–1196, 2014.
- [170] TABER, L. A., AND HUMPHREY, J. D. Stress-modulated growth, residual stress, and vascular heterogeneity. *J Biomech Eng*, 123:528, 2001.
- [171] TAI, Y., WOODS, E. L., DALLY, J., KONG, D., STEADMAN, R., MOSELEY, R., AND MIDGLEY, A. C. Myofibroblasts: Function, Formation, and Scope of Molecular Therapies for Skin Fibrosis. *Biomolecules*, 11(8), 2021.
- [172] TANAKA, M., FUJIKAWA, M., BALZANI, D., AND SCHRÖDER, J. Robust numerical calculation of tangent moduli at finite strains based on complex-step derivative approximation and its application to localization analysis. *Comput Methods Appl Mech Engrg*, 269:454–470, 2014.

- [173] TAYLOR, K. A., FEIG, M., BROOKS, C. L., FAGNANT, P. M., LOWEY, S., AND TRYBUS, K. M. Role of the essential light chain in the activation of smooth muscle myosin by regulatory light chain phosphorylation. *J Struct Biol*, 185(3): 375–382, 2014.
- [174] TIMMIS, A., VARDAS, P., TOWNSEND, N., TORBICA, A., KATUS, H., DE SMEDT, D., GALE, C. P., MAGGIONI, A. P., PETERSEN, S. E., HUCULECI, R., KAZAKIEWICZ, D., DE BENITO RUBIO, V., IGNATIUK, B., RAISI-ESTABRAGH, Z., PAWLAK, A., KARAGIANNIDIS, E., TRESKES, R., GAITA, D., BELTRAME, J. F., MCCONNACHIE, A., BARDINET, I., GRAHAM, I., FLATHER, M., ELLIOTT, P., MOSSIALOS, E. A., WEIDINGER, F., AND ACHENBACH, S. European Society of Cardiology: cardiovascular disease statistics 2021. *Eur Heart J*, 43(8):716–799, 2022.
- [175] TYKOCKI, N. R., BOERMAN, E. M., AND JACKSON, W. F. Smooth Muscle Ion Channels and Regulation of Vascular Tone in Resistance Arteries and Arterioles. *Compr Physiol*, 7:485–581, 2017.
- [176] UCCELLI, A., MORETTA, L., AND PISTOIA, V. Mesenchymal stem cells in health and disease. *Nat Rev Immunol*, 8:726–736, 2008.
- [177] UHLMANN, K., AND BALZANI, D. Chemo-mechanical modeling of smooth muscle cell activation for the simulation of arterial walls under changing blood pressure. *Biomech Model Mechanobiol*, 22:1049–1065, 2023.
- [178] UHLMANN, K., AND BALZANI, D. Homeostatic Kinematic Growth Model for Arteries - Simulation of Residual Stresses and Active Response. *arXiv*, 2025. doi: 10.48550/arXiv.2502.20024.
- [179] UHLMANN, K., ZAHN, A., AND BALZANI, D. Simulation of Arterial Walls: Growth, Fiber Reorientation, and Active Response. In *Solid (Bio)mechanics: Challenges of the Next Decade*, chapter 8, pages 181–209. Springer Nature, 2022.
- [180] UREVC, J., BRUMEN, M., FLIS, V., AND ŠTOK, B. Applying Thermomechanical Analogy to Predict the Arterial Residual Stress State. *Stroj Vestn-J Mech E*, 61, 2015.
- [181] VACANTE, F., DENBY, L., SLUIMER, J. C., AND BAKER, A. H. The function of miR-143, miR-145 and the MiR-143 host gene in cardiovascular development and disease. *Vasc Pharmacol*, 112:24–30, 2019.
- [182] WAGNER, H., AND HUMPHREY, J. Differential passive and active biaxial mechanical behavior of muscular and elastic arteries: basilar versus common carotid. *J Biomech Engrg*, 133:051009 (10 pages), 2011.
- [183] WANG, H. D., RÄTSEP, M. T., CHAPMAN, A., AND BOYD, R. Adventitial fibroblasts in vascular structure and function: the role of oxidative stress and beyond. *Can J Physiol Pharmacol*, 88(3):177–86, 2010.
- [184] WANG, K., MENG, X., AND GUO, Z. Elastin Structure, Synthesis, Regulatory Mechanism and Relationship With Cardiovascular Diseases. *Front Cell Dev Biol*, 9, 2021.

-
- [185] WANG, Y., CONG, Y., LI, J., LI, X., LI, B., AND QI, S. Comparison of Invasive Blood Pressure Measurements from the Caudal Ventral Artery and the Femoral Artery in Male Adult SD and Wistar Rats. *PLoS One*, 8(4):e60625, 2013.
- [186] WANG, Z., GRANGE, M., WAGNER, T., KHO, A. L., GAUTEL, M., AND RAUNSER, S. The molecular basis for sarcomere organization in vertebrate skeletal muscle. *Cell*, 184:P2135–2150, 2021.
- [187] WIN, Z., BUKSA, J. M., STEUCKE, K. E., GANT LUXTON, G. W., BAROCAS, V. H., AND ALFORD, P. W. Cellular Microbiaxial Stretching to Measure a Single-Cell Strain Energy Density Function. *J Biomech Eng*, 139(7):071006, 2017.
- [188] WIRTH, A., AND OFFERMANN, S. Chapter 85 - G-Protein-Coupled Receptors in Smooth Muscle. In *Muscle*, pages 1145–1153. Academic Press, 2012.
- [189] WITTER, K., TONAR, Z., AND SCHÖPPER, H. How many Layers has the Adventitia? – Structure of the Arterial Tunica Externa Revisited. *Anat Histol Embryol*, 46(2):110–120, 2017.
- [190] *World Heart Report 2023: Confronting the World's Number One Killer*. World Heart Federation, Geneva, Switzerland.
- [191] WRIGGERS, P. *Nonlinear Finite Element Methods*. Springer, 2008.
- [192] YAMIN, R., AND MORGAN, K. G. Deciphering actin cytoskeletal function in the contractile vascular smooth muscle cell. *J Physiol*, 590(17):4145–4154, 2012.
- [193] YANG, J., CLARK JR., J. W., BRYAN, R. M., AND ROBERTSSON, C. The myogenic response in isolated rat cerebrovascular arteries: smooth muscle cell model. *Med Eng Phys*, 25:691–709, 2003a.
- [194] YANG, J., CLARK JR., J. W., BRYAN, R. M., AND ROBERTSON, C. The myogenic response in isolated rat cerebrovascular arteries: vessel model. *Med Eng Phys*, 25:711–717, 2003b.
- [195] YAP, C., MIEREMET, A., DE VRIES, C. J. M., MICHA, D., AND DE WAARD, V. Six Shades of Vascular Smooth Muscle Cells Illuminated by KLF4 (Krüppel-Like Factor 4). *Arterioscler Thromb Vasc Biol*, 41(11):2693–2707, 2021.
- [196] YOSIBASH, Z., AND PRIEL, E. Artery active mechanical response: High order finite element implementation and investigation. *Comput Methods Appl Mech Engrg*, 237-240:51–66, 2012.
- [197] YOSIBASH, Z., MANOR, I., GILAD, I., AND WILLENZ, U. Experimental evidence of the compressibility of arteries. *J Mech Behav Biomed*, 39:339–354, 2014.
- [198] YOSSEF, O. E., FARAJIAN, M., GILAD, I., WILLENZ, U., GUTMAN, N., AND YOSIBASH, Z. Further experimental evidence of the compressibility of arteries. *J Mech Behav Biomed*, 65:177–189, 2017.

- [199] YOUNESI, F. S., SON, D. O., FIRMINO, J., AND HINZ, B. *Myofibroblast Markers and Microscopy* *Microscopy Detection Methods in Cell Culture* *Cell cultures and Histology*, pages 17–47. Springer US, New York, NY, 2021.
- [200] YOUNESI, F. S., MILLER, A. E., BARKER, T. H., ROSSI, F. M. V., AND HINZ, B. Fibroblast and myofibroblast activation in normal tissue repair and fibrosis. *Nat Rev Mol Cell Biol*, 2024.
- [201] YUEN, S., OGUT, O., AND BROZOVICH, F. V. MYPT1 Protein Isoforms Are Differentially Phosphorylated by Protein Kinase G. *J Biol Chem*, 286(43): 37274–37279, 2011.
- [202] ZAHN, A. Modeling of growth and fiber reorientation in soft biological tissues. *PhD thesis*, Ruhr Universität Bochum, 2020.
- [203] ZAHN, A., AND BALZANI, D. A combined growth and remodeling framework for the approximation of residual stresses in arterial walls. *Z Angew Math Mech*, 98:2072–2100, 2018.
- [204] ZIENKIEWICZ, O. C., TAYLOR, R. L., AND FOX, D. *The Finite Element Method for Solid and Structural Mechanics*. Butterworth-Heinemann, 7 edition, 2014.

Curriculum Vitae

Klemens Uhlmann
born April 11, 1991 in Schwedt, Germany

Education

- 10.2011 - 10.2017 Civil Engineering, Degree: Diplomingenieur (1.7)
Technische Universität Dresden
Implementation and Numerical Analysis of a Three-Dimensional
Mechanochemical Continuum Model for Smooth Muscle Contraction
- 09.2003 - 06.2010 Secondary Education, Gauss Gymnasium, Schwedt (1.8)

Professional Experience

- 12.2017 - 01.2024 Research Associate, Chair for Continuum Mechanics
Ruhr University Bochum
- 01.2020 - 12.2020 Research Associate, Max Planck Institute
for the Science of Light, Erlangen
- 04.2015 - 03.2017 Student Assistant, Institute of Mechanics and Shell Structure
Technische Universität Dresden
- 08.2015 - 12.2015 Student Assistant, Department of Radiological Sciences
University of California, Los Angeles
- 03.2011 - 09.2011 Internship in Rohrplan
Engineering-Office for Plant and Pipeline Planning, Schwedt
- 07.2010 - 12.2010 Military Service as Signalman in the Navy
Bremerhaven/Kiel

**Mitteilungen aus dem Institut für Mechanik
RUHR-UNIVERSITÄT BOCHUM
Nr. 197**

ISBN 978-3-935892-75-9